Quantum Chemical Studies of Actinides and Lanthanides: From Small Molecules to Nanoclusters

A DISSERTATION
SUBMITTED TO THE FACULTY OF THE GRADUATE SCHOOL
OF THE UNIVERSITY OF MINNESOTA
BY

Bess Vlaisavljevich

IN PARTIAL FULFILLMENT OF THE REQUIREMENTS
FOR THE DEGREE OF
Doctor of Philosophy

Professor Laura Gagliardi

June, 2013

Acknowledgements

There are many people that I would like to thank for all of their support through my graduate school years. First of all, I'd like to thank my advisor Prof. Laura Gagliardi for her encouragement, advice, and providing me with countless opportunities to develop as a scientist. Additionally, I'd like to thank Prof. David Blank and Prof. Chris Cramer for taking the time to be great mentors in teaching. I would also like to thank Prof. Chris Cramer for all of the helpful discussions in research as well.

I'd also like to thank the Chemistry faculty at the University of Minnesota – Twin Cities for all they have taught me. I'd also like to thank Profs. Joe Alia, Nancy Carpenter, Jenn Goodnough, Ted Pappenfus, and Jim Togeas at the University of Minnesota – Morris for starting me off on the right foot in my chemistry career.

I would like thank all of the collaborators from outside the University of Minnesota for the very useful discussions especially Prof. Thomas Albrecht-Schmidt, Prof. Lester Andrews, Prof. Carles Bo, Prof. Peter Burns, Prof. Scott Daly, Prof. Paula Diaconescu, Prof. Greg Girolami, Dr. Ivan Infante, Dr. Jason Keith, Prof. Stephen Liddle, Prof. May Nyman, Dr. Jie Qiu, Dr. Ginger Sigmon, Dr. Riccardo Spezia, and Dr. Tanya Todorova. I'd especially like to thank Dr. Enrique Batista and Dr. Richard Martin for provided a great learning environment during my short visit learning and working with them at LANL.

Next, I'd like to thank Pere Miró for all of the love and support over the last few years not only as my partner in crime but also as a colleague. The many hours we have spent discussing chemistry always reminds me how much I enjoy research even through the difficulties. It's too bad you don't want a cat.

A big thanks to the Gagliardi group members (past and present) for all of the scientific help, for the great friends you have become, and of course good lunchtime

conversation. Thank you Abbas, Allison, Alison, Abdul, Becky, Chad, David, Daniel, Danylo, Dongxia, Drew, Dylan, Ivan, Eileen, Giovanni, Huilang, Josh, Laura F., Laura L., Mike, Rémi, Sarah, and Toni. I especially like to thank Allison Dzubak, Nora Planas, and Dongxia Ma for keeping me company during many trips for coffee and always being willing listen. I'd like to offer a special thanks to Dr. Ivan Infante and Dr. Abdul Rehaman Moughal Shahi for taking the time during my first few years to answer my many many questions. I'd also like to thank the current and former Cramer group members especially Aaron, Ashley, Samat, Stuart, Josh, and Will. I'd also like to thank the other graduate students in my year in particular Deanna, Jacqui, Emily, Darren, Brian, Kelly, and Katie.

Finally I'd like to thank all of my wonderful family and friends. My time in graduate school would have been much less fun if I couldn't share it with all of you. And of course I am forever in debt to parents, my siblings, and the "other V's" (Dan, Molly, Ryan, Anna, Lala, and Gerry). You guys are the best!

Dedication

For
Pere Miró
my father Steve Vlaisavljevich
my mother Colleen Vlaisavljevich
my siblings Eli and Rose Vlaisavljevich

In memory of
my mother Theresa Vlaisavljevich

Abstract

Research into actinides is of high interest because of their potential applications as an energy source and for the environmental implications therein. Global concern has arisen since the development of the actinide concept in the 1940s led to the industrial scale use of the commercial nuclear energy cycle and nuclear weapons production. Large quantities of waste have been generated from these processes inspiring efforts to address fundamental questions in actinide science. In this regard, the objective of this work is to use theory to provide insight and predictions into actinide chemistry, where experimental work is extremely challenging because of the intrinsic difficulties of the experiments themselves and the safety issues associated with this type of chemistry. This thesis is a collection of theoretical studies of actinide chemistry falling into three categories: quantum chemical and matrix isolation studies of small molecules, the electronic structure of organoactinide systems, and uranyl peroxide nanoclusters and other solid state actinide compounds. The work herein not only spans a wide range of systems size but also investigates a range of chemical problems. Various quantum chemical approaches have been employed. Wave function-based methods have been used to study the electronic structure of actinide containing molecules of small to middle-size. Among these methods, the complete active space self consistent field (CASSCF) approach with corrections from second-order perturbation theory (CASPT2), the generalized active space SCF (GASSCF) approach, and Møller-Plesset second-order perturbation theory (MP2) have been employed. Likewise, density functional theory (DFT) has been used along with analysis tools like bond energy decomposition, bond orders, and Bader's Atoms in Molecules. From these quantum chemical results, comparison with experimentally obtained structures and spectra are made.

Contents

List of Tables

List of Figures

Preface

Citations from previously published work reproduced verbatim in this thesis.

Chapter 2: Quantum Chemical and Matrix Isolation Studies of Small Molecules

2.1 Reproduced with permission from:
B. Vlaisavljevich, L. Gagliardi, X. Wang, B. Liang, L. Andrews, and I. Infante *Inorg. Chem.* **2010**, 49, 9230–9235.
Link: `http://pubs.acs.org/doi/abs/10.1021/ic100407e`

2.2 Reproduced with permission from:
X. Wang, L. Andrews, B. Vlaisavljevich, and L. Gagliardi *Inorg. Chem.* **2011**, 50, 3826–3831.
Link: `http://pubs.acs.org/doi/abs/10.1021/ic2003244`

Chapter 3: Combined Theoretical and Experimental Studies of Oraganoactinide Compounds

3.1 Reproduced with permission from:
B. Vlaisavljevich, P. Miró, C. J. Cramer, L. Gagliardi, I. Infante, and S. T. Liddle *Chem. Eur. J.* **2011**, 17 (30), 8424–8433.
Link: `http://onlinelibrary.wiley.com/doi/10.1002/chem.201100774/abstract`

3.2 Reproduced with permission from:
B. Vlaisavljevich, P. Miró, D. Koballa, T. K. Todorova, S. R. Daly, G. S. Girolami, C. J. Cramer, and L. Gagliardi *J. Phys. Chem. C* **2012**, 116, 23194–23200.
Link: `http://pubs.acs.org/doi/abs/10.1021/jp305691y`

3.3 Reproduced with permission from:
B. Vlaisavljevich, P. L. Diaconescu, W. L. Lukens, Jr., L. Gagliardi, and C. C.

Cummins *Organomet.* **2013**, 32, 1341–1352.
Link: http://pubs.acs.org/doi/abs/10.1021/om3010367

Chapter 4: Uranyl Peroxides and Solid State Actinide Compounds

4.1 Reproduced with permission from:
B. Vlaisavljevich, L. Gagliardi, P. C. Burns *J. Am. Chem. Soc.* **2010**, 132 (41), 14503–14508.
Link: http://pubs.acs.org/doi/abs/10.1021/ja104964x

4.2 Coauthors of this chapter are P. Miró, S. Hu, A. Dzubak, R. Spezia, C. J. Cramer, and L. Gagliardi

4.3 Reproduced with permission from:
B. Vlaisavljevich, P. Miró, D. Ma, G. E. Sigmon, P. C. Burns, C. J. Cramer, L. Gagliardi *Chem. Eur. J.* **2013**, 19 (9), 2937–3941.
Link: http://onlinelibrary.wiley.com/doi/10.1002/chem.201204149/abstract

Chapter 1

Introduction

1.1 Introduction

Actinides have been actively studied since the actinide concept was publicly introduced in 1945 [1]. However, uranium, the heaviest abundant element that occurs naturally, has been known and studied for much longer. In fact, compounds containing uranium were used in Roman times as colorants. The uranium mineral pitchblende, now called uraninite, was known as early as the 1500s, and to date mineralogists have discovered a wealth of uranium chemistry in nature including over 200 uranyl (UO_2^{2+}) minerals that are typically soluble in water and react with fossilized plants, methane, and other reducing agents. [1–3] However, it wasn't until 1789 that Martin Heinrich Klaproth officially discovered the first impure uranium oxide. Uranium species continued to be used for the next century, mostly as ceramic dyes. Over time, the radioactive nature of uranium came to light, first through Henri Becquerel's work with uranium salts. It was Marie Curie who coined the term radioactivity and along with her husband, Pierre, worked to quantify the extent of the radiation, not only in uranium, but in thorium, polonium, and radium as well [1, 3]. In 1938, Hahn, Meitner, and Strassman discovered nuclear fission which has led to some of the most important technological and environmental problems facing the modern world [1]. As a result, the primary concern for most actinide chemists today centers on nuclear technologies and the inherent problems associated therein.

Large scale problems have resulted from the atomic age. These include wastes generated by commercial nuclear reactors for electricity, nuclear weapons production

and dismantlement, and the clean up of storage sites remaining from the Cold War. [1] In particular, many processes in the commercial fuel cycle lead to the generation of waste, see Figure 1.1. Approximately 60,000 tons of high-level waste, the most radioactive of the waste forms, is being stored in over 100 "temporary" sites in the United States alone. [3, 4] Across the globe tens of thousands of tons continue to be generated each year. Although this presents challenges from a scientific perspective, the importance of politics cannot be overlooked. The recent disaster at the Fukishima Daiichi power plant reinforced the importance of understanding how actinides behave in nature and drew attention to the impact one nation's nuclear energy program can have on the rest of the world. [5] While accidents are one way actinides can be released into the environment, nations have plans for geological repositories for long term storage of actinide materials. In North America, the only operating repository is the Waste Isolation Pilot Program (WIPP) located east of Carlsbad, New Mexico where waste from the research and production of nuclear weapons is being deposited. [3] It is noteworthy that this waste is much less radioactive than the irradiated fuel from a commercial nuclear reactor; no repository currently accepts this type of waste. Moreover, the political climate has led to the termination of plans for long-term repositories in both the United States and Canada for commercial spent fuel. [3] Despite hesitations in North America, France has made significant investments in the nuclear industry and in 2012 74.8% of the nations energy was generated by nuclear reactors. [6] Not only is France opting to reprocess fuel but continues to plan for the geological storage of high-level waste. [3]. Moreover, China currently has 28 new reactors under construction, more than any other nation. [7] These large scale challenges, while daunting, cannot be tackled by one nation alone and require interdisciplinary research ranging from the fundamental to the applied.

While these challenges are certainly cause for concern, it is unlikely that nuclear power will be forsaken. Global energy demands are increasing and nuclear power is a virtually carbon-free energy source. Given the likelihood that the use of nuclear power will continue, developing a true fuel cycle would greatly reduce the amount of waste that is produced, and fundamental actinide science is an essential component in these efforts. One could imagine working to improve many areas of the cycle from reducing the amount of waste generated in mining and enrichment on the front end to improving the reprocessing and the storage of the waste at the end of the cycle. [2, 3] Efforts in

all areas are necessary to reduce environmental impact; however, the work herein is most relevant for separations required in reprocessing. When one turn in the fuel cycle has been made, 95% of the uranium in the spent fuel rods is unspent. [3] It is not the lack of uranium that renders a fuel rod useless but the presence of fission products that absorb neutrons effectively stopping the reactor. By separating these so-called nuclear poisons like xenon-135 and samarium-149 from the unused uranium, fuel rods can be regenerated and a second turn through the cycle can be made. Technology currently in use is a modified form of the Plutonium–Uranium Extraction (PUREX) process and was developed in 1947. [8] As the name suggests, during this process a series of liquid–liquid ion exchange extractions are performed resulting in the isolation of uranium and plutonium. However, this process generates significant amounts of additional waste and was developed during the Manhattan project to isolate plutonium for weapons production. [3, 8] As a result, reprocessing in the United States with PUREX became politically unfavorable during President Carter's administration due to the fear of weapons proliferation risks. The work in this thesis is motivated by efforts to improve separations chemistry and reprocessing by gaining fundamental insights into the electronic structure and solution chemistry of the actinides. Our hope is that deciphering subtle differences in bonding between uranium and other metals will contribute to the design of improved technologies.

Additionally these differences in bonding are not only important in the PUREX process where high concentrations of actinides are present but also in low concentrations either in the environment or in the laboratory. The coordination chemistry of the actinides is less developed in comparison with the transition metals and high coordination numbers are common. Discoveries of new and unexpected coordination environments occur often. In particular, subtle differences in bonding between the ligand and the valence d and f orbitals are of high interest as efforts to control and exploit these differences is ongoing. While this research is fundamental in nature, it is an essential component in understanding the behavior of low concentrations of actinides in the environment and in water whether it is in the lab, in nature, or following accidents like Fukushima or Chernobyl. Furthermore, actinides can adopt coordination environments otherwise inaccessible with the more commonly studied transition metals and exists in a wide range of oxidation states. Therefore actinides may provide unique opportunities

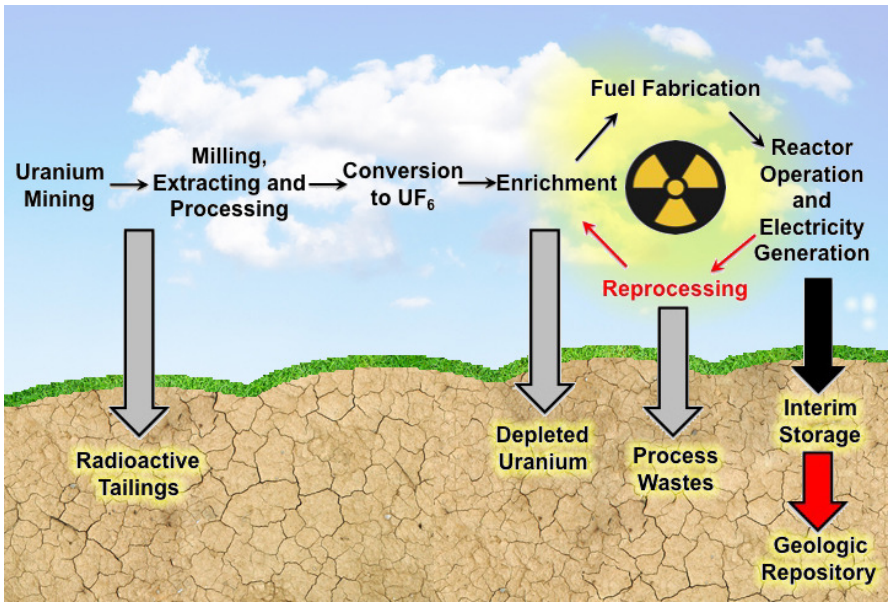

Figure 1.1: Schematic representation of the nuclear fuel cycle. Currently, the United States and Canada do not reprocess spent fuel and a location for a geological repository has not been chosen. For this reason, these portions of the cycle are shown in red.

in catalysis including small molecule activation and multi-electron processes. [9–12]

Herein we present a collection of theoretical studies of actinide containing systems ranging in size from diatoms to the nanoscale exploring a variety of chemical problems. Given the diversity of the systems of interest, the introduction will discuss three topics: quantum chemical and matrix isolation studies of small molecules, the electronic structure of organoactinide systems, and uranyl peroxide nanoclusters and other solid state actinide compounds.

Quantum Chemical and Matrix Isolation Studies of Small Molecules. Multiple bonding between uranium and main group elements is of high interest with special emphasis on the use of U as a catalyst. [10, 13–17] By studying small molecules in the absence of a ligand field containing bonding between uranium and oxygen, nitrogen, phosphorus, sulfur or carbon, for example, insight into new coordination chemistry can be obtained with the goal of inspiring the design of future catalysts. [10] The most common uranium multiple bond occurs in the uranyl diction, UO_2^{2+}. Uranyl is the predominant form of uranium in water and contains two uranium-oxygen triple bonds.

While U(VI)≡O bonds like those in uranyl are common, non-reactive, and have been widely studied, fewer bonds between uranium and the other main group elements are known. Among them, imido (An=NX), phosphinidene (An=PX), U=S, U=CX, and N-U-N molecular linkages have been synthesized. [14–18] Moreover, small molecules such as P≡UF_3, N≡U=O, NH=UH_2, N≡UF_3, CH_2=UH_2, U≡C, and US_2 have been characterized in matrix isolation experiments and via density functional theory. [19–28] The linear NUN molecule is isoelectronic to the uranyl dication and has been observed only by matrix isolation spectroscopy. [19–22, 29] First, Green and Reedy studied the reaction of an 0.5% N_2/Ar mixture within a uranium hollow cathode and observed both UN and NUN. [29] Later work by Andrews and coworkers confirmed the formation of these species obtaining NUN in greater yield [19, 20]

One portion of this thesis examines isolated actinide-containing molecules. By laser ablating uranium metal and permitting it to come in contact with another reactant in a noble gas matrix, a series of products form and are characterized by IR spectroscopy. The information about the electronic structure and geometry of these systems via quantum chemical calculations is then used to assign their IR spectra measured in the matrix. In practice, all isomers that may form under experimental conditions are first studied at the density functional (DFT) level of theory, and many possible products are considered in an initial scan. Geometry optimizations in the gas phase are performed followed by harmonic vibrational analysis. Peak assignments are based on these modes while further support for product formation is provided through the comparison of formation energies for competing reactions. Experiments are performed at very low temperatures (2-5 K); therefore, only the lowest electronic state is accessible and free energies need not be compared.

The success of DFT in studying these species depends on the electronic structure of that particular system. These small molecules may have low-lying excited states arising from near degeneracies in the valence region. In these cases, multireference methods are necessary. Given the high probability of a multiconfigurational ground state, the standard approach has been to first select the most promising candidates using DFT and subsequently perform complete active space self consistent field calculations with corrections from second order perturbation theory (CASSCF/CASPT2). [30–34] The CASSCF approach is a post-Hartree Fock method in which the user chooses a

set of molecular orbitals and corresponding electrons, referred to as the active space. Within the active space, the full configuration interaction (CI) expansion is allowed accounting for all possible electronic configurations. The CI coefficients in this expansion are optimized while simultaneously performing orbital optimization over the entire set of orbitals. As a result, this method is not black-box and requires that a chemically reasonable choice is made. [35]

Fortunately, some guidelines for choosing an active space have been established. [35, 36] The active space should be large enough to account for all of the configurations attributing to the near-degeneracy of states. This likely means including all of the orbitals in the valence space that are close in energy. In practice, one approach would be to include all of the molecular orbitals that are linear combinations of the atomic valence orbitals. In this case, the active space for a uranium containing system should include the thirteen valence orbitals of uranium (7s, 6d, and 5f) along with the valence orbitals and corresponding electrons from each ligand atom. This works well for molecules like diatomic UN where three additional 2p orbitals from N are included along with the 13 orbitals from uranium leading to an active space with nine electrons and sixteen orbitals (see Figure 1.2). In practice, this is not always feasible due to system size and a truncated active space is used. It is important to emphasize that for species with multiple bonding between the uranium and a ligand, both the 5f and 6d orbitals can (and do) engage in covalent bonding. When required for these systems, truncating the active space is often based on ligand field splitting. In particular, orbitals with occupation numbers that are nearly two can be placed in the inactive space and those with occupation numbers that are nearly zero can be taken as virtual. Specifically, occupation numbers greater than 1.98 or less than 0.02 need not be included in the active space. For a given active space, the ground state is determined at the CASPT2 level although spin-orbit coupling can be included *a posteriori* using an effective one electron spin-orbit Hamiltonian based on the mean field approximation of the two electron part, the restricted active space state interaction (RASSI) approach. [37] Analysis of the nature of the multiple bonding in the ground state can be described by computing the effective bond order (EBO). [38] The EBO is defined as half of the difference between the sum of the occupation numbers of the bonding orbitals minus the sum of the occupation numbers of the antibonding orbitals. While the EBO was initially defined for metal

dimers, the concept can be extended to species where the multiple bonding occurs between two different atoms. [39–41] For example, referring again to Figure 1.2, the EBO for UN is 2.87 and therefore can be described as slightly weaker than a triple bond. In Section 2.1, the EBO is used to make comparisons between U-N multiple bonds and U-P multiple bonds.

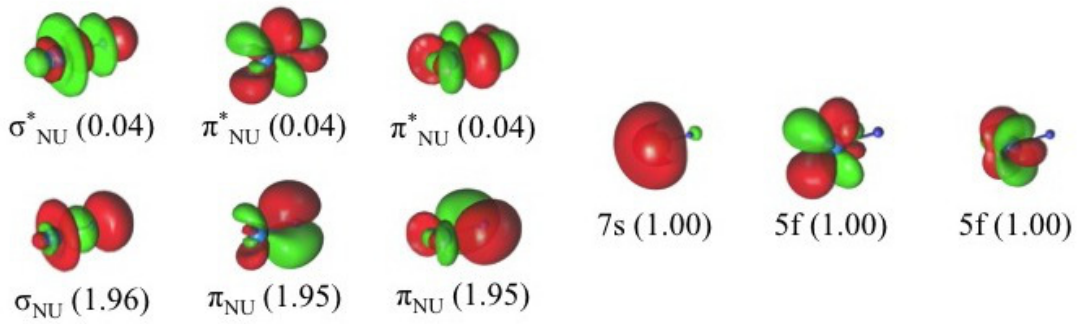

Figure 1.2: Select natural orbitals from the (9,16) active space of UN. Natural orbital occupation numbers are in parentheses. The remaining active orbitals have occupation numbers less than 0.01 and are not shown.

If feasible, CASPT2 geometry optimizations and vibrational frequency calculations are also performed for direct comparison with experimental modes. As expected, the absolute values of the calculated frequencies are shifted from those obtained from experiment in part due to the harmonic approximation. However, the shifts observed are often larger than expected from the harmonic approximation alone since the matrix is not innocent in these experiments. The neon matrix has less of an effect and comparisons with computed spectra (e.g. gas phase) are often in good agreement. This is not true for an argon matrix where the frequencies observed can shift significantly. Perhaps the most cited example is the challenging linear CUO molecule. Li et al. [42] first noted in 2002 that the stretching frequencies of CUO varied depending whether the species was prepared in an argon or neon matrix. These differences were not small: U–O bond stretch was 872.2 and 804.3 cm^{-1} and the U–C stretch was 1047.3 and 852.5 cm^{-1} in argon and neon respectively. What they ultimately concluded was that the

ground state of the CUO molecule shifts from a closed shell $^1\Sigma^+$ ground state to a $^3\Phi$ ground state when going from the neon matrix to the argon matrix. Subsequent studies used CASSCF/CASPT2 and found that a definitive assignment of the CUO ground state remained an open question. [43] This example is cited to emphasize the inherent challenges present in studying small actinide containing systems and to stress the importance of making careful comparisons between experimental and theoretical results.

The importance of fundamental work in uranium coordination chemistry is discussed in the context of the studies in Chapter 2. In section 2.1, we study reactions of laser-ablated U atoms with P_4 molecules upon condensation in excess argon. First, we find that two stable UP_4 adducts are formed that may be considered simple models for P_4 activation products. Additionally, the anticipated PUP reaction product absorption likely falls under the strong P_4 precursor band. The $^3\Phi_u$ ground state of PU(IV)P and the higher energy $^1\Sigma_g^+$ state of PU(VI)P were explored and compared with the $^1\Sigma_g^+$ ground state of NU(VI)N demonstrating that the third row element, P, is less effective for π bond formation than second row element, N. Likewise, in Section 2.2, the reactivity of the stable NU(IV)N molecule is further explored. Terminal uranium nitrides are very reactive, [44] and argon matrix experiments have isolated four unsupported terminal uranium nitride molecules prior to this work UN, NUN, NUO, and NUF_3. In this work, the reactivity of NUN with hydrogen atoms under ultraviolet irradiation is explored and shown to form the uranium(V) nitride imide molecule, N≡U=N−H. This unusual U(V) molecule is identified through infrared spectroscopy and quantum chemical calculations and found to contain a nitride triply bonded to uranium and a parent imine doubly bonded to uranium.

Combined Theoretical and Experimental Studies of Oraganoactinide Compounds. Although uranium coordination and multiple bonding can be explored by stabilizing new structures within a noble gas matrix, the majority of chemistry occurs in the condensed phase. Species that can be isolated in a noble gas matrix can often be stabilized by a ligand field as well. Uranium-nitrogen bonding has been studied in this work and a good example of analogies between bonding motifs in matrix studies and synthetic organoactinide chemistry is the matrix isolated $NH{=}UH_2$ species and a wide variety of uranium imido compounds, including one from Section 3.3 (Figure 1.3). [45]

While this chapter is about organoactinide chemistry in a broader sense, we emphasize that lessons learned from small molecules containing actinides are not mutually exclusive from those explored through the synthesis of organoactinide complexes.

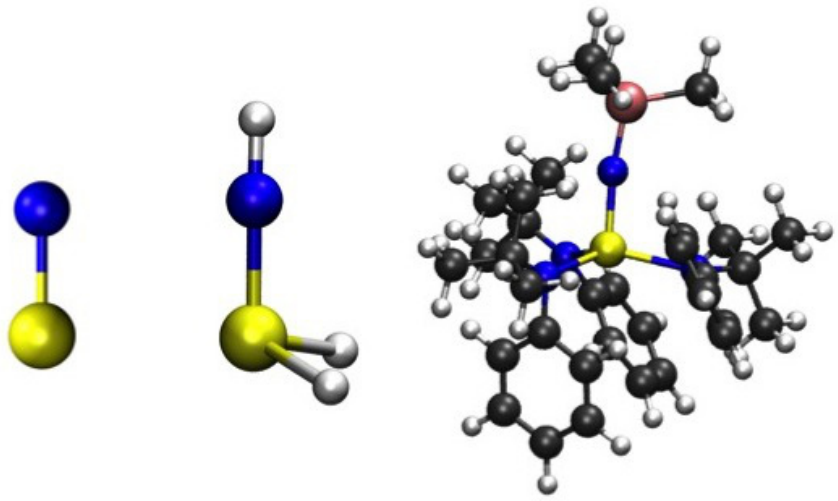

Figure 1.3: From left to right, the UN, NH=UH_2, and $(Me_3SiN)U(N[^t Butyl]Ph)_3$ molecules presented as examples of small actinide containing species studied in a noble gas matrix with bonding analogous to structures synthesized in the solid state.

Additionally, the computational chemistry tools used to study small molecules can be applied to organoactinide systems, with some small distinctions. These systems are larger than those addressed previously and focus on different chemical problems. The presence of the ligand field stabilizes charged metal cations which can reduce the complexity of the electronic structure problem as fewer electrons are present in the valence region; however, the bulk of the ligand must also be taken into account increasing the number of atoms that must be treated. In comparison with matrix studies, much more experimental data is available for these compounds. Single crystal X-ray diffraction is often used to characterize the product and provides a starting point for geometry optimizations with density functional theory. In some cases, bulky groups on the ligand may be truncated provided they are not expected to alter the nature of the ground state, reactivity, or bonding of interest. When truncations are made, comparisons with the experimental structure will be used to ensure that the geometry has not changed

dramatically as a relic of truncation in particular within the first coordination sphere of the metal.

From DFT results, further analysis including the so-called atoms in molecules developed by Bader, Mayer bond orders, and bond energy decomposition are used to quantify bonding interactions in particular to make comparisons between actinide and lanthanide containing systems. [40, 46–50] These tools are often used to describe the extent ionic or covalent interactions play a role in bonding. As was described in the previous section, multiconfigutarional methods like CASSCF/CASPT2 may be necessary for actinide containing systems. For higher oxidation states with fewer valence electrons DFT often performs quite well; however, performing CASSCF/CASPT2 calculations on the DFT geometry is often useful to confirm the DFT ground state and to explore the electronic structure in more detail. This is particularly important when multiple bonding, multiple metal centers, or low-valent oxidation state states are involved. Moreover, even for cases when the ground state is well-described at the DFT level, interpretation of the bonding by inspection of the delocalized Kohn-Sham orbitals can lead to an overestimation of the covalent contributions to bonding. CASSCF natural orbitals are in general more localized and in combination with their occupation numbers can be used to properly characterize a multiple bond.

Actinide chemists are especially interested in distinctions between covalent and ionic bonding as they routinely emphasize this difference between the actinides and the lanthanides. Lanthanides form complexes that predominantly contain trivalent cations and follow clear size-based trends across the period. Ln-ligand bonding is dominated by electrostatics and has negligible "covalent" interactions due to the core-like 4f orbitals. [51] As one moves across the lanthanides from lanthanum to ytterbium, the ionic radii gradually decreases, an effect known as the lanthanide contraction. This leads to changes in coordination chemistry that can be understood by size effects alone.

The actinides, on the contrary, do not follow one trend across the period and a clear division exists between the early and late actinides. This has been attributed to the ability of the 5f and 6d orbitals to engage in covalent bonding, particularly in the early actinides. Thorium occurs predominantly in the (IV) oxidation state in which no valence electrons are present. Furthermore, protactinium has drawn less research attention historically since it does not exist in large quantities, although research interest

has risen in recent years due to the role it is thought to play in a thorium based nuclear fuel cycle. Uranium, neptunium, and plutonium form the next group of actinides. They exist as the actinyl ions, AnO_2^{n+}, in their highest oxidation states although they can access a wide range of oxidation states. For example, uranium can access oxidation states from (II) to (VI) in the solid state. Oxidation states (IV) and (VI) are the most common and are found most often in uranium minerals although some U(V) minerals are known. [3] For example the mineral uraninite is a U(IV) mineral composed mostly of $U(IV)O_2$. When uraninite comes in contact with water, the uranyl ion, UO_2^{2+}, the predominant form of uranium in water is formed. As a result, uranyl mineral deposits are often found on the surface of uraninite. The split between the early and late actinides starts with americium. [52] In general, the late actinides are more lanthanide like and form trivalent cations. [53] Both the transplutonium species and the lanthanides can act as Lewis acids, have large ionic radii, have high coordination numbers (typically 8 or 9), and prefer interactions with hard acid donor atoms such as oxygen or carboxylate, alkoxide, and fluoride anions. [54, 55]. In consequence, separating the higher actinides from lanthanides is a challenging issue. [53, 56, 57] Nevertheless, exploiting subtle differences in the bonding between the lanthanides and actinides can be used to design chelating ligands selective for one ion over another. [1] For example, as early as 1964, the di-(2-ethylhexyl)phosphoric acid (HDEHP) ligand was shown to extract lanthanides much more readily than actinides from aqueous carboxylic acid solutions also containing an aminopolycarboxylic acid chelating agent. [58] Research into separations chemistry has continued and discussions regarding the details of these "subtle differences" between actinides and lathanides have lead to much controversy surrounding the role 5f orbital covalency therein. [51, 59–61] Efforts to understand these differences could make a significant impact in modern nuclear fuel cycles where separations between Am(III) and Cm(III) with trivalent lanthanides are required. [1]

In this work, three problems in organoactinide chemistry are addressed in Chapter 3 with special emphasis on characterizing metal-ligand bonds. First, in Section 3.1, several systems containing heterobimetallic bonds involving one f-block element were studied computationally. Although several other complexes were explored, specific attention was placed on the nature of the bond between U–Re in $\{N(CH_2CH_2NSiMe_3)_3\}URe(\eta^5\text{-}C_5H_5)_2$, [62] and U–Ga in $[\{N(CH_2CH_2NSiMe_3)_3\}U\{Ga(NArCH)_2\}(THF)]$, [63] in

which π bonding interactions were suggested to be present. Through this study we found similar bonding in all of the complexes. Moreover, no 'true' σ and π bonds were present, but rather σ-type donation from the metal ligand fragment to the Ln/An fragment. While a π-donation is possible in the system containing a U–Re bond, this interaction is extremely weak and not expected to alter the reactivity of the species. Alternatively, in Section 3.2, a series of lanthanide and uranium complexes with the dimethyaminodiboranate (DMADB) ligand were studied. These volatile complexes have high coordination numbers (from 12 to 14) and are potential precursors for chemical vapor deposition (CVD). The size effects and strength of the M—H bonding were examined in order to interpret experiment. Finally, in Section 3.3, XANES spectroscopy, X-ray crystallography, and computational studies were used to study an inverse sandwich compound (U-toluene-U) along with a variety of mononuclear uranium amide complexes. While the mononuclear compounds show expected electronic and magnetic properties, the optical and magnetic properties of the toluene-bridged compound are discussed in this section.

Uranyl Peroxides and Solid State Actinide Compounds. Returning to the discussion of uranium in nature, uranyl speciation and crystal chemistry are of high interest in uranium aqueous chemistry. Mineralogists are very interested in uranyl species since they are soluble in water and reactive. There is particular interest in the behavior of uranyl in a peroxide rich environment, since uranyl peroxides are thought to be an important alternation phase of spent nuclear fuel. Spent fuel releases alpha radiation and causes water to undergo alpha radiolysis, see Equation 1.1.

$$H_2O + \alpha^{2+} \rightarrow H^{\bullet} + HO^{\bullet} \tag{1.1}$$

Over time, the generation of hydroxyl radicals will lead to the formation of hydrogen peroxide. Given the importance of understanding the most stable compounds for long-term storage of spent fuel, researchers often turn towards mineralogy. However, only one uranyl peroxide mineral, studtite, has been characterized. [64] Uranyl minerals are often soluble and are shorter lived than U(IV) minerals. The transient nature of these species has reinforced the importance of studying synthetic uranyl compounds. Typical topologies in uranyl crystal chemistry, found both in nature and in the lab, are chain or sheet structures. The uranyl (UO_2^{2+}) oxo group is unreactive and therefore

coordination occurs exclusively in the equatorial plane where typically four to six ligands bind. Some framework topologies are found for uranyl compounds; however, the three-dimensionality arises from the bridging ligand and not the uranyl coordination environment. Studtite is no exception and consists of uranyl hexagonal bipyrimids linked in a chain topology through bridging peroxide groups with the remaining sites in the uranium coordination sphere filled by water ligands (see Figure 1.4). [64] A synthetic version referred to as uranyl peroxide hydrate, $UO_4{\cdot}nH_2O$, can be formed under acidic conditions.

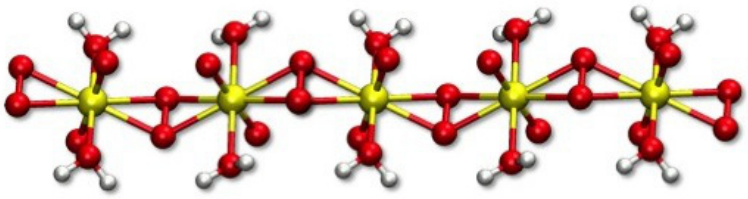

Figure 1.4: A ball and stick representation of the chain topology of the mineral studtite, ($[(UO_2)O_2(H_2O)_2]{\cdot}2(H_2O)$). Interstitial waters are not shown in the figure. These water molecules are present in studtite; however, metastudtite, the lower hydrated version of the mineral, only contains water coordinated to uranyl.

In the last few years, there has been significant interest in exploring other uranyl peroxide phases. Naturally occurring environments that contain uranium deposits that are peroxide rich are not prevalent enough to be used as a model for long term storage of spent fuel. Therefore, work to explore the crystal chemistry of uranyl peroxide compounds in a wide range of conditions is ongoing. Burns and coworkers were the first to synthesize a family of uranyl peroxide nanocapsules in which uranyl polyhedra are bridged to one another through peroxide and hydroxide groups (see Figure 1.5). [65–68] This discovery sparked interest in the solid state actinide community, since these clusters are a significant departure from the expected chain and sheet structures. Furthermore, they present the opportunity to obtain nanoscale control of the actinides. To date, nanocapsules have been characterized containing up to 120 uranyl polyhedra in a variety of high symmetry topologies including fullerenes and some with topological squares. [66, 67] More recently other bridging ligands have been used such as oxalate

or pyrophosphate allowing the synthesis of capsules at a more acidic pH. [69–73] Moreover, this self-assembly occurs in aqueous solution at ambient conditions suggesting that these clusters, although short lived with respect to geological timescales, are likely to exist in environmental conditions. In fact, following the Fukishima Daiichi disaster, it was demonstrated that the combination of seawater and reactor contents could result in a environment favorable for cluster growth [74]. Many questions remain regarding the impact cluster formation would have on the transport of actinides in nature both with respect to situations like Fukishima but also for storage of waste in the geological time scale where many researchers argue that containment will ultimately fail allowing water to come in contact with irradiated fuel. Additionally, a potential application for these capsules in the nuclear fuel cycle has been proposed. Uranyl nanocapsules can be formed readily when the right pH and peroxide concentrations are added to a uranium source in water. On the contrary, peroxide reduces plutonium so it no longer exists as an actinyl ion. Consequently, analogous plutonium capsules cannot be formed under these conditions. Based on this difference, it has been proposed that spent nuclear fuel could be used as the uranium source for uranyl peroxide cluster growth. Once clusters are formed they can be size separated from the ions in solution including plutonium. It should be noted that this separation would not isolate uranium from neutron poisons and further separations would be needed. However, by separating the uranium without isolating plutonium the hope is that political opposition to reprocessing would decrease.

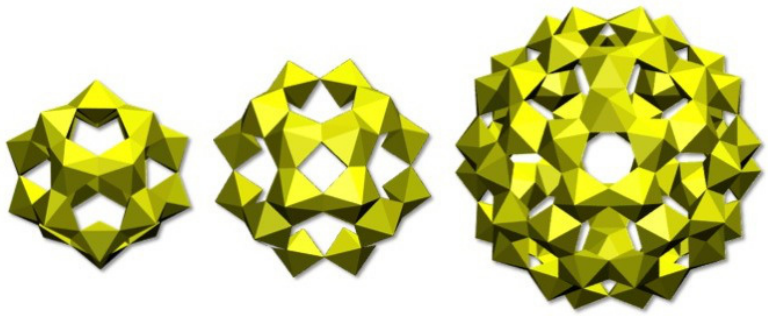

Figure 1.5: Polyhedra representations of the U_{20} cluster, $[(UO_2)_{20}(O_2)_{30}]^{20-}$, the U_{24} cluster, $[(UO_2)(O_2)(OH)]_{24}{}^{24-}$, and the U_{60} cluster, $[(UO_2)(O_2)(OH)]_{60}{}^{60-}$. Species present inside the cluster are not shown or included in the structural formula.

With the wide variety of cluster topologies that have been synthesized, several building blocks were proposed in 2010. [65, 66, 68, 75, 76] Section 4.1 in this thesis details work on the dimeric and pentagonal building blocks, $[(UO_2)_2(O_2)(L)_4]^{6-}$ and $[(UO_2)_5(O_2)_5(L)_5]^{10-}$, respectively (L = $C_2O_4^{2-}$ or O_2^{2-}. We found that the torsion angle U-O_2-U, see Figure 1.6, was more bent in the presence of the smaller alkali counterions than in the presence of the larger counterions consistent with X-ray diffraction data. [75] Additionally work by Miró et al. [76] explored ion pairing between the square, pentagonal, and hexagonal building blocks of the nanoclusters. They found that the square face preferred to have Li^+ or Na^+ underneath it while the pentagonal face could readily accommodate Na^+ or K^+. Alternatively, they found that the hexagonal face could adapt boat or chair conformations and binding energies were not greatly effected by the size of the alkali ion [76].

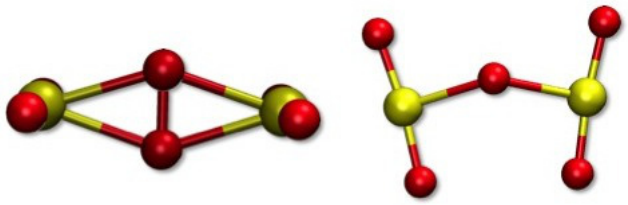

Figure 1.6: The bent U-O_2-U butterfly dihedral angle shown from the top (left) and the side (right).

Analogous to the U_{24} capsule shown in Figure 1.5, a Np_{24} cluster has been synthesized. [65] Due to the increased cost and difficulty associated with neptunium syntheses, less synthetic effort has been undertaken; however, it is likely that a wide range of topologies could be formed with neptunyl as well. Furthermore, the neptunyl cation is analogous to uranyl except it can exist both as $Np(V)O_2^+$ and $Np(VI)O_2^{2+}$. As a result, controlling neptunium speciation while varying conditions for cluster growth is more challenging. Additionally, the oxidation state of neptunium in the Np_{24} cluster has been suggested to be mixed valent; however, more work is necessary to understand the electronic structure of these capsules. The lower charge on neptunyl (V) compared to uranyl and neptunyl (VI) results in an interaction between ions referred to by actinide chemists as a cation–cation interaction (CCI). This term was first coined by Sullivan

et al. [77] after observing short distances between uranyl and neptunyl (V) in aqueous solution. Eventually, it was discovered that the oxygen atom of one actinyl ion was coordinating to a second actinyl ion as an equatorial ligand. Another way to think of this interaction is that the actinide center acts as a Lewis acid while the uranyl oxgen can act as a Lewis base. CCIs are most commonly observed in the solid state for actinyl (V) cations although several compounds with CCIs between actinyl (VI) ions have been reported. Understanding CCIs has important implications in separations and the crystal chemistry of the actinides. For example, CCIs between neptunyl (V) and uranyl (V) cations are important in the proposed mechanism for their disproportionation since electron transfer can occur through the bridging oxo species.

Like the previous sections, a combination of density functional theory and wave function-based methods can be used to obtain information about the electronic structure and bonding. In Section 4.3, the synthesis and characterization of the first 2D neptunyl structure stabilized by side-on cation–cation interactions is studied. In Sections 4.1 the electronic structure of the uranyl peroxide U-O_2-U dihedral angle is studied in detail as its configuration encourages curvature and cage cluster formation. This initial study only explored building blocks of the nanocapulse. While density functional theory has been used to study the full uranyl peroxide nanoclusters $[(UO_2)_{20}(O_2)_{30}]^{-20}$ **(U_{20})** and $[(UO_2)_{28}(O_2)_{42}]^{-28}$ **(U_{28})** these studies were focused on refining the understanding of solid state structures based on single crystal X-ray diffraction. [78, 79] In order to study the water and counterion dynamics of these capsules, a classical force field was developed and is discussed in Section 4.2.

1.2 Organization of the Thesis

The purpose of this thesis is to report work exploring actinide containing systems ranging in size from diatoms to the nanoscale. Toward this end, the thesis is divided into three chapters based on the chemical problem of interest and the system "size".

Chapter 2: Quantum Chemical and Matrix Isolation Studies of Small Molecules This chapter presents quantum chemical and matrix isolation studies of small molecules. These systems are small in size but often require the consideration of

many electronic configurations. Three studies are included. In the first, white phosphorus, P_4, and uranium were allowed to react under matrix conditions in an attempt to form new uranium phosphorus multiple bonds. We show that it was not the sought after PUP species that was formed but a UP_4 compound formed by the insertion of U into a P_4 bond. Next, the reaction of U with N_2/H_2 mixtures to form the N≡U=NH molecule that contains both triple and double uranium-nitrogen bonds as characterized by the infrared spectrum and theoretical computations is included.

Chapter 3: Combined Theoretical and Experimental Studies of Oraganoactinide Compounds This chapter follows a series of studies on organoactinide systems. These systems are mid-range both in the number of atoms and the number of configurations required to be treated appropriately. In this chapter, the first two sctions focus on the differences between the lanthanides and the actinides. In Section 3.1, heterobimetallic bonds containing actinides and lanthanides with transition metals is explored to determine if multiple bonding is present in any of the cases. Section 3.2 examines lanthanide and uranium complexes with the dimethyaminodiboranate (DMADB) ligand and their applications as chemical vapor deposition precursors. Finally, Section 3.3 includes an inverse sandwich complex (a uranium-arene-uranium) in comparison with uranium complexes will well known oxidation states to understand the electronic structure of the new compound.

Chapter 4: Uranyl Peroxides and Solid State Actinide Compounds The chapter includes work on uranyl peroxide nanocluster and other solid state actinide compounds. These systems are most complex in the system size but in general contain less challenging electronic structure problems. In Sections 4.1 to 4.2, the family of uranyl peroxide nano capsules will be discussed. First, a study of the effect of counterions on the U-O_2-U dihedral angle is presented followed by a mechanistic study of the growth of the smallest building block, $(UO_2)_2(O_2)^{2+}$. Following the study of the dimer with quantum mechanical methods, the next section discusses a building block approach for the development of uranyl peroxide force field in order to study water and counterion structure surrounding the capsules. Finally, the study of a neptunyl sheet structure that contains a rare side-on cation-cation interaction is presented in Section 4.3.

Chapter 2

Quantum Chemical and Matrix Isolation Studies of Small Molecules

2.1 U and P_4 Reaction Products: A Quantum Chemical and Matrix Isolation Spectroscopic Investigation

Reactions of laser-ablated U atoms with P_4 molecules upon codeposition in excess argon gave weak new infrared absorptions at 504, 483, and 426 cm^{-1}, which are best identified as binary uranium phosphide UP_4 species based on extensive B3LYP, BPW91, and PBE density functional and CASSCF/CASPT2 wave function based calculations. These UP_4 adducts may be considered as simple models for P_4 activation products by ligand-supported transition and main group metal complexes. The sought-after PUP molecule in the $^3\Phi_u$ ground state probably absorbs under the intense P_4 precursor band near 465 cm^{-1}. The triplet U(IV) molecule PUP is 7 kcal/mol lower in energy than the U(VI) analog, singlet PUP. The $^3\Phi_u$ ground state of PUP, with 2.54 effective bond order computed by CASPT2, may be compared to the $^1\Sigma_g^+$ ground state of NtUtN with 2.87 effective bond order, where third row elements are less effective for π bond formation than second row elements.

2.1.1 Introduction

Multiple bonding between uranium and main group elements is of considerable research interest. [13–18, 80–82]. Uranium forms U=O bonds in many compounds, but fewer U=NX, U=PX, and U=S bonds are known. Imido (An=NX), phosphinidene (An=PX), and N-U-N molecular linkages have been prepared [14, 15, 18, 82] and simple $NH{=}UH_2$, $N{\equiv}UF_3$, $P{\equiv}UF_3$, and US_2 molecules have been produced and identified in matrix isolation experiments and characterized by density functional theory calculations. [25, 26, 83, 84] The simple linear N≡U≡N molecule, which is isoelectronic to the uranyl dication, has been observed only by matrix isolation spectroscopy. [19, 29] Although the O=U=O molecule is also linear, the sulfur analog is bent, on the basis of density functional theory calculations. [83, 85, 86] Accordingly, we set out to prepare the analogous PUP molecule and to characterize its bonding and structure through

Reproduced from B. Vlaisavljevich, L. Gagliardi, X. Wang, B. Liang, L. Andrews, and I. Infante *Inorganic Chemistry* **2010**, 49, 9230–9235.

quantum chemical calculations, which have been effective for the triple-bond-bearing $N{\equiv}UF_3$ and $P{\equiv}UF_3$ molecules. [26]

The activation of white phosphorus by early and late transition metal complexes to incorporate phosphorus into organic molecules is an active field of research. [87–89]. In particular, terminal-P_1, bridging-P_2, and cyclo-P_3 subunits have been included to form new molecules. The reaction of the weakly dimerized dithallene $(TlPhDipp_2)_2$ ($PhDipp_2$ = C_6H_3-2,6-(C_6H_3-2,6-iPr_2)$_2$) with P_4 yields the thallium salt of the diaryl tetraphosphabutadienediide. [90] Recently, osmium tetraphosphorus complexes have been prepared where P_4 tethers two different metal fragments through two phosphorus atoms. [91] Thus, the P_4 molecule is a readily available source of this element for preparing simple binary metal phosphide molecular species without supporting ligands, and accordingly laser-ablated U atoms were reacted with P_4molecules in matrix isolation experiments. Extensive quantum chemical calculations of possible U and P_4 reaction products were performed in this combined investigation.

2.1.2 Experimental and Computational Methods

Laser-ablated U atoms were reacted with P_4 in excess argon or neon during condensation at 5 K using methods described in our previous papers. [25, 26, 83–86, 91, 92] The Nd:YAG laser fundamental (1064 nm, 10 Hz repetition rate with 10 ns pulse width) was focused onto a rotating uranium target (Oak Ridge National Laboratory, high purity, depleted of 235U). The uranium target was filed to remove the oxide coating and immediately placed in the vacuum chamber. White phosphorus was cut under water in a glovebag and placed into a side arm separated by a Teflon needle valve: this simple apparatus was evacuated briefly at room temperature, then P4 was evaporated into argon or neon streams condensing on the cold window. The laser energy was varied about 10-20 mJ/pulse. FTIR spectra were recorded at 0.5 cm^{-1} resolution on a Nicolet 750 with 0.1 cm^{-1} accuracy using a HgCdTe range B detector. Matrix samples were annealed at different temperatures, and selected samples were subjected to photolysis by a medium pressure mercury arc lamp (Philips, 175W) with the globe removed.

Complementary DFT calculations were performed using the Gaussian 09 program, [93] the hybrid B3LYP and pure BPW91 and PBE density functionals, and the 6-311+G(3df)

basis set for phosphorus atoms and the 60 electron SDD pseudopotential for uranium. [94**?** –100] All of the geometrical parameters were fully optimized, and the harmonic vibrational frequencies were obtained analytically at the optimized structures. Additional wavefunction-based calculations were done using CASSCF/CASPT2 and the ANO-RCC-VTZP basis in order to describe the multiconfigurational nature of selected molecules and to analyze the U-P bonding in detail. [30, 33, 101] For UP, an active space comprising nine electrons in 16 orbitals (9el/6orb) was employed. The 16 orbitals are linear combinations of the U 7s, 6d, and 5f atomic orbitals with the P 3p atomic orbitals. For the PUP system, the analogous active space would have been (12el/19orbs). However, this active space is too large to be treated with current implementations of the CASSCF/CASPT2 code. We thus proceeded with a systematic truncation of the active space. We removed from the active space orbitals which are either almost doubly occupied or almost empty, and this leads us to a final active space (12el/13orb), in analogy with our prior study on NUN. [36, 102, 103] For a systematic comparison, we performed calculations also on NU and NUN with the same active spaces as PU and PUP. Finally, we also calculated $U(P_2)_2$ using the (12,12) active space.

Spin-orbit coupling was included using the complete active space interaction method, CASSI, which employs an effective one-electron spin-orbit (SO) Hamiltonian, based on the mean field approximation of the two electronic part. [31, 37] This approach has been successful in studying many actinide-containing systems. [104–108] Effective bond orders, EBO, were calculated as bonding minus antibonding occupancies divided by two.

2.1.3 Results

Infrared spectra of laser-ablated uranium atom reaction products with P_4 in excess argon and neon during condensation at 5 K will be presented in turn. Extensive density functional and CASSCF/CASPT2 calculations were per- formed to characterize possible reaction products, to support their identification, and to explore the bonding in new reaction products. Weak absorptions for common species, such as P_4O at 1241 cm^{-1} and uranium dioxide at 776 cm^{-1}, have been identified in previous papers. [85, 86, 92]

Infrared Spectra of UP_4 Reaction Products. Representative infrared spectra of laser-ablated uranium atom reaction products with P_4 evaporating at room temperature into a condensing excess argon stream illustrated in Figure 2.1 a-d reveal the strong P_4 fundamental at 465 cm^{-1} with a splitting at 461 cm^{-1}, and a weaker band at 610 cm^{-1} is not shown, which is the same as reported previously. [92]Weak, new absorptions were observed at 504, 483, and 426 cm^{-1}. The 504 cm^{-1} band decreased slightly on annealing and was unchanged by >220 nm irradiation, and the latter decreased in favor of a satellite absorption at 424 cm^{-1} on annealing to 22 K and then decreased on >220 nm irradiation and increased slightly on final annealing to 28 K.

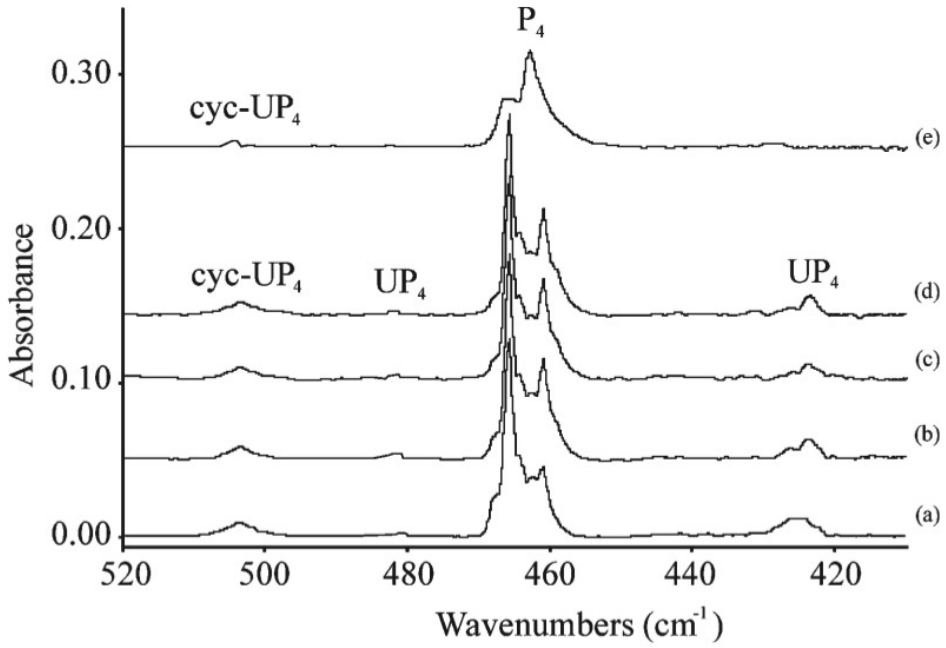

Figure 2.1: Infrared spectra of uranium and P_4 reaction products. (a) U and P_4 codeposited in excess argon at 5 K for 60 min, (b) after annealing to 22 K, (c) after >220 nm irradiation for 20 min, and (d) after annealing to 30 K. (e) U and P_4 codeposited in excess neon at 5 K for 60 min. The UP_4 label represents structure 1, and the cyc-UP_4 label represents isomer structure 7, as illustrated in Figure 2.2.

Table 2.1: Calculated Structural Parameters and Harmonic Frequencies for UP and UP[a]

molecule	CASPT2	B3LYP	BPW91	PBE
UP	2.38[b]	2.38	2.33	2.33
$^4\Gamma$	484 (43)	405 (64)	425 (44)	429 (43)
PUP	2.31/180[b]	2.28/156	2.31/129	2.31/126
$^1\Sigma_g$	523 (σ_u, 65)	485(b_2, 139)	455 (b_2, 59)	468 (41)
	459 (σ_g, 0)	464(a_1, 1)	431 (a_1, 4)	434 (4)
	142 (π_u, 10 x 2)	46(a_1, 23)	43 (a_1, 6)	46 (5)
$^3\Phi_u$	2.36/180[b]	2.33/180	2.34/180	2.34/180
	489 (σ_u, 7)	468(σ_u, 92)	457 (σ_u, 84)	458 (85)
	427 (σ_g, 0)	420 (σ_g, 0)	412 (σ_g, 0)	413 (0)
	131 (π_u, 17 x 2)	49(π_u, 30 x 2)	59 (π_u, 25 x 2)	47 (28 x 2)

A similar experiment in condensing neon gave P_4 absorptions at 607 and 463 cm^{-1} with weak new reaction product counterpart bands at 505 and 428 cm^{-1}, which are shown in Figure 2.1 e.

Calculations on UP, PUP, UP_3, UP_4 Isomers and $P_{2,3,4}$. Computations were done first at the density functional level and then with the CASSCF/CASPT2 method, and the results are summarized in Table 2.1. While doublet, quartet, and sextet states were explored, the ground state for UP is a $\Omega = 1.0$ state and is dominated by quartet states as found in CASSI calculations. The state with the largest contributions are 47% from the $^4\Gamma$; and 32% from the $^4\Phi$ states. Since theses states have the largest contribution to the SO ground state, we calculated the fundamental frequencies for both cases. The $^4\Gamma$ and $^4\Phi$ frequencies were very close at 484 cm^{-1} and 481 cm^{-1} respectively, both being higher with the CASSCF/CASPT2 method. A linear triplet is the ground state for PUP, which is 7 kcal/mol lower in energy than the lowest energy [linear] singlet at the CASSCF/CASPT2 level. Since the singlet and triplet states are close in energy, a CASSI calculation was performed confirming that the spin-orbit ground state is a mixture of triplets. The state described in the bonding subsection contributes to 95% of the spin-orbit state. The B3LYP and BPW91 and PBE approximations find the triplet lower than the singlet by 19 and 16 kcal/ mol, respectively. The important, intense diagnostic antisymmetric P-U-P stretching fundamental for triplet PUP is calculated

at 489, 468, and 457 cm^{-1} for the three methods, and the computed bond lengths are compared in Table 2.1 and with nitrogen analogs in Table 2.2. The antisymmetric P-U-P stretching fundamental for singlet PUP is calculated at 523, 485, and 455 cm^{-1} for the three methods. Interestingly, the lowest quintet cyclic U(PP) isomer is 13 kcal/mol lower in energy than triplet PUP at the PBE level. The cyclic isomer has 466 cm^{-1} (52 km/mol intensity), 314 (1), and 282 (1) frequencies and 2.538 Å U-P and 2.150 Å P-P bond lengths. However, the quintet U(NN) triangular molecule, with 2.093 Å U-N and 1.290 Å N-N bond lengths, is 66 kcal/mol higher in energy than the observed singlet, linear NUN molecule. [19, 29] UP_3 has a quartet state pyramidal structure with the strongest infrared fundamental computed at 475 cm^{-1}.

Table 2.2: Comparison of Electronic States, Bond Orders, and Distances For Uranium Pnictides

system	**electronic state**	**effective bond order**	**bond distance in Å**
PUP	$^3\Phi_u$	2.54	2.36
PUP	$^1\Sigma_g^+$	2.74	2.31
PU	$^4\Gamma$	2.76	2.38
NUN	$^1\Sigma_g^+$	2.87	1.73
NU	$^4\Gamma$	2.85	1.76

The UP_4 geometries explored are illustrated in Figure 2.2. Structure 1 is the global energy minimum in the triplet state, while the quintet state is 8-15 kcal/mol higher and the singlet much higher. Its two strongest infrared bands are 484 cm^{-1} (10 km/mol) and 420 cm^{-1} (15 km/mol) using the PBE functional. Next, the bicyclic $U(P_2)_2$ isomer of UP is a C structured $^3B_2$ state Å (U-P= 2.57 Å, P-P = 2.08 Å, P-U-P angles 104°, 84°) given as structures 3 in Figure 2.2, which is some 15-17 kcal/mol higher with the strongest IR active modes at 548 cm^{-1} (29 km/ mol) using PBE/def-TZVPP. Calculations were performed at the CASSCF/CASPT2 level with the ANO-RCC-VTZP basis sets in C_{2v} symmetry. A (12,12) active space was chosen. Singlet and triplet spin states were considered. The ground state at the CASPT2 level was also the $^3B_2$ state. The cyclic-UP_4 isomer, structure 7 in Figure 2.2, is 13 or 18 kcal/mol higher in energy (Table 2.3). Geometry 5 is 22 kcal/mol higher in energy, and structures 2 and 4 have

one imaginary frequency and are about 20 kcal/mol higher than the global minimum.

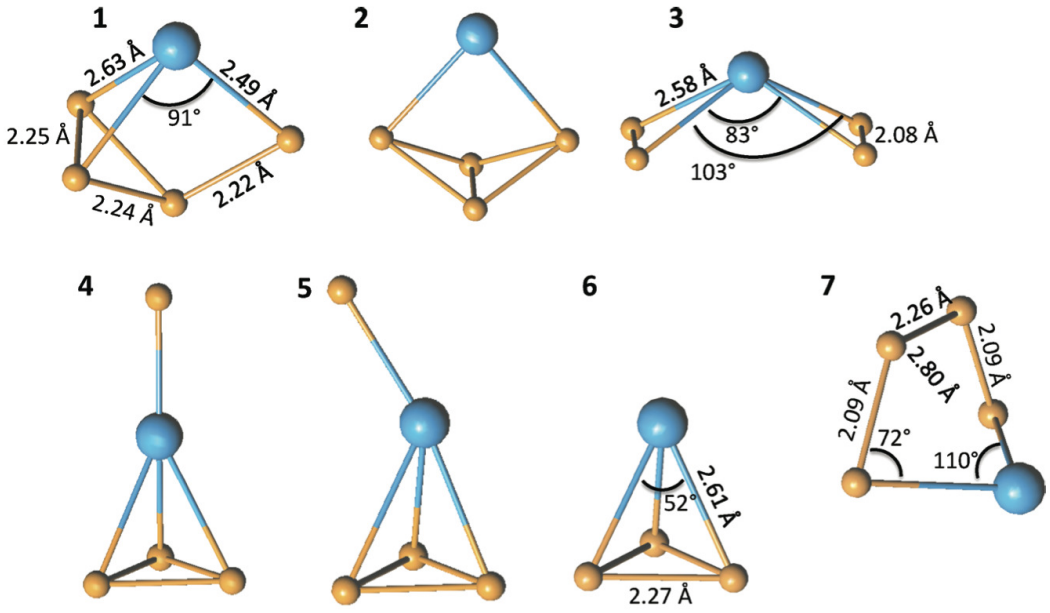

Figure 2.2: Structures considered for the reaction product of U atoms with P_4.

Table 2.3: Computed Energies for U and P_4 Reaction Products

DFT: U(SDD) P(6-311+G(3df)) CAS: ano-rcc-vtzp		
$U + P_4 \rightarrow PUP + P_2$	B3YLP	10.7
	PBE	1.2
	CASPT2	10.2
$U + P_2 \rightarrow PUP$	B3YLP	-35.1
	PBE	-62.7
	CASPT2	-44.8
$U + P_4 \rightarrow UP + P_3$	B3YLP	40.8
	PBE	22.5
	CASPT2	49.3
$U + P_2 \rightarrow UP + P$	B3YLP	50.9
	PBE	24.3
	CASPT2	32.5
$U + P_2 \rightarrow U(PP)$	B3YLP	-59.1
	PBE	-75.5
$U + P_3 \rightarrow UP_3$	B3YLP	-100.8
	PBE	-117.1
$U + P_4 \rightarrow UP_3 + P$	B3YLP	4.6
	PBE	2.1
$U + P_4 \rightarrow UP_4$ (struct. 1)	B3YLP	-75.1
	PBE	-93.1
$U + P_4 \rightarrow UP_4$ (struct. 3)	B3YLP	-60.0
	PBE	-75.6
$U + P_4 \rightarrow UP_4$ (struct. 7)	B3YLP	-62.5
	PBE	-74.9

For calibration the singlet P_2 and P_4 molecules were 24 computed using density functional methods. The computed P_2 values [B3LYP, 812 cm^{-1}, 1.888 Å; BPW91, 782 cm^{-1}, 1.903 Å; PBE, 784 cm^{-1}, 1.904 Å] may be compared to those measured for the gaseous molecule [775 cm^{-1}, 1.894 Å] [109] and the computed P_4 values [B3LYP, 607 cm^{-1} (a_1, 0 km/mol), 460 cm^{-1} (t_2, 0.3 x 3), 367 cm^{-1} (e, 0 x 2), 2.205 Å; BPW91, 599 cm^{-1} (a_1, 0 km/mol), 459 cm^{-1} (t_2, 0.2 x 3), 369 cm^{-1} (e, 0 x 2), 2.211 Å; PBE, 603 cm^{-1} (a_1, 0 km/mol), 462 cm^{-1} (t_2, 0.2 x 3), 372 cm^{-1} (e, 0 x 2), 2.208 Å] are near those measured for the gaseous molecule [601, 466, 361 cm^{-1}; 2.21 Å]. [110, 111]

The P_3 radical ground state has been computed to have an almost isosceles triangular structure, and an argon matrix electronic spectrum has been assigned. [109, 110] Our computed P_3 radical $^2A_2$ ground state values [B3LYP, 631 cm^{-1} (a_1, 0 km/mol), 403 cm^{-1} (a_1, 1), 218 cm^{-1} (b_2, 34), 2.225, 2.079 Å; BPW91, 621 cm^{-1} (a_1, 0 km/mol), 402 cm^{-1} (a_1, 1), 267 cm^{-1} (b_2, 31), 2.259, 2.089 Å; PBE, 624 cm^{-1} (a_1, 0 km/mol), 405 cm^{-1} (a_1, 1), 271 cm^{-1} (b_2, 32), 2.257, 2.088 Å] suffer from too low IR intensity, as a comparison with P_4 illustrates.

Energetics provide a useful guide for the reactions to be expected in this system, and energies from density functional and a few CASPT2 calculations are given in Table 2.3, as such density functional calculations have found considerable application for uranium bearing molecules [24, 26, 112, 113] These reaction energies are only approximate, as spin-orbit coupling is not included. The most exothermic primary reaction gives structure 1.

$$U + P_4 \rightarrow UP_4 \ \Delta E = -90 kcal/mol \ [PBE] \tag{2.1}$$

$$U + P_2 \rightarrow PUP \ \Delta E = -60 kcal/mol \ [PBE] \tag{2.2}$$

Assignments of the Matrix Spectra. The most favorable reaction energetically is to form the adduct structure 1 (Figure 2.2). The strongest PBE computed frequencies, 484 cm^{-1} (10 km/mol) and 420 cm^{-1} (15 km/mol), are within 6 cm^{-1} of the argon matrix values, and for such a complicated molecule, this agreement is sufficient to support assignment of the weak 483 and 426 cm^{-1} bands to structure 1. The next most favorable reaction is to form the cyclic-UP molecule, structure 7. Its strongest calculated frequency, an antisymmetric P-P=P stretching mode, at 523 cm^{-1} (18 km/mol) is slightly higher than the 504 cm^{-1} observed frequency, which is in the range of agreement expected for density functional theory. [All computed frequencies for these molecules are listed in the Supporting Information.] Thus, the best assignment for the 504 cm^{-1} band is the cyclic-UP_4 species. The calculated P-P bond lengths for our structure 7, 2.09, 2.26, and 2.09 Å, bracket the 2.136, 2.143 Åvalues measured for the dithallium complex. [114, 115] Finally, the $U(P_2)_2$ adduct, structure 3, which is a bisdiphosphorus complex, is of comparable stability, but the strongest computed antisymmetric P-P

stretching frequency, 548 cm^{-1}, is too far above the 504 cm^{-1} value to make this assignment. This bis-diphosphorus com- plex is of interest as no such transition metal analogs appear to be known. [87–89]

Tetraphosphorus decomposes thermally to diphosphorus above 800 °C, [111] and it is likely that vacuum ultraviolet radiation in the laser ablation plume will effect some such photodissociation during our sample deposition. The exothermic insertion reaction 2 may contribute to the product yield, but our calculations suggest that the triplet ground state PUP absorption probably falls under the very strong P_4 precursor band where it cannot be observed. Even the slightly more stable cyclic-UP_2 isomer would probably absorb under the P_4 precursor band, based on its strongest computed frequency.

Comparison Calculations on UN and NUN. Calculations were also done for UN and NUN for differences in first and second row element bonding with uranium. Doublet, quartet, and sextet states were considered for NU, and $^2\Gamma$, $^2\Phi$, $^4\Gamma$, and $^4\Phi$ were lowest. At the CASPT2 level, $^4\Gamma$ was the ground state with $^4\Phi$ 3.4 kcal/mol higher. The converged bond length was 1.757 Åand the frequency was 1034 cm^{-1} (275 km/mol intensity) for the $^4\Gamma$ ground UN state, which compare to 1.733 Åand 1095 cm^{-1} (521 km/mol), 1037(0), and 80(49) for NUN. To date, these molecules have only been observed in solid matrices, and the frequencies compare favorably with observations [UN, 1001 cm^{-1} in Ar; NUN, 1051 cm^{-1} in Ar and 1076 cm^{-1} in Ne] [19, 24, 29] and earlier calculations. [24, 36, 85, 86, 102, 103]

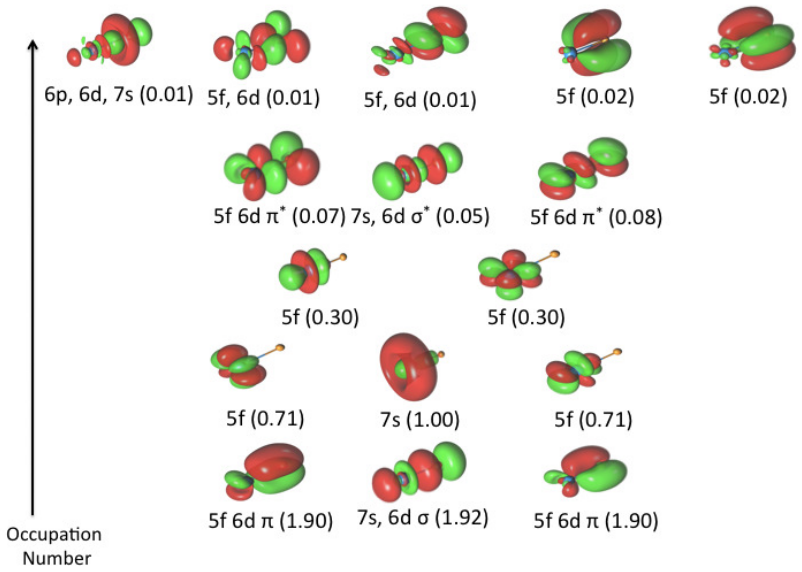

Figure 2.3: CASPT2 molecular orbitals for the major quartet spin-orbit component of the UP ground state plotted using an isodensity of 0.04 e au^{-3}. Occupation numbers are given in parentheses.

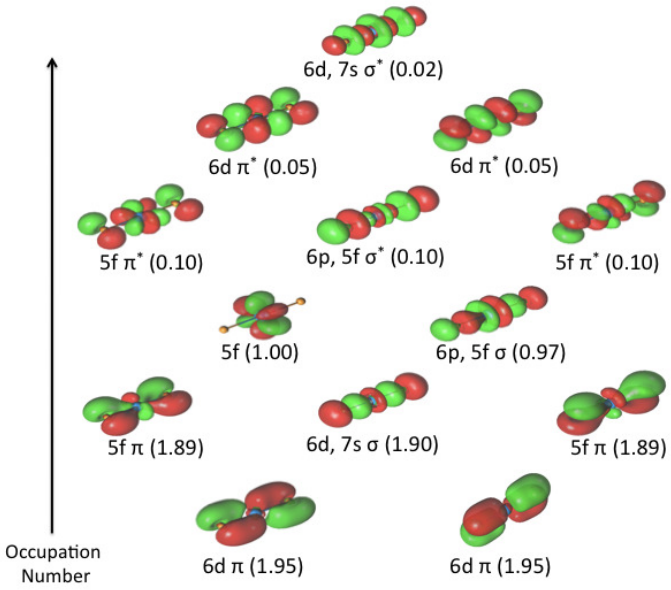

Figure 2.4: CASPT2 molecular orbitals, (12,13) active space, for the $^3\Phi_u$ state of PUP plotted using an isodensity of 0.04 e au^{-3}. Occupation numbers are given in parentheses.

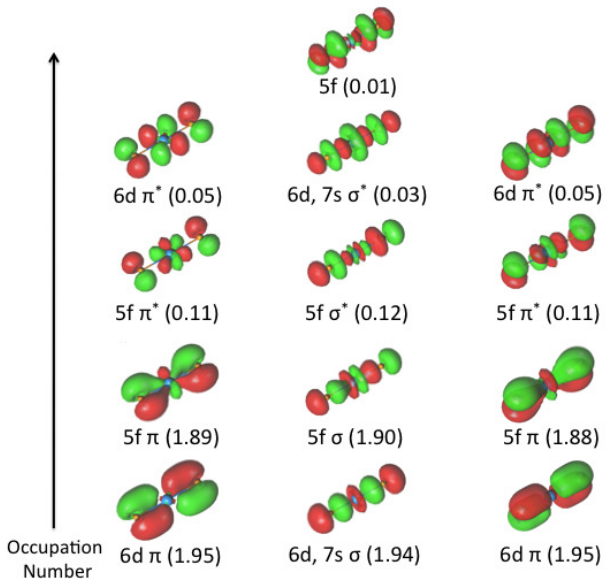

Figure 2.5: CASPT2 molecular orbitals, (12,13) active space, for the $^1\Sigma_g^+$ state of PUP plotted using an isodensity of 0.04 e au^{-3}. Occupation numbers are given in parentheses.

Structure and Bonding in Uranium Phosphides. The bond lengths of the small uranium phosphide molecules investigated here are given in Table 2.1. The hybrid density functional bond lengths are longer and suggest that this functional underestimates the U-P bonding. The CASSCF/CASPT2 molecular orbitals with occupation numbers for the major quartet component of ground state UP are representative of the ground state and are shown in Figure 2.3. The unpaired electrons are in 10 partially occupied MOs, which are localized mostly on the uranium atom. The remaining bonding and antibonding σ and π molecular orbitals give an effective bond order (EBO) of 2.76 for $^4\Gamma$ ground state of U≡P. Our computed bond lengths for UP are much closer to the sum of double bond radii (236 pm) than triple bond radii (212 pm) given by Pyykkö et al. [116, 117] The ground $^3\Phi_u$ PUP electronic state MOs are given in Figure 2.4. The EBO is higher, 2.75, for the higher energy singlet state, than for the lower energy triplet state, 2.54. The five bonding MOs for the triplet state are located at the bottom of Figure 2.4, and one SOMO shown in the middle is localized on U and the other is σ bonding. The MOs for singlet PUP are displayed in Figure 2.5 and may be compared

with those of singlet NUN below.

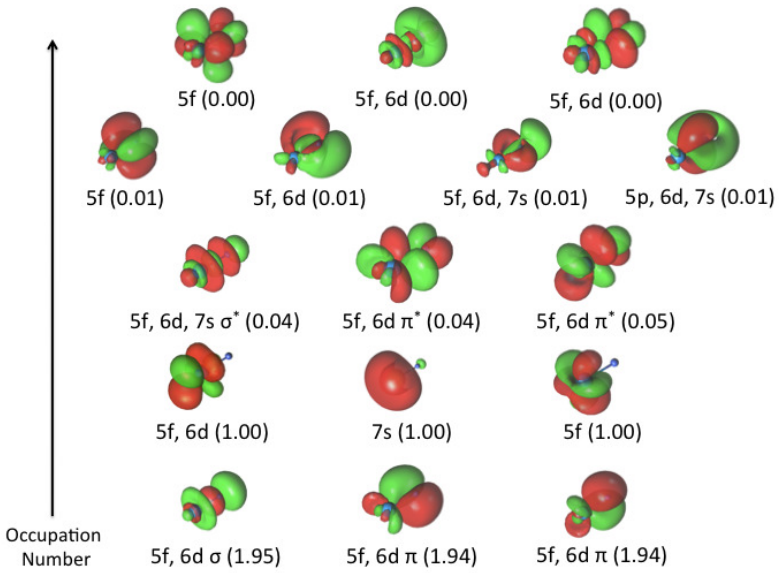

Figure 2.6: CASPT2 molecular orbitals for the $^4\Gamma$ ground state of UN plotted using an isodensity of 0.04 e au^{-3}. Occupation numbers are given in parentheses.

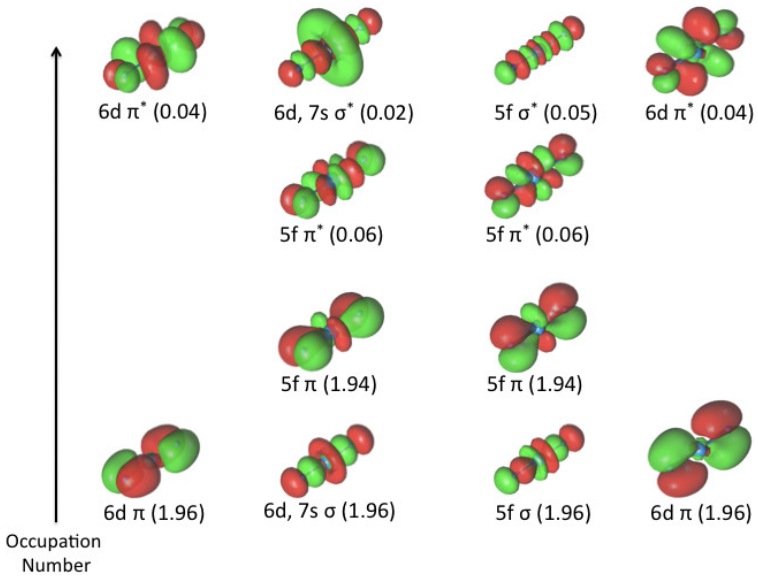

Figure 2.7: CASPT2 molecular orbitals for the $^1\Sigma_g^+$ state of NUN plotted using an isodensity of 0.04 e au^{-3}. Occupation numbers are given in parentheses.

Analogous CASPT2 computations were performed on UN and NUN for reference. The $^4\Gamma$ ground state UN molecule has a 2.85 EBO, and the linear $^1\Sigma_g^+$ ground state NUN molecule has almost the same EBO, 2.87. The UN molecular orbitals are plotted in Figure 2.6: the three unpaired electrons are localized on the uranium center, σ and π bonding MOs are occupied, and the seven highest MOs have virtually no electron occupancy. For NUN, the σ and π bonding and antibonding MO sets are illustrated in Figure 2.7. Both nitrides have fully developed triple bonds, which have slightly higher effective bond orders than the phosphorus analogs.

Overall, the nitrides have a slightly higher bond order compared to the corresponding phosphorus analogs. A close inspection of the natural orbital occupation numbers for singlet NUN and PUP shows that the main difference between the two species concerns the 5f π orbitals, which have an occupation number of 1.94 in the NUN case, and only 1.89 in the PUP case. The corresponding antibonding orbitals have a larger occupation number in PUP than in NUN, which results in a slightly higher effective bond order for the dinitride. In addition, there may be a partial loss of covalent bonding to the more

compact uranium 5f σ_u and π_u orbitals by the more diffuse phosphorus 3p orbitals, compared to nitrogen 2p.

2.1.4 Conclusions

Reactions of laser-ablated U atoms with P_4 molecules upon condensation in excess argon appear to form two stable UP_4 adducts, based on a comparison of calculated and observed frequencies. The structures and relative energies of these adducts have been explored by extensive density functional calculations. These UP_4 adducts may be considered as simple models for P_4 activation products by ligand-supported transition and main group metal complexes. [87–89, 114, 115, 115]

The anticipated triplet PUP reaction product absorption would likely be covered by the strong P_4 precursor band. The $^3\Phi_u$ ground state of PUP, with 2.54 effective bond order computed by CASPT2, is a U(IV) molecule. The higher energy U(VI) $^1\Sigma_g^+$ state of P≡U≡P, with a 2.75 effective bond order computed by CASPT2, may be compared the $^1\Sigma_g^+$ ground state of N≡U≡N with a 2.87 effective bond order, where third row elements are less effective for π bond formation than second row elements. The major quartet ground state component of U≡P, which has a 2.76 effective bond order, may be compared with the $^4\Gamma$ ground state of U≡N, which has a 2.85 effective bond order. A similar relationship with a more pronounced difference has been found for the N≡UF3 and P≡UF3 molecules with 2.78 and 2.39 EBO, respectively. [26]

2.1.5 Acknowledgment

We gratefully acknowledge financial support from DOE Grants Nos. DE-SC0001034 and DE-SC002183, NCSA computing Grant No. CHE07-0004N, and the Swiss National Science Foundation (grant 200020-120007).

2.2 Combined Triple and Double Bonds to Uranium: The N≡U=NH Uranimine Nitride Molecule Prepared in Solid Argon

Reactions of laser-ablated U atoms with N_2 and H_2 mixtures upon codeposition in excess argon at 5 K gave strong NUN and weak UN infrared absorptions and new bands at 3349.7, 966.9, 752.4, and 433.0 cm^{-1} for the unusual new U(V) molecule N≡U=NH, uranimine nitride, containing both triple and double bonds. This identification is based on D and ^{15}N isotopic substitution and comparison with frequencies computed by density functional theory for the 2Δ ground state NUNH. Calculated bond lengths are compared to those of the $^1\Sigma_g^+$ ground state of U(VI) uranium dinitride N≡U≡N, the $^2\Phi$ ground state of the isoelectronic nitride oxide N≡U=O, and the ^3A ground state of the U(IV) uranimine dihydride HN=UH_2 molecule, which have all been prepared in solid argon matrices. Mulliken bond orders based on the CASSCF orbitals for N≡U=N–H are 2.91, 2.19, and 1.05, respectively. Here, the terminal nitride is effectively a triple bond, just as found for N≡U≡N. The solid argon matrix is a convenient medium to isolate reactive terminal uranium nitrides for examination of their spectroscopic properties.

2.2.1 Introduction

Multiple bonding between uranium and main group elements is of considerable research importance, owing to interest in the behavior of 5f electrons as well as nuclear fuels and waste remediation. [13, 14, 17, 44, 81, 82, 118–121] Several ligand-supported imido (U=NX), NUN, and UNU molecular linkages, [13, 14, 81, 82, 118, 119, 121] as well as uranium carbene complexes, have been prepared. [17, 120] Evidence has been presented recently for a transient terminal uranium nitride complex following photolysis of uranium azide complexes. [44] In addition, solid uranium nitrides and carbides are of potential importance as nuclear fuel materials. [122–124]

The U≡N diatomic molecule, prepared first from a nitrogen discharge in the presence

Reproduced from X. Wang, L. Andrews, B. Vlaisavljevich, and L. Gagliardi
Inorganic Chemistry, **2011**, 50, 3826–3831.

of uranium metal, [29] has only been observed to date in solid argon matrices. [23, 29] The nitrogen analog to the uranyl dication, N≡U≡N, was also prepared in this discharge work and later through the insertion of laser-ablated U atoms into dinitrogen during condensation with excess argon. [19] It was also shown that near UV excitation of U atoms in these experiments increased the yield of N≡U≡N through more reaction with N_2 in solid argon. [19] Upon condensation of U atoms and pure dinitrogen, the N≡U≡N molecule so formed is complexed extensively to extra dinitrogen molecules. [20, 22] Subsequently, a variety of simple new uranium-bearing molecules such as HN=UH_2, N≡U=O, N≡UF_3, CH_2 =UH_2, and U≡C containing multiple bonds to uranium have been identified in matrix isolation experiments and characterized through quantum chemical calculations. [24–28, 125] The linear uranium dinitride molecule N≡U≡N, which was the first terminal uranium nitride formed by photolysis, [19] has fully developed triple bonds based on early SCF and recent CASPT2 calculations. [41, 102, 103, 126] Although NUN is isoelectronic with the common UO_2^{2+} uranyl dication, [126], and a stable species in its own right, we wanted to examine the reactivity of NUN with other abundant materials such as hydrogen in order to prepare other derivatives of this stable molecule under matrix isolation conditions. Hence, the reaction of laser ablated U atoms and N_2/H_2 mixtures in condensing excess argon has been investigated, and we found that some of the NUN produced reacts with H atoms to give the linear uranimine nitride molecule NUNH. The formation and isolation of a stable molecule like NUNH in solid argon suggests that it will be possible to prepare more ligand stabilized derivatives of terminal uranium nitrides on a macroscopic scale.

2.2.2 Experimental and Computational Methods

Laser-ablated U atoms were reacted with N_2/H_2 mixtures (Matheson, 0.3 to 0.6% of each reagent) in argon during condensation at 5 K using methods described in our previous papers. [19, 90, 91] The Nd:YAG laser fundamental (1064 nm, 10 Hz repetition rate with 10 ns pulse width) was focused onto a rotating uranium target (Oak Ridge National Laboratory, high purity, depleted of 235U). The uranium target was filed to remove surface oxide and immediately placed in the vacuum chamber. Deuterium gas and $^{15}N_2$ (Cambridge Isotopic Laboratories, 98+%) were used as received. Isotopically scrambled dinitrogen was prepared by tesla coil discharge of $^{14}N_2$ and $^{15}N_2$ for 20 min

at 10−15 Torr of pressure in a Pyrex bulb with a stainless steel valve. FTIR spectra were recorded at 0.5 cm^{-1} resolution on a Nicolet 750 machine with 0.1 cm^{-1} accuracy using a HgCdTe range B detector.

Quantum chemical calculations were performed using the Gaussian 09 program system with the hybrid B3LYP and pure BPW91 density functionals, the 6-311++G(3df,3pd) basis for H and N, and the SDD pseudopotential for U [30 electron core] [93–95, 97–100, 127] as performed for previous uranium-bearing molecules. [123, 125, 126] Additional wave function based calculations were done using CASSCF/CASPT2 and the ANO-RCC- VTZP basis with the MOLCAS 7.2 software in order to describe the multiconfigurational nature of NUN and NUNH and to analyze the UN bonding in detail. [30, 33, 101, 128] The active space employed to describe NUN is composed of 12 electrons in 12 orbitals (12,12). This contains two σ bonding/antibonding pairs and two sets of π bonds (in total, four π bonding orbitals and four π^* antibonding orbitals). In NUNH, one electron in a H 1s orbital is added, resulting in an active space of (13,13). The same bonding and antibonding orbitals are present in NUNH as in NUN with the addition of one nonbonding orbital localized on uranium.

2.2.3 Results and Discussion

Infrared spectra of laser ablated uranium atom reaction products with nitrogen/hydrogen mixtures in excess argon will be presented and compared to density functional calculations of product vibrational frequencies. Multiple bonding in the new NUNH molecule will be discussed.

Infrared Spectra. First, the infrared spectra of laser ablated uranium atom reaction products with nitrogen in excess argon during condensation at 5 K gave strong NUN and weak UN absorptions, as the present lower substrate temperature enabled trapping of the diatomic molecule. [19, 29] The use of isotopically scrambled dinitrogen again verified the symmetrical structure of the linear NUN molecule. Annealing gave evidence for the formation of dinitrogen complexes with both NUN and UN.

Next, spectra were recorded using nitrogen/hydrogen mixtures in excess argon, and the major products for these reagents were observed, as before (NUN at 1050.9 cm^{-1}; A = 0.12; the Ar_nH^+ species at 903 cm^{-1}; and the uranium hydrides at 1483.5, 1423.9, 1371.0, and 1182 cm^{-1}; A = 0.005−0.015). [19, 21, 110] Uranium oxide was detected at

819.8 cm^{-1}. [86]

Table 2.4: Observed and Calculated Frequencies for NUNH Isotopic Molecules in the $^2\Delta$ Ground State[a]

	^{14}**NU**^{14}**NH**					^{14}**NU**^{14}**ND**				
approx. mode	obs[b]	B3LYP[c]	int[c]	BPW91[d]	int[c]	obs[b]	B3LYP[c]	int[c]	BPW91[d]	int[c]
N–H str., σ	3349.7	3530.8	38	3433.3	18	2489.2	2590.4	64	2518.9	40
N≡U str., σ	966.9	1035.4	359	993.1[e]	316	966.5	1035.4	359	992.9	310
U=N str., σ	752.4	784.9	304	771.7[e]	246	742.4	758.3	283	745.5	230
UNH def., π	433.0	425.1	190 x 2	463.8	169 x 2		321.7	129 x 2	353.5	117 x 2
NUN def., π		96.3[f]	65 x 2	89.0	47 x 2		93.7	61 x 2	91.2	50 x 2
	^{15}**NU**^{15}**NH**					^{15}**NU**^{15}**ND**				
approx. mode	obs[b]	B3LYP[c]	int[c]	BPW91[d]	int[c]	obs[b]	B3LYP[c]	int[c]	BPW91[d]	int[c]
N–H str., σ	3342.1	3522.3	34	3425.0	15	2477.6	2577.9		2506.7	
N≡U str., σ	936.5	1002.6	342	961.7[e]	302	936.0	1002.6		961.5	
U=N str., σ	731.3	761.4	283	748.5[e]	228	722.3	737.4		724.9	
UNH def., π	431.0	423.1	186 x 2	461.4	165 x 2		319.0		350.2	
NUN def., π		93.5	61 x 2	89.5	47 x 2		91.1		86.8	

[a]Frequencies and intensities are in cm^{-1} and km/mol. [b]Observed in an argon matrix. [c]Frequencies computed with B3LYP/6-311+G(3df, 3pd). [d]Frequencies computed with BPW91/6-311+G(3df,3pd). [e]Frequencies computed with BPW91 for 15-U-14-H are 961.9 and 771.2 cm^{-1} and for 14- U-15-H are 992.9 and 748.9 cm^{-1}. [f]CASPT2 frequencies (intensities) with no symmetry imposed: 3548 (41), 1020 (384), 787 (283), 519 (112), 303 (1590), and 79 (73).

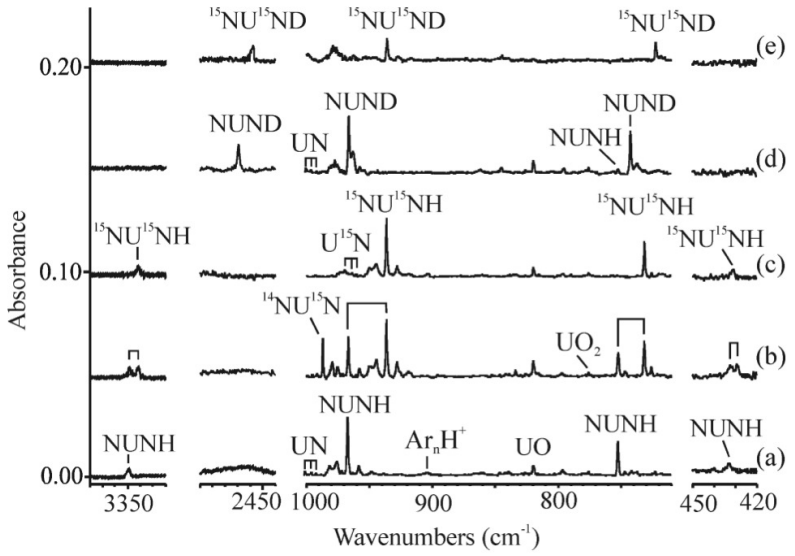

Figure 2.8: Infrared spectra of the major uranium, nitrogen, and hydrogen reaction products upon codeposition in argon at 5 K. (a) U and N_2/H_2 (0.6% each) codeposited in argon at 5 K for 60 min, (b) U and scrambled $^{14,15}N_2/H_2$ (0.6% each), (c) U and $^{15}N_2/H_2$ (0.3% each), (d) U and $^{14}N_2/D_2$ (0.3% each), and (e) U and $^{15}N_2/D_2$ (0.3% each).

Important new absorptions at 3349.7, 966.9, 752.4, and 433.0 cm^{-1} are listed in Table 2.4 along with their isotopic modifications. These new bands are shown in Figure 2.8 for the freshly deposited samples. The NUN band at 1050.9 cm^{-1} (not shown) was 4 times as strong as the new 966.9 cm^{-1} product absorption. Subsequent annealing to 20−30 K had little effect on these bands, but the system pressure increased as H_2 was released by the argon matrix (H_2 boiling point 20.7 K). Although full arc irradiation increased the 1050.9 cm^{-1} NUN band by 20−30% and destroyed the Ar_nH^+ band, as before, [19, 21, 110] the new product bands were not affected.

An additional uranium experiment was done with CO added (0.1%) to the argon sample containing N_2 and H_2 (0.6% each), and the above new bands were observed, along with HCO at 1863 cm^{-1} and weak CUO bands at 852 and 804 cm^{-1}. [110]Annealing to 30 K increased the HCO band by 50% but left the CUO bands unchanged.

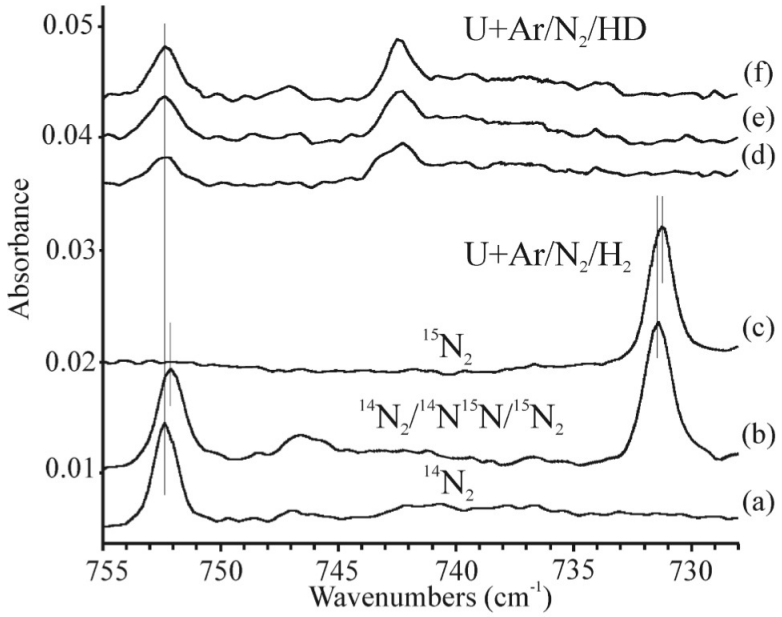

Figure 2.9: Expanded frequency scale spectra of the NU=NH stretching mode from uranium atom reactions with three nitrogen isotopic modifications and H_2 and with N_2 and HD. (a) U and $^{14}N_2/H_2$ (0.6% each) codeposited in argon at 5 K for 60 min, (b) U and scrambled $^{14,15}N_2/H_2$ (0.6% each), (c) U and $^{15}N_2/H_2$ (0.3% each), (d) U and $^{14}N_2$/HD (0.6% each) codeposited in argon at 5 K for 60 min, (e) spectrum recorded after full arc irradiation for 15 min while the sample was temperature-cycled 5 to 20 to 5 K, (f) spectrum recorded after second full arc irradiation for 15 min while the sample was temperature-cycled 5 to 20 to 5 K.

Nitrogen−15 substitution shifted the above bands to 3342.1, 936.5, 731.3, and 431.0 cm^{-1}, confirming the involvement of nitrogen in the vibrational modes responsible for these new absorptions. Reaction with a $^{14}N_2$, $^{14}N^{15}N$, $^{15}N_2$ sample gave apparent doublets (Figure 2.8b), indicating the major involvement of a single N atom in each vibrational mode, but the 752.4 and 731.3 cm^{-1} bands shifted inward to 752.1 and 731.5 cm^{-1} with $^{14}N_2$, $^{14}N^{15}N$, $^{15}N_2$ revealing minor coupling with a second nonequivalent N atom (Figure 2.9b).

The new bands shifted with deuterium substitution using the D_2 reagent to 2489.2, 966.5, and 742.4 cm^{-1} and below our range of detection. Shifted bands were also

observed for uranium deuterides and the Ar_nD^+ species. [21, 110] The 742.4 cm^{-1} deuterium product band revealed a weak satellite at 752.4 cm^{-1} due to the hydrogen counterpart from background hydrogen contamination in the system (Figure 2.8d). The 742.4 cm^{-1} band was also detected in nitrogen experiments without added hydrogen, and the band increased 5-fold with hydrogen added to the reagent mixture.

A final experiment was done using HD as the hydrogen-bearing reagent, and the diagnostic region of the spectrum is shown in Figure 2.9d. The strong bands were observed unresolved at 966.7 cm^{-1}, the average of the above hydrogen and deuterium values, and a sharp doublet at 752.4 and 742.4 cm^{-1} , the same as the above hydrogen and deuterium values. The 752.4−742.4 cm^{-1} doublet absorption verifies the participation of a single H (D) atom in the new product species. Next, annealing and full arc irradiation were performed at the same time, and the spectrum in Figure 2.9e was recorded after full arc irradiation for 15 min while the sample was cycled 5 to 20 to 5 K and the H_2 pumped away, causing a temporary system pressure increase, revealed a 50% increase in the 752.4−42.4 cm^{-1} doublet absorption along with the associated 966.7 cm^{-1} band. A second identical treatment resulted in no system pressure increase, as presumably no HD remained in the sample, but the 752.4−742.4 cm^{-1} doublet absorption increased another 20%, Figure 2.9f.

Identification of NUNH and Vibrational Assignments. The new NUNH molecule is identified by the four fingerprint vibrational modes described above. The vibrational assignments are indicated by characteristic frequencies and their isotopic shifts, as illustrated by isotopic frequency ratios, and comparison to values calculated by density functional theory. The 3349.7 cm^{-1} band shifted to 2489.2 cm^{-1} with deuterium substitution (isotopic frequency ratio 1.3450), which is characteristic of a N−H stretching mode as verified by the nitrogen-15 shift to 3342.1 ccm^{-1} (ratio 1.00227). These band positions and shifts are in very good agreement with the predictions of two density functional calculations using hybrid and pure density functionals (Table 1). The calculated 3530.8 and 3422.3 cm^{-1} harmonic frequencies are 5.4 and 2.5% higher than the observed value, which is in the range found for the B3LYP and BPW91 functionals. [129, 130] This discrepancy is due primarily to anharmonicity in the observed band not accounted for in the harmonic approximation used in the calculations.

Next, the 966.9 cm^{-1} band shifted to 936.5 cm^{-1} with nitrogen-15 (ratio 1.0325),

which is almost the same as the 1.0326 ratio for diatomic UN itself. [29] This agreement clearly identifies a terminal UN vibration. Our DFT calculations predict this mode for NUNH to be 7.1 and 2.7% higher with the same 14/15 isotopic frequency ratio. The lower associated 752.4 cm^{-1} band shifts to 731.3 cm^{-1} with nitrogen-15 (ratio 1.0289), which is less, owing to the involvement of hydrogen in this mode as manifested by the shift to 742.4 cm^{-1} on deuterium substitution. The DFT frequencies in this case are 3.0% higher and 1.0% lower than the argon matrix value, and their 14/15 ratios (1.0309, 1.0310) are slightly higher, again likely due to anharmonicity from the hydrogen participation in this mode. As mentioned above, the reaction with $^{14}N_2$, $^{14}N^{15}N$, $^{15}N_2$ gave slightly shifted doublets (Figure 2.9), indicating the major involvement of a single N atom and the minor coupling with a second nonequivalent N atom (Figure 2.9b). Hence, our identification of NUNH is made from the characterization of one N−H and two different U−N stretching modes.

Finally, the linear NUNH molecule has a degenerate U−N−H bending mode, and our DFT calculations predict this strong mode at 425.1 or 463.8 cm^{-1}, which bracket the observed 433.0 cm^{-1} argon matrix value. These calculations predict 2.0 or 2.4 cm^{-1} nitrogen-15 shifts, which substantiates our identification of the linear NUNH molecule from its matrix infrared spectrum.

It is interesting to compare the NUNH frequencies computed by two density functionals with those from the CASPT2 wave function based method. With linear symmetry imposed, the CASPT2 stretching frequencies were 3561, 1036, and 787 cm^{-1}, and with no symmetry these were almost the same at 3548, 1020, and 787 cm^{-1}, and they agree very well with the DFT frequencies (Table 1), particularly the higher B3LYP values. The slightly bent molecule with no symmetry gave UNH deformation frequencies of 519 and 303 cm^{-1}, which bracket the degenerate DFT values.

Reactions Occurring in the Matrix. Our experiments have shown that the reaction of a laser ablated, excited U atom with molecular nitrogen proceeds directly to form NUN, reaction 1. [19] This reaction requires electronically excited uranium because annealing to allow diffusion and potential reaction of trapped reagents does not increase the yield of NUN, but exposure of the cold matrix sample to ultraviolet light from a mercury arc street lamp to excite U increases the NUN signal 3-fold. [19] This finding is in agreement with a more recent CASSCF/CASPT2 investigation of

the U+N_2 reaction path, which obtained a 25 kcal/mol barrier for this 59 kcal/mol exothermic reaction. [103]

$$U^* + N_2 \rightarrow NUN \quad (2.3)$$

$$NUN^* + H \rightarrow NUNH \quad (2.4)$$

In the present U/N_2/H_2 experiments, the most straightforward reaction to produce NUNH is for vacuum ultraviolet photolysis of H_2 from the laser ablation plume to provide H atoms for direct reaction with NUN to form NUNH during the laser ablation/irradiation/sample deposition process, reaction 2, which is exothermic by 59 kcal/mol (B3LYP) or 40 kcal/mol (CASPT2). First, from many other investigations [131] and matrix isolation work, [132–134] the laser ablation plume contains vacuum-UV radiation, which is capable of dissociating molecular hydrogen into H atoms. [109] The observation of Ar_nH^+ and Ar_nD^+ absorptions provides evidence to substantiate the presence of both H and D atoms and high energy radiation. [92] The detection of HCO in the CO-doped U/N_2/H_2 experiment and its growth on annealing [110, 135] also attest to the formation of H atoms and their reaction in these experiments. Recall, however, that NUNH absorptions do not increase on annealing unless annealing and irradiation are performed simultaneously (Figure 2.9d,e,f). This suggests an energy activation for reaction 2, and PBE/VDZP calculations have found a small 160 cal/mol barrier for reaction 2. Interestingly, this increase of NUNH absorptions under annealing/irradiation conditions where H_2 evaporates from the argon solid, but H atoms remain, based on earlier ESR spectra, [136] provides further evidence for the H atom reaction and casts doubt on any contribution from the 45 kcal/mol endothermic NUN + H_2 → NUNH + H reaction.

There is apparently no significant participation of N_2/H_2 reaction products, as NH and NH_2 are not detected in our samples. [25, 137] Two other products might be considered, quintet U=NH and triplet HN=U=NH, but these are not observed on the basis of frequencies calculated at the DFT level (803 cm^{-1} for the former product and 835 cm^{-1} for the latter). The lack of UNH is probably due to the production of UN signals at less than 1% of NUN absorbance values. Apparently, the reaction of NUN and H_2 does not proceed under the conditions of these experiments, and the available H atoms

probably react with excess NUN rather than with NUNH. Furthermore, the low yield of N atoms, based on the very small yield of UN relative to NUN, is too low to expect any significant reaction with the UH product formed in the U and H_2 reaction. [21]

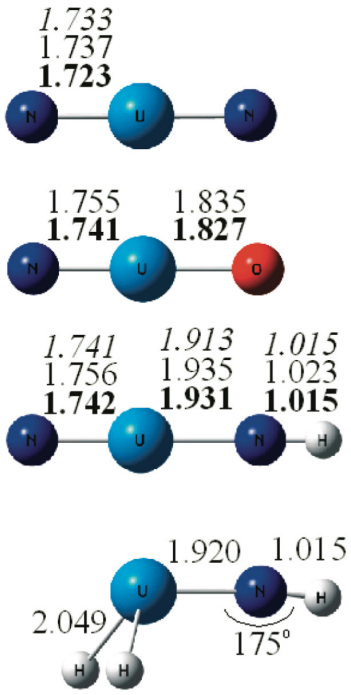

Figure 2.10: Uranium atom reaction product structures and bond lengths (Å) computed with CASPT2 (italic), BPW91 (normal type), and B3LYP calculations (bold type) for N≡U≡N, N≡U=O, N≡U=N–H, and H_2U=NH, respectively.

Multiple Bonding in NUNH. Computed bond lengths for four molecules containing uranium nitrogen multiple bonds are shown in Figure 2.10 using three different theoretical methods. The terminal nitride bond in NUNH is slightly longer than that in NUN, and the 966.9 cm^{-1} stretching frequency is 63 cm^{-1} lower than the 1030 cm^{-1} average value for NUN itself. [19] The imido bond in NUNH is also slightly longer than that in the imine, and the 752.4 cm^{-1} U−N stretching frequency is slightly lower than the H_2UNH imine value of 820 cm^{-1}. [25]

The charge distributions in the NUN and NUNH molecules are very similar (CASSCF

Mulliken partial charges are $^{-0.25}$N$^{+0.50}$U$^{-0.25}$N and $^{-0.29}$N$^{+0.54}$U$^{-0.32}$N$^{+0.06}$H); however, the internal UN bond for NUNH is only a double bond whereas the terminal uranium nitride bond is triple. The Mulliken bond orders based on CASSCF orbitals are N−2.91−U−2.19−N−1.05−H and N−2.89−U−2.89−N.

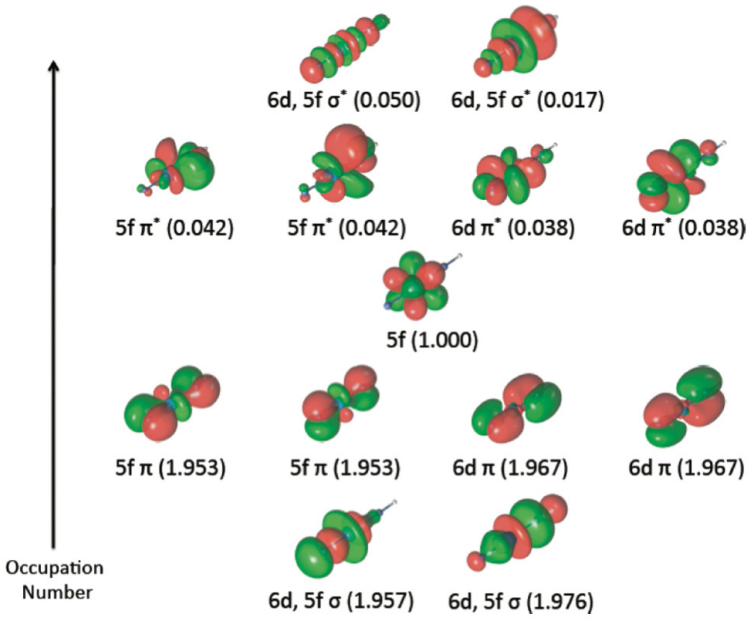

Figure 2.11: Molecular orbitals for NUNH plotted using an isodensity of $0.04e$ au^{-3}.

The CASPT2 orbitals for NUNH are plotted in Figure 2.11. These orbitals are very similar to those of NUN, recently reported, [41] except for the extra electron in the U 5f orbital. It is interesting to note that the σ bonding orbital for the inside U−N bond is extended substantially to include the N−H bond. As a consequence, it makes little contribution to the inside U−N bond, which is a double bond from the contribution of the four bonding orbitals over both N−U−N bonds. The CASSCF bond order for the inside U−N bond is dominated by the 5f π and 6d π bonding orbitals. [138]

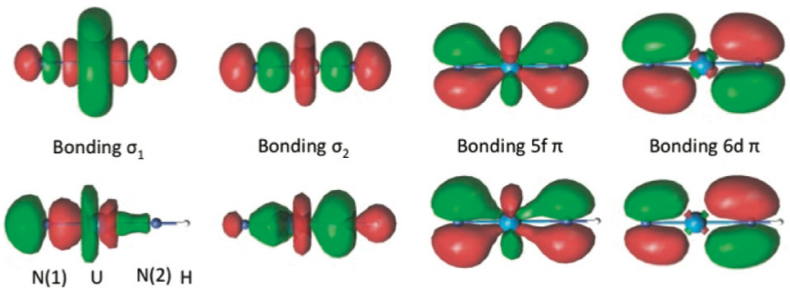

Figure 2.12: Comparison of σ and π bonding orbitals for NUN (top) and NUNH (bottom).

The number of chemical bonds is the same in NUN and NUNH, but they are quite different in important ways (see Figure 2.12). In NUN, the uranium nitrogen bonds are equivalent by symmetry, but in NUNH, on the other hand, the two N−U bonds differ by nearly a bond order because of the presence of the H atom on one side. The π orbitals are only slightly modified because of the presence of the hydrogen atom, while the σ bonds are significantly different. The σ_1 orbital (lower left in Figure 5) is mainly localized on the terminal N(1)−U bond and only very little on the internal U−N(2)H bond. In contrast, the σ_2 orbital is more delocalized like those in NUN.

The hydrogen atom has a slight positive partial charge of 0.06 from Mulliken population analysis at the CASSCF and also CASPT2 level calculations.

CASPT2 frequencies were initially calculated for the structure optimized with linear symmetry. The resulting structure had an imaginary frequency and is therefore not a minimum. Consequently, a full CASPT2 geometry optimization and subsequent frequency calculations were performed without enforcing symmetry constraints. These calculations gave an optimized structure that was slightly bent and had all real frequencies, which is embedded below. The linear structure is 0.2 kcal/mol higher in energy than the bent structure, but this difference in energy is very small and well within the error associated with CASPT2 calculations. Furthermore, the qualitative appearance of the orbitals does not change when symmetry is removed and the orbital occupation numbers and bond orders remain the same. Therefore, the structure is pliable as opposed to “bent. Given that the minimum energy structure at the CASPT2 level is

slightly bent, two frequencies are associated with the UNH bending motion, whereas the symmetric structure has only one degenerate vibrational frequency (Table 1). In solid argon, a single bending mode absorption is observed at 433.0 cm^{-1}.

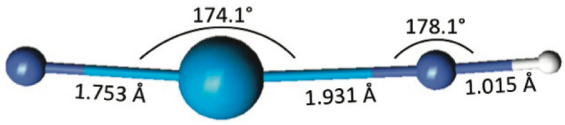

Comparisons with Bulk Uranium Nitride Complexes. The simple uranium nitrides formed in solid argon without stabilizing ligands provide model compounds for bulk uranium nitride complexes. The uranium dinitride NUN molecule formed by direct insertion of excited U atoms into dinitrogen [19] has a computed triple bond length of 1.73 Å (Figure 3). This may be compared to the U=N bond length of 1.848 Å measured for U=(N-t-Bu)$_2$I$_2$-(THF)$_2$. [82] The U=N$_{imido}$ bond length calculated here (1.93 Å) is in the range of that for bulk uranium imido complexes such as Me$_3$SiNU(N[SiMe$_3$]$_2$)$_3$ (1.910 Å), [139] Me$_3$SiNU(N t-BuAr)$_3$ (1.937 Å), [119] and uranium imido halide complexes (1.97 Å). [118]

Finally, we would like to make the point that if molecules such as NUN and NUNH can be formed under the radiation conditions associated with the laser ablation process and isolated in solid argon, then these stable molecules should be isolable with stabilizing ligands at higher temperatures. Such is certainly the case for NUN. [15, 82]

2.2.4 Conclusions

The stable N≡U≡N molecule appears to react with hydrogen atoms under ultraviolet irradiation to form N≡U=N−H, the uranium(V) nitride imide molecule. The relative electronic energy (products minus reactants) of the reaction NUN + H → NUNH is −40 kcal/mol at the CASPT2 level of theory. This unusual U(V) molecule is identified by four fingerprint vibrational modes (N−H, U≡N, and Ud=H stretching and U=N−H bending), and it contains a nitride triply bonded to uranium and a parent imine doubly bonded to uranium. The linear structure shows that the nitrogen lone pair is involved in π bonding orbitals. Terminal uranium nitrides are very reactive, [44] and argon matrix

experiments have isolated five unsupported terminal uranium nitride molecules, UN, NUN, NUO, NUF_3, and NUNH, for infrared spectroscopic characterization.

2.2.5 Acknowledgment

We gratefully acknowledge financial support from DOE Grants Nos. DE-SC0001034 and DE-SC002183, and NCSA computing Grant No. CHE07-0004N. We thank J. T. Yates, Jr. for the $^{15}N_2$ sample.

Chapter 3

Combined Theoretical and Experimental Studies of Oraganoactinide Compounds

3.1 On the Nature of Actinide and Lanthanide–Metal Bonds in Heterobimetallic Compounds

Eleven experimentally characterized complexes containing heterobimetallic bonds between elements of the f-block and other elements were examined by quantum chemical methods : [(η^5-C_5H_5)$_2$(THF) LuRu(η^5-C_5H_5)(CO)$_2$], [(η^5-C_5Me_5)$_2$(I)ThRu (η^5-C_5H_5)(CO)$_2$], (η^5-C_5H_5)$_2$YRe(η^5-C_5H_5)$_2$], {N($CH_2CH_2NSiMe_3$)$_3$}URe(η^5-C_5H_5)$_2$, [Y Ga(NArCH)$_2$C(PPh_2N SiH_3)$_2$H(CH_3OCH_3)$_2$], [{N($CH_2CH_2NSiMe_3$)$_3$} U{Ga(NArCH)$_2$} (THF)], [(η^5-C_5H_5)$_3$UGa(η^5-C_5Me_5)], [Yb(η^5-C_5H_5)Si($SiMe_3$)$_3$(THF)$_2$], [(η^5-C_5H_5)$_3$ U ($SnPh_3$)], [(η^5-C_5H_5)$_3$U-($SiPh_3$)], and (Ph[Me]N)$_3$USi($SiMe_3$). Geometries in good agreement with experiment were obtained at the density functional level of theory. The multi-configurational complete active space self-consistent field method (CASSCF) and subsequent corrections with second order perturbation theory (CASPT2)were applied to further understand the electronic structure of the lanthanide/actinide–metal (or metal–metalloid) bonds. Fragment calculations and energy-decomposition analyses were also performed and indicate that charge transfer occurs from one supported metal fragment to the other, while the bonding itself is always dom nated by ionic character.

3.1.1 Introduction

Chemists have pursued the challenge of synthesizing a wide variety of metal-metal bonds for the past fifty years with motivations ranging from fundamental interest [140–143] to more practical applications for example, molecular wires [144] and small molecule activation. [145] Researchers have asked why stable metal-metal bonding interactions form, what is their reactivity, and what potential uses in catalysis, metal surface chemistry, or bioinorganic reactivity may be possible. [146] While challenging, many attempts to isolate complexes containing main group homodinuclear metal-metal bonds have proven successful and as a result this type of bonding is now generally well understood. [140] In contrast, transition metal heterobimetallic metal-metal bonds are less prevalent since

Reproduced from B. Vlaisavljevich, P. Miró, C. J. Cramer, L. Gagliardi, I. Infante, and S. T. Liddle *Chemistry–A European Journal*, **2011**, 17 (30), 8424–8433.

they present more synthetic challenges; however, the highly ionic bonds in such compounds provide opportunities for very different chemistry than are found for their homobimetallic counterparts. Heterobimetallic bonds have inequivalent metal centers. As a result, one metal center can be tailored to be electron rich or electron deficient and thus exploited for catalysis. [145, 147]

Moving beyond transition metals, metal-metal bonding in the f-block, as a whole, is uncommon and offers even greater synthetic challenges, particularly for actinides. [146] In fact, in f-element chemistry even homodinuclear metal-metal bonding has been elusive, but there have been several actinide-actinide dimers reported in the gas phase. For example, Th_2 was detected both in the gas phase and in a rare gas matrix while U_2 has been detected in the gas phase but not yet isolated. [38, 107, 148–150] However, many challenges remain regarding the preparation of molecules containing actinideactinide bonds, particularly in moving beyond the diatom towards the synthesis of complexes that can be characterized by single-crystal diffraction. In fact, complexes containing homodinuclear unsupported actinide-actinide or lanthanide-lanthanide bonds have not been observed to date, but heterobimetallic metal-metal complexes containing one f-element have been. A comprehensive list of f-element-metal bonds was compiled by Liddle and Mills in a recent review. [146] They categorized the systems into Ln–M and An–M (Ln=lanthanide and An=actinide) bonds where M is a transition metal, a Group 13, a Group 14, or a Group 15 metal or metalloid respectively (selected elements in Groups13–15 are sometimes referred to as metalloids). However, no actinide-group 15 bonds have been observed.

Theoretical investigations can provide insight into the electronic structure of metal-metal bonding and help with the interpretation of experiments. While it is clear that these systems have a large ionic contribution to their bonding, the degree to which covalent interactions may also play a role in the metal-metal bond bears consideration. DFT calculations have been performed on several An/Ln-M systems. [62, 151–153] Two previous DFT studies of particular interest addressed complexes containing a U–Ga bond[18] and a U–Re bond, [62] respectively. In both cases, DFT calculations suggested that the bonds exhibit minor but significant orbital contributions (ca. 30%); not only was a σ-donation between metal centers observed, but visualization of the Kohn-Sham frontier orbitals suggested the presence of weak π-donation from the metal ligands to

uranium. These results spurred our interest in examining systems with unsupported heterobimetallic metal-metal bonds using a high level of theory (CASSCF/CASPT2) to provide a detailed description of the electronic structure of these interactions.

Since our interest focuses on the covalency of these inter- actions, we limited our study to systems containing unsup- ported metalmetal bonds. We considered experimentally characterized systems with an actinide or a lanthanide bond to a single transition metal, Group 13, or Group 14 element: Th–Ru, Lu–Ru, U–Re, Y–Re, U–Ga, Y–Ga, U–Si, and Yb–Si bonds. All the systems have ligands supporting the individual metals. While it is not a lanthanide, yttrium is classified as a rare earth element along with scandium and the lanthanides; therefore, Y–M bonds are included in this study. Specifically, calculations were performed for [(η^5-C_5H_5)$_2$(THF) LuRu (η^5-C_5H_5)(CO)$_2$], [154] [(η^5-C_5Me_5)$_2$(I) ThRu (η^5-C_5H_5)(CO)$_2$], [155] (η^5-C_5H_5)$_2$ YRe (η^5-C_5H_5)$_2$], [151] {N($CH_2CH_2NSiMe_3$)$_3$} URe (η^5-C_5H_5)$_2$, [63] [YGa(NArCH)$_2$ C(PPh_2N SiH_3)$_2$H (CH_3OCH_3)$_2$], [152] [{N($CH_2CH_2NSiMe_3$)$_3$} U{Ga(NArCH)$_2$} (THF)], [63] [(η^5-C_5H_5)$_3$UGa(η^5-C_5Me_5)], [153] [Yb(η^5-C_5H_5)Si($SiMe_3$)$_3$(THF)$_2$], [156] [(η^5-C_5H_5)$_3$ U(Sn Ph_3)], [157] [(η^5-C_5H_5)$_3$U($SiPh_3$)], [158] and (Ph[Me]N)$_3$USi($SiMe_3$). [159] The ligand choice for each system is described in detail in the respective experimental papers.

For the sake of expedience, abbreviations will be used in the following discussion. For example, [(η^5-C_5H_5)$_2$−C(THF)LuRu(η^5-C_5H_5)(CO)$_2$] will be referred to simply as Lu–Ru. Other systems will be referred to in an analogous manner. More than one system was studied containing a U–Si or a U–Ga bond. These will be referred to U–Si-1, U–Si-2, U–Ga-1, and U–Ga-2. The molecules, abbreviations, and formal oxidation states are given in Figure 3.1 and Figure 3.2. Based on the formal oxidation states, one can predict closed shell spin states for all of the cases (with the exception of uranium containing species). For U^{III} a quartet spin state is expected, while for U^{IV} is expected a triplet state.

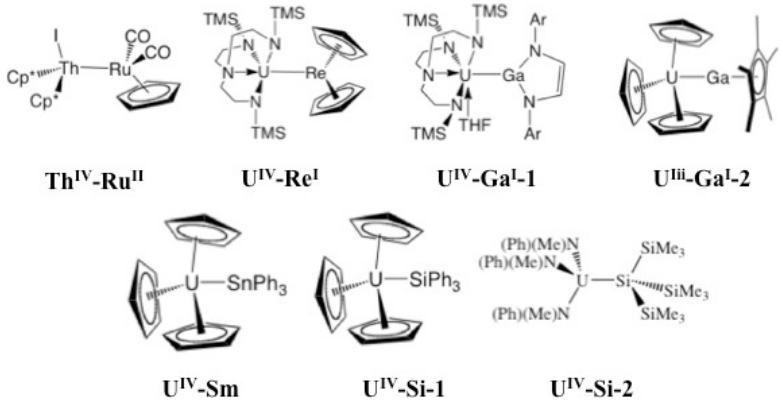

Figure 3.1: Actinide containing systems. Formal oxidation states are indicated in superscript. Ar=2,6-dimethylphenyl, Cp*=C_5Me_5, DME=dimethyl ether, Ph=C_6H_5, TMS=$SiMe_3$.

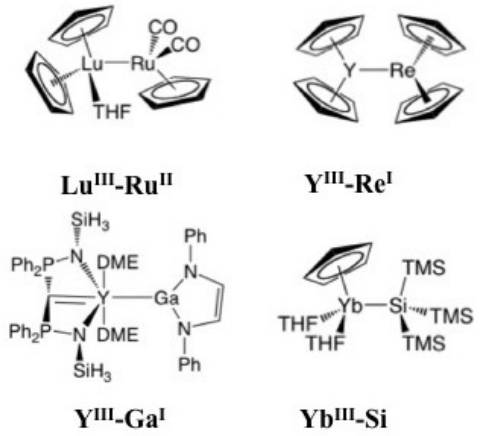

Figure 3.2: Lanthanide containing systems. Formal oxidation states are indicated in superscript. THF = tetrahydrofuran.

3.1.2 Results and Discussions

Several complexes containing either metal-lanthanide or metal-actinide bonds were studied. In choosing systems to compare, we recognize that ligand effects are extremely important in the stability of these systems; therefore, we studied experimentally characterized systems to ensure the relevance of these compounds.

Theoretical calculations. Calculations were performed using density functional theory (DFT) and multiconfigurational methods (CASSCF/CASPT2). [32–34]Density functional theory (DFT) geometry optimizations of the experimentally synthesized clusters were performed using the Turbomole 5.10 package [160] with the Perdew-Burke-Ernzerhof (PBE) exchange-correlation functional [96] and triple-ζ valence plus polarization (def2-TZVPP) [161] basis sets on all atoms, except for actinides and lanthanides where the (def-TZVPP) [162] basis was used. Small core quasi-relativistic pseudopotentials were used for the Th, Lu, U, Y, Yb, Ru, and Re atoms. [163, 164] The resolution of the identity (RI) approximation was used to speed the calculation of the Coulomb integrals. [164–166]

Multiconfigurational complete active space (CASSCF) [32] calculations followed by second-order perturbation theory (CASPT2) [33, 34] were performed on the DFT optimized geometries with the unsupported metal-metal bond distance reoptimized at the CASPT2 level. Thus, a numerical procedure was followed according to which single-point energy calculations were computed for structures for which the metal-metal distance was varied in 0.05 Åincrements while each supported metal fragment remained fixed at its DFT optimized geometry. Using a second-order fit, the minimum metal-metal bond distance was obtained. For systems where multiconfigurational effects were negligible, energies were calculated at the second order Møller-Plesset perturbation (MP2) [167, 168] level in place of CASSCF/CASPT2 (see below).

Scalar relativistic effects were included at the CASSCF/ CASPT2 level using the 2nd order Douglas-Kroll-Hess Hamiltonian [169] and relativistic all electron ANO-RCC basis sets. The metals were treated with the triple-ζ quality basis set (ANO-RCC-VTZP) [101, 170, 171] with the following contractions: In Th and U, the pri–mitive sets were contracted to 9s8p6d4f2g1h. In Y, the contraction was 7s6p4d2f1g while in Lu and Yb 8s7p4d3f2g1h and 8s7p4d3f2g were used, respectively. For the transition metals, the Ru contraction was 7s6p4d2 f1g while the Re contraction was 8s7p5d3f2g. Lastly, the Ga contraction was 6s5p3d2f1g, Sn was 7s6p4d2f1g, and Si was 5s4p2d1f. The main group atoms bonded to the metals were treated with double-ζ basis sets, while the peripheral atoms were treated with minimal basis sets. The ground states of these compounds were always well separated from their lowest excited states and thus spinorbit effects were not included.

The CASSCF/CASPT2 and MP2 calculations were performed with the Molcas 7.4 package. [172] The computational costs arising from the two-electron integrals were drastically reduced by employing the Cholesky decomposition technique [173–175] for the CASSCF/CASPT2 level combined with the Local Exchange screening. [176] Furthermore, the CASSCF/CASPT2 approach has proven to be successful for many actinide-containing systems. [36, 103, 105, 177]

The character of the metal-metal bond was further investigated by performing fragment calculations with energy decomposition as implemented in the Amsterdam Density Functional program (ADF2009) [50] using the local VWN exchange-correlation potential [178] and nonlocal Perdew-Burke- Ernzerhof (PBE) [96] exchange-correlation corrections. A triple-ζ basis set plus two polarization functions was used and relativistic corrections were added using the scalar relativistic zero-order regular approximation (ZORA). [179] No core electrons were frozen.

Active space choice. The active space choice is essential in CASSCF calculations and should include nearly degenerate orbitals in a balanced way. The molecular orbitals in the frontier regions of these compounds consist primarily of linear combinations of metal valence atomic orbitals. As such, we chose to include all molecular orbitals with significant contributions from the valence orbitals of the two metals. Specifically, the valence orbitals close in energy to the HOMO and LUMO were localized on the An/Ln and M centers and were put into the active space (active orbitals are provided in the Supporting Information).

The active spaces for the Lu–Ru and Th–Ru systems contain eight electrons in eight orbitals, denoted as (8,8). Both complexes have closed-shell singlet ground states. The eight orbitals are linear combinations of 4d and 5s orbitals on Ru and 5d and 6s orbitals on Lu (6d and 7s for Th). The 4f orbitals on Lu are highly localized on Lu and quite low in energy; therefore, there they were not included in the active space (a typical situation for 4f electrons). Similarly, the active space for Y–Re contains orbitals consisting of contributions from the Y 4d and 5s orbitals and the Re 6d and 6s orbitals, resulting in a (6,6) active space. Since the ground state of U–Re is a triplet, the six analogous orbitals to Y–Re were included in the active space along with two additional orbitals localized on uranium and contain the two unpaired electrons, resulting in an (8,8) active space. The singly occupied molecular orbitals (SOMOs) were linear combinations of U

5f orbitals. The active spaces for U–Ga-1 and U–Ga-2 contain molecular orbitals that are linear combinations of U 7s, 6d, and 5f, Ga 3s, and 3p orbitals. The two systems differ in the formal oxidation state of uranium, U^{IV} and U^{III} for U–Ga-1 and U–Ga-2, respectively. For U–Ga-1, the doubly occupied orbitals were well separated from the unpaired electrons; therefore, a (2,4) active space was used. For U–Ga-2, a (5,7) active space was used. In this case, three orbitals are essentially singly occupied and one orbital is nearly doubly occupied while the remaining orbitals are nearly empty. However, for the Y–Ga system, the HOMO–LUMO gap at the HF level is very large (185 kcal/mol). The occupied orbitals with Y contributions are much lower in energy than the HOMO. As a result, this complex was studied exclusively with MP2 (HOMO and LUMO are shown in the Supporting Information). Like Y–Ga, Yb–Si was also essentially single reference and was studied with both CASSCF/CASPT2 and MP2. Only a small active space was required and a (2,5) space composed of orbitals that are linear combinations of Yb 6s and Si 3s and 3p orbitals was used. In fact, a (2,2) space may have been large enough, but three additional virtual orbitals in the valence region were included since they contained contributions from Yb and Si as well. These three orbitals had occupation numbers very close to zero. The last two complexes studied contained U–Si bonds, denoted U–Si-1 and U–Si-2. The active space was chosen to include orbitals that have contributions from U 7s, 6d and 5f orbitals, Si 3s and 3p orbitals. The best active space for the triplet ground state of U–Si-1 was a (6,6) space. For U–Si-2, the best active space for the triplet ground state was (4,4).

CASSCF calculations were not performed for U–Sn since the energy-decomposition results (described later in this work) gave the same bonding picture for U–Sn as with its isostructural complex U–Si-1 and we have no reason to suspect CASSCF would show anything different. In the subsequent CASPT2 calculations all orbitals up to the sub-core were frozen. For example, in U–Re, there were 214 doubly occupied orbitals not included in the active space and 104 of these orbitals were frozen in the CASPT2 calculations. In the CASSCF calculations, no orbitals were frozen.

Geometry optimization–DFT Results. Geometries were optimized at the DFT level for all structures shown in Figure 3.1 and Figure 3.2. In general, PBE bond distances and angles are in good agreement with experimental values. Some differences between experimental and calculated geometries are expected to occur because the

calculations were performed in the gas phase; however, bond distances vary at most by 0.1 Åand bond angles by 1–6° (see the Supporting Information for details).

Geometry optimization–CASPT2 Results. CASPT2 calculations were performed on the PBE optimized geometries to further study the interactions contributing to the Ln/An–M bonds. All of the systems studied have electronic ground states well separated from their first excited states and in every case one configuration contributed at least 90% towards the total CASSCF wavefunction. Specifically, the CASSCF wavefunction for Lu–Ru, Th–Ru, U–Ga-1, U–Ga-2, and U–Si-1 contain 92% one configuration, while U–Si-2 is 99% one configuration. Y–Re and U–Re are 96% one configuration, and Yb–Si has one configuration contributing 97%. Y–Ga is a closed shell singlet with a well separated HOMO–LUMO gap. As a result, Y–Ga is, for all purposes, single-reference and was treated with second order Møller-Plesset perturbation theory (MP2) instead of CASPT2. For comparison, MP2 calculations were preformed for Yb–Si as well.

While a full CASPT2 geometry optimization is not feasible, the unsupported Ln–M, or An–M, bond distances were optimized at the CASPT2 level by the numerical procedure described in the methods section. By optimizing the CASPT2 distance, we can check if the qualitative description of the bonding is sensitive to small changes in the geometry. For these systems, no significant changes were observed. The results are given in Table 1 along with the experimental and PBE distances.

Table 3.1: Optimized bond distances in angstroms.

Species	PBE	CASPT2 (MP2)	X-ray diffraction	Sum of the Covalent Radii [180]
Lu–Ru	3.015	2.912	2.995	3.10
Th–Ru	3.070	2.910	3.028	3.26
Y–Re	2.998	2.983	2.962	3.17
U–Re	3.043	2.917	3.048	3.24
Y–Ga	3.119	(2.901)	3.176	2.99
U–Ga-1	3.242	N/A	3.221/3.298	3.06
U–Ga-2	3.065	3.083	3.065/3.080	3.06
Yb–Si	3.022	2.912 (2.900)	3.032	2.92
U–Sn	3.238	N/A	3.166	2.97
U–Si-1	3.106	2.965	N/A[a]	2.97
U–Si-2	3.003	N/A	3.091	2.97

[a] No crystal isolated.

In Table 3.1, the metal-metal bond distances determined via PBE, CASPT2, and MP2 are compared. Also included in the table are the distances determined via X-ray diffraction [62, 63, 151–159] as well as with the sum of the covalent radii. The covalent radii in Table 3.1 are taken from the reference by Mantina et al. [180]The authors report two sets of covalent radii, those by Cordero et al. [181] and those by Pyykkö and Atsumi [182] and they recommend using an average of these values. Comparison with the sum of the covalent radii has been used as a criterion for the existence of a direct metal–metal bond. Looking at Table 3.1, five of the Ac/Ln–M distances from X-ray diffraction are shorter than the sum of the covalent radii while five are longer (no crystal was iso- lated for U–Si-1). While this could suggest that these types of bonds are borderline with respect to being single bonds, recall the uncertainty in the atomic radii is on the order of 0.1 Å, and all the experimental bonds fall within this margin of error. Moreover, the systems in question contain highly ionic bonds and through the use of theory, the nature of the bonding can be further understood.

The DFT optimized metal-metal bond distances agree quite well with experiment. The mean unsigned difference (MUD) between the X-ray and DFT distances is 0.003 Å while the MUD between CASPT2 and experiment is 0.087 Å (it should be recalled

that at the CASPT2 level only one degree of freedom is optimized). Nevertheless, a particularly interesting result occurred for the U–Ga-2 complex. The crystal structure contained two geometries with U–Ga distances of 3.065 Å and 3.080 Å. Our results with PBE gave a distance of 3.065 Å, agreeing perfectly with the first structure, while the CASPT2 bond distance of 3.083 Å was very close to the second structure. In all of the other structures, the PBE An/Ln–M distance was longer than the CASPT2 distance. For the U–Re bond, the procedure used in the CASPT2 optimization was repeated with DFT. The fully optimized DFT geometry had a U–Re distance of 3.043 Å. When only the U–Re distance was varied, the optimized distance was 3.074 Å. Given that only one distance is varied, the distances are in good agreement. Additionally, the energy difference between the structure at 3.074 Å and the optimized structure is 1.1 kcal/mol.

Discussion of the CASSCF results. For homobimetallic bonds, the metal-metal bond is necessarily covalent and often is characterized by a high bond order. For heterobimetallic compounds, one expects important ionic contributions to the bonding due to differences in atomic electronegativities; however, covalent contributions to the bonding may be involved as well. As a rule, the active space in multireference calculations should contain sets of bonding and anti- bonding orbitals. In previous work, [62, 63] not only were U– Ga-1 and U–Re characterized experimentally, they were also studied using fragment analysis as implemented in the Amsterdam Density Functional (ADF) program. The calculations indicated a predominantly ionic bond but noted that the orbital interaction provides a significant contribution to the bonding. In the case of U–Ga-1, the orbital interaction contributes 28% of the total bond energy, while in U–Re the orbital contribution is 32%. But most notably, the DFT calculations suggested σ- and modest π-donation from rhenium (or gallium) to uranium originating from polarization of ligand orbitals towards uranium.

The potential existence of a π-interaction was a very exciting idea, and our objective was to further understand its significance. The CASSCF results for both U–Ga-1 and U–Re do not, however, exhibit any bonding and antibonding pairs of orbitals corresponding to a uranium-metal bond, but orbital interactions between the two metal centers are observed. Unfortunately, defining these orbitals as bonds simply from the qualitative shape of the molecular orbital is not possible. In fact, the CASSCF results suggest that the manner in which we classify the orbital-types in highly ionic bonds

must be approached carefully. In all cases, no pairs of bonding and antibonding orbitals are present and it is thus difficult to talk about s or p bonds. This holds true for all of the complexes reported in this study. Nevertheless, the lack of a s and p bond does not conflict with the previous calculations. [107, 151] Although there are no bonding and antibonding pairs, the previous DFT calculations suggest that orbital interactions contribute about thirty percent to the total bonding energy. The covalent interactions were described as σ and π donations. This means that an occupied orbital on one fragment interacts with an empty orbital on the other fragment transferring electron density from one metal to the other. For all of the systems studied, an orbital corresponding to a σ-donation is observed. U–Ga-1 and U–Re will be discussed in more detail, but for all of the remaining systems no significant additional orbital interactions are observed.

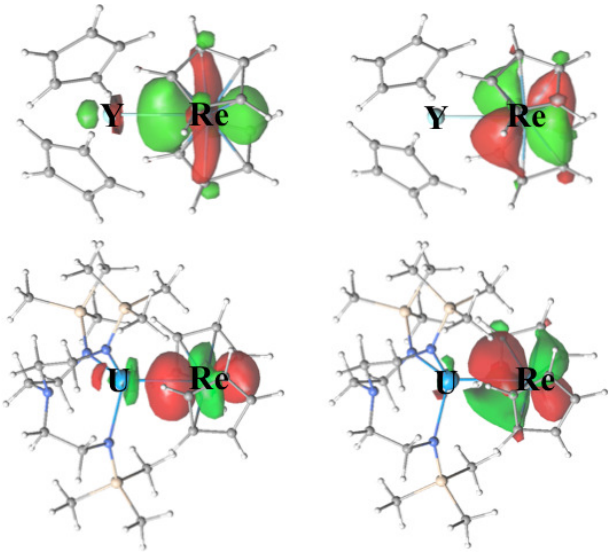

Figure 3.3: Select orbitals from the Y–Re and U–Re CASSCF calculations. The σ-donating orbitals are on the left and the possible π-donating orbitals are on the right.

Turning to U–Re and its lanthanide counterpart Y–Re, the most interesting natural orbitals from the U–Re and Y–Re CASSCF calculations are shown in Figure 3.3. The U–Re orbital on the bottom left (occupation number 1.97) is dominated by the Re $5d_z^2$ orbital with a small uranium contribution. An analogous orbital is also present in Y–Re (occupation number 1.97) and both orbitals are examples of a σ-donation.

Figure 3.3 also includes a natural orbital from both U–Re and Y–Re that is primarily composed of the Re $5d_{xy}$ orbital. This 5d orbital is oriented in the correct direction to participate in a π-interaction; however, and in agreement with the previous calculation, the orbital, as in the case with the σ-interaction, is mainly localized on the Re atom. The analogous Y–Re orbital (occupation number 1.97) has no contribution for yttrium, while the U–Re orbital (occupation number 1.96) has a small uranium contribution. If we plot this orbital at a lower isodensity (0.02 as opposed to 0.04 electrons/volume = electrons/bohr^3) we see an increased π-like appearance; however, interpreting the significance of this orbital is not straightforward.

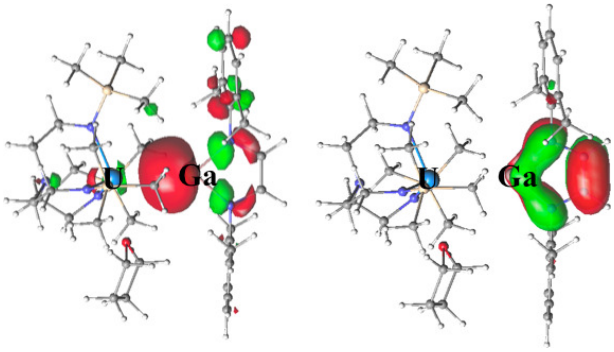

Figure 3.4: Select doubly occupied orbitals from the U–Ga-1 CASSCF calculation. The σ-donating orbital is on the left and possible π-donating orbital is on the right.

Likewise in U–Ga-1, CASSCF results showed an example of σ-donation (Figure 3.4). Although in this system the active space contained only the orbitals corresponding to the two unpaired electrons, larger active spaces were tested but proved to be unnecessary. Looking at the DFT results from the previous work [151], we observe the same orbital ordering in our inactive space as in DFT and can identify the two molecular orbitals in our calculations that were previously described: the σ-donating orbital and possible π-donating orbital (Figure 3.4). In this case, the p-orbital is localized on Ga and the neighboring N atoms even at the lower isodensity value leading us to conclude that a π-interaction is not observed at the CASSCF level.

All in all, the CASSCF results indicate that, while a π interaction is clearly not present in U–Ga-1, it may be possible in U–Re. Since we have reoptimized the geometry, we performed additional DFT calculations, in analogy with those performed

previously, [62, 63] to compute the energy decomposition to make further comparisons with CASSCF and the previous studies.

Energy-decomposition analysis results. These systems are well suited to the application of the energy-decomposition method since they are formed from individually supported fragments. Indeed, the synthesis proceeds by combining the An/Ln fragment and the metal fragment with the final complex formed by salt or alkane elimination. [62, 63, 146, 151, 154–156, 159] The only exception is represented by U–Ga-2 [153] where no salt is eliminated since the two fragments are directly combined. During the fragment analysis, each species is divided into two fragments by breaking the total complex along the An/ Ln–M bond. For U–Ga-2, the fragments, as in the experimental fragments, have zero charges. In the remaining systems, the fragments used in the calculation are charged since in the experiment the fragment charges are balanced by the presence of the counterions that lead to salt formation. In particular, during the fragment analysis the An/Ln fragment is charged +1, while the metal fragment has a charge of –1.

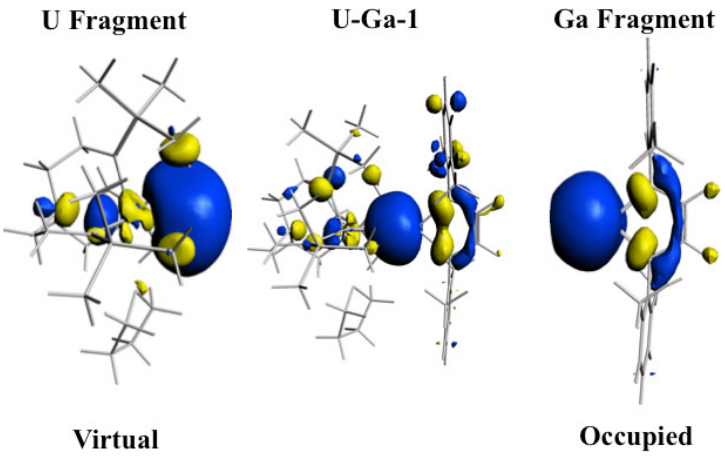

Figure 3.5: σ-donation in U–Ga-1. Center: The orbital from U–Ga-1 fragment calculation with the highest percent contribution from the both the U and Ga fragments. Left: The contributing orbital from the U fragment. Right: The contributing orbital from the Ga fragment.

Table 3.2: Bonding energy and charge transfer between the Ln/An and M fragments.

Species	Bonding Energy (kcal.mol^{-1})	Charge Transfer (An/Ln to M)
Th–Ru	-135.3	0.88
Lu–Ru	-128.6	0.67
U–Re	-128.2	0.74
Y–Re	-156.2	0.89
U–Ga-1	-91.3	0.53
U–Ga-2	-17.8	-0.06
Y–Ga	-95.0	0.46
U–Sn	-120.8	0.49
U–Si-1	-131.4	0.50
U–Si-2	-139.1	0.57
Yb–Si	-109.3	0.54

The total bonding energy and the charge transfer (based on multipole expansion charges [183]) were calculated and the results are reported in Table 3.2. All of these systems, with the exception of U–Ga-2, show qualitatively similar bond energies. The bonding energy in U–Ga-2 is an order of magnitude smaller than the other species; this result is expected since, through simple Coulomb interactions, bringing a positively charged fragment and a negatively charged fragment together should result in a substantially more favorable bonding energy than the combination of two neutral fragments. Furthermore, a charge transfer is observed showing that electron density is transferred from the negatively charged metal fragment to the positively charged An/Ln fragment (with the exception of U–Ga-2). The negatively charged metal fragments present lone pair orbitals that are localized on the metal centers. Inspection of these orbitals in the fragment calculations (see Figure 3.5), indicates lone pair orbitals that contribute to the interactions that Liddle et al. [62, 63] described as σ-donation. Looking more closely at U–Re, an example representative of the σ-donation present in all of the systems can be seen (Figure 3.5). The doubly occupied orbital from the Re fragment calculation (right) is the lone pair on Re. This lone pair interacts with the unoccupied orbital on the U fragment (left) to form the σ-like molecular orbital (center). This qualitative picture, in combination with the charge transfer, supports the idea that a σ-donation is occurring in this complex. Analogous orbitals are seen in all the systems with charged fragments.

As the final electronic structure exhibits nearly complete transfer of this charge density to the An/Ln fragment, as opposed to retention of a dative bond, the nature of the metal-metal interaction is more ionic than covalent.

U–Ga-2 is an exception with respect not only to the bonding energy but also to charge transfer. The lack of charge transfer between the fragments in this compound is a consequence of using neutral fragments during the analysis. For the other systems, a large charge transfer is observed, as expected, since two oppositely charged fragments are joined together. However, the nature of the bond in U–Ga-2 is the same as in the other systems, that is, a s-donation occurs. Furthermore, the percentage of orbital interaction in U–Ga-2 is similar to the one present in the other systems. If we used neutral fragments for the other species, we would see almost no charge transfer as well. Additionally, according to the CASSCF results, the orbitals in the active space are qualitatively similar to those in the HOMOLUMO region of fragment calculations. For these reasons, the U–Ga bond in U–Ga-2 can be considered similar to the Ac/Ln–M bonds present in the other systems.

Returning to the presence of p-donation in U–Re and U–Ga-1, [62, 63] the previously suggested possibility of an, albeit weak, p-donation was based on the visualization of the Kohn-Sham frontier orbitals and the breakdown of their compositions as computed by DFT. The fragment analysis in the current study and those referenced [62, 63] were performed at slightly different levels of theory on different geometries. Specifically, the fragment analysis by Liddle et al. [62, 63] was performed using the BP86 functional with a triple-z basis set (TZP) whereas we used PBE with a triple-ζ plus two polarization-functions (TZ2P) basis.

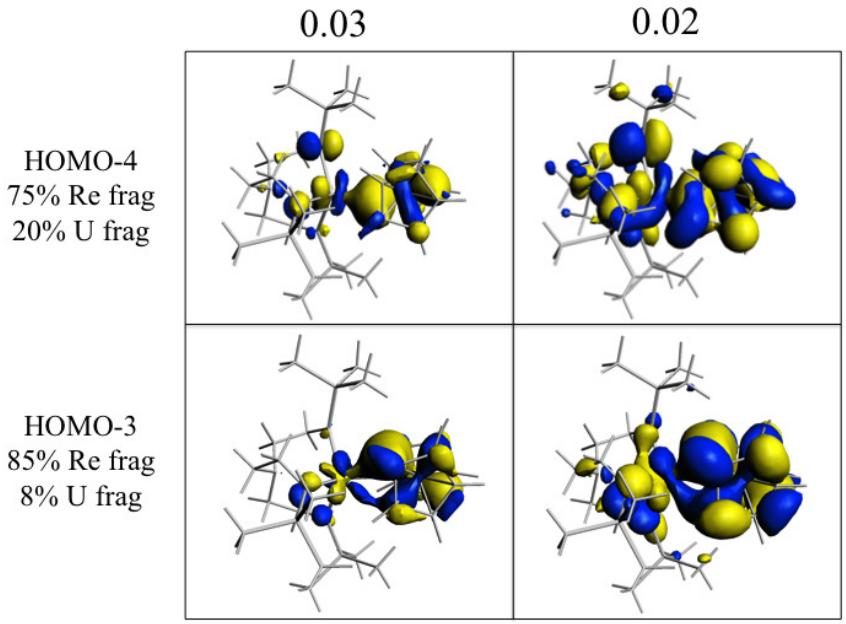

Figure 3.6: U–Re HOMO-3 was plotted at isodensity values 0.03 and 0.02 for calculations performed at the PBE/TZ2P level of theory in order to compare the geometry optimized in this work and that of Gardner et al.

Our energy-decomposition studies further supported the conclusions derived from the CASSCF results: U–Re had some very small orbital interaction reminiscent of a π-bond (even less than in our CASSCF results), but U–Ga-1 did not. Initially we were concerned that our results conflicted with the previous studies, but in fact they do not. For U–Ga-1, different models were used in the previous work and this study. The previous work truncated the $SiMe_3$ groups to SiH_3 accounting for the difference in our results. With the larger model (U–Ga-1) we see the same picture at the CASSCF and DFT levels. For U–Re, the full experimental structure was studied both previously and here, but with different levels of theory. As a comparison, we performed the fragment analysis for U–Re at the geometry reported by Liddle et al. [62] with PBE/TZ2P and reproduced the previous results. For the geometry optimized in this study, at an isodensity value of 0.03 electrons/volume=electrons/bohr^3, we did not observe the same π shaped orbital as seen for the geometry from the previous work; however, if we lower

our isodensity to 0.02 electrons/volume = electrons/bohr^3 our orbitals resemble those shown previously (see Figure 3.6). However, at the lower isodensity, we also saw orbitals in the other systems, like Y–Re, for example, that began to look π-like. For this reason, we are hesitant to interpret the Kohn–Sham orbitals visually and retain our interpretations based on the higher-level CASSCF results.

Table 3.3: Comparison between calculated geometries for U–Re from the current study and previous work by Gardner et al.

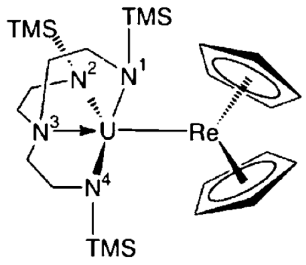

Bond Length (Å)	Current Study	Calculated [62]	Experiment [62]
U–Re	3.043	3.062	3.048
U–N(2)	2.260	2.322	2.283
U–N(4)	2.272	2.307	2.274
U–N(3)	2.775	2.766	2.681
angles(∘)			
N(4)–U–N(2)	103.0	106.0	107.1
N(1)–U–N(2)	110.3	112.4	112.6
N(3)–U–N(2)	69.1	68.1	69.4
Re–U–N(2)	110.7	111.7	110.7
N(1)–U–N(4)	108.6	103.9	105.4
N(3)–U–N(4)	69.2	68.6	69.6
Re–U–N(4)	121.3	120.3	119.1
N(3)–U–N(1)	67.3	68.3	69.5(2)
Re–U–N(1)	102.9	102.7	101.83(16)
Re–U–N(3)	168.4	169.3	169.74(14)

As for the differences between our geometry and those previously reported, they vary only slightly. For example, the U–Re distances in our calculation and Liddle et al. are 3.043 and 3.062 Å respectively in comparison with the experimental distance

of 3.0475(4) Å (see Table 3.3 for a complete comparison of the differences between our structures). Nevertheless, it appears that the shape of the orbital corresponding to a π-interaction is very sensitive to even small geometry changes. This supports the previously suggested idea that the π-donation is a minor component of bonds that are dominated by electrostatics, and therefore sensitive to small fluctuations in the geometry; it is thus unlikely to contribute to the reactivity of the U–Re and U–Ga-1 systems where these types of metal-metal bonds are described as elastic and easily disturbed by crystal packing. [63]

Bonding energies cannot be uniquely described in terms of pure orbital interactions (resonance); in addition, steric and electrostatic contributions must be considered. Fragment analysis expresses the total interaction energy as shown in Equation 3.1,

$$\Delta E_{int} = \Delta E_{electrostatic} + \Delta E_{orbital} + \Delta E_{Pauli} \tag{3.1}$$

in which the terms on the right-hand-side refer to electrostatic interactions, orbital interactions, and Pauli repulsion (the energy cost associated with orthogonalizing the various fragment orbitals as they are brought into contact with one another).

Table 3.4: Energy decomposition performed using Equation 3.1. The percentage of the total attractive interaction of electrostatic and orbital interactions is given in parentheses.

	Repulisive Interaction	Attractive Interaction	
Species	Pauli Repulsion[a]	Electrostatic Interaction[a]	Orbital Interaction[a]
Th–Ru	129.9	-193.4(72.9%)	-71.9(27.1%)
U–Re	160.3	-201.9 (66.7%)	-101.0 (33.3%)
U–Ga-1	73.7	-124.8 (75.6%)	-40.2 (24.4%)
U–Ga-2	49.1	-41.0 (61.2%)	-25.9 (38.8%)
U–Sn	100.2	-159.1 (72.0%)	-61.9 (28.0%)
U–Si-1	99.4	-162.1 (70.2%)	-68.7 (29.8%)
U–Si-2	111.7	-168.6 (67.3%)	-82.1 (32.7%)
Y–Re	94.1	-171.9 (68.9%)	-77.7 (31.1%)
Lu–Ru	87.8	-163.4 (75.5%)	-53.0 (24.5%)
Yb–Si	59.9	-132.1 (78.1%)	-37.1 (21.9%)
Y–Ga	51.5	-110.1 (75.1%)	-36.4 (24.9%)

[a]Energies in kcal.mol^{-1}

The energy-decomposition results obtained using Equation 3.1 are reported in Table 3.4. The percentage of the total attractive interaction of electrostatic and orbital interactions is shown in parentheses and clearly indicates that the most important portion of the attractive interaction is electrostatic. This means that these bonds should be thought of as highly ionic since the ionic contributions are stronger than the orbital contributions. However, orbital interactions are present to a nontrivial degree. While the lanthanide containing systems have slightly smaller orbital contributions than do the actinide containing systems, in general all of the An/ Ln–M bonds are very similar. Y–Re was described as a donoracceptor interaction by Butovskii et al. [151] In our results, not only the Y–Re bond, but all of the Ln/An–M bonds have the same type of donor-acceptor interaction (i.e. σ-donation). The orbital contribution to the U–Re system is nearly the same as the Y–Re system, 33.3% and 31.1% respectively. Again, we emphasize that these interactions are dominated by a σ-donation from the metal ligand center to the An or Ln center in all cases.

To further stress this point, we note that in the energy-decomposition analysis implemented in ADF, a favorable orbital interaction is not always associated with a charge transfer between the two fragments. Instead, when a strong charge rearrangement occurs in one fragment as a result of its interaction with the charge distribution of the other fragment (i.e. internal polarization), then the orbital contribution may still be high despite there being no effective charge transfer between the two moieties. One example of this is the U–Ga-2 complex, which shows the highest percentage of orbital interaction but lacks significant charge transfer. This means that in this particular case, the polarization effect not only is dominant but also is the only contribution to the stabilization of the orbital interaction term upon relaxation of the U–Ga-2 total electron density.

Topological analysis of the electron density. To further assess the character of the chemical bonds involved in these heterobimetallic systems, we decided to apply the quantum theory of atoms in molecules developed by Bader [46, 47] and analyze the topology of the electron density. In AIM theory, a chemical bond exists if a line of locally maximum electron density links two neighboring atoms (along a so-called bond path) and a bond critical point (BCP) exists, which is defined as the minimum in the density along the locally maximal line. At a BCP, the gradient of the electron density 1 is zero while the Laplacian, $\nabla^2\rho$, is the sum of two negative and one positive eigenvalues of the density Hessian matrix, and thus may have either a net positive or net negative value. A positive Laplacian means a local depletion of charge, while a negative value is a sign of a local concentration of charge. The latter is a strong condition for a covalent bond, in the sense that a negative Laplacian indicates always a shared interaction of electron density between two linking atoms, while a closed-shell interaction is associated with a positive Laplacian, consistent with a type of bond that has moved away from covalency due to depletion of charge at the location of the BCP. Since there exists a continuum between a covalent and a non-covalent bond, Bianchi et al. [184] have suggested the classification of the bond between two "closed shel" interacting atoms according also to a second condition, the total electronic energy density at the BCP, $E^e{}_b$. This term is defined as the sum of b the kinetic energy density, G_b, which usually dominates in a non-covalent bond, and the potential energy density V_b, which is usually negative and associated with accumulation of charge between the nuclei. In clear covalent bonds both

the Laplacian and Ee are negative. In less clear cases, b where the Laplacian is slightly positive, the value of $E^e{}_b$ can be used to make a further classification of the bond, from being slightly covalent to purely ionic/nonbonded. In this classification, with $\nabla^2\rho$ ¿ 0, if $E^e{}_b$ is negative, the bond is called dative; if $E^e{}_b$ is close to zero, the bond is metallic; if $E^e{}_b$ is positive, the bond can be either ionic or van der Waals.

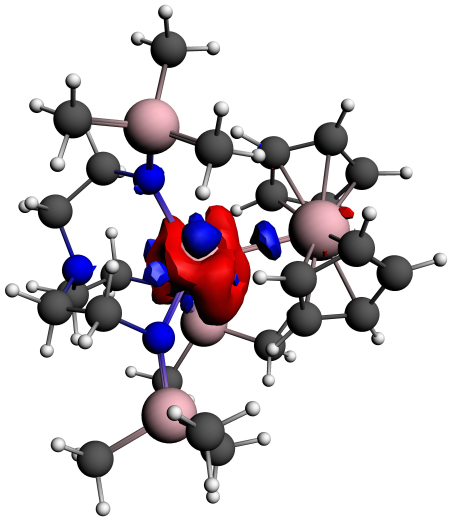

Figure 3.7: Electron density difference between the relaxed electron density of the U–Re supermolecule and the electron density of the separated fragments of U and Re at the position they have in the supermolecule. A red color indicates a depletion of charge and a blue color an increase.

Table 3.5: Theoretical bond critical point properties for the bimetallic species studied. All values are expressed in atomic units.

	ρ_b	$\nabla^2\rho_b$	G_b	G_b/ρ_b	V_b	E^e_b
Th-Ru	0.02271	0.02718	0.01145	0.50418	-0.004656	0.006796
U-Re	0.02659	0.04121	0.01773	0.66679	-0.007423	0.0103
U-Ga-1	0.01492	0.01275	0.005574	0.37359	-0.003189	0.002385
U-Ga-2	0.01561	0.02566	0.00862	0.55221	-0.002205	0.006415
U-Sn	0.02052	0.01193	0.005263	0.25648	-0.002982	0.002281
U-Si-1	0.02287	0.002005	0.005597	0.24473	-0.005096	0.0005013
U-Si-2	0.02469	0.006462	0.00805	0.32604	-0.001606	0.006444
Y-Re	0.02084	0.02199	0.01114	0.53455	-0.005649	0.005496
Lu-Ru	0.01809	0.0455	0.01215	0.67164	-0.000762	0.01139
Yb-Si	0.01612	0.04625	0.01189	0.73759	-0.0003323	0.01156
Y-Ga	0.01364	0.01108	0.005056	0.37067	-0.002285	0.002771

In Table 3.5 we have listed all the parameters needed for a detailed topological analysis of the chemical bond in the heterobimetallic systems considered here. The most salient feature is that for all the complexes the density at the BCP is small and the Laplacian is positive, indicating that in none of the cases is a covalent interaction indicated. Furthermore, $E^e{}_b$ is always slightly positive, suggesting that the bond can be classified as between metallic and ionic. In Figure 3.7, we have also plotted the electron density difference between the relaxed total electron density of the U–Re cluster and the electron density of the isolated fragments at the position they have in the supermolecule. The blue certifies a local depletion of charge and the red a local accumulation. What is evident from Figure 3.6, is that approximately at the BCP between U and Re, there is a depletion of charge, that is, the electrons move away from the center of the bond path that links the two atoms, a clear sign that a closed-shell interaction and not a shared interaction is occurring. Furthermore, it is also clear that there is a strong charge rearrangement on the uranium fragment in the supermolecule as compared to the isolated fragment. This charge rearrangement is associated with the internal polarization described above for the U–Ga-2 case that exhibits an orbital interaction term without significant charge transfer between the two initially neutral fragments.

3.1.3 Conclusion

Several systems containing heterobimetallic bonds involving one f-block element were studied computationally. Specifically the following molecules were investigated: [(η^5-C_5H_5)$_2$(THF) LuRu (η^5-C_5H_5)(CO)$_2$], [154], [(η^5-C_5Me_5)$_2$(I) ThRu (η^5-C_5H_5)(CO)$_2$], [155] (η^5-C_5H_5)$_2$ YRe (η^5-C_5H_5)$_2$], [151] {N($CH_2CH_2NSiMe_3$)$_3$} URe (η^5-C_5H_5)$_2$, [62] [YGa (NArCH)$_2$ C(PPh_2N SiH_3)$_2$H (CH_3OCH_3)$_2$], [152] [{N($CH_2CH_2NSiMe_3$)$_3$} U{Ga(NArCH)$_2$} (THF)], [63] [(η^5-C_5H_5)$_3$ UGa (η^5-C_5Me_5)], [153] [Yb(η^5-C_5H_5) Si($SiMe_3$)$_3$ (THF)$_2$], [156] [(η^5-C_5H_5)$_3$ U ($SnPh_3$)], [158] [(η^5-C_5H_5)$_3$U-($SiPh_3$)], [157] and (Ph[Me]N)$_3$USi($SiMe_3$). [159] Density functional calculations predict geometries in good agreement with experiment. CASSCF/CASPT2 calculations were also performed to better understand the nature of the interactions between the two metal centers. The CASSCF wavefunction indicated that the electronic structure of these systems is not multiconfigurational, and the CASSCF/CASPT2 and DFT results give the same description of the An/Ln–M bond. Even though the actinides are known to have more diffuse f-electrons than the lanthanides, the f-electrons are localized on the Ln/An center and do not engage in bonding in any of the systems studied. Consequently, the metal-metal interaction is qualitatively the same in all cases and no clear differences in bonding can be identified between the 4f and 5f elements. From this perspective, the lanthanides and actinides in these systems can be thought of as hard d-elements.

The results have demonstrated that : (i) the An/Ln–M bonds are primarily ionic; (ii) no 'true' σ and π bonds are present in any of these systems, but rather σ-type donation from the metal ligand fragment to the Ln/An fragment is seen in all cases; (iii) a π-donation is possible in the system containing a U–Re bond, but not observed in the other systems, which reinforces the notion, as suggested previously, that this interaction is extremely weak and not expected to alter the reactivity of the species.

3.1.4 Acknowledgements

This research was supported by Director, Office of Basic Energy Sciences, U.S. Department of Energy under Contract No.USDOE/DE-SC002183, and the Materials Science of Actinides Center, an Energy Frontier Research Center funded by the U.S. Department

of Energy, Office of Science, Office of Basic Energy Sciences under Award Number DE-SC0001089. We also acknowledge support from the U.S. National Science Foundation (CHE-0952054).

3.2 Volatilities of Actinide and Lanthanide *N,N*-Dimethylaminodiboranate Chemical Vapor Deposition Precursors: A DFT Study

N,N-Dimethylaminodiboranate complexes with praseodymium, samarium, erbium, and uranium, which are potential chemical vapor deposition precursors for the deposition of metal boride and oxide thin films, have been investigated by DFT guided by field-ionization mass spectroscopy experiments. The calculations indicate that the volatilities of these complexes are correlated with the M–H bond strengths as determined by Mayer bond order analysis. The geometries of the gas-phase monomeric, dimeric, and trimeric species seen in field-ionization mass spectroscopy experiments were identified using DFT calculations, and the relative stabilities of these oligomers were assessed to understand how the lanthanide aminodiboranates depolymerize to their respective volatile forms during sublimation.

3.2.1 Introduction

Lanthanide-containing materials, such as lanthanide oxides and borides, have interesting optical, [185–187] magnetic, [188–190] and electrical [188, 191, 192] properties that make them useful for technological applications such as capacitors, field effect transistors, displays, thermoelectric devices, light-emitting diodes, and lasers. For many of these applications, defect-free thin films are necessary, and in some cases it is crucial to deposit the films uniformly onto substrates with high aspect ratios. [193] To achieve these results, there is much interest in developing better precursors for the chemical vapor deposition (CVD) and atomic layer deposition (ALD) of lanthanide-containing thin films. [194, 195]

For transition metals, some of the most volatile compounds known are homoleptic compounds containing the borohydride ligand, BH_4^-, and these have been shown to be

Reproduced from B. Vlaisavljevich, P. Miró, D. Koballa, T. K. Todorova, S. R. Daly, G. S. Girolami, C. J. Cramer, and L. Gagliardi

Journal of Physical Chemistry C, **2012**, 116, 23194–23200.

useful CVD precursors. [196–203] Homoleptic borohydride compounds of the lanthanides are known but they are not particularly volatile [204–208] because their solid state structures are polymeric. [209–211] By comparison, actinide borohydrides in the +4 oxidation state such as $U(BH_4)_4$ are reasonably volatile despite the fact that some of them are also polymeric in the solid state. [212]

Recently, a new class of metal borohydrides has been described that contain the *N,N*-dimethylaminodiboranate anion, $H_3BNMe_2BH_3^-$(DMADB) (Figure 3.8). [213–215] DMADB is a polydentate ligand capable of chelating a single metal center or bridging between two metal centers.

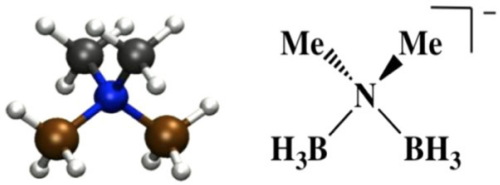

Figure 3.8: Ball and stick (left) and schematic (right) structure of the *N,N*-dimethyl aminodiboranate (DMADB) ligand. Color code: Nitrogen in blue, carbon in gray, boron in bronze, and hydrogen in white.

Compared to the smaller BH_4^- ligand, the DMADB ligand better saturates the coordination sphere of large metals in lower oxidation states. [213] Consequently, lanthanide complexes containing DMADB ligands are among the most volatile compounds known for these elements. [214, 216]

Several $M(DMADB)_3$ complexes with trivalent lanthanides (all except promethium) and an actinide (uranium) have been reported. [214–216] Because the DMADB ligand can chelate to or bridge between two metal centers, a variety of solid-state structures have been observed depending on the size of the M^{3+} ion: the coordination number increases from 12 to 14 as the ionic radius of the metal center becomes larger. [217] As shown in Figure 3.9, the relatively small erbium ion Er^{3+} (r_{Er} = 0.89 Å) forms a dinuclear structure, $Er_2(DMADB)_6$, in which the Er centers are linked by two bridging DMADB ligands, each end of which forms two Er−H bonds. Additionally, each Er center has two chelating DMADB ligands, each providing four Er−H bonds, giving a total coordination number of 12.

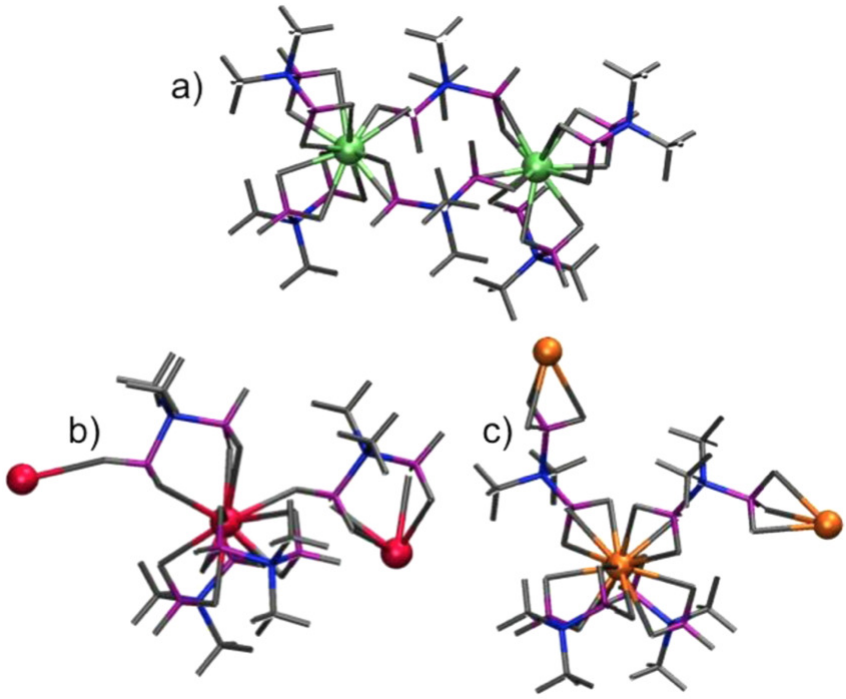

Figure 3.9: Single crystal X-ray diffraction structures. (a) $Er_2(DMADB)_6$ dimer, (b) fragment of the $Sm(DMADB)_3$ or U_A polymeric chain, (c) fragment of the $Pr(DMADB)_3$ or U_B polymeric chain. Color code: Erbium in green, samarium/uranium in red, praseodymium/uranium in orange, nitrogen in blue, boron in magenta, carbon and hydrogen in gray.

For the somewhat larger samarium ion Sm^{3+} (r_{Sm} = 0.96 Å), all three ligands chelate via four Sm−H bonds, but an intermolecular Sm−H bond links the Sm centers together into a chain bringing the total coordination number to 13. In contrast, the even larger praseodymium ion Pr^{3+} (r_{Pr} = 0.99 Å) is coordinated by two chelating DMADB ligands, each of which forms four Pr−H bonds. Moreover, each Pr atom coordinates to two additional bridging DMADB ligands that link the metal centers into a polymeric chain. Each end of the bridging ligands forms three Pr−H bonds resulting in a total coordination number of 14. Finally, for $U(DMADB)_3$, two structural isomers have been synthesized. Isomer U_A is isostructural with 13-coordinate $Sm(DMADB)_3$ and crystallizes from pentane, whereas isomer U_B is isostructural with 14-coordinate

$Pr(DMADB)_3$ and crystallizes from toluene.

The volatility of the lanthanide DMADB complexes increases as the radius of the metal ion decreases. Interestingly, even the polymeric lanthanide DMADB compounds are volatile and sublime readily without significant decomposition at temperatures below 100°C. [214] The high volatility of the polymeric compounds suggests that there is a low barrier for depolymerization to form low molecular weight species (e.g., monomers and dimers). In contrast, and for reasons not well understood, attempts to sublime the isomorphous uranium analogues under identical conditions result only in thermal decomposition at elevated temperatures. [213]

Here, we present an analysis of the electronic structures of lanthanide and uranium DMADB complexes to identify the factors that may account for the differences in volatility. Density functional theory calculations, guided by field ionization mass spectrometry data, were used to identify the volatile lanthanide aminodiboranate species generated during sublimation, and to assess their relative stabilities.

3.2.2 Computational and Experimental Details

DFT calculations were performed at the PBE/def-TZVP [96, 163, 218, 219] level using the Turbomole 5.10.2 program. [160] Scalar relativistic effects were incorporated by employing effective core potentials (def-ECP) with 60 (U) and 28 (Er, Pr, Sm) core electrons, respectively; [218] spin−orbit effects were not included. The resolution of the identity approximation was introduced for the Coulomb integrals. [164, 165] In addition, single point calculations were performed using the Gaussian09 package. [93] As in the optimization, the PBE functional was employed. The Stuttgart/Dresden (SDD) basis set with the ECP60MWB_SEG core potential was used for U, whereas the SDD/ECP28MWB_SEG basis set was used for Sm, Pr, and Er. [218, 220] The 6-311G(d,p) basis set was used on all nonmetal centers. [221] Integral evaluation was performed with an ultrafine grid and the nature of all stationary points was verified by vibrational analysis, which was subsequently used to compute the zero-point vibrational energies and molecular partition functions required to obtain thermal corrections to the energy. Mayer bond orders (MBOs) [48, 49] were computed using the MN-GSM package together with a locally modified version of Gaussian09. [222] MBO analysis has been widely used to study lanthanide–ligand and actinide–ligand interactions. [112, 223, 224]

The effect of long-range weak interactions (i.e., dispersion) between the large number of methyl groups present in the systems was included a posteriori using the DFT-D3 package developed by Grimme. [225, 226] Standard PBE parameters with Becke and Johnson damping functions were used. [227–229] DFT, along with the use of ECP basis sets, has been used successfully for actinide and lanthanide containing systems. [**?**]

The Ln(DMADB)$_3$ complexes, [214, 216] where Ln=Pr, Sm, and Er, and the two isomers of U(DMADB)$_3$, [213, 215] were prepared as described previously. Field ionization mass spectra (FI-MS) were recorded on a Micromass 70-VSE mass spectrometer. The shapes of all peak envelopes correspond with those calculated from the natural abundance isotopic distributions in the observed spectra.

3.2.3 Results and Discussion

Electronic Structure of Solid-State Uranium and Lanthanide Aminodiboranates Models. Understanding the factors that affect volatility is important for the development of practical CVD/ALD precursors. We have previously noted that *N,N*-dimethylaminodiboranate (DMADB) complexes of stoichiometry M(DMADB)$_3$ are highly volatile if the metal is a lanthanide but decompose under the same conditions without subliming if the metal is uranium. [213–216]

To determine the reasons for the difference in behavior, we performed density functional theory studies on finite size complexes. An oligomer model containing four metal centers (part a of Figure 3.10) gave metal−hydrogen distances that agreed well with those observed experimentally. The Er dimer was studied without truncation. For all of the M^{III}(DMADB)$_3$ species, the computed ground state is high spin as expected; thus, each trivalent metal center has two, five, three, and three unpaired electrons for Pr, Sm, Er, and U, respectively.

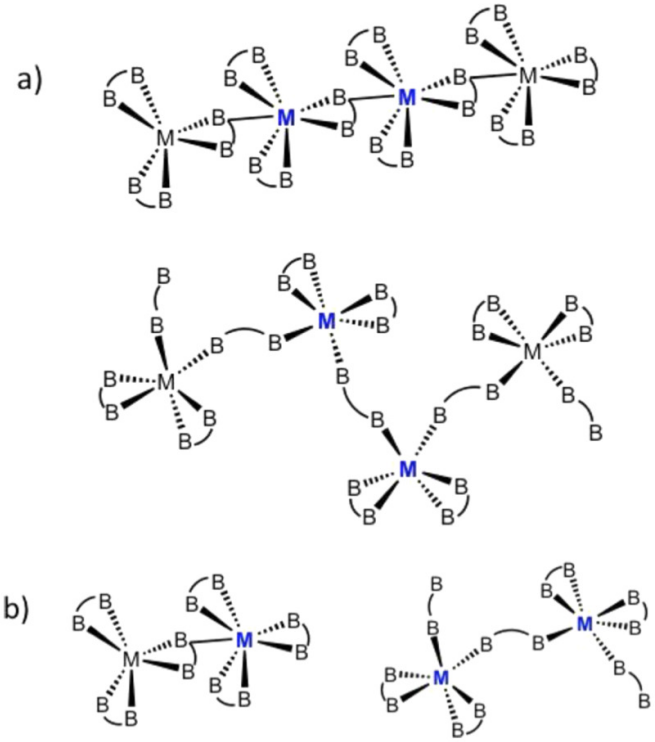

Figure 3.10: (a) Schematic representation of the tetrameric oligomers used to model the solid state polymeric chains. Metal centers whose distances are included in Table 3.6 are in blue. Top: $Sm_4(DMADB)_{12}$ and $U_4(DMADB)_{12}$ (U_A). Bottom: $[Pr_4(DMADB)_{13}]^-$ and $[U_4(DMADB)_{13}]^-$ (U_B). (b) Dimeric models used to compute Mayer bond orders. Left: $Sm_2(DMADB)_6$ and $U_2(DMADB)_6$ (U_A). Right: $[Pr_2(DMADB)_7]^-$ and $[U_2(DMADB)_7]^-$ (U_B). Metal centers whose bond orders are included in Table 3.6 are in blue.

The optimized geometries are compared with available single crystal X-ray diffraction data in Table 1. Distances are reported for the two central metals in the truncated chains. The experimental positions of the hydrogen atoms can be determined less accurately than those of the boron atoms; however, theory gives good agreement with both experimental M−B and M−H distances. The computed and experimental B−N−B angles are very similar for the bridging ligands but can deviate up to two degrees for the chelating ligands (details in the Supporting Information). This deviation is also

observed for the Er dimer, for which a truncated model was unnecessary, and thus is not an artifact of the model choice. The results suggest that the tetrameric oligomer is a good model of the infinite chain, and any small deviations in the metrical parameters are likely due to packing effects.

Table 3.6: Selected Geometric Parameters Obtained from Ground State Geometry Optimization; Average Distances Are Reported for the Two Central Metal Centers (Part a of Figure 3.10) in Å; Average Individual Mayer Bond Orders Are Given along with the Number of Such Bonds Per Metal Center[a]

		Chelating DMADB Ligands				Bridging DMADB Ligands				Total Mayer Bond Order	
M		M–B dist	M–B MBO	M–H dist	M–H MBO	M–B dist	M–B MBO	M–H dist	M–H MBO	M–B	M–H
Pr	calcd	2.867	0.35 x 4	2.447	0.14 x 8	2.629	0.31 x 2	2.472	0.09 x 6	2.01	1.66
	exptl	2.877		2.443		2.666		2.469			
U_B	calcd	2.843	0.39 x 4	2.419	0.21 x 8	2.605	0.28 x 2	2.451	0.10 x 6	2.12	2.28
	exptl	2.879		2.487		2.667		2.498			
Sm	calcd	2.808	0.36 x 6	2.404	0.18 x 12	3.728	[b]	2.592	0.10 x 1	2.16[b]	2.26
	exptl	2.885		2.494		3.524	2.495				
U_A	calcd	2.815	0.41 x 6	2.398	0.24 x 12	3.623	[b]	2.486	0.16 x 1	2.46[b]	3.04
	exptl	2.885		2.494		3.524		2.495			
Er	calcd	2.723	0.36 x 4	2.335	0.22 x 8	2.684	0.44 x 2	2.324	0.20 x 4	2.32	2.56
	exptl	2.756		2.366		2.735		2.303			

[a]MBOs for dimers. Geometric parameters for the dimers are given in the Supporting Information.

[b]No bond order computed for the bridging M–B interaction because a H atom is located in the bond path.

The molecular orbital picture is the same for all four metal complexes. The highest occupied orbitals are all singly occupied (SOMOs), and consist largely of localized 4f (or 5f) atomic orbitals that do not engage in bonding. Below the SOMOs are doubly occupied orbitals corresponding to delocalized bonding in the −BH3 groups of the DMADB ligands (Supporting Information). These orbitals have little metal contribution and are qualitatively the same for the lanthanide and uranium species. All in all, the simple molecular orbital picture provides little if any information about why the actinide and lanthanide DMADB complexes behave differently when heated.

Mayer bond order analyses were performed on dimeric models of the metal DMADB

complexes (part b of Figure 3 for Pr, Sm, and U, and part a of Figure 2 for Er) to quantify the nature of the M−H and M−B interactions (Table 3.6). Each individual bond has a small bond order of ∼0.35 for M−B and ∼0.2 for M−H. These values are only slightly smaller than those computed using a similar methodology for a high-spin iron borohydride compound. [230] Whereas it may seem surprising that the M−B bond order is larger than the M−H bond order, the molecular orbitals show that the electron density is distributed over the entire BH_3 group; therefore, it is likely that this electron density is contributing to the M−B bond order observed. Each M−B bond should be regarded as part of the interaction of the metal center with the entire BH_3 group rather than as a simple covalent M−B bond. For all of the compounds studied, the bond orders tend to increase as the metal ion becomes smaller. Interestingly, the bond orders are generally larger for the chelating ligands than for the bridging ligands suggesting that the M−H bonds to the bridging ligands are more likely to break when the compounds are heated. Furthermore, the difference in bond strengths between the U and isostructural Ln analogues is evident. In particular, the total M−H bond order for U_B is 0.62 larger than for the isostructural Pr species, and the total M−H bond order for U_A is 0.78 larger than for the isostructural Sm species. This result suggests that more energy will be required to depolymerize the uranium complexes than the lanthanide analogues.

Fragmentation of the Solid-State Structures. During sublimation, the solid polymeric $M(DMADB)_3$ complexes must depolymerize by breaking metal-ligand bonds to generate volatile gas-phase species. To gain insights into the energetics of these bond breaking processes, we have carried out calculations of the energy required to remove a DMADB ligand from negatively charged $M(DMADB)_4{}^?$ species to form the neutral monomer. A schematic representation of the species examined in this study is given in Figure 3.11.

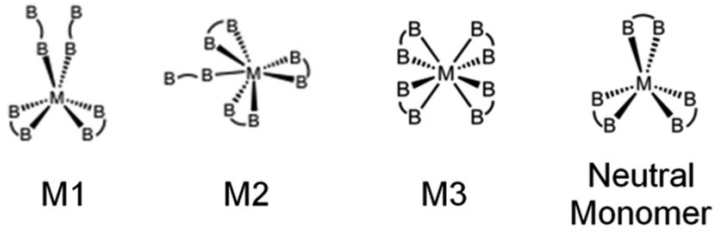

Figure 3.11: Schematic representation of the monomeric anions studied for M = U, Pr, Sm, and Er.

These structures were fully optimized. In all cases, the neutral monomer is 12-coordinate. For Pr and U, structure M1 has the same 14-coordinate geometry as seen in the solid state for these compounds. For Er, structure M1 optimizes to a 13-coordinate geometry instead of the 12-coordinate geometry seen in the solid state; one of the terminal ligands is bound by means of three hydrogen bridges instead of two. For Sm and U, M2 has a 14-coordinate environment in which the ligand that coordinates through only one B−H−M interaction in the solid state coordinates through two interactions. Finally, structure M3, which possesses four chelating ligands, allowed us to explore whether such structures with higher coordination numbers are energetically accessible. The coordination number decreases with the size of the ion: U is 15-coordinate, Pr and Sm are 14-coordinate, and Er is 12-coordinate.

The ligand dissociation energies for M1, M2, and M3 are presented in Table 2 as a function of the metal ion. Dispersion effects were particularly important, and were typically on the order of 5 kcal/mol. (Note: unless otherwise specified all energies reported in the following text are dispersion-corrected free energies, ΔG_D. Table 2 gives both uncorrected ΔG and corrected ΔG_D values.) In most cases, more energy is required to remove a ligand from M3 than from M1 or M2. The data show that the smallest ligand dissociation energy (5.7 kcal/mol) is seen for $Er(DMADB)_4^-$ versus 12.0 kcal/mol for $Sm(DMADB)_4^-$ and 17.0 kcal/mol for $Pr(DMADB)_4^-$. Thus, it becomes easier to form a neutral $M(DMADB)_3$ monomer by dissociation of a ligand as the lanthanide atom becomes smaller.

Table 3.7: Selected Geometric Parameters Obtained from Ground State Geometry Optimization; Average Distances Are Reported for the Two Central Metal Centers (Part a of Figure 3.10) in Å; Average Individual Mayer Bond Orders Are Given along with the Number of Such Bonds Per Metal Center[a]

	Pr		Sm		Er		U	
	ΔG	ΔG_D	ΔG	ΔG_D	ΔG	ΔG_D	ΔG	ΔG_D
M1	12.9	17.0	[a]	[a]	1.3	5.7	14.6	19.1
M2	[a]	[a]	6.8	12.0	[a]	[a]	11.8	19.1
M3	11.4	19.3	9.6	17.3	0.2	9.7	14.6	20.2

[a]Not computed because this structure is not related to the experimental structure.

Despite the fact that Er_{3+} is the smallest lanthanide ion studied here and consequently the positive charge density at the metal center in $Er(DMADB)_3$ should be higher than that in its Pr and Sm analogues, our results show that the higher positive charge density does not lead to stronger metal-ligand binding as one would expect from a classical ionic bond model. Instead, saturating the metal coordination sphere and ligand relaxation play a key role in accounting for the observed trends. The dissociation energies reflect the energetic cost of removing a DMADB ligand from the M^{3+} coordination sphere and the energy required for the resulting under-coordinated complexes to rearrange to more favorable molecular geometries.

If we assume that these ligand dissociation energies for the $M(DMADB)_4^-$ species are correlated with the ligand dissociation energies required to depolymerize the solid state structures, then we would expect the volatility to increase in the order Pr < Sm < Er, as is in fact observed experimentally. All these trends are also correlated with the size of the lanthanide ion. The DMADB complex of the largest lanthanide in this series (Pr), which is a 14-coordinate polymer, is the least volatile, whereas the DMADB complex of the smallest lanthanide in this series (Er), which is a 12-coordinate dimer, is the most volatile.

Finally, the ligand dissociation energy of 19.1 kcal/mol for the M1 and M2 structures of the U species $U(DMADB)_4^-$ is larger than those of all of the lanthanide $Ln(DMADB)_4^-$ compounds studied. Specifically, this energy is 7.1 kcal/mol larger than its isostructural Sm analogue and 2.1 kcal/mol larger than its isostructural Pr

analogue. We point out that the Pr species is already the least volatile of the lanthanide compounds, and thus the U compound should require even more energy to convert its polymer into a monomeric form. This result is consistent with the experimental finding that the U complex decomposes under conditions at which the lanthanide complexes sublime.

Gas-Phase Species Present during CVD/ALD. The nature of the gas-phase species formed upon sublimation of the $M(DMADB)_3$ complexes has previously been investigated experimentally by positive-ion field ionization mass spectroscopy (FI-MS). [213, 214] For the larger lanthanides Pr and Sm, mononuclear, dinuclear, and trinuclear species are detected in the FI-MS spectra; in most cases, one DMADB ligand has been lost to form these cationic species. In contrast, for Er, only mononuclear and dinuclear species are observed (Table 3.8).

Table 3.8: FI-MS Results for $Ln(DMADB)_3$[a]

	ML_2^+		ML_3^+		$M_2L_5^+$		$M_3L_8^+$	
	mass	int	mass	int	mass	int	mass	int
Pr	285	35	356	65	642	35	999	10
Sm	296	95	367	80	660	100	1029	10
Er			381	100	693	15		

[a]Mass is given in m/z and the relative intensity in %. [214]

These results provide insight into the species actually present in the gas phase under CVD and ALD conditions, with the caveat that only neutral species are likely to be present under the latter conditions. Hence, the FI-MS results were used as a starting point for constructing the gas-phase models we analyzed computationally. Specifically, we investigated the mononuclear species $Ln(DMADB)_3$, the dinuclear species $Ln_2(DMADB)_6$, and the trinuclear species $Ln_3(DMADB)_9$. Schematic representations of the structures considered are given in Figure 3.12 (the structure of the neutral monomer is given in Figure 4). No gas-phase structures of $U(DMADB)_3$ or its oligomers were investigated because this compound is not volatile.

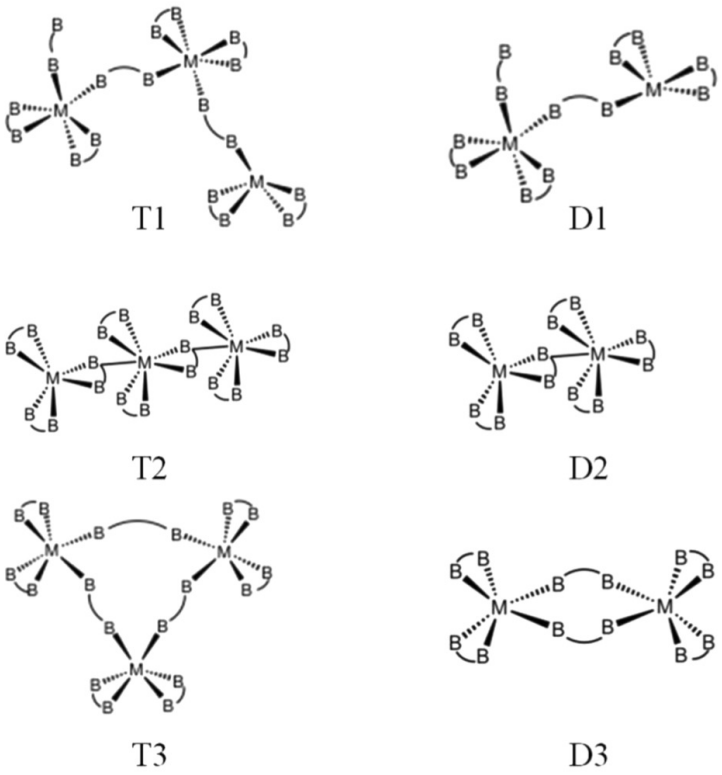

Figure 3.12: Gas-phase clusters studied for M = Pr, Sm, and Er. The DMADB ligand has been depicted schematically for simplicity. All of the structures shown are electrically neutral.

For $Pr(DMADB)_3$, the polymeric structure of the solid precursor can be cut to form the trimer denoted T1, in which one of the metal centers is only 11-coordinate. It is likely that this linear fragment will rearrange in such a way that all of the metal centers are 12-, 13-, or 14-coordinate; one possible rearranged structure is the cyclic structure T3. In fact, we calculate that this transformation is downhill energetically by $\Delta G_D = -9.3$ kcal/mol (Table 3.9). Another possible structure is the acyclic trimer T2, and indeed our calculations show that the T1 to T2 rearrangement is downhill energetically by about the same amount, $\Delta G_D = -11.7$ kcal/mol. Our results demonstrate that T1 is not present in the gas phase due to its instability with respect to both T2 and T3. For $Sm(DMADB)_3$, structure T2 is closely related to the experimental solid-state structure.

Our calculations show that it is 7.0 kcal/mol more stable than structure T3.

Table 3.9: Gibbs Free Energies of Isomerization Reactions in the Gas Phase (And Dispersion Corrected Values) Reported in kcalmol^{-1}

Pr	ΔG	ΔG_D
T1 $\rightarrow$ T2	-18.3	-11.7
T1 $\rightarrow$ T3	-19.8	-9.3
T2 $\rightarrow$ T3	-1.5	2.4
D1 $\rightarrow$ D2	-16.2	-21.3
D1 $\rightarrow$ D3	-21.4	-25.4
D2 $\rightarrow$ D3	-5.2	-4.1
Sm	ΔG	ΔG_D
T2 $\rightarrow$ T3	4.0	7.0
D2 $\rightarrow$ D3	2.1	3.4

Turning to dinuclear species, we first note that structure D1 is again a fragment of the polymeric structure seen for Pr(DMADB)$_3$. As before, one of the metal centers is only 11-coordinate, and rearrangement should occur to form structures such as D2 or D3. In fact, we calculate that structure D1 is highly unstable with respect to both D2 and D3, and that conversion to the latter is downhill energetically by $\Delta G_D = -21.3$ and -25.4 kcal/mol, respectively. For Sm(DMADB)$_3$, structure D2 most closely resembles the solid-state structure. Once again, our calculations show that D2 is 3.4 kcal/mol more stable than structure D3.

Furthermore, our DFT results demonstrate that the lowest energy trimers are unstable with respect to decomposition into the dimer and the neutral monomer, as shown in Table 3.10. FI-MS data support this conclusion because the relative intensities are much lower for the trimers than for the dimers and monomers. Dispersion effects play an important role in the stability of the dimeric species with respect to the monomeric species for both Sm and Pr. When dispersion is accounted for, the dimers are more stable than the monomers, although only by a few kcal/mol. In contrast, for Er the calculations show that the monomers are more stable than the dimers by 7.6 kcal/mol.

Table 3.10: Gibbs Free Energies (And Dispersion Corrected Values) in kcalmol^{-1} for the Decomposition of Gas-Phase Clusters (M = the Neutral Monomer Ln(DMADB)$_3$)

		ΔG	ΔG_D
Pr	T3 $\rightarrow$ D3 + M	-13.3	-5.4
	T2 $\rightarrow$ D3 + M	-14.8	-3.0
	D3 $\rightarrow$ 2M	-5.0	2.7
Sm	T2 $\rightarrow$ D2 + M	-14.2	-5.7
	D2 $\rightarrow$ 2M	-7.6	1.4
Er	D3 $\rightarrow$ 2M	-16.5	-7.6

Thus, we conclude that the Er precursor, which is a dimer in the solid state, probably sublimes as a monomer. This finding is supported by the relative intensities of the peaks in the FI-MS spectra: the ErL_3^+ peak has a relative intensity of 100%, whereas the $Er_2L_5^+$ peak has a relative intensity of only 15%.

The relative stabilities of the monomers and dimers are again consistent with expectations based on ionic radii. Monomers are relatively more stable for smaller lanthanides such as Er, whereas dimers are relatively more stable for larger lanthanides such as Sm and Pr. For all three lanthanides, the monomer has a coordination number of 12, which is equal to the experimental coordination number seen in the crystal structures for Er but less than the coordination numbers of 13 and 14 seen for the Sm and Pr complexes. For the larger lanthanides, the dimeric structures are favored because they permit the ligands to form more Ln$-$H bonds with the metal centers.

3.2.4 Conclusions

The observed decrease in the volatility of Ln(DMADB)$_3$ complexes with an increase in the size of the lanthanide ion is a result of the larger energy required to break the metal-DMADB bonds, a process that is necessary to convert the solid state species (which are oligomers or polymers with bridging DMADB ligands). Neutral gas-phase species from monomers to trimers were studied and long-range weak interactions (dispersion) were found to make significant contributions to the energies of these species. The Sm oligomers in the gas phase maintain the connectivity of the solid state, whereas the Pr species undergo ligand rearrangement. In all cases, trimeric and dimeric structures are unstable and readily decompose into monomers in the gas phase, and the relative

energies of these species are correlated with their relative intensities as determined by FI-MS. For Sm and Pr, the monomers and dimers have similar stabilities and exist in equilibrium in the gas phase. In contrast, the Er dimer is unstable in the gas phase with respect to the neutral monomer. Mayer bond orders demonstrated that the M−H bonds are stronger for the uranium species than their lanthanide analogues, which explains why $U(DMADB)_3$ decomposes rather than sublimes when it is heated.

3.2.5 Acknowledgements

The authors would like to acknowledge Danylo Zherebetskyy for useful discussions. This research was supported by Director, Office of Basic Energy Sciences, U.S. Department of Energy under Contract No. USDOE/DESC002183. We also acknowledge support from the U.S. National Science Foundation under grant CHE-0952054 for support for PM and CJC and under grant CHE 11-12360 to GSG. Finally, we thank the PG Research Foundation for support of S.R.D.

3.3 Investigations of the Electronic Structure of Arene-Bridged Diuranium Complexes

The electronic structure of the arene-bridged complex (μ-toluene)U_2(N[^{t}Bu]Ar)$_4$ (**1a2**-μ-toluene, Ar = 3,5-$C_6H_3Me_2$) has been studied in relation to a variety of mononuclear uranium amide complexes, and their properties have been discussed comparatively. The syntheses, molecular structures (X-ray crystal structures and solution behavior based on variable-temperature NMR spectroscopic data), and corresponding spectroscopic (X-ray absorption near-edge structure and UV-vis-near-IR absorption) and magnetic properties are presented and interpreted with reference to results of density functional theory (DFT) and complete active space self-consistent field with corrections from second-order perturbation theory (CASSCF/CASPT2) calculations performed on model compounds. While the mononuclear compounds display expected electronic and magnetic properties for uranium complexes, **1a2**-μ-toluene shows complicated properties in contrast. XANES spectroscopy, X-ray crystallography, and both density functional and CASSCF/CASPT2 results are consistent with the following electronic structure interpretation: f orbitals host the unpaired electrons, followed energetically by two δ bonds formed by filled uranium f orbitals and LUMOs of toluene.

3.3.1 Introduction

Arene-bridged complexes constitute a general bonding motif for organouranium compounds featuring benzene/toluene, [12, 231–238] naphthalene, [239] biphenyl, [240] cycloheptatrienyl, [241, 242] or cyclo-octatetraene [239] as the bridging arene ligand. In most cases, as well as in actinocene complexes, δ bonding [243] between f orbitals of uranium and ligand LUMOs (lowest unoccupied molecular orbitals) of the appropriate symmetry is considered to play a major role. [12, 231, 234] Like π bonding in transition-metal chemistry, δ bonding may be key to understanding uranium complexes; however,

Reproduced from B. Vlaisavljevich, P. L. Diaconescu, W. L. Lukens, Jr., L. Gagliardi, and C. C. Cummins

Organometallics **2013**, 32, 1341–1352.

the electronic structures of arene-bridged diuranium complexes have rarely been investigated beyond the usual techniques. [12, 234]

Amide ligands have become ubiquitous in transition-metal chemistry, [244–247] and they also proved successful in supporting interesting actinide complexes. [9, 11, 121, 235, 247–256] Their versatility is largely based on the tunability of electronic and steric properties that takes advantage of the ability to modify the two substituents of the nitrogen donor. [244, 257] These properties allowed the isolation and characterization of arene-bridged diuranium complexes in which the arene is either toluene or benzene. [231]

The focus of this report is to investigate the electronic structure of the arene-bridged complex (μ-toluene)U_2(N[^{t}Bu]-Ar)$_4$ (**1a**$_2$-μ-toluene, Ar = 3,5-$C_6H_3Me_2$) by comparison with the mononuclear complexes (THF)U(N[Ad]Ar)$_3$ (**2b**-THF, Ad = 1-adamantyl, THF = tetrahydrofuran), IU(N[^{t}Bu]Ar)$_3$ (**2a**-I), IU(N[Ad]Ar)$_3$ (**2b**-I), and (Me_3SiN)U(N[Ad]Ar)$_3$ (**2b**-$NSiMe_3$), such that a range of uranium formal oxidation states is surveyed. In order to understand the properties of a unique compound such as **1a**$_2$-μ-toluene, the rest of the series is based on classical uranium amide compounds, for which there is no ambiguity about the oxidation state. The syntheses, molecular structures (X-ray crystal structures and solution behavior based on variable-temperature NMR spectroscopic data), and corresponding spectroscopic (X-ray absorption near-edge structure and UV-vis-near-IR absorption) and magnetic properties are discussed and interpreted with reference to results of computational studies performed on model compounds; X-ray absorption near-edge structure (XANES) spectroscopic characterization of arene-bridged diuranium complexes has not been reported previously.

3.3.2 Results and Discussion

Syntheses and X-ray Crystal Structures. The synthesis of compound **1a**$_2$-μ-toluene and the X-ray crystal structure of the related (μ-toluene)U_2(N[Ad]Ar)$_4$ (**1b**$_2$-μ-toluene) as well as reactivity studies have been reported previously. [231] Scheme 1 (Figure 3.13) describes the syntheses of all the complexes discussed here. UI(THF) [258, 259] is a versatile starting material and can be [81] employed to obtain tris(amido)uranium iodide complexes **2a**-I and **2b**-I or can be used to generate **1a**$_2$-μ-toluene and textbf2b-THF directly. In general, compounds based on the N-tert-butylanilide ligand are

more lipophilic and, in practice, are less crystalline than compounds based on the N-adamantylanilide ligand.

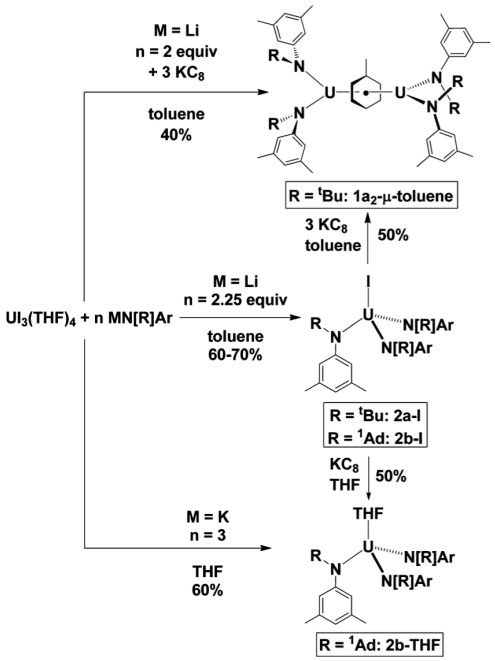

Figure 3.13: Syntheses of uranium complexes discussed in the text

Reduction of the tris(amido)uranium iodide compounds affords either arene-bridged diuranium complexes, when the arene is used as a solvent, [231] or uranium tris(amide) complexes with a molecule of THF coordinated to the uranium center, when THF is used as a solvent. [250] Finally, **2b**-$NSiMe_3$ is obtained from the reaction of Me_3SiN_3 with **2b**-THF, which can be generated in situ or isolated prior to the reaction (eq 1).

The formulation of these compounds was verified by X-ray crystallography (Figures 3.14–3.16). A metrical parameter present throughout the entire series is the distance U-N_{amide}(av). This distance of 2.334(13) Åin **1b**$_2$-μ-toluene is slightly shorter than the 2.346(9) Åfound for **2b**-THF (Figure 1); both values are ca. 0.1 Ålonger than the corresponding distances in **2b**-I (Figure 2) and **2b**-$NSiMe_3$ (Figure 3.16), at 2.204(9) and 2.245(7) Å, respectively. The trend observed here is in good agreement with the results of XANES experiments (see below), which show that the effective charges on the uranium center are similar for **1a**$_2$-μ-toluene and uranium(III) compounds, on one

hand, and for **2b**-I and **2b**-$NSiMe_3$, on the other hand.

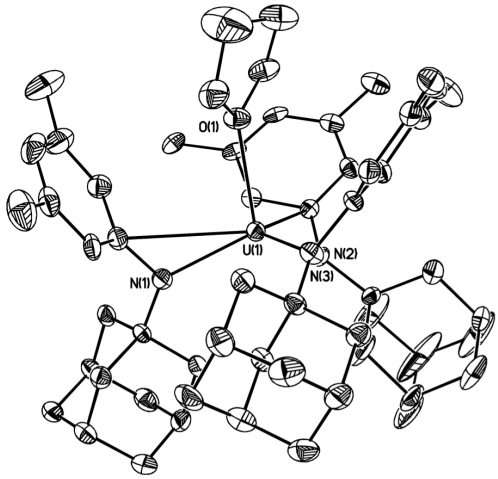

Figure 3.14: Structural drawing of **2b**-THF with thermal ellipsoids at the 35% probability level and hydrogen atoms omitted for clarity. Selected distances (Å): U–N(av), 2.346(9); U–O, 2.489(5).

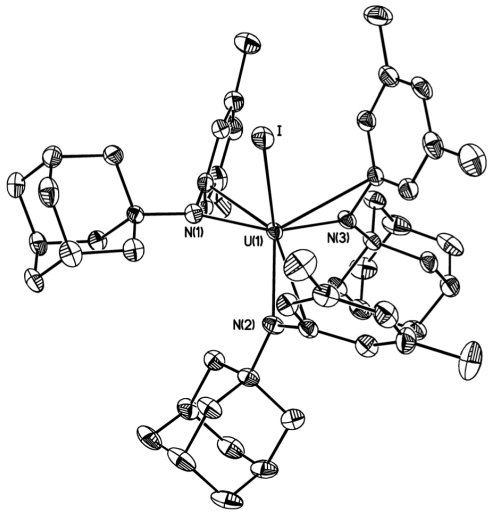

Figure 3.15: Structural drawing of **2b**-I with thermal ellipsoids at the 35% probability level and hydrogen atoms omitted for clarity. Selected distances (Å): U–N(av), 2.204(9); U–I, 3.0682(4).

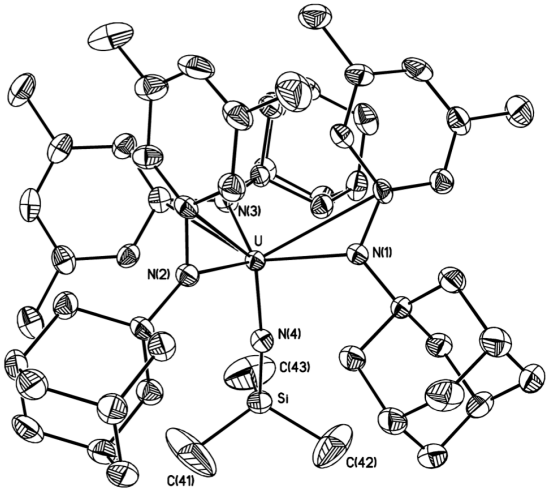

Figure 3.16: Structural drawing of **2b**-$NSiMe_3$ with thermal ellipsoids at the 35% probability level and hydrogen atoms omitted for clarity. Selected distances (Å): U–Namide(av), 2.245(7); U–Nimide, 1.943(4).

The structure of **2b**-$NSiMe_3$ (Figure 3.16) distinguishes itself by the U–N_{imide} distance of 1.943(4) Å, which is ca. 0.3 Åshorter than the average U–N_{amide} distance (2.245(7) Å) in the same compound. Short U–N_{imide} distances and angles close to 180° at N_{imide} (170.1(13)° in **2b**-$NSiMe_3$) have been associated with multiple-bond character between the uranium center and the imide nitrogen atom, [81] in accordance with our findings from CASSCF calculations on a model compound (see Computational Results).

The structure of **1b**$_2$-μ-toluene features an average distance of 2.594(30) Åbetween uranium and the carbon atoms of the bridging toluene molecule that is similar to those in other toluene- or benzene-bridged diuranium complexes. [12, 234] These values are among the shortest such distances registered for carbon atoms of arenes coordinated to uranium centers. For example, the average U–C distance is 2.647(10) Åin uranocene, U(η^8-C_8H_8)$_2$, [260] and 2.807(18) Åin U(η^5-C_5H_5)$_4$, [261] while in benzene complexes such as U(η^6-C_6Me_6)-(BH_4)$_3$ [262] and U(η^6-C_6H_5Me)($AlCl_4$)$_3$, [263] the average U–C distance is significantly longer: 2.93(2) and 2.94(1) Å, respectively. The average C–C distance of 1.438(13) Åfor the bridging toluene in **1b**$_2$-μ-toluene is ca. 0.04 Ålonger than the corresponding distances in free toluene. [264] In complexes of toluene such as K(18-crown-6)(toluene), [265] C–C distances average 1.398(21) Å. The longer C–C

distances for **1b**$_2$-μ-toluene in comparison to those found in free toluene or toluene radical anion are consistent with a substantial covalent overlap between filled uranium f orbitals and LUMOs of the bridging toluene, as found from DFT calculations on model compounds. [231] Furthermore, high-level CASSCF calculations support this conclusion (see Computational Results).

NMR Spectroscopy Studies on 1a2-μ-toluene: Probing Stability and Fluxionality. ^{1}H NMR analysis showed that the bridging toluene in **1a**$_2$-μ-toluene exchanges slowly with C_6D_6 (5% exchange in 24 h) at room temperature. Since **1a**$_2$-μ-toluene is thermally stable, [231] arene exchange was also studied at higher temperatures. Preliminary results show that the bridged toluene exchanges with C_6D_6 faster than the bridged benzene in (μ-benzene)U_2(N[^{t}Bu]Ar)$_4$ (**1a**$_2$-μ-benzene) [231] exchanges with toluene-d_8. Furthermore, the bridging toluene did not exchange with p-xylene over a 24 h period. These results are similar to those reported by Evans et al. [12] and show an opposite trend from that found for transition-metal complexes. [266] For transition-metal complexes, the bond between the HOMOs all of the protons of the molecule. Although the graphs for the protons belonging to the bridging toluene are slightly curved, those for the amide protons are linear, indicating Curie–Weiss behavior. [267] This finding suggests that the dinuclear compound is the only species in solution detectable by NMR spectroscopy.

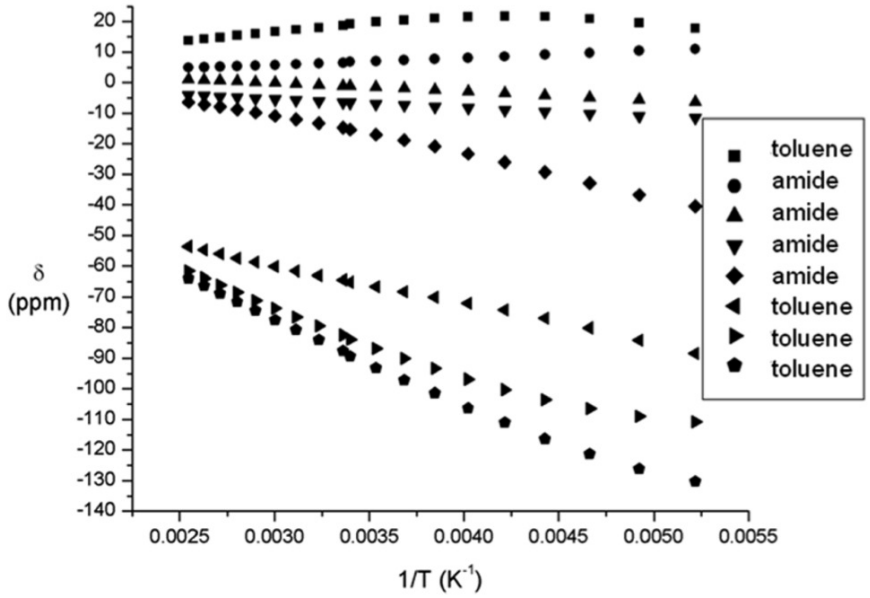

Figure 3.17: Plot of δ versus 1/T for **1a2**-μ-toluene.

Electronic Spectra. Electronic spectra of uranium complexes are usually complicated due to the splitting by ligand-field and spin-orbit coupling of a multitude of states derived from f^n configurations. The electronic spectra are comprised of f $\rightarrow$ f, f $\rightarrow$ d, and charge-transfer bands. Usually, bands are assigned on the basis of the magnitude of the molar absorption coefficient and the position of a band in a spectrum. [258, 268–270] Therefore, for the compounds discussed here, bands present in the UV region (200?400 nm), due to their high intensity ($\epsilon \approx 105$ M^{-1} cm^{-1}), can be assigned to $\pi \rightarrow \pi^*$ transitions of the arene rings (see the Supporting Information, Figures SX5 and SX6). Additionally, intense absorption bands present in the visible region (400?800 nm) that have ($\epsilon \approx 103$ M^{-1} cm^{-1} could be either f $\rightarrow$ d or charge-transfer transitions (Figures SX5 and SX6).

The most interesting region of the electronic spectra for uranium compounds is the near-IR region (spectra reported here were recorded from 1500 to 800 nm, Figure 3.18), because most compounds show "fingerprint" features. These characteristics are assigned to Laporte-forbidden f $\rightarrow$ f transitions and have molar absorption coefficients in the range 10-10^2 M^{-1} cm^{-1}. With the exception of the U(III) compound **2b**-THF (ϵ =

100-260 M^{-1} cm^{-1}) the other mononuclear compounds show weak bands in the near-IR region ($\epsilon < 100$ M^{-1} cm^{-1}). As observed for other toluene or benzene-bridged diuranium systems, [12, 234] $\mathbf{1a}_2$-μ-toluene has intense bands (ϵ = 200?600 M^{-1} cm^{-1}) in this region. The increased intensity of the f-f transitions in uranium complexes has previously been attributed to intensity stealing, [269] which is an increase in intensity in formally forbidden transitions due to the presence of significant covalent bonding. [271] The observation of intense f-f bands for only $\mathbf{1a}_2$-μ-toluene suggests that the bonding between the uranium centers and the bridging toluene ligand is significantly covalent. Previous reports used the similarity between the near-IR spectra of toluene or benzene-bridged diuranium systems and uranium(III) complexes as an indication that the electronic structure of the diuranium compounds is consistent with the presence of uranium(III) metal centers, in agreement with our XANES results (see below).

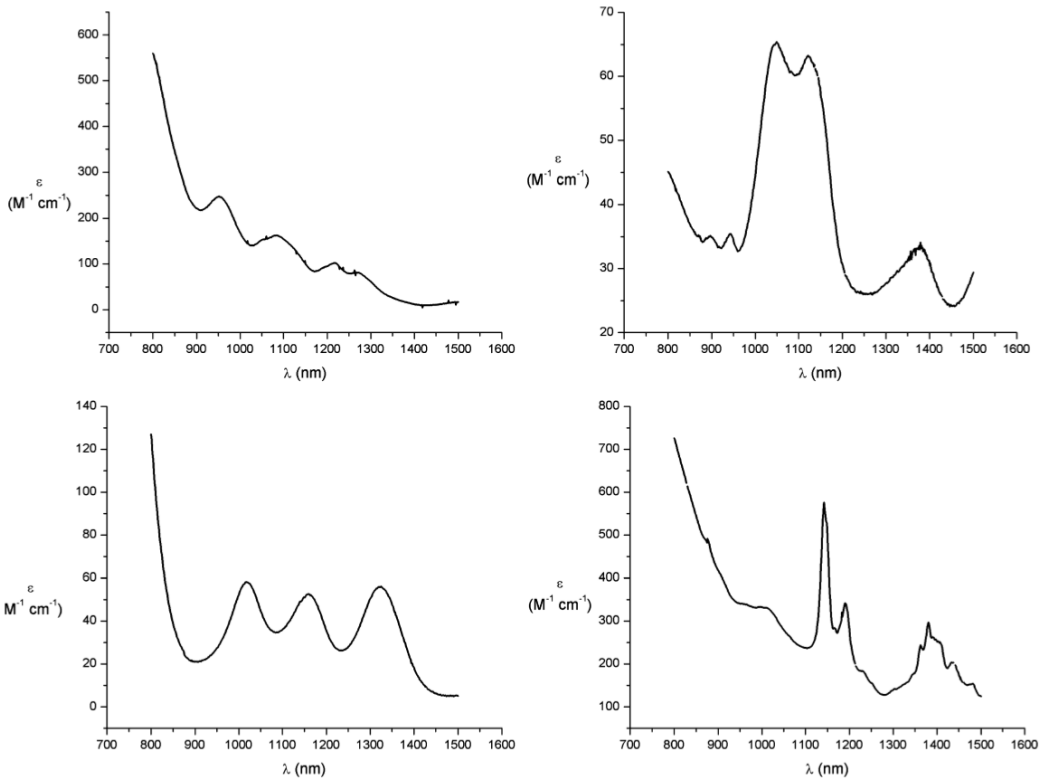

Figure 3.18: Near-IR spectra at 25 °C of **2b**-THF in THF (top left), **2b**-I in toluene (top right), **2b**-$NSiMe_3$ in toluene (bottom left), and **1a2**-μs-toluene in toluene (bottom right).

Solid-State Magnetic Susceptibility Measurements. Although magnetic properties of uranium compounds are usually difficult to interpret, [272**?**] SQUID measurements were carried out on the whole series of complexes considered here in order to compare the behavior of the mononuclear compounds to that of **1a2**-μ-toluene. It is notable that the magnetic moment for **1a**$_2$-μ-toluene (Figure 3.19) is temperature dependent (from 0.25 μ_B at 5 K to 1.50 μ_B at 300 K; values for one uranium center), while the mononuclear compounds present Curie-Weiss behavior in the 5-300 K temperature range (except for the TIP intervals for **2a**-I and **2b**-I, Figure 7). In addition, for **1a**$_2$-μ-toluene (Figure 6), although paramagnetic behavior is observed over the temperature intervals 5-50 and 170-300 K, as the temperature is lowered to around 125 K, the

magnetic susceptibility of the sample passes through a maximum and begins to decrease at lower temperatures. Between 95 and 125 K the minimum values in the $1/\chi$ versus T graph are characteristic of a transition to antiferromagnetic behavior. [234, 273, 274]

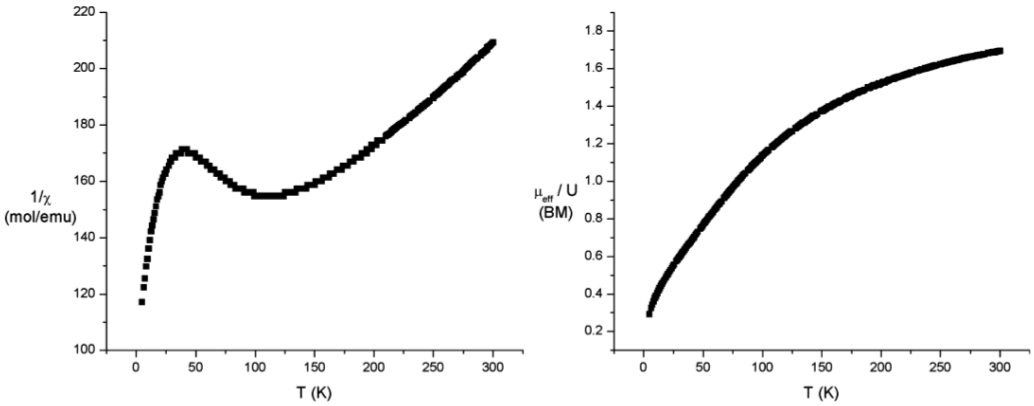

Figure 3.19: Plots of $1/\chi$ (left) and μ_{eff} (right) versus T for **1a2**-μ-toluene.

This overall behavior is in contrast to that found for the analogous bridging-toluene complex $[(U(BIPM^{TMS}H)(I))_2(\mu\text{-}\eta^6\text{:}\eta^6\text{-}C_6H_5CH_3)]$ ($BIPM^{TMS}$ =$C(PPh_2NSiMe_3)_2$), which did not show strong antiferromagnetic coupling. [234]

The magnetic behavior of the mononuclear complexes is as expected and follows some general trends. For example, at low temperatures, the graphs for **2a**-I and **2b**-I (Figure 3.20) show temperature-independent paramagnetism (TIP, 5-25 K for **2a**-I and 5-15 K for **2b**-I). TIP behavior is specific to even-electron species, since at low temperatures the ground state can be an orbital singlet. [275] Kramers ions, i.e. odd-electron species, such as the U(III) (**2b**-THF) and U(V) (**2b**-$NSiMe_3$) compounds (Figure 3.21), would never present a singlet ground state; therefore, their low-temperature magnetic behavior is different from that of U(IV) compounds. The determined μ_{eff} values for **2b**-THF (3.20 μ_B), **2b**-I (3.52 μ_B, 20-300 K), and **2a**-I (3.18 μ_B, 50-300 K) are within the range for uranium(III) and uranium(IV) complexes. The magnetic moment obtained for **2b**-$NSiMe_3$ is 1.81 μ_B, smaller than the other magnetic moments of the mononuclear compounds but consistent with values for similar uranium(V) compounds. [276]

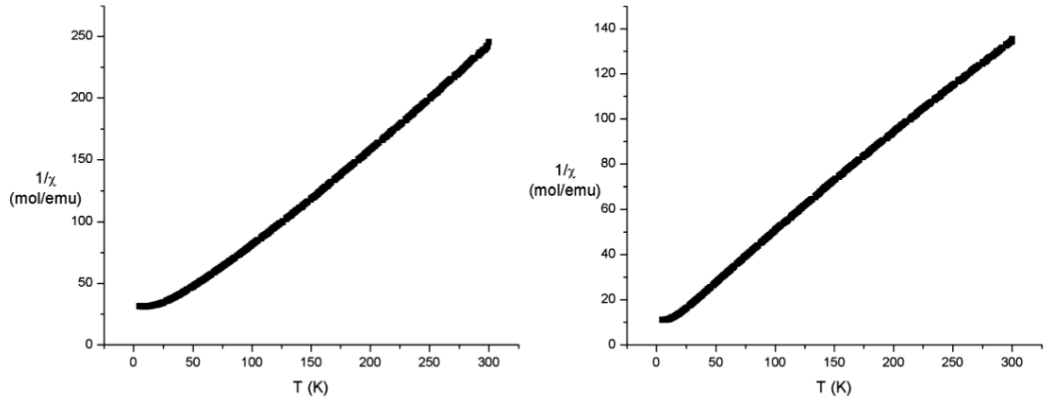

Figure 3.20: Plots of $1/\chi$ versus T for **2a**-I (left) and **2b**-I (right).

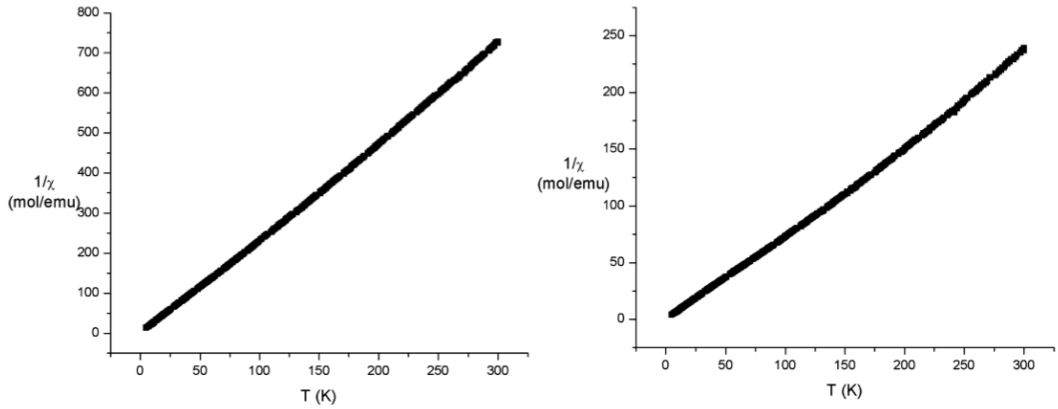

Figure 3.21: Plots of $1/\chi$ versus T for **2b**-THF (left) and **2b**-$NSiMe_3$ (right).

X-ray Absorption Near-Edge Structure (XANES) Spectroscopy Results. The chemical shift of the absorption edge reflects the effective charge of the absorbing atom. [277, 278] For uranium complexes, the U L_3 absorption edge, which corresponds to a $2p_{3/2}$ to $6d_{5/2}$ transition, has been shown to vary systematically with the uranium oxidation state. [279, 280] Therefore, the chemical shifts of the U L_3 absorption edge are affected by changes in shielding of the $2p_{3/2}$ electrons and can be used to compare the effective charges on the uranium centers in different complexes. Although effective

charges can be correlated to the oxidation state of the absorbing atom, other factors, including coordination geometry and the degree of covalency in the ligand-metal interactions, may also be significant. For a series of formally trivalent organometallic and inorganic uranium compounds, the average chemical shift of the absorption edge relative to a UO_2Cl_2 sample is -6.0(5) eV, and for a series of formally tetravalent uranium complexes, the average shift is -3.1(6) eV, as shown in Table 3.11 and Figure 3.22. Both sets of compounds include different coordination geometries and ligands with widely varying electronegativities.

Table 3.11: U L_3 Chemical Shifts of Uranium Complexes[a]

compound	edge shift versus 0.1 M UO_2Cl_2 (eV)	oxidation state
1a2-μ-toluene	-5.1	3
$U[N(SiMe_3)_2]_3$ [281]	-6.3	3
$(Cp^{\ddagger}_2UOH)_2$ [281]	-6.4	3
$(Cp^{\ddagger}_2UF)_2$ [281]	-5.0	3
$(Cp^{\ddagger}_2UCl)_2$ [281]	-6.3	3
$(Cp^{\ddagger}_2UBr)_2$ [281]	-5.7	3
$(Cp"UF)_2$ [281]	-5.9	3
$(Cp"UCl)_2$ [281]	-6.4	3
$(Cp"UBr)_2$ [281]	-5.6	3
$IU(DME)(NC[^tBu]Mes)_3$ [239]	-3.3	4
2a-I	-3.8	4
$(Cp^{\ddagger}_2UO)_2$ [281]	-2.0	4
$Cp^{\ddagger}_2UF_2$ [281]	-2.4	4
$Cp^{\ddagger}_2UCl_2$ [281]	-2.9	4
$Cp^{\ddagger}_2UBr_2$ [281]	-3.5	4
$Cp^{\ddagger}_2UI_2$ [281]	-3.6	4
$Cp"UF_2$ [281]	-2.6	4
$Cp"UCl_2$ [281]	-2.4	4
$Cp"UBr_2$ [281]	-3.7	4
$Cp"UI_2$ [281]	-3.6	4

[a]Abbreviations: $Cp^{\ddagger}$ = 1,3-$(Me_3C)_2C_5H_3$, Cp" = 1,3-$(Me_3Si)_2C_5H_3$, DME = 1,2-dimethoxyethane.

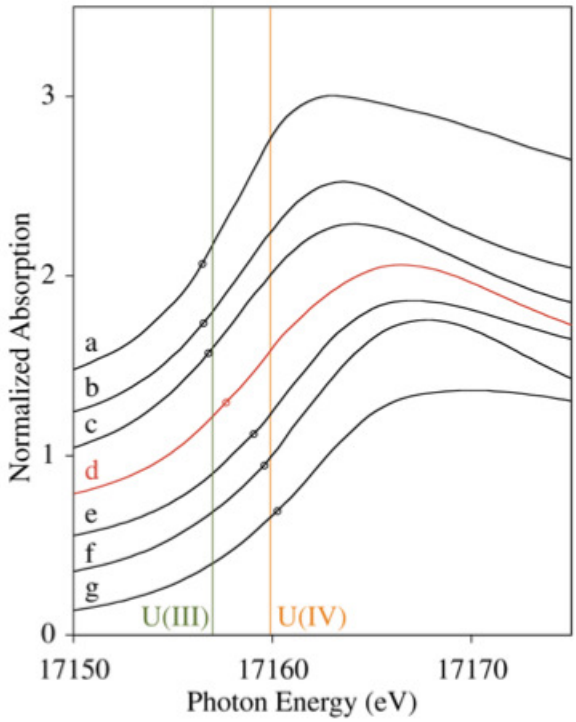

Figure 3.22: U L_3 absorption edges of selected organouranium complexes. The edge height is normalized such that the absorption at the edge step is equal to 1. The edge energies are referenced to the half-height of a 0.1 M UO_2Cl_2 in 1 M HCl solution set at 17163 eV. The compounds are (a) $U[N(SiMe_3)_2]_3$, (b) $[Cp"_2UCl]_2$, [281] (c) $[Cp^{\ddagger}_2UOH]_2$, [281] (d) (μ-C_7H_8)[U(N [^{t}Bu]Ar)$_2$]$_2$ (**1a2**-μ-toluene), (e) IU(N[^{t}Bu]Ar)$_3$(**2a**-I), (f) IU(DME)(NC [^{t}Bu]Mes)$_3$, [239] and (g) (Me_3SiN)U(N[Ad]Ar)$_3$ (**2b**-$NSiMe_3$). The point closest to the half-height is circled. The average edge shifts of U(III) and U(IV) complexes are indicated by the vertical lines.

In the family of complexes (μ-arene)[U(N[R]Ar)$_2$]$_2$, the bonding lies somewhere between two extremes: (1) a neutral arene ligand coordinated by two U(II) centers and (2) an arene tetraanion with two U(IV) centers (Figure 3.23). A series of the U L_3 absorption edges of selected uranium complexes is shown in Figure 9. Since the chemical shift of **1a**$_2$-μ-toluene is -5.1 eV, the effective charge of the U center in the complex is mostly similar to that of U(III) complexes. A description of the bonding more detailed

than that presented here requires information about the overlap between the ligand and metal orbitals, [282] as well as their relative energies. Nonetheless, the observed chemical shift of the U L_3 edge is consistent with a strong, covalent interaction between the arene π_u^* orbitals and the δ_u orbitals of the two uranium centers. In particular, the observed chemical shift of $\mathbf{1a}_2$-μ-toluene is consistent with its formulation as two U(III) centers bridged by a toluene(2–) ligand, where the f electrons on the U(III) center are stabilized by back-bonding with the bridging ligand.

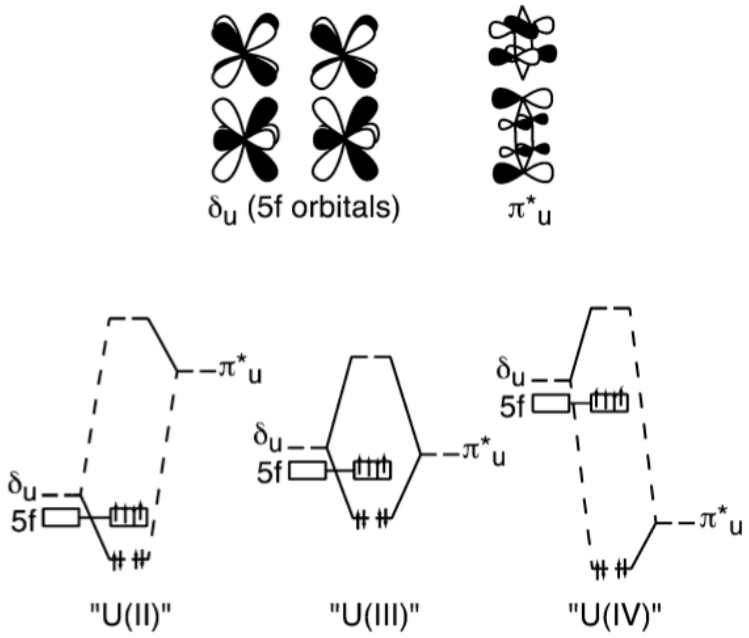

Figure 3.23: Bonding scenarios in arene-bridged diuranium complexes. The relative energies of the 5f and π_u orbitals affect the XANES edge shift.

It is important to note that the bonding picture described here shares characteristics with those of actinocene complexes An(C8H8)2 (An = actinide), which have been intensely researched and investigated. [283–285] The similarities between the two classes of complexes stem from the analogous symmetry of frontier orbitals for both the metal and the arene ligand. The differences consist of the oxidation state of the metal and the energy of arene orbitals. As pointed out recently, [51] tuning of both contributors influences greatly the extent of covalency in actinide complexes.

Computational Results. *DFT Calculations.* Geometries were optimized for the DFT ground state for model systems based on the **2b**-THF, **2b**-I, **2b**-$NSiMe_3$, and **1a2**-μ-toluene structures. **2b**-THF and **2b**-I are U(III) and U(IV) compounds and have quartet and triplet ground states, respectively. In both cases, the experimental and calculated structures are in very good agreement, as shown in Table 3.12 and Table S1 (Supporting Information). Both doublet and quartet spin states were explored for **2b**-$NSiMe_3$. The doublet is 33.3 kcal/ mol lower in energy at the B-97D level of theory than for the quartet. Moreover, the doublet geometry is in good agreement with experimental parameters, whereas the quartet has an average U–N_{amide} distance of 2.40 Å, as opposed to the 2.24 Åobserved experimentally. Finally, **1a2**-μ-toluene was optimized for the quintet state. While the singlet and triplet spin states should be considered, these states suffer from spin contamination at the DFT level, and therefore the energetics are unreliable. For this reason, only the quintet state was considered with DFT, while all of the spin states were studied at the CASSCF/CASPT2 level of theory (see below). Average distances and angles are in good agreement with experimental parameters (Table 3.12). The dihedral angles are expected to deviate more than the other parameters due to the ligand truncation; however, the calculated values are within 10° of experiment (Table S1), with the exception of the B-97D N_{imide}–U–N–$C_{tert?butyl}$ dihedral angle in **2b**-$NSiMe_3$, which deviates by 15°.

Table 3.12: Average Distances (Å) and Angles (°) for Calculated and Experimentally Obtained Structures

		av distance (Å)		angle (°)	
		U–N	U–X	X–U–N	U–Y–Z
2b-THF (X = O)	exptl	2.35	2.49	98.89/108.2/116.0	
	B-97D	2.30	2.50	92.3/115.6/116.3	
	PBE	2.32	2.41	96.0/107.8/121.9	
2b-I (X = I)	exptl	2.20	3.07	94.3/113.3/126.2	
	B-97D	2.23	3.07	92.2/113.0/123.2	
	PBE	2.23	3.07	91.7/113.9/125.8	
2b-$NSiMe_3$ (X, Y = N_{imide}; Z=Si)	exptl	2.25	1.94	103.2/103.7	170.3
	B-97D	2.27	1.94	102.4/103.2	168.8
	PBE	2.28	1.95	106.0/108.6	171.2
1a2-μ-toluene (X = N; Y=U, Z=N)	exptl	2.33	2.59	103.2/103.7	126.4/127.0/129.8/129.9
	B-97D	2.33	2.62	104.2/105.3	124.7/126.2/128.2/130.6
	PBE	2.33	2.60	103.8/104.6	126.4/127.0/128.3/129.5

CASSCF/CASPT2 Results. The electronic structure was further explored by performing complete active space self-consistent field calculations with corrections from second-order perturbation theory (CASSCF/CASPT2) on the optimized geometries. In CASSCF, a set of orbitals in the valence region is defined, together with the electrons associated with these orbitals. Within this orbital space, which is referred to as the active space, the electronic configurations that can be obtained by distributing the electrons in the active orbitals in all possible ways are considered. [164] The total wave function is constructed as a linear combination of all these electronic configurations. The orbitals lower in energy than the active space are doubly occupied, while those that are higher in energy are unoccupied. When possible, all valence orbitals should be included in the active space; however, in practice this is not always required. For the higher oxidation states of uranium, it is common practice to include only the seven U 5f orbitals in the active space, since the 6d and 7s orbitals are higher in energy and consequently unoccupied. [35] For **2b**-THF and **2b**-I, the ligands do not engage in strongly covalent interactions with the U center, and as a result only the 5f orbitals need to be included in the active space with either three or two electrons, respectively (see Figures

S8 and S9 in the Supporting Information). The ground state of **2b**-THF is a quartet, while the ground state of **2b**-I is a triplet, as expected for U(III) and U(IV) compounds, respectively.

Alternatively for **2b**-$NSiMe_3$, including only the seven U 5f orbitals in the active space would not properly describe the covalent bonding between the imide nitrogen and uranium. For this reason, the three N 2p orbitals must be included in the active space as well, resulting in an active space of 7 electrons in 10 orbitals. However, in practice this space was too small, as CASSCF and CASPT2 predicted different ground states. We found that including 6 additional doubly occupied orbitals containing contributions from the U 6p, U 5d, and N 2s orbitals in the active space was very important in obtaining consistency between CASSCF and CASPT2 energies. With this larger space of 19 electrons in 15 orbitals, the doublet was the ground state at the CASSCF and CASPT2 levels by 51.5 and 18.7 kcal.mol^{-1}, respectively. Furthermore, the bond between U and N_{imide} is a double bond, as shown in Figure S10 (Supporting Information).

For **1a2**-μ-toluene, the active space consists of 8 electrons in 14 orbitals. One can think of this as including the 7 U 5f orbitals on each center and the corresponding electrons; however, the resulting molecular orbitals corresponding to U–arene–U bonding contain contributions from both 5f and 6d orbitals. The singlet, triplet, quintet, and septet spin states were explored. The ground state at the CASPT2 level is the singlet; however, the triplet and quintet are only 0.7 and 2.5 kcal.mol^{-1} higher in energy, respectively. Spin-orbit effects were not included in these calculations. Additionally, the orbital pictures are the same for all three states. Two sets of δ bonds composed of occupied uranium 5f orbitals donating into π antibonding orbitals on the toluene group are present along with four singly occupied 5f orbitals (Figures 3.24 and 3.25). The quintet is high spin and consists of one dominating configuration contributing 87% to the total wave function. Alternatively, the singlet and triplet are much more multireference in nature and the total wave function contains contributions from several electronic configurations (Table 3.13). Finally, the septet state was explored and is 34.5 kcal.mol^{-1} higher in energy than the singlet.

Table 3.13: Electronic Configurations Contributing to the Total Wave Function in **1a2**-μ-toluene

spin state	configuration	% of the total wave function
quintet	$\delta^2\delta^2 5f^1 5f^1 5f^1 5f^1$	87.1
triplet	$\delta^2\delta^2 5f^1 5f^2 5f^1 5f^0$	17.1
	$\delta^2\delta^2 5f^2 5f^1 5f^0 5f^1$	21.2
	$\delta^2\delta^2 5f^0 5f^1 5f^2 5f^1$	20.6
	$\delta^2\delta^2 5f^1 5f^0 5f^1 5f^2$	17.4
singlet	$\delta^2\delta^2 5f^2 5f^2 5f^0 5f^0$	14.2
	$\delta^2\delta^2 5f^2 5f^0 5f^2 5f^0$	13.9
	$\delta^2\delta^2 5f^1 5f^1 5f^1 5f^1$	14.3
	$\delta^2\delta^2 5f^0 5f^2 5f^0 5f^2$	13.7
	$\delta^2\delta^2 5f^0 5f^0 5f^2 5f^2$	13.5

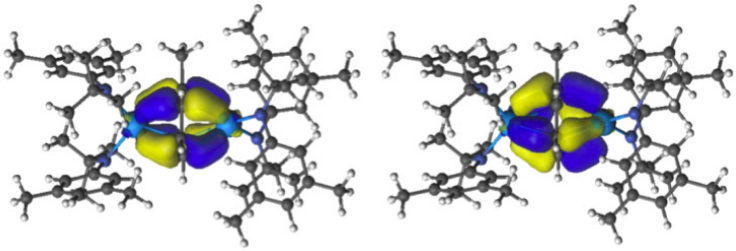

Figure 3.24: δ bonding natural orbitals [286] from **1a2**-μ-toluene. From left to right, the natural orbital occupation numbers are 1.86 and 1.87. Legend: U, light blue; N, blue; C, gray; H, white.

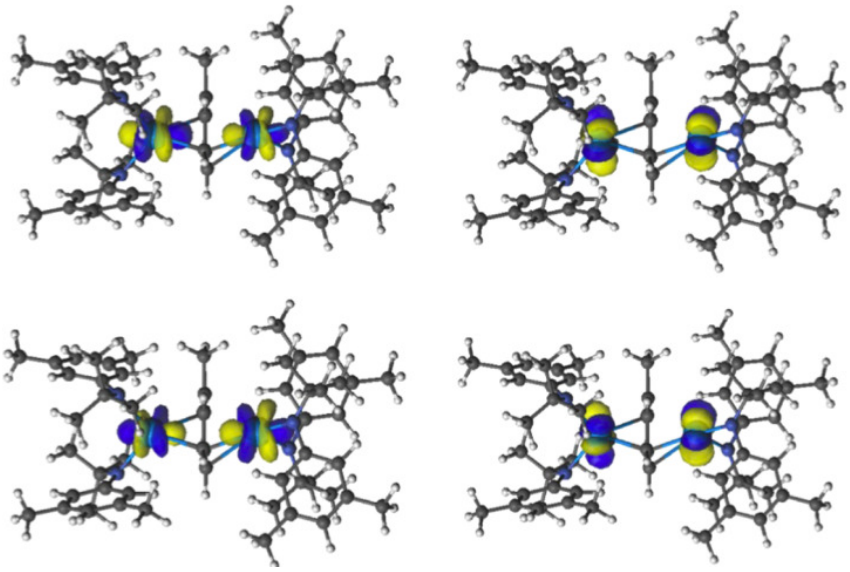

Figure 3.25: Singly occupied natural orbitals of **1a2**-μ-toluene. Legend: U, light blue; N, blue; C, gray; H, white.

LoProp Charges. Atomic charges were computed from the CASSCF results using the LoProp approach (Table 3.14). LoProp charges are reported, since this procedure is stable with respect to the basis set and provides physically meaningful localized properties. [287] First, by comparison of the uranium partial charges it is observed that, as expected, the partial charge of the U(III) compound **2b**-THF is less than that of the U(IV) compound **2b**-I. Additionally, the ground state of **2b**-$NSiMe_3$ is a doublet, corresponding to a U(V) center. The partial charge on uranium in **2b**-$NSiMe_3$ is consistent with this assignment, as it is higher than in **2b**-I. Finally, the partial charges on the U centers in **1a2**-μ-toluene are consistent with a +3 oxidation state. Additionally, the sum of the charges on the bridging toluene group is -1.95, indicating that charge transfer occurs from the uranium centers to the bridging toluene ligand, which is consistent with both the observed reactivity (**1a2** coordinated preferentially the least electron rich bridging arene) and the chemical shift observed by XANES spectroscopy.

Table 3.14: LoProp Charges for the Ground State CASSCF Wave Function

	2b-THF	**2b**-I	**2b**-$NSiMe_3$	**1a2**-μ-toluene
U	2.20	2.76	3.04	2.33/2.34
N	-0.84	-0.84	-0.79	-0.54
	-0.77	-0.86	-0.85	-0.52
	-0.80	-0.85	-0.83	-0.54
				-0.54
other	-0.55 (O)	-0.75 (I)	-1.20 (N_{imide}	-1.95 (toluene (sum))

Consistent with a +5 oxidation state assignment, the reaction of **2b**-$NSiMe_3$ with lithium under argon or with KC_8 in THF resulted in the formation of $[Li(OEt_2)][(Me_3SiN)U(N[Ad]\text{-}Ar)_3]$ (Li[**b2**-$NSiMe_3$]; Figure 3.26) or $K[(Me_3SiN)U(N[Ad]\text{-}Ar)_3]$ (K[**2b**-$NSiMe_3$]; eq 2). The longer distances U–N_{amide} = 2.357(5) Å(av) and U–$NSiMe_3$ =2.050(3) Åas compared to the corresponding values in **2b**-$NSiMe_3$ are indicative of a more electron rich uranium center.

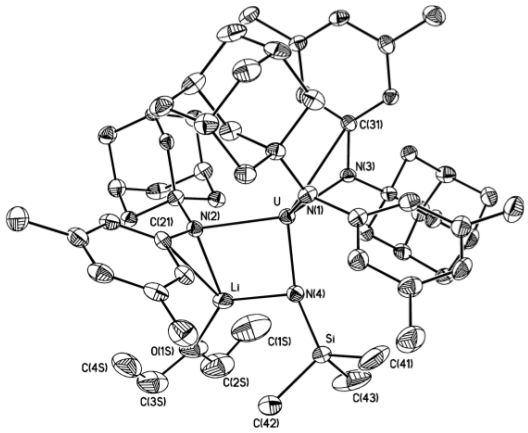

Figure 3.26: Structural drawing of $[Li(OEt_2)][(Me_3SiN)U(N[Ad]Ar)_3]$ (Li[**2b**-$NSiMe_3$]) with thermal ellipsoids at the 35% probability level and hydrogen atoms omitted for clarity. Selected distances (Å): U–N_{ligand}(av), 2.357(5); U–N_{imide}, 2.050(3).

3.3.3 Conclusions

The compound **1a2**-μ-toluene was studied in relation to a variety of mononuclear uranium amide complexes, and its properties were discussed with reference to their properties. While the mononuclear compounds display the expected electronic and magnetic properties, **1a2**-μ-toluene showed complicated characteristics in contrast. The optical and magnetic properties of **1a2**-μ-toluene are difficult to relate to reported examples of mononuclear uranium organometallic complexes. XANES spectroscopy, X-ray crystallography, and computational studies corroborate the following electronic structure interpretation: the f orbitals of the two uranium centers host the four unpaired electrons, followed energetically by two covalent δ bonds formed by filled uranium f orbitals overlapping with the LUMOs of toluene, in accord with our original analysis. [231]An effective electronic charge of the metal centers was determined by XANES and is comparable to values encountered for classical uranium(III) compounds; these results are consistent with the presence of a covalent bond between uranium and toluene that is reflected in the metrical parameters of **1b2**-μ-toluene, as determined by X-ray crystallography.

3.3.4 Experimental Section

General Considerations. Unless stated otherwise, all operations were performed in a Vacuum Atmospheres drybox under purified nitrogen or using Schlenk techniques under an argon atmosphere. Anhydrous diethyl ether was purchased from Mallinckrodt; *n*-pentane, *n*-hexane, and tetrahydrofuran (THF) were purchased from EM Science. Diethyl ether, toluene, benzene, *n*-pentane, and *n*-hexane were dried and deoxygenated by the method of Grubbs. [288] THF was distilled under nitrogen from purple sodium benzophenone ketyl and was transferred under nitrogen into glass vessels before being pumped into the drybox. C_6D_6 was purchased from Cambridge Isotopes and was degassed and dried over 4 Åsieves. The 4 Åsieves, alumina, and Celite were dried under reduced pressure overnight at a temperature just above 200 °C. $UI_3(THF)_4$, [258] KC_8, [289] $KCH_2C_6H_5$, [290] HN[Ad]Ar, [291] and compounds **1a2**-μ-toluene, [231] **1b2**-μ-toluene, [231] **2a**-I,1 **2b**-I [250] were prepared according to literature methods. Me_3SiN_3 was passed through alumina and stored in a refrigerator at -35 °C. Other

chemicals were used as received. ^{1}H NMR spectra were recorded on Varian XL-300 and Varian INOVA-501 spectrometers at room temperature unless specified otherwise. Chemical shifts are reported with respect to internal or external solvent: 7.16 ppm (C_6D_6). UV-vis spectra were recorded on a HP spectrophotometer from 200 to 1100 nm using matched 1 cm quartz cells, and near-IR spectra were recorded on a PS spectrophotometer from 800 to 1500 nm using matched 1 cm quartz cells; all spectra were obtained using a solvent reference blank. Numerical modeling of all data was done using the program Origin 6.0. CHN analyses were performed by H. Kolbe Mikroanalytisches Laboratorium (Mülheim an der Ruhr, Germany).

Synthesis of KN[Ad]Ar. A 500 mL round-bottom flask was charged with HN[Ad]Ar (8.52 g, 33 mmol) and diethyl ether (300 mL), and the solution was frozen. Solid $KCH_2C_6H_5$ (4.35 g, 33 mmol) was added to the thawing solution, and the reaction mixture was warmed to room temperature and stirred for 2-3 h. Filtration of the resulting solution afforded a white solid that was washed with pentane and dried under reduced pressure. The KN[Ad]Ar obtained amounted to 7.93 g (27 mmol, 82% yield). 1H NMR (300 MHz, C_6D_6, 22 °C): δ 6.28 (s, 1H, *p*-Ar); 6.22 (s, 2H, *o*-Ar); 2.23 (s, 6H, Ar-Me); 1.95 (s, 3H, Ad-CH); 1.83 (s, 6H, Ad-CH_2); 1.52 (s, 6H, Ad-CH_2).

Synthesis of (THF)U(N[Ad]Ar)$_3$ (2b-THF). A 100 mL round-bottom flask was charged with $UI_3(THF)_4$ (0.526 g, 0.56 mmol), KN[Ad]Ar (0.510 g, 1.74 mmol, 3 equiv), and a stirring bar and then placed in the cold well. Thawing THF (50 mL) was added to the solid mixture as quickly as possible and the reaction mixture stirred for 45 min. Filtration of the reaction mixture through Celite afforded a solution from which the solvent was removed. The solid obtained was collected on a frit and washed with small portions of diethyl ether (2–15 mL). The solid obtained on the frit was dried and redissolved in diethyl ether, and the solution was concentrated and placed in a freezer at -35 °C. After several days, the solution was decanted and the black microcrystalline solid (**2b**-THF; 0.304 g, 0.29 mmol, 51% yield) dried under reduced pressure. ^{1}H NMR (300 MHz, C_6D_6, 22 °C): δ 37.55 (s, 4H, THF-CH_2); 0.65 (bs, 9H, *o*- and *p*-Ar); 0.23 (s, 9H, Ad-CH); 0.13 (d, 18H, Ad-CH_2); -0.13 (d, 18H, Ad-CH_2); -6.64 (s, 18H, Ar-Me); -15.80 (s, 4H, THF-CH_2). Anal. Calcd for $C_{58}H_{83}N_3OU$: C, 64.72; H, 7.77; N, 3.90. Found: C, 64.79; H, 7.93; N, 3.72.

Synthesis of $(Me_3SiN)U(N[Ad]Ar)_3$ (2b-$NSiMe_3$). *(a). From 2b-THF.* Solutions in THF of **2b**-THF (1.169 g, 1.14 mmol, 80 mL) and Me_3SiN_3 (0.144 g, 1.25 mmol, 1.1 equiv, 20 mL) were frozen. To the thawing solution of **2b**-THF was added dropwise a solution of Me_3SiN_3, and the reaction mixture was warmed to room temperature and stirred for 1 h. After the reaction was finished, the solvent was removed under reduced pressure, the obtained solid was dissolved in pentane, and the new solution was concentrated and stored at -35 °C for several days. **2b**-$NSiMe_3$ was obtained as a black, crystalline solid in two crops amounting to 0.586 g (0.56 mmol, 49% yield).

(b). From $UI_3(THF)_4$ Directly. $UI_3(THF)_4$ (1.193 g, 1.31 mmol) and KN[Ad]Ar (1.156 g, 3.94 mmol, 3 equiv) were mixed as solids in a 250 mL round-bottom flask and placed in the cold well. To the stirred mixture was added thawing THF (100 mL). The reaction mixture was warmed to room temperature and stirred for a total of 35 min, after which it was filtered through Celite and and the resulting solution frozen again. To this thawing solution was added dropwise a thawing solution of Me_3SiN_3 (0.136 g, 1.18 mmol, 0.9 equiv) in THF (20 mL). After the addition was finished, the removal of solvent was started immediately. The obtained solid was extracted with pentane, and the solution was filtered through Celite. The solvent was removed, and the last two operations were repeated. The new solution was concentrated to ca. 20 mL and placed in a -35 °C freezer. **2b**-$NSiMe_3$ was obtained as a black, crystalline solid in two crops amounting to 0.521 g (0.50 mmol, 38% yield). 1H NMR (300 MHz, C_6D_6, 22 °C): δ 11.95 (bs, 2H, *o*-Ar); 8.28 (s, 3H, Si-CH_3); 6.24 (s, 1H, *p*-Ar); 2.03 (s, 6H, Ar-Me); 1.09 (s, 3H, Ad-CH); -0.06 (d of d, 6H, Ad-CH_2); -5.59 (bs, 6H, Ad-CH_2). Anal. Calcd for $C_{57}H_{81}N_4SiU$: C, 62.90; H, 7.50; N, 5.15. Found: C, 62.80; H, 7.52; N, 5.11.

Synthesis of $[Li(OEt_2)][(Me_3SiN)U(N[Ad]Ar)_3]$. Small cubes of lithium (two to three) were washed with hexanes and transferred under argon to a round-bottom flask charged with a magnetic stirring bar. To this flask was transferred via cannula a THF solution (25 mL) of **2b**-$NSiMe_3$ (0.699 g, 0.67 mmol) prepared in the glovebox. The reaction mixture was stirred for 2 h at room temperature, after which the solvent was removed under reduced pressure. The flask was taken into the box, the solid obtained was extracted with pentane, and the new solution was filtered through Celite. After the solvent was removed from the filtrate, extraction with pentane and filtration were repeated and the new solution was concentrated and placed in a -35 °C

freezer. $[Li(OEt_2)][(Me_3SiN)U(N[Ad]Ar)_3]$ was obtained as orange crystals in two crops amounting to 0.502 g (0.43 mmol, 64% yield). ^{1}H NMR (300 MHz, C6D6, 22 °C): δ 11.49 (bs, 6H, Et_2O-CH_3); 10.61 (bs, 6H, *o*-Ar); 9.12 (s, 9H, Si-CH_3); 8.10 (s, 3H, *o*-Ar); 7.13 (d, 4H, Et_2O-CH_2); 2.06 (s, 18H, Ar-Me); -1.99 (d of d, 18H, Ad-CH_2); -3.34 (s, 9H, Ad-CH); -15.16 (bs, 18H, Ad-CH_2). Anal. Calcd for $C_{61}H_{91}N_4SiOLiU$: C, 62.59; H, 7.78; N, 4.79. Found: C, 62.60; H, 8.35; N, 4.71.

Synthesis of K[(Me$_3$SiN)U(N[Ad]Ar)$_3$]. A thawing slurry of KC_8 (0.188 g, 1.39 mmol, 2.8 equiv) in THF (15 mL) was added dropwise to a thawing THF solution (20 mL) of **2b**-$NSiMe_3$ (0.518 g, 0.50 mmol). The reaction mixture was warmed to room temperature and stirred for 1.5 h, after which the solvent was removed under reduced pressure. The solid obtained was extracted with diethyl ether and the new solution filtered through Celite. After the solvent was removed from the filtrate, the extraction with diethyl ether and the filtration were repeated and the new solution was concentrated and placed in a -35 °C freezer. K[**2b**-$NSiMe_3$] was obtained as dark orange crystals in one crop amounting to 0.415 g (0.38 mmol, 77% yield). 1H NMR (300 MHz, C_6D_6, 22 °C): δ 20.67 (s, 3H, Si-CH_3); 4.75 (s, 1H, *p*-Ar); 1.99 (s, 3H, Ad-CH); 0.82 (d of d, 6H, Ad-CH_2); 0.09 (s, 6H, Ar-Me); -1.05 (bs, 2H, *o*-Ar); -2.58 (bs, 6H, Ad-CH_2).

Thermal Stability of 1a2-μ-toluene. In one experiment, variable-temperature ^{1}H NMR studies in octane-d_{18} showed that **1a2**-μ-toluene is stable up to 110 °C. The spectra were acquired from 20 to 110 °C at 10 °C intervals, and after reaching 110 °C, another spectrum was obtained on the same sample back to 20 C. In another experiment, 40 mg of **1a2**-μ-toluene in 20 mL of heptane was heated at 80 C for 24 h. A ^{1}H NMR spectrum of a sample taken from that solution indicated that the compound did not decompose.

Arene Exchange Experiments. **1a2**-μ-toluene was dissolved in C_6D_6, the solution was transferred to an NMR tube, and the NMR tube was sealed and then placed in a heated oil bath. After 24 h at 90 °C, analysis of the ^{1}H NMR spectrum indicated 3% exchange based on the integration of the peaks at ca. -7 ppm (Me-Ar). Integration of the same peak indicated 14% exchange after an additional 24 h at 100 °C and 18% exchange after another 48 h. A similar experiment conducted with **1a2**-μ-benzene dissolved in toluene-d_8 showed 6% exchange after 48 h at 100 °C and 11% exchange on the basis of the integration of the *t-Bu* peaks (ca. 7 ppm) after a total of 96 h. For

the exchange experiment with p-xylene, **1a2**-μ-toluene was dissolved in p-xylene, the solution was transferred to a tube, and the tube was sealed and heated in an oil bath at 90 °C. After 24 h, the tube was taken into the box and broken and its contents were transferred to a vial. Volatiles were removed. Analysis of the compounds ^{1}H NMR spectrum (C_6D_6, 300 MHz, 22 °C) indicated no transformation of **1a2**-μ-toluene.

X-ray Crystal Structures. X-ray data collections were carried out on a Siemens Platform three-circle diffractometer with a CCD detector using Mo Kα radiation (λ = 0.71073 Å). The data were processed utilizing the program SAINT supplied by Siemens Industrial Automation, Inc. The structures were solved by direct methods (SHELXTL v5.03 by G. M. Sheldrick and Siemens Industrial Automation, Inc., 1995) in conjunction with standard difference Fourier techniques. [292]

XANES Measurements. In an Ar-filled glovebox, approximately 10 mg of uranium complex was powdered and mixed with dry boron nitride. The samples were packaged in aluminum holders with Kapton tape. The samples were sealed in glass jars with Teflon tape inside the drybox. Everything except for the Teflon tape was baked out at 110 °C for several days. The samples showed no signs of decomposition either before or immediately after the XANES experiment. After several hours in the air, the samples began to discolor around the edges. X-ray absorption spectra were acquired at the Stanford Synchrotron Radiation Lightsource (SSRL) at beamline 11-2 or 4-1 using a Si(220) double-crystal monochromator detuned 50% to reduce the higher order harmonic content of the beam. X-ray absorption spectra were obtained in the transmission mode at room temperature using argon-filled ionization chambers. The data analysis was performed by standard procedures using the EXAFSPAK suite of programs developed by G. George of the SSRL. The background was removed by fitting a polynomial to the pre-edge data. Edge shifts are determined from the half-height of the U L_3 absorption edge at 17166 eV and are referenced to the half-height of a 0.1 M solution of UO_2Cl_2 in hydrochloric acid.

Magnetic Susceptibility Measurements. Magnetic susceptibility measurements were recorded using a SQUID magnetometer at 5000 G. The samples were prepared in the glovebox (50–100 mg), loaded in a gelatin capsule that was positioned inside a plastic straw, and carried to the magnetometer in a tube under N_2. The sample was quickly inserted into the instrument and centered, and data were obtained from 5 to 300

K. The contribution from the sample holders was not accounted for. The diamagnetic contributions were calculated and subtracted from χmol. Effective magnetic moments were calculated either by linear regression from plots of $1/\chi$mol versus T (K) for Curie–Weiss behavior or by using the formula 2.828(Tχmol)1/2 for non-Curie–Weiss behavior. Samples used were recrystallized multiple times. Measurements for the same compound were carried out on differently recrystallized samples.

Computational Details. Geometry optimizations were performed with DFT using the Perdew–Burke–Ernzerhof (PBE) [96] exchange-correlation functional and the dispersion corrected B-97D functional [293] with def-TZVP basis sets [162] for all atoms as implemented in the TURBOMOLE 5.10.2 package. [160] The corresponding def-ECP [219] was used for U, and the resolution of the identity (RI) approximation was used for the Coulomb integrals. [164, 165] All stationary points were confirmed as minima by vibrational analysis. Due to the large size of the ligands, the 1-adamantyl groups were replaced with tert-butyl groups and the 3,5-$C_6H_3Me_2$ groups were replaced with phenyl groups.

Subsequently, the electronic structure was further investigated using complete active space self-consistent field theory (CASSCF) [32] with second-order perturbation theory (CASPT2) [33, 34] on top of the B97-D geometry using the Molcas 7.7 package. [172] Relativistic effects were included through the use of the scalar Douglas–Kroll–Hess (DKH) Hamiltonian. [169, 294] ANO-RCC basis sets of triple-ζ quality were used for U, O, and N, while a minimal basis set was used for peripheral C and H atoms. In **1a2**-μ-toluene, the C and H atoms of toluene were treated with the ANO-RCC basis set of double-ζ quality. [170, 295] Additionally, the Cholesky decomposition technique was used combined with local exchange screening to reduce the computational costs involved in generating the two-electron integrals significantly. [173–176] Atomic charges were computed at the CASSCF level for the ground state using the LoProp procedure. [287]

3.3.5 Acknowledgment

For support of this work, we are grateful to the National Science Foundation (CHE-9988806), the Packard Foundation (Fellowship to C.C.C., 1995-2000), and the National Science Board (Alan T. Waterman award to C.C.C., 1998). P.L.D. thanks Daniel J. Mindiola for help with the structures of **2b**-I and **2b**-THF, Dr. Daniel Grohol and

Professor Daniel G. Nocera for suggestions and discussions of the magnetic properties, and Aetna Wun for help with recording the near-IR spectra. Portions of this work were supported by the U.S. Department of Energy, Basic Energy Sciences, Chemical Sciences, Biosciences, and Geosciences Division, and were performed at Lawrence Berkeley National Laboratory under Contract No. DE-AC02-05CH11231 and at the Stanford Synchrotron Radiation Lightsource, a Directorate of the SLAC National Accelerator Laboratory and an Office of Science User Facility operated for the U.S. Department of Energy Office of Science by Stanford University. Computational studies were funded by the DOE through Grant No. DE-SC002183.

Chapter 4

Uranyl Peroxides and Solid State Actinide Compounds

4.1 Understanding the Structure and Formation of Uranyl Peroxide Nanoclusters by Quantum Chemical Calculations

Quantum chemical calculations were performed to understand the formation of nanoscale cage clusters based on uranyl ions. We investigated the uranyl-peroxide-uranyl interaction and compared the geometries of clusters with and without such interactions. We show that a covalent interaction along the U-O_{peroxo} bonds causes the U-O_2-U dihedral angle to be bent, and it is this inherent bending of the configuration that encourages curvature and cage cluster formation. The U-O_2-U dihedral angle of the peroxo bridge is tuned by the size or electronegativity of the counterion present.

4.1.1 Introduction

Hexavalent uranium, as the linear $(UO_2)^{2+}$ uranyl ion, [1] is central to the chemistry of this element. We previously reported 13 nanoscale cage clusters that are based on uranyl ions. [65, 68, 296–298] This class of polyoxometalates self-assembles in aqueous solutions under ambient conditions. The uranyl ions are in hexagonal bipyramidal polyhedra with O atoms of the uranyl ions at their apexes. Each bipyramid shares three equatorial edges with other bipyramids, with two or three of these shaded edges corresponding to peroxide groups. These cage clusters are a major departure from the extended sheets that normally result from linkage of uranyl bipyramids. [299, 300] Their creation requires circumventing the sheet-forming tendencies of the polyhedra to cause curvature. We argued such curvature arises because the uranyl-peroxide-uranyl interaction is inherently bent. [68] Here we examine the quantum chemical details of this interaction.

We have conducted computational studies of the uranyl-peroxide-uranyl interaction and compared the geometries of clusters with and without such interactions. Several

Reproduced from B. Vlaisavljevich, L. Gagliardi, P. C. Burns
Journal of the American Chemical Society **2010**, 132 (41), 14503–14508.

clusters isolated in crystal structures provide the starting points for our work (Figure 4.1). The cluster $[(UO_2)_2(O_2)_5]^{6-}$ is from $Na_2Rb_4(UO_2)(O_2)(H_2O)$ [301] and contains two uranyl hexagonal bi-pyramids that share a peroxide edge. Each bipyramid has two additional peroxide edges. The U-O_2-U dihedral angle is 153.1°. For comparison, the cluster $[(UO_2)(O_2)_2(OH)]_2{}^{6-}$, from $K_6[(UO_2)(O_2)_2(OH)]_2(H_2O)_7$, [301] contains two hexagonal bipyramids with a shared edge that is two hydroxyl groups. The U-$(OH)_2$-U dihedral angle is 180°. The cluster $[(UO_2)_2(O_2)(C_2O_4)_4]^{6-}$, from $K_6[(UO_2)_2(O_2)(C_2O_4)_4]$, [68] contains two uranyl hexagonal bipyramids with a shared peroxide equatorial edge. The remaining two equatorial edges of each bipyramid are defined by bidentate oxalate groups. The U-O_2-U dihedral angle is 152.9°. A larger cluster with composition $[(UO_2)(O_2)(C_2O_4)]_5{}^{10-}$ is from $K_{10}[(UO_2)(O_2)(C_2O_4)]_5(H_2O)_{13}$. [68] It consists of a five-membered ring of bipyramids, and the shared edges are peroxide gsroups. Again, each bipyramid contains one bidentate oxalate group. The dihedral angles of the U-O_2-U bridges range from 137.5° to 144.5°.

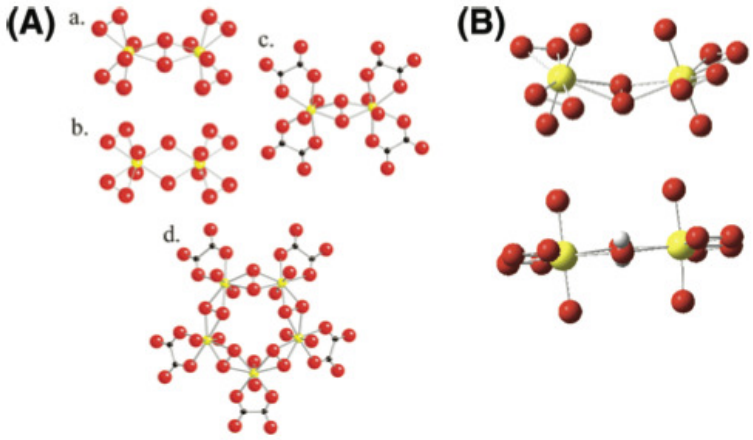

Figure 4.1: (A) Model clusters derived from experimentally determined crystal structures. (a) $[(UO_2)_2(O_2)_5]^{6-}$, designated 2U-P as shown and 2U-P-A with counterions A added. (b) $[(UO_2)(O_2)_2(OH)]_2^{6-}$, designated 2U-OH-A with counterions added. (c) $[(UO_2)_2(O_2)(C_2O_4)_4]^{6-}$, designated 2U-P-Ox-A with counterions added. (d) $[(UO_2)(O_2)(C_2O_4)]_5^{10-}$, designated 5U-P-Ox-A with counterions added. Calculations were also done for a hypothetical cluster with composition $[(UO_2)_2(OH)_2(C_2O_4)_4]^{6-}$ derived from structure c by replacing the peroxo by two hydroxo ions. This is designated 2U-OH-Ox-A with counterions added and 2U-OH-A-H_2O with two H_2O groups added. U, yellow; O, red; C, black. (B) Enlarged picture of the peroxo structure (structure a in panel A) versus hydroxo structure (structure b in panel A), where the bending of the peroxo is emphasized.

4.1.2 Theoretical Calculations

Calculations were performed by density functional theory (DFT) and multiconfigurational methods (CASSCF/CASPT2) for the experimentally observed clusters as well as for a hypothetical cluster derived from $[(UO_2)_2(O_2)(C_2O_4)_4]^{6-}$ by replacing the peroxide group shared between the uranyl ions with two hydroxyl groups. Full geometry optimizations were performed without imposing any symmetry constraint. The starting structures were were taken from experiment, when available. Counterions were evenly distributed around these starting structures for each cluster. All systems under consideration have a singlet spin state as the ground state.

Density functional theory (DFT) geometry optimizations of the experimentally synthesized clusters were performed with the Perdew-Burke-Ernzerhof (PBE) exchange-correlation functional [96] and triple-ζ valence plus polarization (def-TZVP) [162, 164, 165] basis sets on all atoms. Quasirelativistic pseudopotentials were used for U atoms, with 60 core electrons. [162, 164] The TURBOMOLE 5.10 program package was employed. [160, 162]

Multiconfigurational complete active space (CASSCF) [32] calculations followed by second-order perturbation theory (CASPT2) [33] were performed at the DFT optimized geometries of 2U−P−Na and 2U−P−Ox−Na. Both systems are essentially single-configurational. However, in the peroxo cases, the molecular orbitals are more delocalized than in the hydroxo cases. Scalar relativistic effects were included by use of the Douglas-Kroll-Hess [169, 294] Hamiltonian and the relativistic all-electron ANO-RCC basis sets with double-ζ quality (ANO-RCC-VDZP) [170, 295] with the following contractions: [8s 7p 5d 3f 1g] for U and [3s 2p 1d] for O and C. The ANO-RCC-MB basis set was employed for H with a contraction of [1s]. Several active spaces were tested. An ideal active space for a single uranyl ion would include 12 electrons in 12 orbitals (see for example ref [102, 302]). In the diuranyl compound, one should have 24 electrons in 24 orbitals in the active space, and this would still not describe the interaction with the two uranyls and the peroxo unit. We have thus decided to include only the highest occupied-lowest unoccupied molecular orbital (HOMO-LUMO) uranyl-based orbitals, namely, the bonding and antibonding σ_u orbitals and the orbitals describing the interaction between U and the bridging peroxo. In total, the active space contains eight electrons in eight orbitals. Four of them are the uranyl bonding and antibonding orbitals and four of them are the U-O(peroxo) bonding orbitals, which are linear combinations of the 7s, 6d, and 5f orbitals of U and 2p of O. Including the nonbonding U 5f-based orbitals in the active space does not have an effect. It is sufficient to correlate them in the subsequent CASPT2 treatment. For the pentauranyl complex we have not performed CASSCF/CASPT2 calculations because a system with five U atoms is prohibitively large to be treated with this method.

Explicit water molecules and a reaction field Hamiltonian were included in some of the calculations in order to estimate the effect of the environment. The CASSCF/CASPT2 calculations were performed with the Molcas 7.3 package. [128] The computational

costs arising from the two-electron integrals were drastically reduced by employing the Cholesky decomposition (CD) technique in all CASSCF/CASPT2 calculations [173–175] combined with the local exchange (LK) screening. [176] The CASSCF/ CASPT2 approach is successful in studying many actinide- containing systems. [36, 103, 104, 177, 177, 303] There have also been cases in which the CASSCF/CASPT2 method has not been successful, for example, in predicting the ground state of CUO. [43] However in this case the energy difference between the possible candidates as ground state is lower than the error associated with the method (ca. 0.1-0.2 eV in energy differences when spin-orbit coupling is not included).

4.1.3 Results and Discussion

Cluster compositions and descriptors are reported in Figure 4.1, and optimized geometries are given in Tables 4.1– 4.5. From geometry optimization it turned out that the uranyl groups are not symmetry-related in any of the structures.

Table 4.1: Most significant structural parameters of some of the clusters examined, having Na as a counterion[a]

	distance (Å)					angle (deg)	
	U–O	U–O	O-O		O–O		OUO
cluster	uranyl	per	per	U–U	uranyl–uranyl	UOOU	uranyl
2U-P-Ox	1.821	2.450	1.434	4.685	4.889	180.0	175.7
2U-P-Na	1.896-1.953	2.509-2.366	1.477	4.414	3.140-5.592	144.7	173.9-174.6
2U-OH-Na	1.950-1.964	2.433-2.471	2.603	4.160	3.974-4.102	178.5	174.5-174.6
2U-OH-Ox-Na	1.864-1.865	2.331-2.359	2.343	4.063	5.009-5.012	179.9	150.5
2U-P-Ox-Na	1.831-1.840	2.325-3.343	1.435	4.065	3.143-5.924	132.1	164.0-164.4
5U-P-Ox-Na	1.801-1.889	2.362-2.456	1.448-1.477	4.119-4.242	2.832-5.691	134.5-1396	172.7-177.7

[a]When two values are reported, they represent the shortest and longest ones, respectively.

Table 4.2: Most significant structural parameters of 2U-P-A clusters in the presence of different counterions[a]

	distance (Å)						angle (deg)
	U–O	U–O	O-O		O–O		OUO
A	uranyl	per	per	U–U	uranyl–uranyl	UOOU	uranyl
Li	1.888-1.959	2.360-2.521	1.471	4.342	3.181-5.637	139.9	167.1-167.9
Na	1.895-1.947	2.369-2.502	1.472	4.397	3.110-5.614	143.6	174.0-174.5
K	1.894-1.938	2.361-2.503	1.469	4.434	3.273-5.486	147.1	175.8-176.9
Rb	1.906-1.944	2.341-2.534	1.481	4.516	3.530-5.205	155.5	172.8-176.0
Cs	1.903-1.930	2.390-2.575	1.469	4.552	3.876-5.001	164.3	175.1-177.3

[a]When two values are reported, they represent the shortest and longest ones, respectively.

Table 4.3: Most significant structural parameters of 2U-OH-A clusters in the presence of different counterions[a]

	distance (Å)						angle (deg)
	U–O	U–O	O-O		O–O		OUO
A	uranyl	per	per	U–U	uranyl–uranyl	UOOU	uranyl
Li	1.976	2.045-2.406	2.63	4.028	3.642-3.645	180.0	168.8-168.9
Na	1.950-1.964	2.420-2.458	2.595	4.135	3.941-4.077	178.3	174.5-174.6
K	1.925-1.940	2.416-2.525	2.544	4.143	3.410-4.754	156.8	176.6-178.4
Rb	1.923-1.938	2.410-2.531	2.774	4.112	3.780-4.025	177.4	172.5-174.2
Cs	1.920-1.933	2.426-2.517	2.75	4.079	3.823-3.925	179.6	173.2-174.1

[a]When two values are reported, they represent the shortest and longest ones, respectively.

Table 4.4: Most significant structural parameters of 2U-P-Ox-A clusters in the presence of different counterions[a]

	distance (Å)						angle (deg)
	U–O	U–O	O-O		O–O		OUO
A	uranyl	per	per	U–U	uranyl–uranyl	UOOU	uranyl
Li	1.831-1.922	2.306-2.519	1.443	3.818	2.899-5.884	115.4	155.4-173.6
Na	1.832-1.840	2.322-2.353	1.431	4.060	3.170-5.848	131.9	164.8-165.1
K	1.833-1.839	2.349-2.362	1.433	4.324	3.695-5.568	149.0	170.0-170.2
Rb	1.833-1.838	2.356-2.363	1.435	4.479	4.499-5.044	170.6	170.8-170.9
Cs	1.831-1.839	2.369-2.375	1.435	4.494	4.337-5.156	167.0	171.8-172.3

[a]When two values are reported, they represent the shortest and longest ones, respectively.

Table 4.5: Most significant structural parameters of 5U-P-Ox-A clusters in the presence of different counterions[a]

	distance (Å)					angle (deg)	
	U–O	U–O	O-O		O–O		OUO
A	uranyl	per	per	U–U	uranyl–uranyl	UOOU	uranyl
Li	1.798-1.858	2.300-2.440	1.441-1.480	4.088-4.170	2.648-5.903	129.5-132.6	172.8-177.0
Na	1.802-1.865	2.316-2.452	1.442-1.474	4.121-4.240	2.830-5.689	134.5-139.4	173.7-177.8
K	1.819-1.864	2.318-2.453	1.444-1.468	4.282-4.448	3.163-5.585	143.1-158.7	173.9-179.0
Rb	1.825-1.866	2.332-2.451	1.446-1.465	4.346-4.467	3.400-5.479	148.6-157.5	173.5-178.2
Cs	1.834-1.864	2.333-2.471	1.448-1.462	4.418-4.475	3.714-5.231	157.0-158.7	174.4-176.9

[a]When two values are reported, they represent the shortest and longest ones, respectively.

Initially, we optimized the geometry of the $[(UO_2)_2(O_2)_5]^{6-}$ cluster (Figure 4.1A, structure a) without counterions (2U−P). This gave a geometrically reasonable cluster (Table 4.1), although the U-O_2-U dihedral angle optimized to 180° in contrast to experimentally determined values. Insertion of six Na counterions into this cluster (2U−P−Na), together with full geometry optimization, gave longer bond lengths within the cluster and an optimized U-O_2-U dihedral angle of 145°. Constraining the dihedral angle to 180° and reoptimizing the geometry of the cluster increased the energy by about 20 kcal/mol. We also determined the energy difference between the planar and bent structures for 2U−OH−Na. The structure with a dihedral angle of 160° is 2 kcal/mol

higher in energy than the planar structure, and the structure with a dihedral angle of 140° is 6 kcal/mol higher in energy than the planar structure. In the 2U−OH−Na case, the energy difference between planar and bent is thus less enhanced than in the 2U−P−Na case. Optimization of the geometry of the $[(UO_2)(O_2)_2(OH)]_2^{6-}$ cluster (Figure 4.1A, structure b) with six Na counterions added (2U−OH−Na) resulted in a distance between the OH groups of the shared edge of 2.603 Åand a U−$(OH)_2$−U dihedral angle of about 180°. Addition of two H2O groups to the cluster (2U−OH−Na−H_2O) did not appreciably change the optimized geometry of the cluster and again gave a U−$(OH)_2$-U dihedral angle of 180°. The geometry of the cluster $[(UO_2)_2(O_2)(C_2O_4)_4]^{6-}$ (Figure 4.1A, structure c), with the addition of six Na counterions, was optimized (2U−P−Ox−Na). The resulting bond lengths are reasonable although the uranyl ion is more bent than normal (Table 4.1). The optimized U−O_2−U dihedral angle is 132°. For comparison, the peroxide group was replaced by two hydroxyl groups and the geometry was reoptimized (2U−OH−Ox−Na). The optimized bond lengths of this hypothetical cluster are reasonable, but the uranyl ions (OUO) are unreasonably bent at 151°. The U−$(OH)_2$−U dihedral angle was 180°.

The cluster $[(UO_2)(O_2)(C_2O_4)]_5^{10-}$ (Figure 4.1A, structure d) was optimized with 10 added Na counterions (5U−P−Ox−Na). The geometry has reasonable bond lengths and uranyl ion angles ranging from 173° to 178°. It contains five peroxide groups that bridge between uranyl ions, and the optimized cluster has U-O_2-U dihedral angles of 135-140°.

In Table 4.1 we also report the U−U and O−O (uranyl-uranyl) distances. There is clearly a correlation between the O−O (uranyl-uranyl) and the UOOU dihedral angle: for the cases in which the angle is close to 180°, the O−O (uranyl-uranyl) distance is larger than the shortest O−O (uranyl-uranyl) distance for the cases in which the dihedral is bent. One can rationalize this trend as follows: in 2U−P−Ox, with no counterions and a total charge of −6, the planar structure corresponds to the least repulsion among the charges in excess. In 2U−P−Na, 2U−P−Ox−Na, and 5U−P−Ox−Na, the bending of the dihedral angle, which is possible because the presence of the bridging peroxo ensures the maximum Coulombic attraction between the uranyl oxygens and the counterions. In 2U−OH−Na and 2U−OH−Ox−Na, on the other hand, the OH groups, unlike the peroxo group, do not play a bridging role and they do not favor bending.

We performed a full characterization of the wave function in the case of 2U−P−Na in order to better understand the electronic structure of this species and provide insight concern- ing the origin of the bent U-O_2-U interactions. The optimized cluster 2U−P−Na has a U-O_2-U dihedral angle of 145°. Projections of selected molecular orbitals, from a CASSCF/ CASPT2 calculation, responsible for the bonds present in this cluster are shown in Figure 4.2. The calculation revealed the presence of a bonding molecular orbital along the U-O_{peroxo} bond, the top one in Figure 2. This orbital is a linear combination of the peroxo π along the plane and the U 6p orbitals. The 6p orbitals are usually described as corelike orbitals, so one wonders why instead the uranium 5f and 6d orbitals do not participate in the interaction with the peroxo. The reason is that the 5f and 6d orbitals are mainly involved in the interaction with the uranyl oxygens and the 6p are the next orbitals energetically available for the interaction with the peroxo and they point in the right direction. In the analogous hydroxyl cluster, 2U−OH−Na, in contrast, there is no such bonding orbital along the corresponding U-$O_{hydroxo}$ bond since there is not an analogous hydroxyl π molecular orbital of the right symmetry to be combined with the U orbitals. All orbitals on the OH−OH moiety are fully localized on each individual OH group and there is no covalent interaction between the two OH groups. Calculated partial charges for the 2U−P−Na cluster are +2.03 to +2.12 for the U cation, −0.67 to −0.99 for the O atoms of the uranyl ions, and −0.67 to −0.75 for the O atoms of the peroxide groups. The partial charges of the 2U−OH−Na−H_2O cluster are +2.16 to +2.19 for the U cation, −0.79 to −0.97 for the O atoms of the uranyl ions, and −0.91 to −0.92 for the O atoms of the hydroxyl groups. The presence of a bonding molecular orbital along the U-O_{peroxo} bond, together with the observation that the O atoms of the hydroxyl group are more ionic than those of the peroxide group, confirms that there is some covalent bonding in the case of the peroxide bridge. In Figure 2 we also report the orbitals in the HOMO-LUMO region, which are mainly localized on the two uranyl moieties. These four orbitals are similar in the peroxo and hydroxo cases.

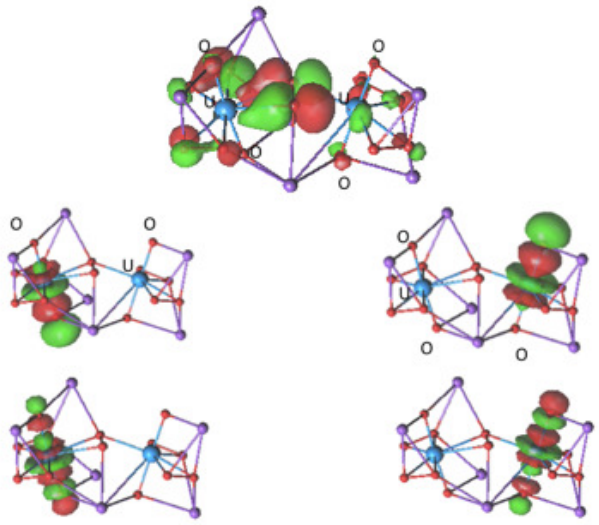

Figure 4.2: Selected molecular orbitals responsible for the bonds in cluster 2U-P-Na. The upper orbital shows the covalent interaction between the central peroxo and the two U atoms. The other four orbitals are those in the HOMO-LUMO region and they are entirely uranyl-based. U, blue; O, red; Na, purple.

We propose that the difference in bonding along the U-O_{peroxo} and U-$O_{hydroxo}$ bonds revealed by our calculations is responsible for the bent U-O_2-U dihedral angle, while the U-$(OH)_2$-U dihedral angle in the comparable cluster tends to be planar. However, recall the calculations on the 2U−P and 2U−P−Na clusters indicate that the U-O_2-U dihedral angle becomes bent only when the charge of the uranyl polyhedra is balanced by counterions. A possible explanation for the bent U-O_2-U dihedral angles observed experimentally and confirmed by our calculations is that the counterions in our calculations interact with the uranyl ion O atoms, making the U atoms more available for interactions with the equatorial O atoms of peroxide or hydroxyl groups; however, while in the peroxo-bridged cluster a U-O_{peroxo} covalent bond forms. This cannot happen in the hydroxo-bridged case because the O atoms of the hydroxyl groups are polarized by the presence of the H atoms.

The argument usually advanced to explain the formation of cation-oxo ligand interactions is that strong equatorial donors increase the negative charge on the oxo ligands,

thereby increasing their Lewis basicity. This was discussed in a paper by Clark et al.; [304] on the basis of their argument, the hydroxo complex should exhibit stronger uranyl interactions (over the peroxo), because it is a stronger donor. Ingram et al. [305] also discussed the same issue and showed that the Lewis basicity increases with the number of coordinated hydroxides. However, according to Ingram et al. [305] the hydroxide is not necessarily a stronger donor and peroxide forms in some complexes very short bonds with uranyl, in agreement with our interpretation of the results we obtain.

The observation that counterions are needed in our model clusters to produce bent U-O_2-U dihedral angles prompted us to hypothesize that counterions may permit tuning of the U-O_2-U dihedral angle. We optimized the geometries for each of the clusters under study using Li, Na, K, Rb or Cs as the counterions (designated A in the descriptors). The resulting geometries are presented in Tables 4.2-4.5. The optimized geometries of the two uranyl bipyrimid polyhedra in the simplest cluster 2U−P−A remain essentially constant despite changing the counterion, with the exception of the uranyl ion bond angle, which is more bent in the case of A) Li. The U-O_2-U dihedral angle of the peroxo bridge steadily increases with the size (and decreasing electronegativity) of the counterion, from 140° in the case of A) Li to 164° for A) Cs. In Figure 4.3 we report the peroxo dihedral angle as a function of the ionic radius of the counterion for the 2U−P−A clusters. In Table 4.6 we report Mulliken charges for the 2U−P−A clusters for various counterions. In going from Li to Cs, the uranyls become less ionic and the Operoxo more negatively charged as the UOOU dihedral angle increases.

Table 4.6: Most significant structural parameters of 5U-P-Ox-A clusters in the presence of different counterions[a]

	Li	Na	K	Rb	Cs
U	+0.94 to +1.02	+0.62 to +0.68	+0.64 to +0.69	+0.60 to +0.70	+0.55 to +0.64
O_{yl}	-0.67 to -0.47	-0.69 to -0.53	-0.69 to -0.52	-0.68 to -0.54	-0.64 to -0.56
O_{peroxo}	-0.36 to -0.34	-0.44 to -0.34	-0.45 to -0.34	-0.46 to -0.41	-0.41 to -0.37

[a]When two values are reported, they represent the shortest and longest ones, respectively.

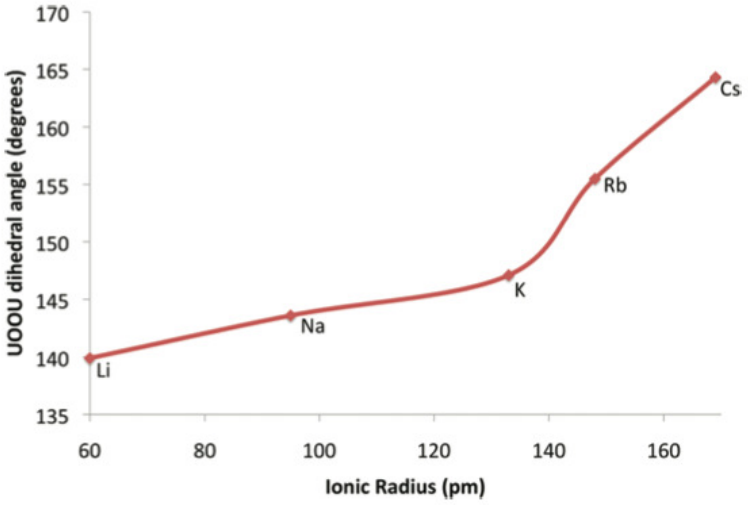

Figure 4.3: Peroxo dihedral angle as a function of the ionic radius [306] of the counterions in the 2U-P-A clusters

We also determined the energy difference between the planar and bent structures for 2U−P−A, for A) Li to Cs. The energy difference between planar and bent decreases along the series, going from 37 kcal/mol for Li to 6 kcal/mol for Cs. This trend is consistent with the trend in the bending angle.

For comparison, optimized geometries for the hydroxo- bridged clusters 2U-OH-A and 2U-OH-A-H2O are listed in Table 3. For 2U-OH-A the calculated geometries of the uranyl polyhedra do not differ much as the counterion is changed, except again in the case of A = Li, where the uranyl ion bond angle is more bent than the others. The U-(OH)2-U dihedral angles for the bridging hydroxo edge are 180 within uncertainty for A = Li, Na, Rb, and Cs. For A = K, the dihedral angle is 157°. We attribute the nonplanarity of the bridge to counterions bridging between two uranyl ion O atoms, which would encourage bending in a pliable system. It also seems plausible that K has the perfect ionic radius to bridge two uranyl ion oxygens.

Where two H_2O groups are added to the optimization (2U−OH−A−H_2O), the U-$(OH)_2$-U dihedral angle for the bridging hydroxo edge is 180° within uncertainty for A = Li and Na. For A = K, Rb, and Cs, the dihedral angles are 153°, 161° and 170°, respectively.

Optimizations for the 2U−P−Ox−A clusters (Table 4) result in generally reasonable polyhedral geometries with the exception of the uranyl ion bond angles, which are more bent than expected. The U-O_2-U dihedral angles of the peroxo bridge steadily increase with the size of the counterion, ranging from 115° for A=Li to 171° for A=Rb and 167° for A=Cs. Calculations for the hypothetical 2U−OH−Ox−A cluster provided optimized geometries that are generally incompatible with those expected from experimental studies of other clusters, with O−O distances between hydroxyl groups being too short and uranyl ion bonds departing too far from linearity. We emphasize that this cluster has not been obtained experimentally. Despite the shortcomings in the polyhedral geometries, the U-$(OH)_2$-U dihedral angles for the bridging hydroxo edge are 180° within uncertainty for A = Na, K, Rb, and Cs. In the case of A = Li, the dihedral angle is 150°.

Geometric parameters for the optimized 5U−P−Ox−A clusters are reported in Table 5. There are five uranyl ions that share five peroxo bridges, forming a pentagonal ring. The calculated bond lengths and angles of the uranyl bipyramids are consistent with experimentally derived values and differ only slightly with the identity of the counterion present. In contrast, the U-O_2-U dihedral angles vary considerably and systematically with the ionic radii of the counterions, from 129-133° for A = Li to 157-158° for A = Cs. In other words, increasing the size of the counterion associated with the five-membered ring significantly flattens the overall structure.

4.1.4 Conclusions

Formation of closed clusters of uranyl peroxide polyhedra is spontaneous in aqueous solutions under ambient conditions, and such clusters can persist for months in solution. [65, 68, 296–298] Their topologies are highly complex, containing 20-60 uranyl ions. There are many possible topologies for the clusters, including fullerene topologies and some that contain topological squares. Three fundamental questions have arisen concerning these nanoscale clusters and their self-assembly in solution:

(1) What factor(s) cause the polyhedra to assemble into nanostructures rather than into conventional extended structures?

(2) Why do clusters with different sizes assemble, currently ranging from 20 to 60

uranyl polyhedra?

(3) For a given number of vertices, what determines which topological isomer is selected?

We have recently concluded that isomer selection is dominated by symmetry. [67, 297] Specifically, for a given number of uranyl polyhedra, the cluster with the highest possible symmetry (excluding those that would require unreasonable edges) will form because this is compatible with the most even distribution of any strain associated with the required curvature. Our calculations now allow us to address the first two questions. All electroneutral clusters containing a peroxo bridge between uranyl bipyramids have strongly bent U-O_2-U dihedral angles. The corresponding U-$(OH)_2$-U dihedral angle in model clusters tends to be flat, although a bent angle is not prohibited. It is the covalent interaction that extends along the U-O_{peroxo} bonds that causes the U-O_2-U dihedral angle to be bent, and it is this inherent bending of the configuration that encourages curvature and cage cluster formation. Our calculations have also shown that the U-O_2-U dihedral angle of the peroxo bridge is tuned by the size or electronegativity of the counterion present. In other words, different counterions favor different *degrees of curvature*, which is reflected in the range of cluster sizes.

4.1.5 Acknowledgements

This research was supported by Director, Office of Basic Energy Sciences, U.S. Department of Energy under Contract USDOE/DE-SC002183, and the Materials Science of Actinides Center, an Energy Frontier Research Center funded by the U.S. Department of Energy, Office of Science, Office of Basic Energy Sciences under Award DE-SC0001089.

4.2 Uranyl-Peroxide Nanocapsules in Aqueous Solution

The self-assembly of uranyl-peroxide nanoclusters in aqueous solution is unique in uranium chemistry and has potential applications in the fabrication and reprocessing of actinide-based materials. We present the first study of these species in aqueous solution by means of classical molecular dynamics simulations. We have parameterized a uranyl-peroxide force field from interaction energies computed with second order Møller-Plesset perturbation theory and fit to a Born-Huggins-Meyer potential. Bonded parameters were fit from density functional theory calculations. The solvent and counterion structure of four different systems ($[(UO_2)]^{2+}$ ($\mathbf{U}_1$), $[(UO_2)_2(O_2)]^{2+}$ ($\mathbf{U}_2$), $[(UO_2)_5(O_2)_5]$ ($\mathbf{U}_5$), and $[(UO_2)_{20}(O_2)_{30}]^{20-}$ ($\mathbf{U}_{20}$) has been studied in aqueous solution.

4.2.1 Introduction

Uranium is the second most abundant actinide in Earth's crust and a major source of energy which has led to the storage of over 65,000 tons of waste in the U.S. alone. Additionally, tens of thousands of tons are produced each year worldwide. Despite the challenges, many countries depend on the industrial-scale use of actinides as fuels for commercial nuclear power plants and this has a considerable impact on the environment. [2] Understanding and controlling the solution chemistry of the uranyl ion, $[U^{VI}O_2]^{2+}$, is central to the development of an advanced nuclear energy cycle. To this end, gaining nanoscale control over actinide materials is of high interest and promises a more effective method for processing nuclear materials with applications not only in materials fabrication but also in the reprocessing of irradiated fuel. [66] Furthermore, actinide clusters have the potential to form under environmental conditions and open questions persist regarding the impact this would have on the mobility of actinides under environmental conditions. [74]

Pursuing this goal, a family of nanocapsules in which uranyl polyhedra are bridged through peroxide and hydroxide groups has been discovered. More recently, larger linking groups like oxalate or pyrophosphate have been incorporated into cluster topologies. [69–72] The self-assembly of these species in strongly basic aqueous solution at

---

Manuscript in preparation.

Coauthors: P. Miró, S. Hu, A. Dzubak, R. Spezia, C. J. Cramer, and L. Gagliardi

room temperature is unique in uranium chemistry. In all cases, the uranyl polyhedron is a hexagonal bipyramid, the apices of which correspond to the oxygen atoms of the uranyl cation. The bipyramids then bind to each other by sharing equatorial edges with adjacent polyhedra. Clusters containing up to 120 uranyl polyhedra have been characterized and exhibit a wide range of high symmetry topologies including fullerenes. [65–68, 73]

The presence of uranyl-peroxide bridging groups is fundamental in capsule formation. The pliability of the U-O_2-U dihedral angle allows for the formation of non-planar species that, in the end, close as a capsule.[75, 76] Additionally, the alkali countercations present during synthesis play a critical role as the curvature of the resulting capsule is controlled, to some extent, by cation coordination. [69, 78, 79] To date, experiments and quantum chemical studies have been able to provide information on the position of the encapsulated counterions but not of the counterions outside the capsule. [69] Furthermore, the solvent structure and counterion positions inside the capsules larger than U_{28} remains unknown. In analogy to what has been observed in the field of classical polyoxometalates, these polyanionic capsules likely interact with cations in solution.[307] Understanding the solvent and counterion dynamics surrounding uranyl-peroxide nanocapsules is fundamental in the design of new nanocapsules in order to avoid or enhance the trapping neutron poisons for use in an advanced nuclear fuel cycle through size separation techniques. [69]

As a first step in this direction, we have developed uranyl-peroxide force field and have studied four systems: ($[(UO_2)]^{2+}$ ($\mathbf{U}_1$), $[(UO_2)_2(O_2)]^{2+}$ ($\mathbf{U}_2$), $[(UO_2)_5(O_2)_5]$ ($\mathbf{U}_5$), and $[(UO_2)_{20}(O_2)_{30}]^{20-}$ ($\mathbf{U}_{20}$) (Figure 4.4) by means of classical molecular dynamics simulations. All of these species have been experimentally synthesized. U_2, the smallest known uranyl-peroxide system, has been proposed as the first step towards the formation of U_5, U_{20}, and other nanocapsules. [68, 301] Analogously U_5 has been proposed as the building block of the U_{20} nanocapsule that is composed of twelve pentagonal faces. [68, 75, 76, 78]

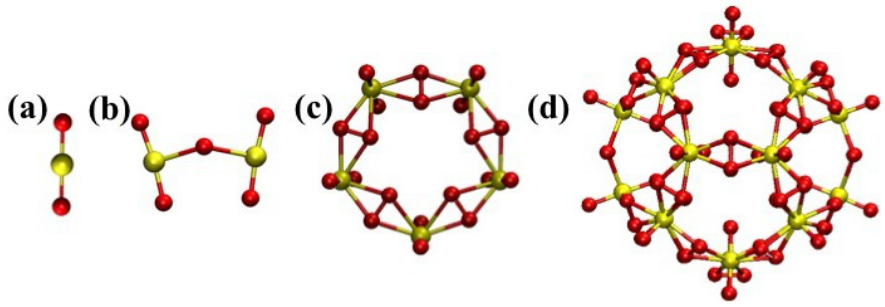

Figure 4.4: Uranyl and uranyl-peroxide systems studied in this work: $[(UO_2)]^{2+}$ ($\mathbf{U}_1$) (a), $[(UO_2)_2(O_2)]^{2+}]$ ($\mathbf{U}_2$) (b), $[(UO_2)_5(O_2)_5]$ ($\mathbf{U}_5$) (c), and $(UO_2)_{20}(O_2)_{30}]^{20-}$ ($\mathbf{U}_{20}$) (d). Color code: Uranium in yellow, oxygen in red and hydrogen in white.

4.2.2 Computational Details

Classical Molecular Dynamics

All of the molecular dynamic simulations were performed using the DLPOLY classic package developed at Daresbury Laboratory. [308] The systems were simulated using the force field parameterized in this work (see Section 4.2.2 for details). The solvent, water, molecules were described using the TIP3P water force field and the sodium ions using the parameters proposed by Lee and Rasaiah. [309, 310]

Electrostatic interactions were accounted for by using the Ewald summation technique with a convergence parameter of 0.210 and considering a maximum of six wave vectors in each direction. The Verlet leapfrog algorithm was used to integrate the equations of motion with a time step of 1 fs and a cutoff of 10 Å. In order to optimize the CPU usage, we have used a Verlet neighbor list with a cutoff radius of 11 Å. The rigid body rotational motion is handled under the leapfrog scheme with Finchams implicit quaternion algorithm [311] with a tolerance of 10^{-6}. All of the simulations were performed at room temperature (298 K) with a pressure of 1 atm.

The systems were solvated using a different number of water molecules depending on the system size. The smaller species (U_1 and U_2) were simulated including 512 water molecules meanwhile simulations for the larger species U_5 and U_{20} included 1024 and 2048 water molecules, respectively. In the U_{20} simulations, twenty Na^+ ions were also included to neutralize the system. After the NPT equilibration for the flexible

simulations, the simulation box was 25.1, 24.9, 31.3, and 39.3 Å^3 for U_1, U_2, U_5 and U_{20}, respectively.

All of the systems were equilibrated running 100ps NVT followed by 500ps NPT. In the NVT simulations, the temperature was kept fixed using the Nosé-Hoover thermostat with a relaxation time equal to 20 fs. [312, 313] In the NPT simulations, the pressure was kept fixed using the Nosé-Hoover barostat with a relaxation time equal to 40 fs. Once equilibrated, we performed production simulations in different ensembles (NPT, NVT and NVE). The details of the production runs for each system are given in the Supporting Information. In the production simulations, the positions and velocities of the system were stored every 10 time steps for analysis *a posteriori*.

Second-Order Møller-Plesset Perturbation Theory Calculations

Second order Møller-Plesset perturbation calculations on U_1 and U_2 were used to generate interaction curves with water. They were performed using the Molcas 7.6 package. [172] The counterpoise correction was used to account for basis set superposition error and relativistic effects were treated through the use of the scalar Douglas-Kroll-Hess (DKH) Hamiltonian. [169, 294] An ANO-RCC-VDZP basis set was used for all atoms. [170, 295] Additionally, the Cholesky decomposition technique was combined with Local Exchange screening to significantly reduce the computational cost involved in generating the two-electron integrals. [173–176]

Density Functional Theory Calculations

Geometry optimizations were performed for U_2, U_5, and U_{20} using density functional theory (DFT) within the Amsterdam Density Functional (ADF2010) program. [50] The Perdew-Burke-Ernzerhof exchange-correlation functional (PBE) was employed together with a triple-ζ plus two polarization function basis set on all atoms. [96, 314] For non-hydrogen atoms, a relativistic frozen-core potential was used. Relativistic corrections were introduced by the scalar-relativistic zero-order regular approximation (ZORA). [179] Solvent effects were introduced using the continuous solvent model COSMO, [315] and geometries were fully optimized taking advantage of symmetry when present.

Uranyl-peroxide Force Field Parameterization in aqueous solution

The non-bonded interactions were parameterized from second order Møller-Plesset perturbation (MP2) calculations, [168] while the bonded interactions were parameterized from density functional theory (DFT) calculations. [96] We computed several U_1-water and U_2-water interaction energy curves with different water orientations in order to sample the most relevant interactions between the uranyl and peroxide fragments with solvent (Figure 4.5). Interaction energies were computed at the MP2 level of theory using the Molcas software package. [172] The U_1 geometry was fixed at d_{U-O}=1.705 Å and the TIP3P geometry was used for water. The non-bonded interaction is composed of two terms: an electrostatic/Coulomb term and a non-electrostatic term.

For the electrostatic term, we used the atomic partial charges for U_1, U_2 and U_5 species we used the quadrupolar charges derived from the scheme developed by Swart et al. [183] (Table 4.7). The large negative charge in the U_{20} nanocapsule leads to a set of DFT charges that are significantly different from the species used in the parameterization of the non-bonded terms. In consequence, we used the oxygen charges from U_2 for both the uranyl and peroxide oxygen atoms in the nanocapsule and scaled the uranium charge to maintain the overall charge of the capsule. The electrostatic term was subtracted from the curves prior to fitting the non-electrostatic term to a Born-Huggins-Mayer (BHM) potential of the form

$$V_{ij}^{NB} = \sum_{i,j}(A_{ij}e^{-B_{ij}r_{ij}} + \frac{C_{ij}}{r_{ij}^6} + \frac{D_{ij}}{r_{ij}^8}) \tag{4.1}$$

where $A_{i,j}$, $C_{i,j}$ and $B_{i,j}$ are the parameters defined for each atom couple and $r_{i,j}$ is the distance. The parameters of O-O_{water}, U-O_{water} and $O_{peroxide}$-O_{water} couples are presented in Table 4.8. The non-electrostatic parameters between the oxygen centers in the studied species and the sodium counterions were considered to be equivalent to the water-sodium parameters. Meanwhile, the uranium-sodium terms were considered to be negligible.

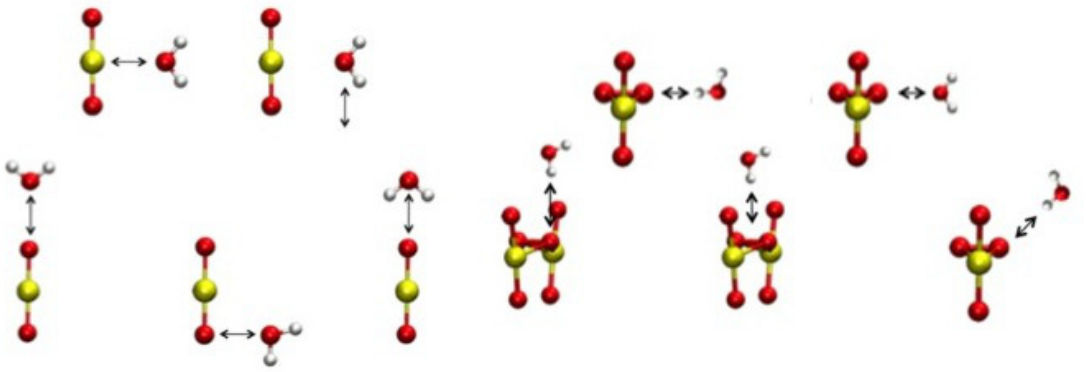

Figure 4.5: The pathways along which interaction energy curves were derived for the U_1-water and U_2-water interactions. Color code: Uranium in yellow, oxygen in red and hydrogen in white.

Table 4.7: Atomic partial charges used for electrostatic term in the molecular dynamics simulations.

Species	U	O_{uranyl}	$O_{peroxide}$
U_1	2.540000	-0.270000	–
U_2	2.459900	-0.467100	-0.525700
U_5	2.426986	-0.591360	-0.672133
U_{20}	1.511300	-0.467100	-0.525700

Table 4.8: Intermolecular parameters for non-bonded term using the Born-Huggins-Mayer potential presented in Eq. 4.1

		A_{ij}	B_{ij}	C_{ij}	D_{ij}
Atom i	Atom j	kJ Å^{12}/mol	kJ Å^6/mol	kJ Å^6/mol	kJ Å^8/mol
U	O_{water}	360.92331	0.68480	58103.45591	-283958.20450
O_{uranyl}	O_{water}	-3898.95694	1.30286	-59841.66996	138921.01370
$O_{peroxide}$	O_{water}	-29.49020	0.21039	-8536.38565	0.00000

The U-O_{uranyl} and $O_{peroxide}$-$O_{peroxide}$ bond stretch parameters were fit to a harmonic potential (Eq. 4.2) from the vibrational frequencies obtained at the DFT level.

Single point calculations at the same level of theory were performed along the (O_{uranyl}-U-O_{uranyl}) and (O_{uranyl}-U-$O_{peroxide}$) reaction coordinates in U_1 and U_2, respectively. The potential energy curves were fit to a harmonic potential (Eq. 4.3). Moreover, the pliability of the U-($O_{peroxide}$)$_2$-U dihedral angle has been demonstrated both experimentally and computationally.[40, 75, 301] Our force field does not define any explicit dihedral, since they are already included indirectly (e.g. O_{uranyl}-U-$O_{peroxide}$ already defines the U-($O_{peroxide}$)$_2$-U dihedral double well). All of the bonded parameters are summarized in Tables 4.8 and 4.9.

$$V_{ij}^{B} = \frac{1}{2} K_{ij} (r_{ij} - r_{ij}^{0})^2 \tag{4.2}$$

$$V_{ijk}^{B} = \frac{1}{2} K_{ijk} (\phi_{ijk} - \phi_{ijk}^{0})^2 \tag{4.3}$$

Table 4.9: Parameters for the bond stretching and angle bending modes using the potentials presented in Eq. 4.2 and 4.3 respectively.

Atom i	Atom j	Atom k	K_{ij}/K_{ijk} kJ/mol	${d_{ij}}^0/{\phi_{ijk}}^0$ Åor deg.
U	O_{uranyl}	–	8537.71935	1.769
O_{uranyl}	U	O_{uranyl}	657.61177	180.0
$O_{peroxide}$	$O_{peroxide}$	–	4848.29742	1.4455
U	$O_{peroxide}$	–	1876.71236	2.3382
O_{uranyl}	U	$O_{peroxide}$	590.80666	93.0

4.2.3 Results

Uranyl and uranyl-peroxide dimer

The first step in the validation of the uranyl-peroxide force field is to study the fundamental nanocapsules building blocks used in the parameterization process (U_1 and U_2). For U_1, we compare our results with previous experimental results [316] and simulations performed with classical molecular dynamics both with non-polarizable [317–319] and polarizable [302] force fields. Unlike U_1, there are no previous studies on U_2 in solution; therefore, a direct comparison with experiment cannot be made. The structural hydration properties of U_1 and U_2 are summarized in Table 4.10.

Table 4.10: Structural hydration properties of U_1 and U_2 species. $r_{U-Owater}$ corresponds to the first peak in the U-O_{water} g(r) and the corresponding coordination number (CN). Distances are in Å and for the flexible simulations the $r_{U-Ouranyl}$ value is an average.

	Method	Polarizable	Flexible	$r_{U-Ouranyl}$	$r_{U-Owater}$	$CN_{U-Owater}$
U_1 (This work)	cMD	No	No	1.705	2.39	5
U_2 (This work)	cMD	No	No	1.802	2.42	3.8
U_1 (This work)	cMD	No	Yes	1.78	2.39	5
U_2 (This work)	cMD	No	Yes	1.78	2.42	4.0
U_1 (Wipff et al. [317, 318])	cMD	No	Yes	1.80	2.45	5
U_1 (Rai et al. [319])	cMD	No	No/Yes[a]	1.76	2.41	5
U_1 (Hagberg et al. [302])	cMD	Yes	No	1.705	2.40	5
U_1 (Experimental [316])	–	–	–	1.77	2.41	5.3

[a]Bond distances were fixed but angles were allowed to vary in some MC simulations.

In order to study the structure of the various solvation shells, we plotted the radial distribution function, g(r), of different atom pairs in the U_1 and U_2 simulations. When comparing the rigid simulations, the first peak in the U-O_{water} g(r) corresponds to the first solvation shell and has an equilibrium distance near 2.4 Å in both U_1 and U_2 (Figure 4.6). The U-O_{water} distance and coordination number (CN) in U_1 is in good agreement with previous experimental and simulated results (Table 4.10). The biggest difference between the solutes is the CN. Our simulations confirm that one uranyl unit alone, U_1, coordinates five water molecules in its equatorial plane while in U_2 four waters coordinate to each uranium center. Recall that each uranium also coordinates an η^2-O_2 ligand making the total CN equal to six in U_2. Moreover, the U-O_{water} distance in U_2 is slightly longer when compared with U_1; however, this distance is consistent with the change in coordination number (Table 4.10). In 2005, Burns reported a survey of the known uranyl minerals and inorganic compound and found the average distances between uranium and equatorial oxygen atoms in pentagonal bipyrimids was 2.37 Å while in hexagonal bipyrimids it was 2.45 Å. [320]

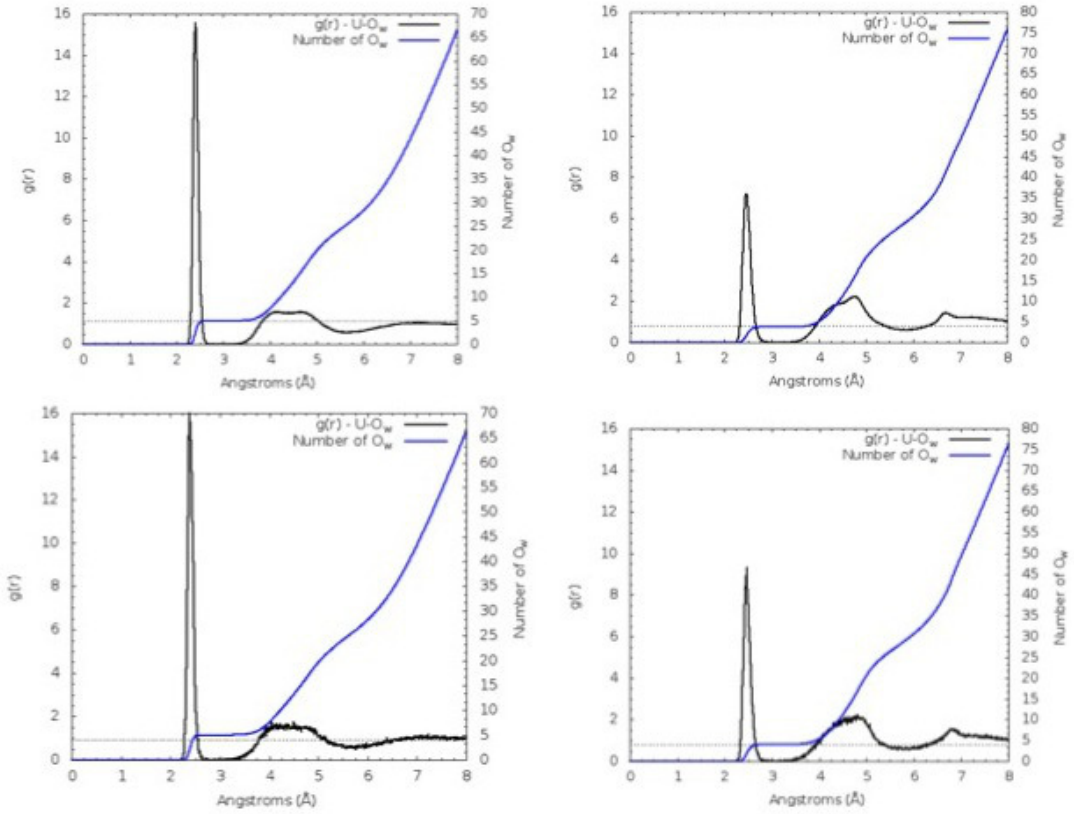

Figure 4.6: Radial Distribution Function between U-O_{water} of the rigid (top) and flexible (bottom) U_1 and U_2 simulations. The O_{water} CN in the uranium center is also plotted on the right axis. For both simulations, the total simulation time was 5ns NVT and 1ns NPT. Horizontal dashed line indicates the uranyl coordination number of five and four for U_1 and U_2 respectively. The RDF goes to 1 at long distances but is not shown in the plotted range of the x-axis.

Both the rigid and the flexible simulations predict a U-O_{water} distance in uranyl equal to 2.39 Å(CN=5) in good agreement with the previous simulations and EXAFS studies. [316] However, in U_2 the coordination number increases from 3.8 to 4.0 when the force field is allowed to be flexible. A hexa coordinate uranium center is predominant in uranyl-peroxide species and has been observed experimentally in many dimeric species and nanocapsules. [66]

The tridimensional probability distribution of the solvent surrounding U_1 and U_2 can be analyzed by means of spatial distribution functions (SDF) (Figure 4.7). The U_1 SDF shows the water oxygen probability distributed in the equatorial plane and two rings (above and under) where the hydrogen probability is located (perpendicular to the U_1 axis). Furthermore, in U_2 four probability basins for the water oxygens are found for each uranium center confirming the RDF results presented in Figure 4.6.

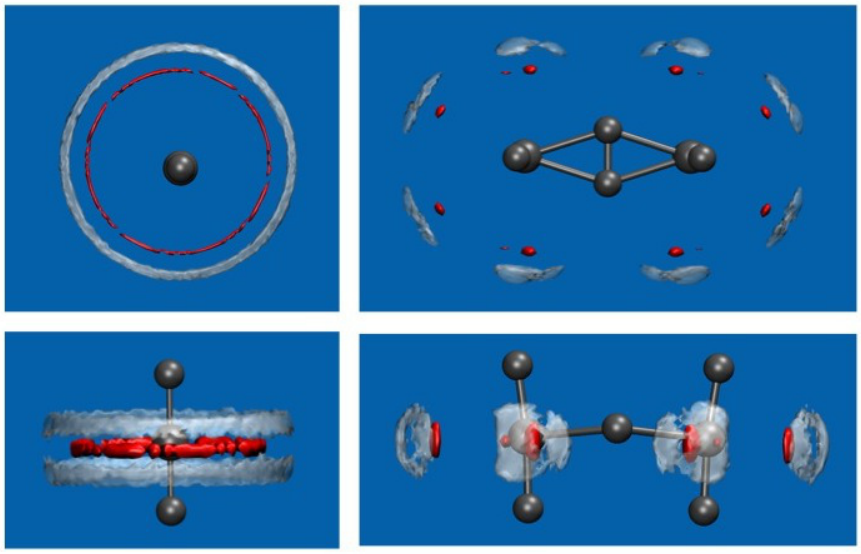

Figure 4.7: Top and side view of the spatial distribution function (SDF) of the rigid U_1 (left) and U_2 (right) at isosurfaces of 0.6 and 0.4, respectively, from the 1 ns NVT simulations. The water oxygen and hydrogen probabilities are shown red and semitransparent white. The U_1 and U_2 structures are shown in grey.

The flexible simulations allow thermal fluctuations of U_1 and U_2 from their equilibrium structure. The average values for the bond, angle and dihedral oscillations in time for both systems are presented in Table 4.11. The average U-O_{uranyl} bond and O_{uranyl}-U-O_{uranyl} angle are in good agreement with experimentally determined values. [320**?**] Likewise, the U-$(O_{peroxide})_2$-U butterfly dihedral fluctuates during the simulation ranging from around 160° to 180° in U_2 with an average of 172.9°. One should remember the large pliability of the U-$(O_{peroxide})_2$-U dihedral angle when calculated and experimental values are compared. It has been shown that the crystal packing effects have a direct influence on the observed dihedral angle in the X-ray crystal structure, explaining the

observed difference. [321] Additionally, the U-($O_{peroxide}$)$_2$-U dihedral value in solution remains experimentally unknown.

Table 4.11: Comparison between the calculated and experimental average (1ns) distances, angles and the U-($O_{peroxide}$)$_2$-U dihedral angle in flexible U_1 and U_2. Distances are in Å and angles in degrees.

	U_1	U_2	
	Flexible MD	Flexible MD	Exp. [68]
d(U-O_{uranyl})	1.78	1.78	1.79
d($O_{peroxide}$-O_{uranyl})	–	1.41	1.47
d(U-$O_{peroxide}$)	–	2.41	2.33
α(O_{uranyl}-U-O_{uranyl})	175.7	175.3	177.5
ϕ(U-($O_{peroxide}$)$_2$-U)	–	172.9	153.0

The strength of an apical interaction between water and the uranyl oxygen was long debated in the scientific community being nowadays it is clear that the uranyl oxygen does not interact strongly with water molecules. [302, 316, 319] This behavior is highly dependent on the force field used and previously reported non-polarizable force fields were unable to correctly describe this interaction. [317, 318] Polarizable potentials were in agreement with experimental results. In Figure 4.8 we present the O_{uranyl}-O_{water} and O_{uranyl}-H_{water} g(r), which shows the absence of strong apical hydrogen bonds in our simulations. The observed peak at approximately 3 Å in the O_{uranyl}-O_{water} g(r) corresponds to the five equatorial water molecules. Likewaise, the first two peaks in the O_{uranyl}-H_{water} plot are assigned to the H atoms of these waters. This description is consistent with what was reported by Hagberg et al. in which the equatorial waters were also the nearest neighbors of the uranyl oxygen atoms. [302]

Uranyl-peroxide Pentamer

After validating the uranyl-peroxide force field for the smallest building blocks, we employed it to predict hydration properties for the U_5 cluster. Although experimental data is not available for comparison, the simulations showed that water around the isolated pentagonal face is even more ordered than in the dimer. Both the rigid and flexible simulations predicted similar U-O_{water} radial distribution functions (see Figure 4.9). The

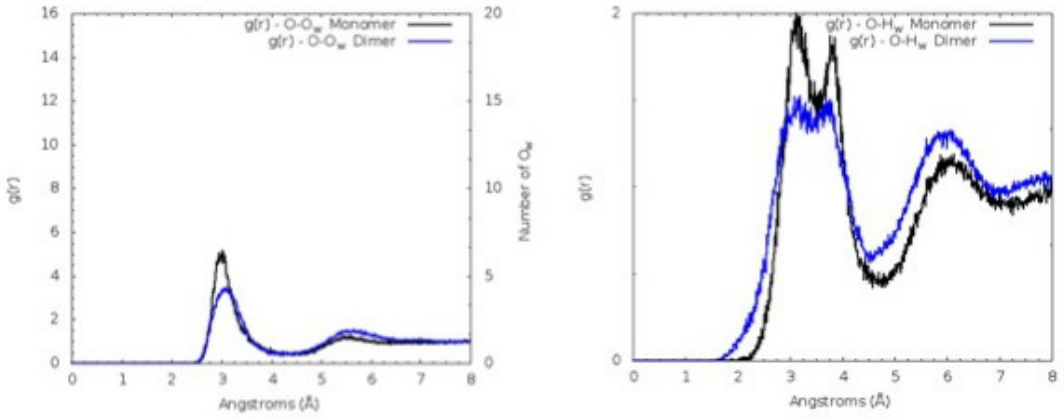

Figure 4.8: The O_{uranyl}-O_{water} g(r) for U_1 flexible (left) and the O_{uranyl}-H_{water} g(r) for U_1 and U_2 for the flexible (right). Plots for the rigid simulation (not shown) shown the same picture.

first peak is centered at 2.42 Å, and the same average U-O_{water} distance is observed in the first coordination shell as was seen in U_2. In U_5, each uranium center is coordinated to two η^2-O_2^{2-} ligands and has a water coordination number of 2.0. The subsequent peaks in the U-O_{water} RDF correspond to water ligands located on neighboring uranium centers.

Additionally, the SDF was plotted to show water coordination in three-dimensions (Figure 4.10). As is the case for U_2, the equatorial water molecules are represented by probability basins; two for each uranium center. The most interesting feature is that a single water molecule sits underneath the five uranyl oxygen atoms in the center of the pentagonal face. This is consistent with X-ray diffraction studies that show a counterion occupies this position. [68]

While there is no experimental information for U_5 in solution, the $K_{10}[(UO_2)(O_2)(C_2O_4)]_5(H_2O)_{13}$ [68] cluster has been experimentally characterized in the solid state. This structure contains an oxalate ligand in the position of the two equatorial water molecules present in our simulations. A comparison between relevant geometric parameters can be made (Table 4.12) between the solid state and the average values from our flexible simulation. In the simulation, the average U-O_{uranyl} bond distance and O_{uranyl}-U-O_{uranyl} angle are 1.77 Å and 173.5° respectively. Furthermore, the U-$(O_{peroxide})_2$-U

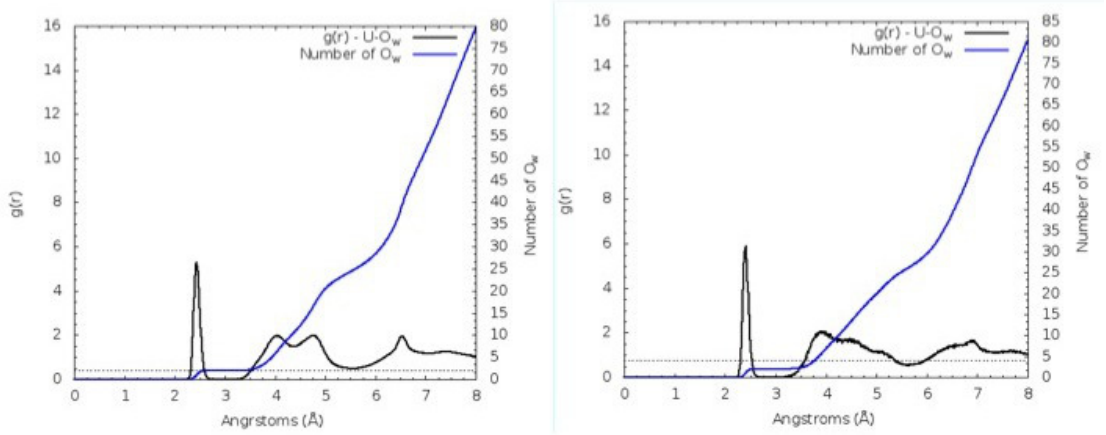

Figure 4.9: Radial Distribution Function between U-O_{water} of the rigid (left) and flexible (right) U_5 simulations. The O_{water} CN in the uranium center is also plotted (right axis). The total simulation time was 5ns NVT and 1ns NPT for both rigid and flexible simulations. The horizontal dashed line indicates the uranyl-water coordination number of two. The RDF goes to 1 at long distances but is not shown in the plotted range of the x-axis.

angle fluctuates during the simulation with an average of 169.5°. Again, these values are in reasonable agreement.

Table 4.12: Comparison between the calculated and experimental average (50ps) distances, angles and the U-$(O_{peroxide})_2$-U dihedral angle in flexible U_5. Distances are in Å and angles in degrees.

	U_5	
	Flexible MD	Exp. [68]
d(U-O_{uranyl})	1.77	1.80
d($O_{peroxide}$-O_{uranyl})	1.42	1.48
d(U-$O_{peroxide}$)	2.41	2.35
α(O_{uranyl}-U-O_{uranyl})	173.5	178.8
ϕ(U-$(O_{peroxide})_2$-U)	169.5	143.6

Finally, during the flexible simulations, the entire U_5 face can flip from concave to convex. Analogous inversion has been shown for uranyl peroxide squares in the U_{24}-P

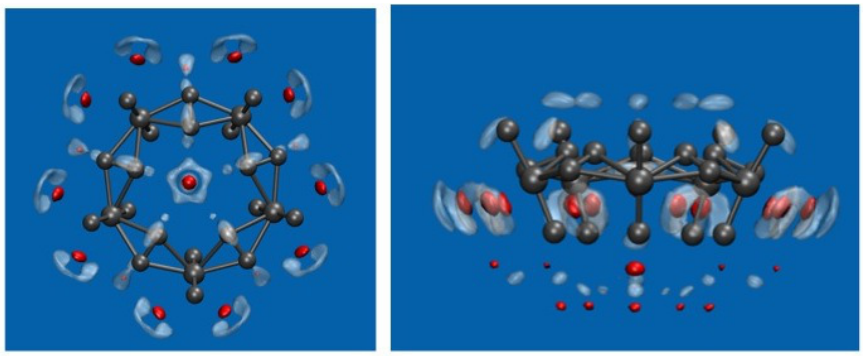

Figure 4.10: Top and side view of the spatial distribution function (SDF) of the rigid U_5 at an isosurface of 0.1 from the 1ns NVT simulation. The water oxygen and hydrogen probabilities are shown red and semitransparent white while the U_5 structure is in grey.

capsule by phosphorus NMR. [322] Although the $U_{24}P$ capsule does not contain any pentagonal faces, the fact that uranyl peroxide square faces have been observed to invert suggests that the inversion of U_5 observed in our simulations is not a relic of our calculations.

Uranyl-peroxide U_{20} Nanocapsule

Sigmon et al. [68] synthesized the smallest known uranyl-peroxide nanocapsule U_{20} containing 12 pentagonal faces. We selected this capsules to validate our force field as well as to study the dynamics of solvent and counterions interactions with the nanocapsules. The U_5 simulations revealed highly stable site for a water molecule in this pentagonal structure. In consequence, our initial structures position a water molecule in each of the faces of U_{20}. To explore the loading of water in the central part of U_{20} we ran simulations with initial configurations ranging from 6 to 10. In this initial study, no sodium counterions were placed inside the internal cavity of the capsule. Future studies using molecular dynamics in combination with Grand Canonical Monte Carlo simulations are required to gain a detailed understanding of the number of water and counterions present inside the capsule at equilibrium.

Analysing the results, we find that one water molecule is present at the center of the capsule. The RDF between this water and the remaining solvent molecules is given

in Figure 4.11. From the O_{center}-O_{water} RDF alone, it is clear that the water inside the capsule is ordered. The encapsulated water is divided into two groups as shown by two distinct peaks each representing 12 water molecules. The first occurs at 2.5 Å from the center and the second at 5.2 Å. Therefore, 25 water molecules are present inside the U_{20} capsule which has a volume of approximately 200 $Å^3$ (a radius of 6 Å).

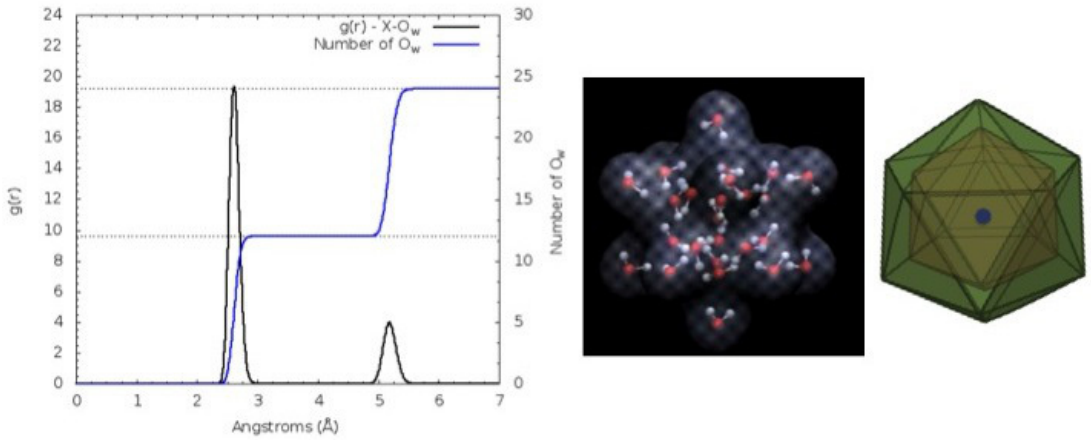

Figure 4.11: Radial Distribution Function between the center of the flexible U_{20} nanocapsule and O_{water} (left). The number of water molecules as a function of the distance to the center of the capsule is also plotted (right axis). The total simulation time was 500ps NVT. The RDF goes to 1 at long distances but is not shown in the plotted range of the x-axis. Moreover, the structure of the two concentric water clusters of I_h symmetry are presented (right)

The encapsulated water is highly ordered as it can be seen in Figure 4.11. In analogy to U_5 a water molecule is present under each pentagonal face corresponding to the second peak at 5.2 Å in the RDF. Most interestingly, 12 additional waters are encapsulated in the internal cavity of U_{20} in a highly ordered I_h symmetry ice-like water cluster. We should note that in this simulation the Na^+ ions were far from the capsule and as a result no cation was able to the capsule. Additional simulations show that Na^+ is small enough to enter the capsule and are able to break the water structure. In analogy with classical giant polyoxomolybdates, we postulate that if a larger counterion unable to enter the capsule were to be used that the inner a water cluster could be isolated in the X-ray crystal structure. [323] Although more simulations are required

to fully explore the manner in which counterions interact with the capsule, we have observed three different interaction sites thus far. In particular, the Na^+ ion interacts with the pentagonal face either outside the capsule, inside the capsule displacing one of the outermost waters inside the cluster, or further inside the capsule displacing the waters in the icosahedron.

4.2.4 Conclusions

We have developed a force field based on *ab initio* calculations on U_1 and U_2 making use of an accurate but computationally inexpensive Born-Huggins-Mayer (BHM) two-body potential. Through a building block approach, this force field can be used to study uranyl-peroxide nanocapsules in aqueous solution. This force field can be extended to other linking groups in a straight-forward manner. Simulations of small units (U_1, U_2 and U_5) are consistent with solution and solid state data for uranyl and uranyl peroxide species. The effect of the flexibility of the system on its interaction with solvent molecules was explored and found to be minimal. Furthermore, the U_{20} nanocapsule was also studied with both rigid and flexible models and a highly symmetric water cluster was found to occupy the capsule when Na^+ counterions are far from the capsule.

4.2.5 Acknowledgements

This work was supported by the Materials Science of Actinides Center, an Energy Frontiers Research Center funded by the Office of Science, U.S. Department of Energy, grant No. DE-SC0001089 [B.V. and L.G.]; the National Science Foundation through the University of Minnesota MRSEC under award No. DMR-0819885 [D.M.]; and National Science Foundation grant No. CHE-0952054 [C.J.C. and P.M.].

4.3 Synthesis and Characterization of the First 2D Neptunyl Structure Stabilized by Side-on Cation-Cation Interactions

4.3.1 Introduction

Sullivan et al. first introduced the concept of a cation-cation interaction (CCI) in actinide chemistry after observing unexpectedly short distances between $[U^{VI}O_2]^{2+}$ and $[U^{V}O_2]^{+}$ cations in aqueous solution. [77] Subsequently, analogous interactions have been observed among actinyl cations $[AnO_2]^{n+}$ and also between actinyl cations and transition-metal cations. In actinide chemistry, a CCI occurs if an "yl" O atom of one actinyl ion coordinates a second actinyl ion. CCIs are most common for An^{V} cations, especially Np^{V}, although several compounds with CCIs between $An^{V}I$ actinyl ions have been reported. The CCIs between Np^{V} and U^{V} actinyl cations are important in the disproportionation of An^{V} species, because electron transfer can occur through the bridging oxo species. CCIs increase the complexity of actinide speciation in solution, and the topology and dimensionality of solid-state compounds. [324–328]

Species containing CCIs have been widely characterized in the solid state, in solution, and in melts by using spectroscopic techniques, such as IR/Raman, UV/Vis, large-angle X-ray scattering (LAXS), extended X-ray absorption fine structure (EXAFS), and high-energy X-ray scattering (HEXS). [329–335] In the solid state, the CCI between two $[AnO_2]^{n+}$ cations adopts two forms: the common T-shaped (or end- cations adopts two forms: the common T-shaped (or end-on) and the rare H-shaped (or side-on) interactions. The nature of these interactions cannot be explained by simple electrostatics and is best described by noting that an actinide atom acts as a Lewis acid, whereas an oxo oxygen plays the role of a Lewis base. However, despite the large number of experimental data available, structures containing CCIs cannot be designed *a priori*,

Reproduced from B. Vlaisavljevich, P. Miró, D. Ma, G. E. Sigmon, P. C. Burns, C. J. Cramer, L. Gagliardi

Chemistry – A European Journal **2013**, 19 (9), 2937–3941.

because understanding of the nature of these interactions remains limited.

Herein, the synthesis and characterization of a new sheet structure,$K[(Np^{V}O_2)(OH)_2]$ $2H_2O$ (**1**), which provides a rare example of side-on CCIs, is presented (Figure 4.12). Specifically, this compound is the first to contain a side-on CCI in an extended sheet structure. To date, only two molecular complexes containing a side-on CCI have been reported: $Na_4[(NpO_2)_2C_{12}O_{12}]$ H_2O (**2**) by Couson et al. and $[(Np^{V}O_2)_2(bpy)_2(C_7H_4O_2F)_2]$ (**3**) by Grigoriev et al. [336, 337] These were synthesized under anhydrous conditions, whereas **1** is the first structure with a side-on CCI to be synthesized in water.

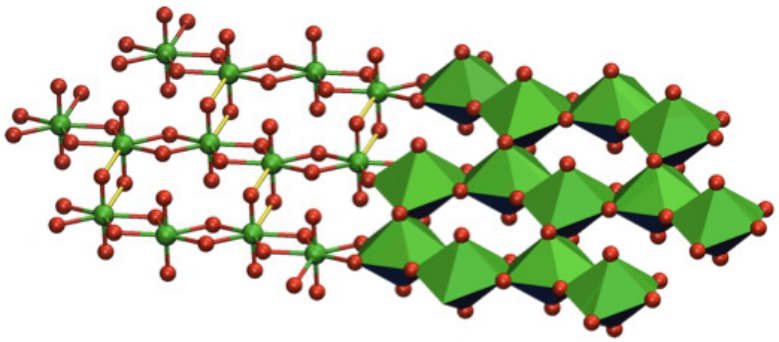

Figure 4.12: Ball-and-stick and polyhedral representations of the X-ray structure of $K[(Np^{V}O_2)(OH)_2]\cdot 2H_2O$. The CCIs are highlighted in yellow. Interstitial water molecules and potassium cations have been omitted for clarity. Color code: Np in green; O in red.

The unit cell of **1** contains a single asymmetrical $[(NpO_2)]^{+}$ cation with Np≡O bond lengths ranging from 1.86 to 1.91 Åand a bond angle of 178.2°. The neptunyl at ion has four hydroxyl ligands and a neptunyl oxo oxygen (CCI) in the equatorial plane. The resulting pentagonal bipyrimid has Np−O(H) bond lengths ranging from 2.38 to 2.52 Å. The X–ray structure of **1** is consistent with previously reported species containing $[NpO_2]$, in which the Np≡O and the equatorial Np≡O bond lengths are approximately 1.84 and 2.46 Å, respectively. [296] Adjacent neptunyl pentagonal bipyramids share edges defined by two hydroxyl groups, forming infinite chains.

Cationcation interactions link the chains into a 2D sheet, in which each neptunyl ion of a given chain accepts a CCI, and donates a CCI, both with a symmetrically identical neptunyl ion of an adjacent chain (Figure 4.12). In contrast to the situation

for the previously reported structures 2 and 3, chelating ligands do not bridge the two neptunyl moieties involved in the side-on CCI. This confirms that the side-on CCI can exist without the presence of chelating bidentate ligands, and that the interaction does not exist due only to ligand stabilization.

The neptunyl sheets in **1** are anionic, and the charge is balanced by interstitial K cations. A single symmetrically distinct K site is located between the oxygen atoms of two adjacent neptunyl cations, as well as a hydroxyl ligand that bridges between them. Five interstitial water molecules complete the coordination sphere of the potassium cation. Each H_2O group is bonded to two K cations, providing bridges between adjacent sheets of neptunyl polyhedra.

The structure of **1** has some features in common with $Na[(Np^{V}O_2)(OH)_2]$. [338, 339] In complex $Na[(Np^{V}O_2)(OH)_2]$, neptunyl pentagonal bipyrimids share equatorial edges defined by hydroxyl groups, forming chains analogous to those in **1**. However, in $Na[(Np^{V}O_2)(OH)_2]$, the chains are linked through end-on CCIs to form a framework with Na^+ cations located within interstitial spaces.

In compounds **2** and **3**, the Np≡O bond lengths are similar and range from 1.81 to 1.91 Å, with the Np≡O corresponding to the CCI interaction ranging from 1.86 to 191 Å. In compounds **1**, **2**, and **3** the netpunyl ions are coordinated by five equatorial ligands. Despite this, **2** and **3** have slightly shorter distances between the two neptunyl moieties involved in the CCI (d_{Np-Np} 3.48 and 3.44 Å, respectively) than **1** (d_{Np-Np} 3.54 Å). Inspired by these small but potentially significant geometric differences, we studied the electronic structure of all three complexes in an effort to probe not only the nature of the side-on CCI, but also the extent to which ligand effects may alter this interaction. Consequently, the electronic structures of these complexes have been studied by using a suite of quantum chemical methods ranging from DFT to high-level multiconfigurational methods, such as the complete active space self-consistent field theory with corrections from second-order perturbation theory complete active-space self-consistent field/second-order perturbation theories (CASSCF/CASPT2) [32–34, 170, 295] and the generalized active-space self-consistent field (GASSCF) theory. [340] Details of the computational study are presented in the Supporting Information.

Of compounds **1**, **2**, and **3** , only **3** contains an isolated CCI complex, whereas **1** and **2** contain neptunyl polyhedra linked into extended structures. The chain topology of **1**

has been truncated to give a model for computations that contains six neptunyl moieties and one CCI (Figure 4.13). Four different clusters were studied : $[(Np^{V}O_2)_6(OH)_8(H_2O)_8]^{2-}$ (**1a**), $K_4[(Np^{V}O_2)_6(OH)_8(H_2O)_8]^{2+}$ (**1b**), $[(Np^{V}O_2)_6(OH)_{16}]^{10-}$ (**1c**), and $K_4[(Np^{V}O_2)_6(OH)_{16}]^{6-}$ (**1d**) to probe the CCI environment. In compound **2**, each carboxyl group in the benzenehexacarboxylic acid coordinates to a neptunyl-neptunyl unit, effectively isolating the CCI in the sheet structure. A single CCI interaction with the four ligands coordinating to the neptunyl moieties included was selected. However, the noncoordinating carboxyl groups on each ligand were replaced with hydrogen atoms, resulting in the model presented in Figure 4.13. Two additional models, $[(Np^{V}O_2)_2(H_2O)_8]^{2+}$ (**4**) and $[(Np^{V}O_2)_2]^{2+}$ (**5**) were also considered. All of the geometries were optimized by using DFT for the highest spin state. ref9

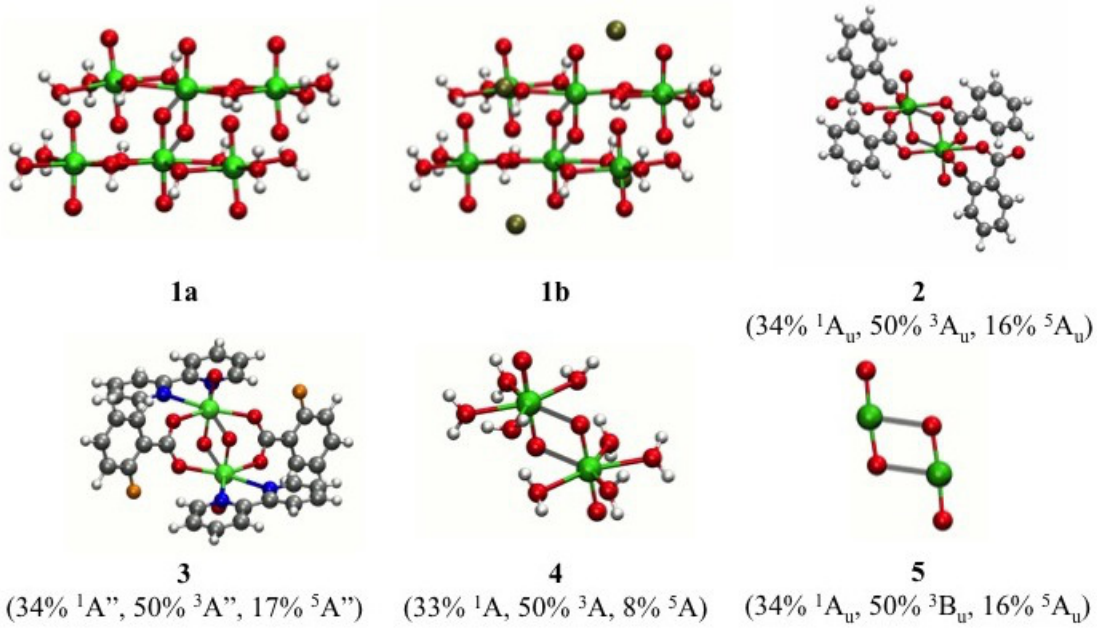

Figure 4.13: Studied species: $[(Np^{V}O_2)_6(OH)_8(H_2O)_8]^{2-}$ **(1a)**, $K_4[(Np^{V}O_2)_6(OH)_8(H_2O)_8]^{2+}$ **(1b)**, $[(Np^{V}O_2)_2(C_7H_5O_2)_4]^{6-}$ **(2)**, $[(Np^{V}O_2)_2(bpy)_2(C_7H_4O_2F)_2]$ **(3)**, $[(Np^{V}O_2)_2(H_2O)_8]^{2+}$ **(4)**, and $[(Np^{V}O_2)_2]^{2+}$ **(5)**. Spinorbit-coupled ground states are given in parentheses. Color code: Np in green; N in blue; O in red; C in grey; F in orange; and K in brown. CCIs are presented in grey.

Geometry optimizations of the model systems were compared with experimental results obtained by single-crystal X-ray diffraction analysis (Table S3 in the Supporting Information). Our model systems have bond lengths and angles winton the Np dimer that are in good agreement with experiment. A comparison of the calculated geometry of **3** with that obtained by X-ray diffraction analysis shows very small deviations of 0.02 Å for bond lengths and 0.7° for angles. Addtionally, model systems **1a-d** and **2** were truncated from extended solids and deviate at the most by 0.11 Å for bond lengths and 1.9° for the angles from the X-ray diffraction data.

Although the model systems **1a-d** are computationally intractable at our highest level of theory, multiconfigurational CASSCF/CASPT2 calculations were performed on

the other complexes (**2**-**5**) to investigate ligand effects relative to the CCI. [32–34, 170, 295] Each neptunyl moiety has a $5f^2$ configuration on the metal center, and CASPT2 indicated degenerate singlet, triplet, and quintet states for the dimer. The spin-orbit ground states are similar regardless of model choice with the largest contribution coming from the triplet in all cases (Figures 4.13 and 4.14; for details, see the Supporting Information).

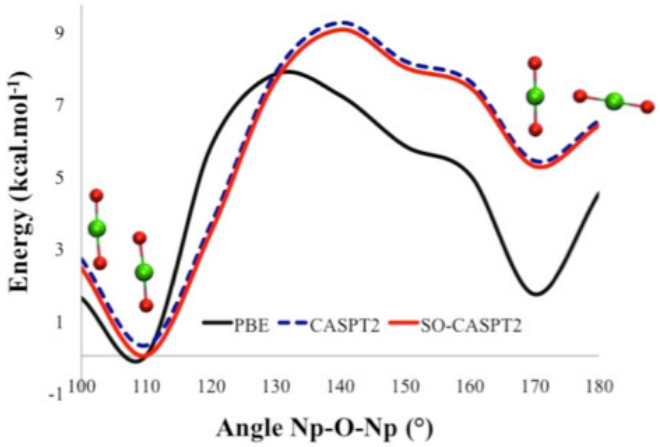

Figure 4.14: Constrained potential energy surface for the PBE/def-TZVP energies (^{5}A), CASPT2 (^5A_g), and SO-CASPT2 states.

Based on the computed results, we can conclude that although the ligands studied are chemically very different, none possess a ligand field strong enough to break the degeneracies in the pure-spin states or to alter the electronic structure of the spin-orbit ground state. A scan of one potential energy surface connecting the side-on CCI to the end-on CCI was performed, and the pure-spin contributions to the spin-orbit ground state remained the same at all points (Figure 4.14). Although magnetic measurements were not available for **1**, several neptunyl compounds with CCIs underwent magnetic ordering at low temperatures. [338, 339, 341–343] We contend that the coupling of the ground-state spin through the CCI could contribute to the antiferromagnetic ordering in these species.

To probe the nature of the CCI, the topology of the electron density from DFT calculations for the high spin states of complexes **1** to **5** was analyzed. Topological

analysis of the electron density revealed two bond critical points (BCP) between the neptunium centers and the oxygen atoms in the second moiety. These interactions are ionic in nature, because the Laplacian at the BCP is positive, but the energy density is slightly negative, which points to some dative character as well. No relevant electron density topology indicative of a Np−Np direct bond was found between the two neptunium centers. All of the parameters derived from the topological analysis of the electron density are presented in the Supporting Information.

To confirm the Lewis acid/base description of the CCI bond, the extended transition state (ETS) method combined with natural orbitals for chemical valence (NOCV) theory was used to study the CCI bonding in **4** and **5** (Figure 4.15). [344, 345] ETS–NOCV partitions the total energy into contributions from each natural orbital. The natural orbitals revealed that the CCI is a donation from the occupied O 2p orbitals of the neptunyl ion to the empty 6d orbitals of the Np center. This is in agreement with the generally accepted idea that CCIs are an acid/base interaction, in which the neptunium and oxygen ligands assume the roles of a Lewis acid and Lewis base, respectively (see the Supporting Information for details). In all the studied species, two natural orbitals were identified as having Np−O interactions between the neptunyl ions with contributions of −16.9/−11.4 and −12.8/−7.8 kcal/mol for **4** and **5**, respectively. All of the other natural orbital interactions contribute less than 5 kcal/mol.

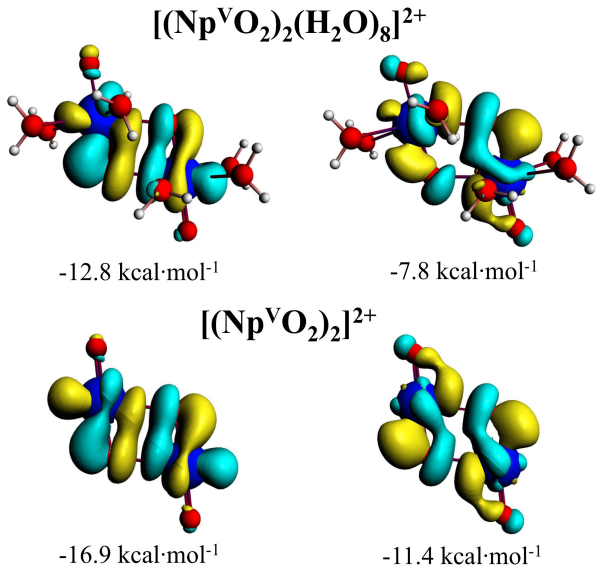

Figure 4.15: Natural orbitals for chemical valence (NOCV) with the largest contributions to the total CCI bonding energy for **4** and **5**.

Furthermore, the shared electron number between the Np and other O involved in the CCI was computed, because this can be used to evaluate the strength of the interaction. [346] Independently of the chosen cluster model, compound **1** was predicted to have stronger CCIs with shared electron numbers of approximately 0.2 compared to all of the other species that have values of approximately 0.08, which suggest a higher stability of the CCI in **1**.

In conclusion, the synthesis and characterization of the first 2D neptunyl structure stabilized by side-on cation cation interactions was present. The chains in $K[(Np^{V}O_2)(OH)_2].2H_2O$ are linked into an extended sheet by CCIs. In contrast with side-on CCIs previously reported, the interaction in **1** is not induced/stabilized by ligands (i.e., through chelation).

Analysis of the electronic structure of **1** showed no direct Np−Np bond. Bonding in the CCI is intend localized between the neptunium and oxo centers of adjacent neptunyl moeties. In general, the electronic structure of the CCI is not sensitive to the neptunyl equatorial ligands. CASSCF/CASPT2 and GASSCF calculations revealed that the unpaired 5f electrons localized on the neptunium centers couple in a spin-orbit ground

state composed of singlet (34%), triplet (50%), and quintet (16%) pure-spin states for all of the systems studied. Furthermore, the side-on CCI has a closed shell interaction and is best thought of as a Lewis acid/base interaction independent of the neptunyl equatorial ligands.

4.3.2 Experimental Section

Synthesis: CAUTION!!! Neptunium and its daughter products are radioactive and should only be handled by trained personnel in appropriate facilities.

A stock solution of Np^V was prepared by purifying the neptunium by using a cation-exchange column containing Dowex-50-X8 resin. The neptunium was dissolved in hydrochloric acid (1 M) to a concentration of 102 mmil Np^V. A Jasco UV/Vis spectrometer was used to confirm the oxidation state of the Np^V stock solution. In a glass vial, aqueous KOH (0.600 mL, 2 M) and hydrogen peroxide (0.200 mL, 30%) were combined, followed by the addition of Np^V stock solution (0.207 mL, 102 mmol) in HCl (1= M). The vial was covered with Parafilm containing two small holes to facilitate slow evaporation in air. The initial solution was dark red, and over five days it became colorless with a green-brown fine-grained precipitate. Approximately ten black crystals of $K[(Np^VO_2)(OH)_2].2H_2O$ were formed and obtained for crystallographic studies. The total yield of $K[(Np^VO_2)(OH)_2].2H_2O$ was less than 10% based on neptunium. We attempted to increase the yield in subsequent synthesis without success. A Bruker SMART APEX II CCD diffractometer with graphite-mono- chromatized Mo_{Ka} radiation was used to collect a sphere of three-dimensional diffraction data for a crystal of $K[(Np^VO_2)(OH)_2].2H_2O$. A semi-empirical absorption correction was applied by modeling the crystal as an ellipsoid by using the Bruker program XPREP. The structure was solved by direct methods and refined in space group P1. The Bruker SHELXL Version 5 system of programs was used to solve and refine the crystal structure. Refinement was straightforward, with the final cycles including the atomic positional parameters for all atoms including hydrogen and anisotropic displacement parameters for all nonhydrogen atoms. Np sheet : space group : P1; a = 5.826(2), b = 5.933(2), c = 9.217(3) Å; R1 = 3.78% for 1347 $F_o \geq 4\sigma F_o$; S=1.044; 1411 refined parameters; wR_2 = 9.68%.

4.3.3 Computational Details

Geometry optimizations were performed with DFT by using the PerdewBurkeErnzerhof (PBE) exchange-correlation functional with def-TZVP basis sets [96, 162, 164, 165, 315] for all atoms by using Turbomole 5.9. The broken-symmetry singlet and high-spin quintet were explored for **2**-**5**, whereas for **1**, only the high-spin state was studied. To further analyze the DFT results, single-point calculations were performed on the optimized geometries by using the Amsterdam Density Functional (ADF 2010.02) program. We used the hybrid implementation of the PBE functional (PBE0) and the TZ2P basis set. [50, 314, 347]The ETS method combined with NOCV theory was used. [344, 345] When feasible, CASSCF with CASPT2 [32–34, 170, 295] and GASSCF [340] calculations were performed with ANO-RCC basis sets by using Molcas 7.7. Spinorbit coupling was included a posteriori by using the SO-CASPT2 approach. [31, 37] See the Supporting Information for complete computational details and a discussion of the active-space choice.

4.3.4 Acknowledgements

This work was supported by the Chemical Sciences, Geosciences, and Biosciences Division, Office of Basic Energy Sciences, Office of Science, U.S., Department of Energy (grant No. DE-FG0207ER15880 [P.C.B. and G.E.S.]; U.S. Department of Energy, Office of Basic Energy Sciences, Heavy Element Chemistry Program under grant No. DESC002183 [L.G.]; the Materials Science of Actinides Center, an Energy Frontiers Research Center funded by the Office of Science, U.S. Department of Energy, grant No. DE-SC0001089 [B.V.]; the National Science Foundation through the University of Minnesota MRSEC under award No. DMR-0819885 [D.M.]; and National Science Foundation grant No. CHE-0952054 [C.J.C. and P.M.] .

References

[1] Morrs, L. R., Edelstein, N. M., Fuger, J., and Katz, J. J. (eds.) (2006) *The Chemistry of the Actinide and Transactinide Elements*. Springer.

[2] Runde, W. (2000) The Chemical Interactions of Actinides in the Enviorment. *Los Alamos Science*, **26**, 392–410.

[3] Burns, P. C. and Sigmon, G. E. (eds.) (2013) *Uranium: Cradle to Grave*, vol. 43 of *Short Course Series*. Mineralogical Association of Canada (MAC).

[4] Bell, J. W. (2009) A Radioactive Topic. *Access*, pp. 23–25.

[5] Taira, T. and Hatoyama, Y. (2011) Nuclear Energy: Nationalize the Fukushima Daiichi Atomic Plant. *Nature*, **480**, 313–314.

[6] (2012), Nuclear Share of Electricity Generation in 2012. Reported by the International Atomic Energy Agency (IAEA).

[7] (2013), Under Construction Reactors. Reported by the International Atomic Energy Agency (IAEA).

[8] Anderson, H. and Asprey, L. B. (1960), Solvent Extraction Process for Uranium. US Patent 2924506.

[9] Arnold, P. L. (2011) Uranium-Mediated Activation of Small Molecules. *Chem. Commun.*, **47**, 9005–9010.

[10] Fox, A. R., Bart, S. C., Meyer, K., and Cummins, C. C. (2008) Towards Uranium Catalysts. *Nature*, **455**, 341–349.

[11] Hayes, C. E. and Leznoff, D. B. (2010) Diamido-Ether Uranium(IV) Alkyl Complexes as Single-Component Ethylene Polymerization Catalysts. *Organomet.*, **29**, 767–774.

[12] Evans, W. J., Kozimor, S. A., Ziller, J. W., and Kaltsoyannis, N. (2004) Structure, Reactivity, and Density Functional Theory Analysis of the Six-Electron Reductant, $[(C_5Me_5)_2U]_2(\mu\text{-}\eta^6\text{:}\eta^6\text{-}C_6H_6)$, Synthesized via a New Mode of $(C_5Me_5)_3M$ Reactivity. *J. Am. Chem. Soc.*, **126**, 14533–14547, pMID: 15521774.

[13] Burns, C. J. (2005) Bridging a Gap in Actinide Chemistry. *Science*, **309**, 1823–1824.

[14] Evans, W. J., Kozimor, S. A., and Ziller, J. W. (2005) Molecular Octa-Uranium Rings with Alternating Nitride and Azide Bridges. *Science*, **309**, 1835–1838.

[15] Hayton, T. W., Boncella, J. M., Scott, B. L., Batista, E. R., and Hay, P. J. (2006) Synthesis and Reactivity of the Imido Analogues of the Uranyl Ion. *J. Am. Chem. Soc.*, **128**, 10549–10559.

[16] Ephritikhine, M. (2006) The Vitality of Uranium Molecular Chemistry at the Dawn of the XXIst Century. *Dalton Trans.*, pp. 2501–2516.

[17] Cantat, T., Arliguie, T., Noel, A., Thuery, P., Ephritikhine, M., Le Floch, P., and Mezailles, N. (2009) The U=C Double Bond: Synthesis and Study of Uranium Nucleophilic Carbene Complexes. *J. Am. Chem. Soc.*, **131**, 963–972.

[18] Arney, D. S. J., Schnabel, R. C., Scott, B. C., and Burns, C. J. (1996) Preparation of Actinide Phosphinidene Complexes: Steric Control of Reactivity. *J. Am. Chem. Soc.*, **118**, 6780–6781.

[19] Hunt, R. D., Yustein, J. T., and Andrews, L. (1993) Matrix Infrared-Spectra of NUN Formed by the Insertion of Uranium Atoms into Molecular Nitrogen. *J. Chem. Phys.*, **98**, 6070–6074.

[20] Kushto, G. P., Souter, P. F., and Andrews, L. (1998) An Infrared Spectroscopic and Quasirelativistic Theoretical Study of the Coordination and Activation of Dinitrogen by Thorium and Uranium Atoms. *J. Chem. Phys.*, **108**, 7121–7130.

[21] Souter, P. F., Kushto, G. P., Andrews, L., and Neurock, M. (1997) Experimental and Theoretical Evidence for the Formation of Several Uranium Hydride Molecules. *J. Am. Chem. Soc.*, **119**, 1682–1687.

[22] Sankaran, K., Sundararajan, K., and Viswanathan, K. S. (1999) A Matrix Isolation FTIR Investigation of Laser-Ablated Uranium Oxide in Argon and Nitrogen Matrices. *Bull. Mater. Sci.*, **22**, 785–790.

[23] Kushto, G. P., Souter, P. F., Andrews, L., and Neurock, M. (1997) A Matrix Isolation FT-IR and Quasirelativistic Density Functional Theory Investigation of the Reaction Products of Laser-Ablated Uranium Atoms with NO, NO_2 and N_2O. *J. Chem. Phys.*, **106**, 5894–5903.

[24] Zhou, M. F. and Andrews, L. (1999) Infrared Spectra and Pseudopotential Calculations for NUO^+, NUO, and NThO in Solid Neon. *J. Chem. Phys.*, **111**, 11044–11049.

[25] Wang, X., Andrews, L., and Marsden, C. J. (2008) Reactions of Uranium Atoms with Ammonia: Infrared Spectra and Quasi-Relativistic Calculations of the U:NH_3, H_2N-UH, and HN=UH_2 Complexes. *Chem. Eur. J.*, **14**, 9192–9201.

[26] Andrews, L., Wang, X., Lindh, R., Roos, B. O., and Marsden, C. J. (2008) Simple NUF_3 and PUF_3 Molecules with Triple Bonds to Uranium. *Angew. Chem. Int. Ed.*, **47**, 5366–5370.

[27] Lyon, J. T., Andrews, L., Malmqvist, P.-A., Roos, B. O., Yang, T., and Bursten, B. E. (2007) Infrared Spectrum and Bonding in Uranium Methylidene Dihydride, CH_2=UH_2. *Inorg. Chem.*, **46**, 4917–4925.

[28] Roos, B. O., Lindh, R., Cho, H.-G., and Andrews, L. (2007) Agostic Interaction in the Methylidene Metal Dihydride Complexes H_2MCH_2 (M = Y, Zr, Nb, Mo, Ru, Th, or U). *J. Phys. Chem. A*, **111**, 6420–6424.

[29] Green, D. W. and Reedy, G. T. (1976) Identification of UN in Ar Matrices. *J. Chem. Phys.*, **65**, 2921–2922.

[30] Roos, B. O. (1987) The Complete Active Space Self-Consistent Field Method and its Applications in Electronic Structure Calculations. Lawley, K. P. (ed.), *Advances in Chemical Physics; Ab Initio Methods in Quantum Chemistry–II*, New York, p. 399, John Wiley & Sons Ltd.

[31] Roos, B. O. and Malmqvist, P. A. (2004) Relativistic Quantum Chemistry: The Multiconfigurational Approach. *Phys. Chem. Chem. Phys.*, **6**, 2919–2927.

[32] Roos, B. O., Taylor, P. R., and Siegbahn, P. E. M. (1980) A Complete Active Space SCF Method (CASSCF) Using a Density-Matrix Formulated Super-CI Approach. *Chem. Phys.*, **48**, 157–173.

[33] Andersson, K., Malmqvist, P. A., and Roos, B. O. (1992) 2nd-Order Perturbation-Theory with a Complete Active Space Self-Consistent Field Reference Function. *J. Chem. Phys.*, **96**, 1218–1226.

[34] Andersson, K., Malmqvist, P. A., Roos, B. O., Sadlej, A. J., and Wolinski, K. (1990) 2nd-Order Perturbation-Theory with a CASSCF Reference Function. *J. Phys. Chem.*, **94**, 5483–5488.

[35] Veryazov, V., Malmqvist, P. A., and Roos, B. O. (2011) How to Select Active Space for Multiconfigurational Quantum Chemistry? *Int. J. Quantum Chem.*, **111**, 3329–3338.

[36] Gagliardi, L. and Roos, B. O. (2007) Multiconfigurational Quantum Chemical Methods for Molecular Systems Containing Actinides. *Chem. Soc. Rev.*, **36**, 893–903.

[37] Malmqvist, P. A., Roos, B. O., and Schimmelpfennig, B. (2002) The Restricted Active Space (RAS) State Interaction Approach with Spin-Orbit Coupling. *Chem. Phys. Lett.*, **357**, 230–240.

[38] Roos, B. O., Malmqvist, P.-A., and Gagliardi, L. (2006) Exploring the Actinide-Actinide Bond: Theoretical Studies of the Chemical Bond in Ac_2, Th_2, Pa_2, and U_2. *J. Am. Chem. Soc.*, **128**, 17000–17006.

[39] Fohlmeister, L., Liu, S., Schulten, C., Moubaraki, A., B an Stasch, Cashion, J. D., Murray, K. S., Gagliardi, L., and Jones, C. (2012) Low-Coordinate Iron(I) and Manganese(I) Dimers: Kinetic Stabilization of an Exceptionally Short Fe–Fe Multiple Bond. *Angew. Chem. Int. Ed.*, **51**, 8294–8298.

[40] Vlaisavljevich, B., Miró, P., Cramer, C. J., Gagliardi, L., Infante, I., and Liddle, S. T. (2011) On the Nature of Actinide– and Lanthanide–Metal Bonds in Heterobimetallic Compounds. *Chem. Eur. J.*, **17**, 8424–8433.

[41] Vlaisavljevich, B., Gagliardi, L., Wang, X., Liang, B., Andrews, L., and Infante, I. (2010) U and P_4 Reaction Products: A Quantum Chemical and Matrix Isolation Spectroscopic Investigation. *Inorg. Chem.*, **49**, 9230–9235.

[42] Li, J., Bursten, B. E., Liang, B., and Andrews, L. (2001) Noble Gas-Actinide Compounds: Complexation of the CUO Molecule by Ar, Kr, and Xe Atoms in Noble Gas Matrices. *Science*, **295**, 2242–2245.

[43] Roos, B. O., Widmark, P. O., and Gagliardi, L. (2003) The Ground State and Electronic Spectrum of CUO: A Mystery. *Faraday Discuss.*, **124**, 57–62.

[44] Thomson, R. K., Cantat, T., Scott, B. L., Morris, D. E., Batista, E. R., and Kiplinger, J. L. (2010) Uranium Azide Photolysis Results in C-H Bond Activation and Provides Evidence for a Terminal Uranium Nitride. *Nat. Chem.*, **2**, 723–729.

[45] Vlaisavljevich, B., Diaconescu, P. L., Lukens, W. L., Gagliardi, L., and Cummins, C. C. (2013) Investigations of the Electronic Structure of Arene–Bridged Diuranium Complexes. *Organometallics*, **32**, 1341–1352.

[46] Bader, R. F. W. (1998) A Bond Path: A Universal Indicator of Bonded Interactions. *J. Phys. Chem. A*, **102**, 7314–7323.

[47] Bader, R. F. W. (1990) *Atoms in Molecules: A Quantum Theory*. Clarendon Press.

[48] Mayer, I. (1983) Charge, Bond Order and Valence in the Ab Initio SCF Theory. *Chem. Phys. Lett.*, **97**, 270–274.

[49] Bridgeman, A. J., Cavigliasso, G., Ireland, L. R., and Rothery, J. (2001) The Mayer Bond Order as a Tool in Inorganic Chemistry. *J. Chem. Soc. Dalton Trans.*, pp. 2095–2108.

[50] te Velde, G., Bickelhaupt, F. M., Baerends, E. J., Guerra, C. F., Van Gisbergen, S. J. A., Snijders, J. G., and Ziegler, T. (2001) Chemistry with ADF. *J. Comput. Chem.*, **22**, 931–967.

[51] Neidig, M. L., Clark, D. L., and Martin, R. L. (2013) Covalency in f-Element Complexes. *Coord. Chem. Rev.*, **257**, 394–406.

[52] Kaltsoyannis, N. (1999) *The f Elements*. Oxford University Press.

[53] Nash, K. L. (1999) *Metal-Ion Separation and Preconcentration: Progress and Opportunities*. Oxford University Press.

[54] Choppin, G. R. (1983) Solution Chemistry of the Actinides. *Radiochim. Acta*, **32**, 43–53.

[55] Aspinall, H. C. (2001) *Chemistry of the f-Block Elements*. Gordon and Breach Publishers.

[56] Nash, K. L. and Choppin, G. R. (1997) Separations Chemistry for Actinide Elements: Recent Developments and Historical Perspective. *Sep. Sci. Technol.*, **32**.

[57] Nash, K. L. (1993) *Solv. Extr. Ion Exch.*, **11**, 729–768.

[58] Weaver, B. and Kappelmann, F. A. (1964), Talspeak: A New Method of Separating Americium and Curium from the Lanthanides by Extraction from an Aqueous Solution of an Aminopolyacetic Acid Complex with a Monoacidic Organophosphate or Phosphonate, Oak Ridge National Laboratory.

[59] Choppin, G. R. (2002) Covalency in f-Element Bonds. *J. Alloys Compd.*, **344**, 55–59.

[60] Denning, R. G. (1992) Electronic Structure and Bonding in Actinyl Ions. *Struct. Bond.*, **79**, 215–276.

[61] Burns, C. J. and Bursten, B. E. (1989) Comments. *Inorg. Chem.*, **9**, 61.

[62] Gardner, B. M., McMaster, J., Lewis, W., and Liddle, S. T. (2009) Synthesis and Structure of $[N(CH_2CH_2NSiMe_3)_3URe(\eta^5\text{-}C_5H_5)_2]$: A Heterobimetallic Complex with an Unsupported Uranium-Rhenium Bond. *Chem. Commun.*, pp. 2851–2853.

[63] Liddle, S. T., McMaster, J., Mills, D. P., Blake, A. J., Jones, C., and Woodul, W. D. (2009) σ and π Donation in an Unsupported Uranium-Gallium Bond. *Angew. Chem. Int. Ed.*, **48**, 1077–1080.

[64] Burns, P. C. and Kubatko, K. A. (2003) Studtite, $[(UO_2)(O_2)(H_2O)_2](H_2O)_2$: The First Structure of a Peroxide Mineral. *Am. Mineral.*, **88**, 1165–1168.

[65] Burns, P. C., Kubatko, K. A., Sigmon, G., Fryer, B. J., Gagnon, J. E., Antonio, M. R., and Soderholm, L. (2005) Actinyl Peroxide Nanospheres. *Angew. Chem. Int. Ed.*, **44**, 2135–2139.

[66] Qiu, J. and Burns, P. C. (2013) Clusters of Actinides with Oxide, Peroxide, or Hydroxide Bridges. *Chem. Rev.*, **113**, 1097–1120.

[67] Unruh, D. K., Burtner, A., Pressprich, L., Sigmon, G. E., and Burns, P. C. (2010) Uranyl Peroxide Closed Clusters Containing Topological Squares. *Dalton Trans.*, **39**, 5807–5813.

[68] Sigmon, G. E., Ling, J., Unruh, D. K., Moore-Shay, L., Ward, M., Weaver, B., and Burns, P. C. (2009) Uranyl-Peroxide Interactions Favor Nanocluster Self-Assembly. *J. Am. Chem. Soc.*, **131**, 16648–16649.

[69] Qiu, J., Nguyen, K., Jouffret, L., Szymanowski, J. E. S., and Burns, P. C. (2013) Time-Resolved Assembly of Chiral Uranyl Peroxo Cage Clusters Containing Belts of Polyhedra. *Inorg. Chem.*, **52**, 337–345.

[70] Ling, J., Qiu, J., Sigmon, G. E., Ward, M., Szymanowski, J. E. S., and Burns, P. C. (2010) Uranium Pyrophosphate/Methylenediphosphonate Polyoxometalate Cage Clusters. *J. Am. Chem. Soc.*, **132**, 13395–13402.

[71] Ling, J., Wallace, C. M., Szymanowski, J. E. S., and Burns, P. C. (2010) Hybrid Uranium-Oxalate Fullerene Topology Cage Clusters. *Angew. Chem. Int. Ed.*, **49**, 7271–7273.

[72] Ling, J., Qiu, J., Szymanowski, J. E. S., and Burns, P. C. (2011) Low-Symmetry Uranyl Pyrophosphate Cage Clusters. *Chem. Eur. J.*, **17**, 2571–2574.

[73] Ling, J., Qiu, J., and Burns, P. C. (2012) Uranyl Peroxide Oxalate Cage and Core–Shell Clusters Containing 50 and 120 Uranyl Ions. *Inorg. Chem.*, **51**, 2403–2408.

[74] Armstrong, C. R., Nyman, M., Shvareva, T., Sigmon, G. E., Burns, P. C., and Navrotsky, A. (2011) Uranyl Peroxide Enhanced Nuclear Fuel Corrosion in Seawater. *Proc. Natl. Acad. Sci. USA*, **109**, 1874–1877.

[75] Vlaisavljevich, B., Gagliardi, L., and Burns, P. C. (2010) Understanding the Structure and Formation of Uranyl Peroxide Nanoclusters by Quantum Chemical Calculations. *J. Am. Chem. Soc.*, **132**, 14503–14508.

[76] Miró, P., Pierrefixe, S., Gicquel, M., Gil, A., and Bo, C. (2010) On the Origin of the Cation Templated Self-Assembly of Uranyl-Peroxide Nanoclusters. *J. Am. Chem. Soc.*, **132**, 17787–17794.

[77] Sullivan, J. C., Zielen, A. J., and Hindman, J. C. (1961) Specific Interaction between Np(V) and U(VI) in Aqueous Perchloric Acid Media. *J. Am. Chem. Soc.*, **83**, 3373–3378.

[78] Miró, P. and Bo, C. (2012) Uranyl-Peroxide Nanocapsules: Electronic Structure and Cation Complexation in $[(UO_2)_{20}(\mu\text{-}O_2)_{30}]^{20-}$. *Inorganic Chemistry*, **51**, 3840–3845.

[79] Gil, A., Karhánek, D., Miró, P., Antonio, M. R., Nyman, M., and Bo, C. (2012) A Journey Inside the U_{28} Nanocapsule. *Chem. Eur. J.*, **18**, 8340–8346.

[80] Gagliardi, L. and Pyykko, P. (2004) Theoretical Search for Very Short Metal-Actinide Bonds: NUIr and Isoelectronic Systems. *Angew. Chem. Int. Ed.*, **43**, 1573–1576.

[81] Brennan, J. G. and Andersen, R. A. (1985) Electron-transfer reactions of trivalent uranium - preparation and structure of (mec5h4)3u=nph and [(mec5h4)3u]2mu-eta-1,eta-2-phnco]. *J. Am. Chem. Soc.*, **107**, 514–516.

[82] Hayton, T. W., Boncella, J. M., Scott, B. L., Palmer, P. D., Batista, E. R., and Hay, P. J. (2005) Synthesis of Imido Analogs of the Uranyl Ion. *Science*, **310**, 1941–1943.

[83] Liang, B. Y., Andrews, L., Ismail, N., and Marsden, C. J. (2002) The First Infrared Spectra and Quasirelativistic DFT Studies of the US, US_2, and US_3 Molecules. *Inorg. Chem.*, **41**, 2811–2813.

[84] Unpublished neon matrix spectrum of US_2 reveals the antisymmetric stretching mode at 442.3 cm^{-1}.

[85] Hunt, R. D. and Andrews, L. (1993) Reactions of Pulsed-Laser Evaporated Uranium Atoms with Molecualar-Oxygen - Infrared-Spectra of UO, UO_2, UO_3, UO^{2+}, $UO_2{}^{2+}$, and UO_3-o_2 in Solid Argon. *J. Chem. Phys.*, **98**, 3690–3696.

[86] Zhou, M. F., Andrews, L., Ismail, N., and Marsden, C. (2000) Infrared Spectra of UO_2, $UO_2{}^+$, and $UO_2{}^-$ in Solid Neon. *J. Phys. Chem. A*, **104**, 5495–5502.

[87] Cossairt, B. M., Piro, N. A., and Cummins, C. C. (2010) Early-Transition-Metal-Mediated Activation and Transformation of White Phosphorus. *Chem. Rev.*, **110**, 4164–4177.

[88] Caporali, M., Gonsalvi, L., Rossin, A., and Peruzzini, M. (2010) P_4 Activation by Late-Transition Metal Complexes. *Chem. Rev.*, **110**, 4178–4235.

[89] Scheer, M., Balázs, G., and Seitz, A. (2010) P_4 Activation by Main Group Elements and Compounds. *Chem. Rev.*, **110**, 4236–4256.

[90] Andrews, L. (2004) Matrix Infrared Spectra and Density Functional Calculations of Transition Metal Hydrides and Dihydrogen Complexes. *Chem. Soc. Rev.*, **33**, 123–132.

[91] Andrews, L. and Cho, H.-G. (2006) Matrix Preparation and Spectroscopic and Theoretical Investigations of Simple Methylidene and Methylidyne Complexes of Group 4-6 Transition Metals. *Organomet.*, **25**, 4040–4053.

[92] Withnall, R. and Andrews, L. (1988) Matrix Reactions of Oxygen-Atoms with P_4 - Infrared-Spectra of P_4O, P_2O, PO, and PO_2. *J. Am. Chem. Soc.*, **110**, 5605–5611.

[93] Frisch, M. J., et al. (2009). Gaussian 09 Revision A.1, Gaussian Inc. Wallingford CT.

[94] Becke, A. D. (1993) Density-functional Thermochemistry .3. The role of Exact Exchange. *J. Chem. Phys.*, **98**, 5648–5652.

[95] Lee, C. T., Yang, W. T., and Parr, R. G. (1988) Development of the Colle-Salvetti Correlation-Energy Formula into a Functional of the Electron-Density. *Phys. Rev. B*, **37**, 785–789.

[96] Perdew, J. P., Burke, K., and Ernzerhof, M. (1996) Generalized gradient approximation made simple. *Phys. Rev. A*, **77**, 3865–3868.

[97] Becke, A. D. (1997) Density-functional Thermochemistry .5. Systematic Optimization of Exchange-Correlation Functionals. *J. Chem. Phys.*, **107**, 8554–8560.

[98] Perdew, J. P., Burke, K., and Wang, Y. (1996) Generalized Gradient Approximation for the Exchange-Correlation Hole of a Many-Electron System. *Phys. Rev. B*, **54**, 16533–16539.

[99] Frisch, M. J., Pople, J. A., and Binkley, J. S. (1984) Self-Consistent Molecular Orbital Methods .25. Supplementary Functions for Gaussian-Basis Sets. *J. Chem. Phys.*, **80**, 3265–3269.

[100] Kuchle, W., Dolg, M., Stoll, H., and Preuss, H. (1994) Energy-Adjusted Pseudopotentials for the Actinides - Parameter Sets and Test Calculations for Thorium and Thorium Monoxide. *J. Chem. Phys.*, **100**, 7535–7542.

[101] Roos, B. O., Lindh, R., Malmqvist, P. A., Veryazov, V., and Widmark, P. O. (2005) New Relativistic ANO Basis Set for Transition Metal Atoms. *J. Phys. Chem. A*, **109**, 6575–6579.

[102] Gagliardi, L. and Roos, B. O. (2000) Uranium Triatomic Compounds XUY (X,Y = C,N,O): A Combined Multiconfigurational Second-Order Perturbation and Density Functional Study. *Chem. Phys. Lett.*, **331**, 229–234.

[103] Gagliardi, L., La Manna, G., and Roos, B. O. (2003) On the Reaction of a Uranium Atom with a Nitrogen Molecule: A Theoretical Attempt. *Faraday Discuss.*, **124**, 63–68.

[104] Gagliardi, L. (2003) When Does Gold Behave as a Halogen? Predicted Uranium Tetraauride and Other MAu_4 Tetrahedral Species, (M = Ti, Zr, Hf, Th). *J. Am. Chem. Soc.*, **125**, 7504–7505.

[105] Gagliardi, L. and Cramer, C. J. (2006) Quantum Chemical Characterization of the Bonding of N-Heterocyclic Carbenes to Cp_2M^I Compounds [M = Ce(III), U(III)]. *Inorg. Chem.*, **45**, 9442–9447.

[106] Infante, I., Gagliardi, L., and Scuseria, G. E. (2008) Is Fullerene C_{60} Large Enough to Host a Multiply Bonded Dimetal? *J. Am. Chem. Soc.*, **130**, 7459–7465.

[107] Infante, I., Raab, J., Lyon, J. T., Liang, B., Andrews, L., and Gagliardi, L. (2007) Experimental and Theoretical Evidence for $U(C_6H_6)$ and $Th(C_6H_6)$ Complexes. *J. Phys. Chem. A*, **111**, 11996–12000.

[108] Infante, I., Gagliardi, L., Wang, X., and Andrews, L. (2009) Binding Motifs for Lanthanide Hydrides: A Combined Experimental and Theoretical Study of the $MH_x(H_2)_y$ Species (M = La-Gd; x=1-4; y=0-6). *J. Phys. Chem. A*, **113**, 2446–2455.

[109] Huber, K. P. and Herzber, G. (1979) *Constants of Diatomic Molecules*. Van Nostrand Reinhold.

[110] Jacox, M. E. (2003) Vibrational and Electronic Energy Levels of Polyatomic Transient Molecules. Supplement B. *J. Phys. Chem. Ref. Data*, **32**, 1–441.

[111] Cotton, F. A., Wilkinson, G., Murillo, C. A., and Bochman, M. (1999) *Advanced Inorganic Chemistry*. Wiley, 6th edn.

[112] Lyon, J. T., Hu, H.-S., Andrews, L., and Li, J. (2007) Formation of Unprecedented Actinide Carbon Triple Bonds in Uranium Methylidyne Molecules. *Proc. Natl. Acad. Sci. USA*, **104**, 18919–18924.

[113] Zhou, M. F., Andrews, L., Li, J., and Bursten, B. E. (1999) Reaction of Laser-Ablated Uranium Atoms with CO: Infrared Spectra of the CUO, CUO^-, OUCCO, (η^2-C-2)UO_2, and U$(CO)_x$ (x=1-6) Molecules in Solid Neon. *J. Am. Chem. Soc.*, **121**, 9712–9721.

[114] Fox, A. R., Wright, R. J., Rivard, E., and Power, P. P. (2005) Tl-2[Aryl$_2$)P_4]: A Thallium Complexed Diaryltetraphosphabutadienediide and its Two-Electron Oxidation to a Diaryltetraphosphabicyclobutane, Aryl$_2P_4$. *Angew. Chem. Int. Ed.*, **44**, 7729–7733.

[115] Caporali, M., Di Vaira, M., Peruzzini, M., Seniori Costantini, S., Stoppioni, P., and Zanobini, F. (2010) Synthesis, Characterization and Hydrolysis of Osmium Tetraphosphorus Complexes. *Eur. J. Inorg. Chem.*, **2010**, 152–158.

[116] Pyykko, P., Riedel, S., and Patzschke, M. (2005) Triple-Bond Covalent Radii. *Chem. Eur. J.*, **11**, 3511–3520.

[117] Pyykko, P. and Atsumi, M. (2009) Molecular Double-Bond Covalent Radii for Elements Li-E112. *Chem. Eur. J.*, **15**, 12770–12779.

[118] Graves, C. R., et al. (2008) Organometallic Uranium(V)-Imido Halide Complexes: From Synthesis to Electronic Structure and Bonding. *J. Am. Chem. Soc.*, **130**, 5272–5285.

[119] Odom, A. L. (1998) Ph.D. thesis, Massachusetts Institute of Technology, Cambridge, MA.

[120] Stevens, R. C., Bau, R., Cramer, R. E., Afzal, D., Gilje, J. W., and Koetzle, T. F. (1990) Multiple Bond Character in Cp_3U=CHPMe_3 - 1st Low-Temperature Neutron-Diffraction Analysis of a Uranium Organometallic Complex. *Organomet.*, **9**, 694–697.

[121] Fox, A. R., Arnold, P. L., and Cummins, C. C. (2010) UraniumNitrogen Multiple Bonding: Isostructural Anionic, Neutral, and Cationic Uranium Nitride Complexes Featuring a Linear U=N=U Core. *J. Am. Chem. Soc.*, **132**, 3250–3251, pMID: 20178384.

[122] Petti, D., Crawford, D., and Chauvin, N. (2009) Fuels for Advanced Nuclear Energy Systems. *MRS Bulletin*, **34**, 40–45.

[123] Silva, G. W. C., Yeamans, C. B., Sattelberger, A. P., Hartmann, T., Cerefice, G. S., and Czerwinski, K. R. (2009) Reaction Sequence and Kinetics of Uranium Nitride Decomposition. *Inorg. Chem.*, **48**, 10635–10642.

[124] Streit, M. and Ingold, F. (2005) Nitrides as a Nuclear Fuel Option. *J. Eur. Ceram. Soc.*, **25**, 2687–2692.

[125] Wang, X., Andrews, L., Malmqvist, P.-A., Roos, B. O., Goncalves, A. P., Pereira, C. C. L., Marcalo, J., Godart, C., and Villeroy, B. (2010) Infrared Spectra and Quantum Chemical Calculations of the Uranium Carbide Molecules UC and CUC with Triple Bonds. *J. Am. Chem. Soc.*, **132**, 8484–8488.

[126] Pyykko, P., Li, J., and Runeberg, N. (1994) Quasi-Relativistic Pseudopotential Study of Species Isoelectronic to Uranyl and the Equatorial Coordination of Uranyl. *J. Phys. Chem.*, **98**, 4809–4813.

[127] Becke, A. D. (1988) Density-Functional Exchange-Energy Approximation with Correct Asymptotic-Behavior. *Phys. Rev. A*, **38**, 3098–3100.

[128] Karlstrom, G., et al. (2003) MOLCAS: A Program Package for Computational Chemistry. *Comput. Mater. Sci.*, **28**, 222–239.

[129] Andersson, M. P. and Uvdal, P. (2005) New Scale Factors for Harmonic Vibrational Frequencies Using the B3LYP Density Functional Method with the Triple-ζ Basis Set 6-311+G(d,p). *J. Phys. Chem. A*, **109**, 2937–2941.

[130] Scott, A. P. and Radom, L. (1996) Harmonic Vibrational Frequencies: An Evaluation of Hartree-Fock, Moller-Plesset, Quadratic Configuration Interaction, Density Functional Theory, and Semiempirical Scale Factors. *J. Phys. Chem.*, **100**, 16502–16513.

[131] Flesch, R., Schurmann, M. C., Hunnekuhl, M., Meiss, H., Plenge, J., and Ruhl, E. (2000) A Pump-Probe Photoionization Mass Spectrometer Utilizing Tunable Extreme Ultraviolet Laser-Produced-Plasma Radiation. *Rev. Sci. Instrum.*, **71**, 1319–1324.

[132] Andrews, L., Kushto, G. P., Zhou, M. F., Willson, S. P., and Souter, P. F. (1999) Infrared Spectrum of CCH^+ in Solid Argon and Neon. *J. Chem. Phys.*, **110**, 4457–4466.

[133] Andrews, L. and Cho, H. G. (2005) Infrared Spectrum and Structure of CH_2=ThH_2. *J. Phys. Chem. A*, **109**, 6796–6798.

[134] Jacox, M. E. (1977) Matrix-Isolation Study of IR-Spectrum and Structure of CH_3 Free-Radical. *J. Mol. Spectrosc.*, **66**, 272–287.

[135] Milligan, D. E. and Jacox, M. E. (1969) Matrix-Isolation Study of the Infrared and Ultraviolet Spectra of the Free Radical HCO. The Hydrocarbon Flame Bands. *J. Chem. Phys.*, **51**, 277–288.

[136] Foner, S. N., Cochran, E. L., Bowers, V. A., and Jen, C. K. (1960) Multiple Trapping Sites for Hydrogen Atoms in Rare Gas Matrices. *J. Chem. Phys.*, **32**, 963–971.

[137] Milligan, D. E. and Jacox, M. E. (1964) Infrared Studies of the Photolysis of HN_3 in Inert and Reactive Matrices. The Infrared Spectrum of NH. *J. Chem. Phys.*, **41**, 2838–2841.

[138] In order to explore the bonding in NUNH at the DFT level, NBO calculations were performed with the B3LYP functional. The terminal NU triple bond contains two σ and four π bonding electrons. The inside UN bond contains four π bonding electrons, and the NH bond involves two σ bonding electrons. B3LYP predicts a

larger partial charge on the hydrogen, ca. 0.24. This difference should be attributed to two effects: the basis set employed in the CASSCF/CASPT2 calculations is different compared to the one employed in the B3LYP calculations, and it is well-known that Mulliken population analysis is very sensitive to the basis set. The CASSCF/CASPT2 density is different from the B3LYP density, as expected, and this is reflected in the partial charges. CASSCF theory describes systems in a more "covalent" manner because of the presence of the bonding and antibonding pair of orbitals in the wave functions, and it is thus not unexpected that it predicts the system to be more covalent than a single determinant method like B3LYP.

[139] Zalkin, A., Brennan, J. G., and Andersen, R. A. (1988) Tris(bis(trimethylsilyl)amido](trimethylsilylimido)uranium(V). *Acta Crystallogr. Sect. C*, **44**, 1553–1554.

[140] Collman, J. P. and Boulatov, R. (2002) Heterodinuclear Transition-Metal Complexes with Multiple Metal-Metal Bonds. *Angew. Chem. Int. Ed.*, **41**, 3948–3961.

[141] Cotton, F. A., Curtis, N. F., Harris, C. B., Johnson, B. F., Lippard, S. J., Mague, J. T., Robinson, W. R., and Wood, J. S. (1964) Mononuclear and Polynuclear Chemistry of Rhenium (III): Its Pronounced Homophilicity. *Science*, **145**.

[142] Cotton, F. A. (1965) Metal-Metal Bonding in $[Re_2X_8]^{2-}$ Ions and Other Metal Atom Clusters. *Inorg. Chem.*, **4**, 334–336.

[143] Cotton, F. A. (1993) *Multiple Bonds Between Metal Atoms*. Walton, 2nd edn.

[144] Chisholm, M. H. and Patmore, N. J. (2007) Studies of Electronic Coupling and Mixed Valency in Metal-Metal Quadruply Bonded Complexes Linked by Dicarboxylate and Closely Related Ligands. *Acc. Chem. Res.*, **40**, 19–27.

[145] Greenwood, B. P., Rowe, G. T., Chen, C.-H., Foxman, B. M., and Thomas, C. M. (2010) Metal-Metal Multiple Bonds in Early/Late Heterobimetallics Support Unusual Trigonal Monopyramidal Geometries at Both Zr and Co. *J. Am. Chem. Soc.*, **132**, 44–45.

[146] Liddle, S. T. and Mills, D. P. (2009) Metal-Metal Bonds in f-Element Chemistry. *Dalton Trans.*, pp. 5592–5605.

[147] Nolan, S. P., Porchia, M., and Marks, T. J. (1991) Organo-f-Element Thermochemistry - Actinide Group-14 Element and Actinide Transition-Element Bond Disruption Enthalpies and Stoichiometric Catalytic Chemical Implications Thereof in Heterbimetallic Tris(Cyclopentadienyl)Uranium(IV) Compounds. *Organomet.*, **10**, 1450–1457.

[148] Raab, J., Lindh, R. H., Wang, X., Andrews, L., and Gagliardi, L. (2007) A Combined Experimental and Theoretical Study of Uranium Polyhydrides with New Evidence for the Large Complex $UH_4(H_2)_6$. *J. Phys. Chem. A*, **111**, 6383–6387.

[149] Wang, X., Andrews, L., Infante, I., and Gagliardi, L. (2008) Infrared Spectra of the $WH_4(h_2)_4$ Complex in Solid Hydrogen. *J. Am. Chem. Soc.*, **130**, 1972–1978.

[150] Wang, X., Andrews, L., and Gagliardi, L. (2008) Infrared Spectra of ThH_2, ThH_4, and the Hydride Bridging $ThH_4(H_2)_x$ (x=1-4) Complexes in Solid Neon and Hydrogen. *J. Phys. Chem. A*, **112**, 1754–1761.

[151] Butovskii, M. V., Tok, O. L., Wagner, F. R., and Kempe, R. (2008) Bismetallocenes: Lanthanoid-Transition-Metal Bonds Through Alkane Elimination. *Angew. Chem. Int. Ed.*, **47**, 6469–6472.

[152] Liddle, S. T., Mills, D. P., Gardner, B. M., McMaster, J., Jones, C., and Woodul, W. D. (2009) A Heterobimetallic Gallyl Complex Containing an Unsupported Ga-Y Bond. *Inorg. Chem.*, **48**, 3520–3522.

[153] Minasian, S. G., Krinsky, J. L., Rinehart, J. D., Copping, R., Tyliszczak, T., Janousch, M., Shuh, D. K., and Arnold, J. (2009) A Comparison of 4f vs 5f Metal-Metal Bonds in $(CpSiMe_3)_3M$-ECp* (M = Nd, U; E = Al, Ga; Cp* = C_5Me_5): Synthesis, Thermodynamics, Magnetism, and Electronic Structure. *J. Am. Chem. Soc.*, **131**, 13767–13783.

[154] Beletskaya, I. P., Voskoboynikov, A. Z., Chuklanova, E. B., Kirillova, N. I., Shestakova, A. K., Parshina, I. N., Gusev, A. I., and Magomedov, G. K. I. (1993) Bimetallic Lanthanide Complexes with Lanthanide Transition-Metal Bonds

- Molecular-Structure of $(C_4H_8O)(C_5H_5)_2$Lu-Ru$(CO)_2(C_5H_5)$ - The Use of La-139 NMR-Spectroscopy. *J. Am. Chem. Soc.*, **115**, 3156–3166.

[155] Sternal, R. S., Brock, C. P., and Marks, T. J. (1985) Metal Metal Bonds Involving Actinides - Synthesis and Characterization of a Complex Having an Unsupported Actinide to Transition-Metal Bond. *J. Am. Chem. Soc.*, **107**, 8270–8272.

[156] Corradi, M. M., Frankland, A. D., Hitchcock, P., Lappert, M. F., and Lawless, G. A. (1996) Synthesis, Structure and Reactivity of [Yb(η-C_5Me_5)Si$(SiMe_3)_3(THF)_2$]. *Chem. Commun.*, pp. 2323–2324.

[157] Porchia, M., Casellato, U., Ossola, F., Rossetto, G., Zanella, P., and Graziani, R. (1986) Synthesis and Crystal-Structure of a Triscyclopentadienyl(Triphenyltin)Uranium - The 1st Example of a Uranium Tin Bond. *J. Chem. Soc. Chem. Commun.*, pp. 1034–1035.

[158] Porchia, M., Brianese, N., Casellato, U., Ossola, F., Rossetto, G., Zanella, P., and Graziani, R. (1989) Tri(η-cyclopentadienyl)Uranium(IV) Silyl and Siloxide Compounds - Crystal-Structure of [U(η^5-$C_5H_5)_3(OSiPh_3)$] - Insertion of Isocyanide into a Uranium-Silicon Bond. *J. Chem. Soc. Dalton Trans.*, pp. 677–681.

[159] Diaconescu, P. L., Odom, A. L., Agapie, T., and Cummins, C. C. (2001) Uranium-Group 14 Element Single Bonds: Isolation and Characterization of a Uranium(IV) Silyl Species. *Organomet.*, **20**, 4993–4995.

[160] Ahlrichs, R., Bar, M., Haser, M., Horn, H., and Kolmel, C. (1989) Electronic-Structure Calculations on Workstation Computers - The Program System Turbomole. *Chem. Phys. Lett.*, **162**, 165–169.

[161] Hellweg, A., Haettig, C., Hoefener, S., and Klopper, W. (2007) Optimized Accurate Auxiliary basis Sets for RI-MP2 and RI-CC2 Calculations for the Atoms Rb to Rn. *Theor. Chem. Acc.*, **117**, 587–597.

[162] Schafer, A., Huber, C., and Ahlrichs, R. (1994) Fully Optimized Contracted Gaussian-Basis Sets of Triple-ζ Valence Quality for Atoms Li to Kr. *J. Chem. Phys.*, **100**, 5829–5835.

[163] Cao, X. Y. and Dolg, M. (2001) Valence Basis Sets for Relativistic Energy-Consistent Small-Core Lanthanide Pseudopotentials. *J. Chem. Phys.*, **115**, 7348–7355.

[164] Eichkorn, K., Weigend, F., Treutler, O., and Ahlrichs, R. (1997) Auxiliary Basis Sets for Main Row Atoms and Transition Metals and Their Use to Approximate Coulomb Potentials. *Theor. Chem. Acc.*, **97**, 119–124.

[165] Eichkorn, K., Treutler, O., Ohm, H., Haser, M., and Ahlrichs, R. (1995) Auxiliary Basis-Sets to Approximate Coulomb Potentials. *Chem. Phys. Lett.*, **240**, 283–289.

[166] Von Arnim, M. and Ahlrichs, R. (1998) Performance of Parallel TURBOMOLE for Density Functional Calculations. *J. Comput. Chem.*, **19**, 1746–1757.

[167] Bartlett, R. J. (1981) Many-Body Perturbation-Theory and Coupled Cluster Theory for Electron Correlation in Molecules. *Annu. Rev. Phys. Chem.*, **32**, 359–401.

[168] Møller, C. and Plesset, M. S. (1934) Note on an Approximation Treatment for Many-Electron Systems. *Phys. Rev.*, **46**, 618–622.

[169] Hess, B. A. (1986) Relativistic Electronic-Structure Calculations Employing a 2-Component No-Pair Formalism with External-Field Projection Operators. *Phys. Rev. A*, **33**, 3742–3748.

[170] Roos, B. O., Lindh, R., Malmqvist, P. A., Veryazov, V., and Widmark, P. O. (2005) New Relativistic ANO Basis Sets for Actinide Atoms. *Chem. Phys. Lett.*, **409**, 295–299.

[171] Roos, B. O., Lindh, R., Malmqvist, P.-A., Veryazov, V., Widmark, P.-O., and Borin, A. C. (2008) New Relativistic Atomic Natural Orbital Basis Sets for Lanthanide Atoms with Applications to the Ce Diatom and LuF_3. *J. Phys. Chem. A*, **112**, 11431–11435.

[172] Aquilante, F., et al. (2010) Software News and Update MOLCAS 7: The Next Generation. *J. Comput. Chem.*, **31**, 224–247.

[173] Aquilante, F., Pedersen, T. B., Lindh, R., Roos, B. O., De Meras, A. S., and Koch, H. (2008) Accurate Ab Initio Density Fitting for Multiconfigurational Self-Consistent Field Methods. *J. Chem. Phys.*, **129**, 024113.

[174] Aquilante, F., Malmqvist, P.-A., Pedersen, T. B., Ghosh, A., and Roos, B. O. (2008) Cholesky Decomposition-Based Multiconfiguration Second-Order Perturbation Theory (CD-CASPT2): Application to the Spin-State Energetics of Co-III(diiminato)(NPh). *J. Chem. Theory Comput.*, **4**, 694–702.

[175] Aquilante, F., Gagliardi, L., Pedersen, T. B., and Lindh, R. (2009) Atomic Cholesky Decompositions: A Route to Unbiased Auxiliary Basis Sets for Density Fitting Approximation with Tunable Accuracy and Efficiency. *J. Chem. Phys.*, **130**, 154107.

[176] Aquilante, F., Pedersen, T. B., and Lindh, R. (2007) Low-Cost Evaluation of the Exchange Fock Matrix from Cholesky and Density Fitting Representations of the Electron Repulsion Integrals. *J. Chem. Phys.*, **126**, 194106.

[177] Gagliardi, L., Heaven, M. C., Krogh, J. W., and Roos, B. O. (2005) The Electronic Spectrum of the UO_2 Molecule. *J. Am. Chem. Soc.*, **127**, 86–91.

[178] Vosko, S. H., Wilk, L., and Nusair, M. (1980) Accurate Spin-Dependent Electron Liquid Correlation Energies for Local Spin-Density Calculations - A Critical Analysis. *Can. J. Phys.*, **58**, 1200–1211.

[179] Van Lenthe, E., Baerends, E. J., and Snijders, J. G. (1994) Relativistic Total-Energy Using Regular Approximations. *J. Chem. Phys.*, **101**, 9783–9792.

[180] Mantina, M., Cramer, C. J., and Truhlar, D. G. (2010) *CRC Handbook of Chemistry and Physics*. Constants, Books, CRC Press, 91st edn.

[181] Cordero, B., Gomez, V., Platero-Prats, A. E., Reves, M., Echeverria, J., Cremades, E., Barragan, F., and Alvarez, S. (2008) Covalent Radii Revisited. *Dalton Trans.*, pp. 2832–2838.

[182] Pyykko, P. and Atsumi, M. (2009) Molecular Single-Bond Covalent Radii for Elements 1-118. *Chem. Eur. J.*, **15**, 186–197.

[183] Swart, M., Van Duijnen, P. T., and Snijders, J. G. (2001) A Charge Analysis Derived from an Atomic Multipole Expansion. *J. Comput. Chem.*, **22**, 79–88.

[184] Bianchi, R., Gervasio, G., and Marabello, D. (2000) Experimental Electron Density Analysis of $Mn_2(CO)_{10}$: Metal-Metal and Metal-Ligand Bond Characterization. *Inorg. Chem.*, **39**, 2360–2366.

[185] Bunzli, J. C. G. and Piguet, C. (2005) Taking Advantage of Luminescent Lanthanide Ions. *Chem. Soc. Rev.*, **34**, 1048–1077.

[186] Carlos, L. D., Ferreira, R. A. S., Bermudez, V. d. Z., and Ribeiro, S. J. L. (2009) Lanthanide-Containing Light-Emitting Organic-Inorganic Hybrids: A Bet on the Future. *Adv. Mater.*, **21**, 509–534.

[187] Kido, J. and Okamoto, Y. (2002) Organo Lanthanide Metal Complexes for Electroluminescent Materials. *Chem. Rev.*, **102**, 2357–2368.

[188] Etourneau, J. (1985) Critical Survey of Rare-Earth Borides - Occurence, Crystal-Chemistry and Physical-Properties. *J. Less-Common Met.*, **110**, 267–281.

[189] Gasgnier, M. (1991) Rare-Earth Elements in Permanent-Magnets and Superconduction Compounds and Alloys (Except New High - T^c Ceramics) as Thin-Films, Thin-Crystals and Thinned Bulk Materials. *J. Mater. Sci.*, **26**, 1989–1999.

[190] Collocott, S. J., Dunlop, J. B., Lovatt, H. C., and Ramsden, V. S. (1999) Rare-Earth Permanent Magnets: New Magnet Materials and Applications. *Rare Earths '98*, **315-3**, 77–83.

[191] Robertson, J. (2004) High Dielectric Constant Oxides. *Eur. Phys. J.-Appl. Phys.*, **28**, 265–291.

[192] Scullin, M. L., Yu, C., Huijben, M., Mukerjee, S., Seidel, J., Zhan, Q., Moore, J., Majumdar, A., and Ramesh, R. (2008) Anomalously Large Measured Thermoelectric Power Factor in $Sr_{1-x}La_xTiO_3$ Thin Films Due to $SrTiO_3$ Substrate Reduction. *Appl. Phys. Lett.*, **92**, 202113.

[193] Crowell, J. E. (2003) Chemical Methods of Thin Film Deposition: Chemical Vapor Deposition, Atomic Layer Deposition, and Related Technologies. *J. Vac. Sci. Technol., A*, **21**, S88–S95.

[194] George, S. M. (2010) Atomic Layer Deposition: An Overview. *Chem. Rev.*, **110**, 111–131.

[195] Yanguas-Gil, A., Yang, Y., Kumar, N., and Abelson, J. R. (2009) Highly Conformal Film Growth by Chemical Vapor Deposition. I. A Conformal Zone Diagram Based on Kinetics. *J. Vac. Sci. Technol., A*, **27**, 1235–1243.

[196] Jensen, J. A., Gozum, J. E., Pollina, D. M., and Girolami, G. S. (1988) Titanium, Zirconium, and Hafnium Tetrahydroborates as Tailored CVD Precursors for Metal Diboride Thin-Films. *J. Am. Chem. Soc.*, **110**, 1643–1644.

[197] Kumar, N., Yang, Y., Noh, W., Girolami, G. S., and Abelson, J. R. (2007) Titanium Diboride Thin Films by Low-Temperature Chemical Vapor Deposition from the Single Source Precursor $Ti(BH_4)_3$(1,2-dimethoxyethane). *Chem. Mater.*, **19**, 3802–3807.

[198] Kumar, N., Yanguas-Gil, A., Daly, S. R., Girolami, G. S., and Abelson, J. R. (2008) Growth Inhibition to Enhance Conformal Coverage in Thin Film Chemical Vapor Deposition. *J. Am. Chem. Soc.*, **130**, 17660–17661.

[199] Sung, J. W., Goedde, D. M., Girolami, G. S., and Abelson, J. R. (2002) Remote-Plasma Chemical Vapor Deposition of Conformal ZrB_2 Films at Low Temperature: A Promising Diffusion Barrier for Ultralarge Scale Integrated Electronics. *J. Appl. Phys.*, **91**, 3904–3911.

[200] Jayaraman, S., Gerbi, J. E., Yang, Y., Kim, D. Y., Chatterjee, A., Bellon, P., Girolami, G. S., Chevalier, J. P., and Abelson, J. R. (2006) HfB_2 and Hf–B–N Hard Coatings by Chemical Vapor Deposition. *Surf. Coat. Tech.*, **200**, 6629–6633.

[201] Yang, Y., Jayaraman, S., Kim, D. Y., Girolami, G. S., and Abelson, J. R. (2006) CVD Growth Kinetics of HfB_2 Thin Films from the Single-Source Precursor $Hf(BH_4)_4$. *Chem. Mater.*, **18**, 5088–5096.

[202] Yang, Y., Jayaraman, S., Kim, D. Y., Girolami, G. S., and Abelson, J. R. (2006) Crystalline Texture in Hafnium Diboride Thin Films Grown by Chemical Vapor Deposition. *J. Cryst. Growth*, **294**, 389–395.

[203] Yang, Y., Jayaraman, S., Sperling, B., Kim, D. Y., Girolami, G. S., and Abelson, J. R. (2007) In situ Spectroscopic Ellipsometry Analyses of Hafnium Diboride Thin Films Deposited by Single-Source Chemical Vapor Deposition. *J. Vac. Sci. Technol., A*, **25**, 200–206.

[204] Mirsaidov, U., Shaimuradov, I. B., and Khikmatov, M. (1986) X-ray Diffraction Investigation of Lanthane, Neodymium and Luthecium Tetrahydroborate Tristetrahydrofuranates. *Russ. J. Inorg. Chem.*, **31**, 1321–1323.

[205] Shaimuradov, I. B., Badalov, A. B., Marufi, V. K., and Mirsaidov, U. (1991) Certain Properties of Tetrahydroborate Tristetraydrofuranates of Rare-Earth-Metals. *Russ. J. Inorg. Chem.*, **36**, 1353–1353.

[206] Shinomoto, R., Zalkin, A., and Edelstein, N. M. (1987) Preparation of Some Lewis Base Adducts of Tris(methyltrihydroborato)Ho and Yb amd Crystal-Structures of Tris(methyltrihydrdoborato)Ytterbium(III)etherate and Tris(methyltrihydrdoborato)Holmium(III)bis(pyridine). *Inorg. Chim. Acta*, **139**, 97–101.

[207] White, J. P., Deng, H. B., and Shore, S. G. (1991) Borohydride Complexes of Europium(II) and Ytterbium(II) and their Conversion to Metal Borides -Structures of $(L)_4Yb[BH_4]_2$ (L = CH_3CN, C_5H_5N). *Inorg. Chem.*, **30**, 2337–2342.

[208] Zange, E. (1960) Entwicklung eines Mikroverfahrens zur Darstellung von Boranaten der schweren Lanthaniden. *Chem. Ber.*, **93**, 652–657.

[209] Bernstein, E. R., Hamilton, W. C., Keiderling, T. A., La Placa, S. J., Lippard, S. J., and Mayerle, J. J. (1972) 14-Coordinate Uranium(IV). Structure of Uranium Borohydride by Single-Crystal Neutron Diffraction. *Inorg. Chem.*, **11**, 3009–3016.

[210] Schlesinger, H. I. and Brown, H. C. (1953) Uranium(IV) Borohydride. *J. Am. Chem. Soc.*, **75**, 219–221.

[211] Shinomoto, R., Gamp, E., Edelstein, N. M., Templeton, D. H., and Zalkin, A. (1983) Syntheses and Crystal-Structures of the Tetrakis(methyltrihydroborato) Compounds of Zirconium(IV), Thorium(IV), Uranium(IV), and Neptunium(IV). *Inorg. Chem.*, **22**, 2351–2355.

[212] Ephritikhine, M. (1997) Synthesis, Structure, and Reactions of Hydride, Borohydride, and Aluminohydride Compounds of the f-Elements. *Chem. Rev.*, **97**, 2193–2242.

[213] Daly, S. R. and Girolami, G. S. (2010) Synthesis, Characterization, and Structures of Uranium(III) N,N-Dimethylaminodiboranates. *Inorg. Chem.*, **49**, 5157–5166.

[214] Daly, S. R., Kim, D. Y., Yang, Y., Abelson, J. R., and Girolami, G. S. (2010) Lanthanide N,N-Dimethylaminodiboranates: Highly Volatile Precursors for the Deposition of Lanthanide-Containing Thin Films. *J. Am. Chem. Soc.*, **132**, 2106–2107.

[215] Daly, S. R. and Girolami, G. S. (2010) Uranium-Hydrogen Interactions: Synthesis and Crystal Structures of Tris(N,N-Dimethylaminodiboranato)uranium(III). *Chem. Commun.*, **46**, 407–408.

[216] Daly, S. R., Kim, D. Y., and Girolami, G. S. (2012) Lanthanide N,N-Dimethylaminodiboranates as a New Class of Highly Volatile Chemical Vapor Deposition Precursors. *Inorg. Chem.*, **51**, 7050–7065.

[217] Shannon, R. D. (1976) Revised Effective Ionic-Radii and Systematic Studies of Interatomic Distances in Halides and Chalcogenides. *Acta Crystallogr. Sect. A*, **32**, 751–767.

[218] Cao, X. Y. and Dolg, M. (2002) Segmented Contraction Scheme for Small-Core Lanthanide Pseudopotential Basis Sets. *Comp. Theor. Chem.*, **581**, 139–147.

[219] Cao, X. Y. and Dolg, M. (2004) Segmented Contraction Scheme for Small-Core Actinide Pseudopotential Basis Sets. *Comp. Theor. Chem.*, **673**, 203–209.

[220] Dolg, M., Stoll, H., and Preuss, H. (1989) Energy-Adjusted Ab Initio Pseudopotentials for the Rare-Earth Elements. *J. Chem. Phys.*, **90**, 1730–1734.

[221] Krishnan, R., Binkley, J. S., Seeger, R., and Pople, J. A. (1980) Self-Consistent Molecular-Orbital Methods .20. Basis Set for Correlated Wave-Functions. *J. Chem. Phys.*, **72**, 650–654.

[222] Olson, R. M., et al. (2011), MN-GSM Version 2011, University of Minnesota.

[223] Arnold, P. L., Turner, Z. R., Kaltsoyannis, N., Pelekanaki, P., Bellabarba, R. M., and Tooze, R. P. (2010) Covalency in Ce-IV and U-IV Halide and N-Heterocyclic Carbene Bonds. *Chem. Eur. J.*, **16**, 9623–9629.

[224] Xu, W., Jin, X., Chen, M., Pyykko, P., Zhou, M., and Li, J. (2012) Rare-Earth Monocarbonyls MCO: Comprehensive Infrared Observations and a Transparent Theoretical Interpretation for M = Sc; Y; La-Lu. *Chem. Sci.*, **3**, 1548–1554.

[225] Grimme, S., Antony, J., Ehrlich, S., and Krieg, H. (2010) A Consistent and Accurate Ab Initio Parametrization of Density Functional Dispersion Correction (DFT-D) for the 94 Elements H-Pu. *J. Chem. Phys.*, **132**, 154104.

[226] Grimme, S., Ehrlich, S., and Goerigk, L. (2011) Effect of the Damping Function in Dispersion Corrected Density Functional Theory. *J. Comput. Chem.*, **32**, 1456–1465.

[227] Becke, A. D. and Johnson, E. R. (2005) Statistical Mechanical Theory for Steady State Systems. II. Reciprocal Relations and the Second Entropy. *J. Chem. Phys.*, **122**, 154101.

[228] Johnson, E. R. and Becke, A. D. (2005) A Post-Hartree-Fock Model of Intermolecular Interactions. *J. Chem. Phys.*, **123**, 024101.

[229] Johnson, E. R. and Becke, A. D. (2006) A Post-Hartree-Fock Model of Intermolecular Interactions: Inclusion of Higher-Order Corrections. *J. Chem. Phys.*, **124**, 174104.

[230] Mehn, M. P., Brown, S. D., Paine, T. K., Brennessel, W. W., Cramer, C. J., Peters, J. C., and Que, L. (2006) High-Spin and Low-Spin Iron(II) Complexes with Facially-Coordinated Borohydride Ligands. *Dalton Trans.*, pp. 1347–1351.

[231] Diaconescu, P. L., Arnold, P. L., Baker, T. A., Mindiola, D. J., and Cummins, C. C. (2000) Arene-Bridged Diuranium Complexes: Inverted Sandwiches Supported by δ Backbonding. *J. Am. Chem. Soc.*, **122**, 6108–6109.

[232] Evans, W. J., Traina, C. A., and Ziller, J. W. (2009) Synthesis of Heteroleptic Uranium (μ-η^6:η^6-C_6H_6)$_2$– Sandwich Complexes via Facile Displacement of (η^5-C_5Me_5)$^{1-}$ by Ligands of Lower Hapticity and Their Conversion to Heteroleptic Bis(imido) Compounds. *J. Am. Chem. Soc.*, **131**, 17473–17481, pMID: 19929023.

[233] Evans, W. J. and Kozimor, S. A. (2006) Expanding the Chemistry of U^{3+} Reducing Agents. *Coord. Chem. Rev.*, **250**, 911–935.

[234] Mills, D. P., Moro, F., McMaster, J., van Slageren, J., Lewis, W., Blake, A. J., and Liddle, S. T. (2011) A Delocalized Arene-Bridged Diuranium Single-Molecule Magnet. *Nat. Chem.*, **3**, 454–460.

[235] Monreal, M. J., Khan, S. I., Kiplinger, J. L., and Diaconescu, P. L. (2011) Molecular Quadrangle Formation from a Diuranium μ-η^6,η^6–toluene complex. *Chem. Commun.*, **47**, 9119–9121.

[236] Patel, D., Moro, F., McMaster, J., Lewis, W., Blake, A. J., and Liddle, S. T. (2011) A Formal High Oxidation State Inverse-Sandwich Diuranium Complex: A New Route to f-Block-Metal Bonds. *Angew. Chem. Int. Ed.*, **50**, 10388–10392.

[237] Arnold, P. L., Mansell, S. M., Maron, L., and McKay, D. (2012) Spontaneous Reduction and C–H Borylation of Arenes Mediated by Uranium(III) Disproportionation. *Nat. Chem.*, **4**, 668–674.

[238] Mougel, V., Camp, C., Pécaut, J., Copéret, C., Maron, L., Kefalidis, C. E., and Mazzanti, M. (2012) Siloxides as supporting ligands in uranium(iii)-mediated small-molecule activation. *Angew. Chem. Int. Ed.*, **124**, 12446–12450.

[239] Diaconescu, P. L. and Cummins, C. C. (2002) Diuranium Inverted Sandwiches Involving Naphthalene and Cyclooctatetraene. *J. Am. Chem. Soc.*, **124**, 7660–7661.

[240] Diaconescu, P. L. and Cummins, C. C. (2012) μ–η^6,η^6–Arene-Bridged Diuranium Hexakisketimide Complexes Isolable in Two States of Charge. *Inorg. Chem.*, **51**, 2902–2916.

[241] Arliguie, T., Lance, M., Nierlich, M., Vigner, J., and Ephritikhine, M. (1994) Inverse Cycloheptatrienyl Sandwich Complexes. Crystal Structure of $[U(BH_4)_2(OC_4H_8)_5][(BH_4)_3U(\mu\text{-}\eta^7,\eta^7\text{-}C_7H_7)U(BH_4)_3]$. *J. Chem. Soc., Chem. Commun.*, **0**, 847–848.

[242] Arliguie, T., Lance, M., Nierlich, M., and Ephritikhine, M. (1997) Inverse Cycloheptatrienyl Sandwich Complexes of Uranium and Neodymium. *J. Chem. Soc., Dalton Trans.*, **0**, 2501–2504.

[243] Lein, M., Frunzke, J., and Frenking, G. (2003) Structures and Bonding of the Sandwich Complexes $[Ti(\eta^5\text{-}E_5)_2]_2$- (E = CH, N, P, As, Sb): A Theoretical Study. *Inorganic Chemistry*, **42**, 2504–2511, pMID: 12691555.

[244] Kempe, R. (2000) Highlights in the Renaissance of Amidometal Chemistry. *Angew. Chem. Int. Ed.*, **39**, 468–493.

[245] Gade, L. H. (2002) Transition Metal Complexes with Polydentate Amido Ligands: Novel Structural Building Blocks and Chemical Reagents. *J. Organomet. Chem.*, **661**, 85–94.

[246] Gade, L. H. and Mountford, P. (2001) New Transition Metal Imido Chemistry with Diamido-Donor Ligands. *Coord. Chem. Rev.*, **216–217**, 65–97.

[247] Diaconescu, P. L., Odom, A. L., Agapie, T., and Cummins, C. C. (2001) Uranium–Group 14 Element Single Bonds: Isolation and Characterization of a Uranium(IV) Silyl Species. *Organomet.*, **20**, 4993–4995.

[248] Diaconescu, P. L. (2010) Reactions of Aromatic N–Heterocycles with d^0f^n–Metal Alkyl Complexes Supported by Chelating Diamide Ligands. *Acc. Chem. Res.*, **43**, 1352–1363.

[249] Fox, A. R. and Cummins, C. C. (2009) UraniumNitrogen Multiple Bonding: The

Case of a Four-Coordinate Uranium(VI) Nitridoborate Complex. *J. Am. Chem. Soc.*, **131**, 5716–5717, pMID: 19341243.

[250] Odom, A. L., Arnold, P. L., and Cummins, C. C. (1998) Heterodinuclear Uranium/Molybdenum Dinitrogen Complexes. *Journal of the American Chemical Society*, **120**, 5836–5837.

[251] Roussel, P., W. Alcock, N., and Scott, P. (1998) Triamidoamine Complexes of Scandium, Yttrium and the Lanthanides. *Chem. Commun.*, **0**, 801–802.

[252] Stewart, J. L. and Andersen, R. A. (1998) Trivalent Uranium Chemistry: Molecular Structure of $[(Me_3Si)_2N]_3U$. *Polyhedron*, **17**, 953–958.

[253] Cruz, C. A., Emslie, D. J. H., Harrington, L. E., Britten, J. F., and Robertson, C. M. (2007) Extremely Stable Thorium(IV) Dialkyl Complexes Supported by Rigid Tridentate 4,5-Bis(anilido)xanthene and 2,6-Bis(anilidomethyl)pyridine Ligands. *Organomet.*, **26**, 692–701.

[254] Cruz, C. A., Emslie, D. J. H., Harrington, L. E., and Britten, J. F. (2008) Single and Double Alkyl Abstraction from a Bis(anilido)xanthene Thorium(IV) Dibenzyl Complex: Isolation of an Organothorium Cation and a Thorium Dication. *Organomet.*, **27**, 15–17.

[255] Cruz, C. A., Emslie, D. J. H., Robertson, C. M., Harrington, L. E., Jenkins, H. A., and Britten, J. F. (2009) Cationic Thorium Alkyl Complexes of Rigid NON- and NNN-Donor Ligands: π-Arene Coordination as a Persistent Structural Motif. *Organomet.*, **28**, 1891–1899.

[256] Jantunen, K. C., Batchelor, R. J., and Leznoff, D. B. (2004) Synthesis, Characterization, and Organometallic Derivatives of Diamidosilyl Ether Thorium(IV) and Uranium(IV) Halide Complexes. *Organomet.*, **23**, 2186–2193.

[257] Cummins, C. C. (1998) Reductive Cleavage and Related Reactions Leading to Molybdenum-Element Multiple Bonds: New Pathways Offered by Three-Coordinate Molybdenum(III). *Chem. Commun.*, **0**, 1777–1786.

[258] Avens, L. R., Bott, S. G., Clark, D. L., Sattelberger, A. P., Watkin, J. G., and Zwick, B. D. (1994) A Convenient Entry into Trivalent Actinide Chemistry: Synthesis and Characterization of $AnI_3(THF)_4$ and $An[N(SiMe_3)_2]_3$ (An = U, Np, Pu). *Inorg. Chem.*, **33**, 2248–2256.

[259] Clark, D. L., Sattelberger, A. P., Bott, S. G., and Vrtis, R. N. (1989) Lewis Base Adducts of Uranium Triiodide: A New Class of Synthetically Useful Precursors for Trivalent Uranium Chemistry. *Inorg. Chem.*, **28**, 1771–1773.

[260] Avdeef, A., Raymond, K. N., Hodgson, K. O., and Zalkin, A. (1972) Two Isostructural Actinide π Complexes. Crystal and Molecular Structure of Bis(cyclooctatetraenyl)uranium(IV), $U(C_8H_8)_2$, and Bis(cyclooctatetraenyl)thorium(IV), $Th(C_8H_8)_2$. *Inorg. Chem.*, **11**, 1083–1088.

[261] Burns, J. H. (1974) The Molecular and Crystal Structure of Tetracyclopentadienyluranium(IV). *J. Organomet. Chem.*, **69**, 225–233.

[262] Baudry, D., Bulot, E., Charpin, P., Ephritikhine, M., Lance, M., Nierlich, M., and Vigner, J. (1989) Arene Uranium Borohydrides: Synthesis and Crystal Structure of η-$(C_6Me_6)U(BH_4)_3$. *J. Organomet. Chem.*, **371**, 155–162.

[263] Garbar, A. V., Leonov, M. R., Zakharov, L. N., and Struchkov, Y. T. (1996) *Russ. Chem. Bull.*, **45**, 451–454.

[264] Madelung, O. (ed.) (1987) *In Landolt-Börnstein: Numerical Data and Functional Relationships in Science and Technology*. Springer.

[265] Hitchcock, P. B., Lappert, M. F., and Protchenko, A. V. (2001) The First Crystalline Alkali Metal Salt of a Benzenoid Radical Anion without a Stabilizing Substituent and of a Related Dimer: X-ray Structures of the Toluene Radical Anion and of the Benzene Radical Anion Dimer Potassium-Crown Ether Salts. *J. Am. Chem. Soc.*, **123**, 189–190, pMID: 11273622.

[266] Duff, A. W., Jonas, K., Goddard, R., Kraus, H. J., and Krueger, C. (1983) The First Triple-Decker Sandwich with a Bridging Benzene Ring. *J. Am. Chem. Soc.*, **105**, 5479–5480.

[267] La Mar, G. N., Horrocks, W. d. W., and Holm, R. H. (1973) *NMR of Paramagnetic Molecules; Principles and Applications*. Academic Press.

[268] Cantat, T., Graves, C. R., Jantunen, K. C., Burns, C. J., Scott, B. L., Schelter, E. J., Morris, D. E., Hay, P. J., and Kiplinger, J. L. (2008) Evidence for the Involvement of 5f Orbitals in the Bonding and Reactivity of Organometallic Actinide Compounds: Thorium(IV) and Uranium(IV) Bis(hydrazonato) Complexes. *J. Am. Chem. Soc.*, **130**, 17537–17551.

[269] Morris, D. E., Da Re, R. E., Jantunen, K. C., Castro-Rodriguez, I., and Kiplinger, J. L. (2004) Trends in Electronic Structure and Redox Energetics for Early-Actinide Pentamethylcyclopentadienyl Complexes. *Organomet.*, **23**, 5142–5153.

[270] Schelter, E. J., Yang, P., Scott, B. L., Thompson, J. D., Martin, R. L., Hay, P. J., Morris, D. E., and Kiplinger, J. L. (2007) Systematic Studies of Early Actinide Complexes: Uranium(IV) Fluoroketimides. *Inorg. Chem.*, **46**, 7477–7488, pMID: 17691767.

[271] Lever, A. B. P. (1984) *Inorganic Electronic Spectroscopy*, vol. 33. Elsevier.

[272] Castro-Rodriguez, I., Olsen, K., Gantzel, P., and Meyer, K. (2003) Uranium Tris-aryloxide Derivatives Supported by Triazacyclononane: Engendering a Reactive Uranium(III) Center with a Single Pocket for Reactivity. *J. Am. Chem. Soc.*, **125**, 4565–4571, pMID: 12683828.

[273] Kozimor, S. A., Bartlett, B. M., Rinehart, J. D., and Long, J. R. (2007) Magnetic Exchange Coupling in Chloride-Bridged 5f-3d Heterometallic Complexes Generated via Insertion into a Uranium(IV) Dimethylpyrazolate Dimer. *J. Am. Chem. Soc.*, **129**, 10672–10674, pMID: 17691779.

[274] Rinehart, J. D., Harris, T. D., Kozimor, S. A., Bartlett, B. M., and Long, J. R. (2009) Magnetic Exchange Coupling in Actinide-Containing Molecules. *Inorg. Chem.*, **48**, 3382–3395.

[275] Stewart, J. L. and Andersen, R. A. (1995) Crystal Structures of $[(Me_3Si)_2N]_4U_2[\mu$-N(H)-(mesityl)$]_2$; Compounds with Asymmetrically Bridging Primary Amide and Imide Groups. *New J. Chem.*, **19**, 587–595.

[276] Rosen, R. K., Andersen, R. A., and Edelstein, N. M. (1990) $[(MeC_5H_4)_3U]_2[\mu$-1,4-$N_2C_6H_4]$: A Bimetallic Molecule with Antiferromagnetic Coupling Netween the Uranium Centers. *J. Am. Chem. Soc.*, **112**, 4588–4590.

[277] Brown, F. C. (1980) *Synchrotron Radiation Research*, chap. 4, pp. 27–60. Plenum Press.

[278] Koningsberger, D. C. and Prins, R. (eds.) (1988) *X-ray Absorption: Principles, Applications, Techniques of EXAFS, SEXAFS, and XANES*. Wiley.

[279] Bertsch, P. M., Hunter, D. B., Sutton, S. R., Bajt, S., and Rivers, M. L. (1994) In situ Chemical Speciation of Uranium in Soils and Sediments by Micro X-ray Absorption Spectroscopy. *Environ. Sci. Technol.*, **28**, 980–984.

[280] Kalkowski, G., Kaindl, G., Brewer, W. D., and Krone, W. (1986) X-Ray Absorption by Uranium Systems at Various Thresholds. *J. Phys. Colloq.*, **47**, 943.

[281] Lukens, W. W., Allen, P. G., Bucher, J. J., Edelstein, N. M., Hudson, E. A., Shuh, D. K., Reich, T., and Andersen, R. A. (1999) Structures of Substituted-Cyclopentadienyl Uranium(iii) Dimers and Related Uranium Metallocenes Deduced by EXAFS. *Organomet.*, **18**, 1253–1258.

[282] Kozimor, S. A., Yang, P., Batista, E. R., Boland, K. S., Burns, C. J., Clark, D. L., Conradson, S. D., Martin, R. L., Wilkerson, M. P., and Wolfsberg, L. E. (2009) Trends in Covalency for d- and f-Element Metallocene Dichlorides Identified Using Chlorine K-Edge X-ray Absorption Spectroscopy and Time-Dependent Density Functional Theory. *J. Am. Chem. Soc.*, **131**, 12125–12136, pMID: 19705913.

[283] Boerrigter, P. M., Baerends, E. J., and Snijders, J. G. (1988) A Relativistic LCAO Hartree-Fock-Slater Investigation of the Electronic Structure of the Actinocenes $M(COT)_2$, M = Th, Pa, U, Np and Pu. *Chem. Phys.*, **122**, 357–374.

[284] Brennan, J. G., Green, J. C., and Redfern, C. M. (1989) Covalency in Bis([8]annulene)uranium from Photoelectron Spectroscopy with Variable Photon Energy. *J. Am. Chem. Soc.*, **111**, 2373–2377.

[285] Li, J. and Bursten, B. E. (1998) Relativistic Density Functional Study of the Geometry, Electronic Transitions, Ionization Energies, and Vibrational Frequencies of Protactinocene, Pa(η^8-C_8H_8)$_2$. *J. Am. Chem. Soc.*, **120**, 11456–11466.

[286] Löwdin, P.-O. (1955) Quantum Theory of Many-Particle Systems. I. Physical Interpretations by Means of Density Matrices, Natural Spin-Orbitals, and Convergence Problems in the Method of Configurational Interaction. *Phys. Rev.*, **97**, 1474–1489.

[287] Gagliardi, L., Lindh, R., and Karlstrom, G. (2004) Local Properties of Quantum Chemical Systems: The LoProp Approach. *J. Chem. Phys.*, **121**, 4494–4500.

[288] Pangborn, A. B., Giardello, M. A., Grubbs, R. H., Rosen, R. K., and Timmers, F. J. (1996) Safe and Convenient Procedure for Solvent Purification. *Organomet.*, **15**, 1518–1520.

[289] Schwindt, M. A., Lejon, T., and Hegedus, L. S. (1990) Improved Synthesis of (Aminocarbene)Chromium(0) Complexes with Use of C_8K-Generated $Cr(CO)_5^{2-}$. Multivariant Optimization of an Organometallic Reaction. *Organomet.*, **9**, 2814–2819.

[290] Miura, Y., Oka, H., Yamano, E., and Morita, M. (1997) Convenient Deuteration of Bromo Aromatic Compounds by Reductive Debromination with Sodium Amalgam in CH_3OD. *J. Org. Chem.*, **62**, 1188–1190.

[291] Ruppa, K. B. P., Desmangles, N., Gambarotta, S., Yap, G., and Rheingold, A. L. (1997) Preparation and Characterization of a Homoleptic Vanadium(III) Amide Complex and Its Transformation into Terminal Chalcogenide Derivatives [(3,5-Me_2Ph)AdN]$_3$VE (E = S, Se; Ad = Adamantyl). *Inorg. Chem.*, **36**, 1194–1197.

[292] Sheldrick, G. M. (2008) A short history of *SHELX*. *Acta Crystallogr. Sect. A*, **64**, 112–122.

[293] Grimme, S. (2006) Semiempirical GGA-type Density Functional Constructed with a Long-Range Dispersion Correction. *J. Comput. Chem.*, **27**, 1787–1799.

[294] Douglas, M. and Kroll, N. M. (1974) Quantum Electrodynamical Corrections to the Fine Structure of Helium. *Ann. Phys.*, **82**, 89–155.

[295] Roos, B. O., Lindh, R., Malmqvist, P. A., Veryazov, V., and Widmark, P. O. (2004) Main Group Atoms and Dimers Studied with a New Relativistic ANO Basis Set. *J. Phys. Chem. A*, **108**, 2851–2858.

[296] Forbes, T. Z., McAlpin, J. G., Murphy, R., and Burns, P. C. (2008) Metal-Oxygen Isopolyhedra Assembled into Fullerene Topologies. *Angew. Chem. Int. Ed.*, **47**, 2824–2827.

[297] Sigmon, G. E., Unruh, D. K., Ling, J., Weaver, B., Ward, M., Pressprich, L., Simonetti, A., and Burns, P. C. (2009) Symmetry Versus Minimal Pentagonal Adjacencies in Uranium-Based Polyoxometalate Fullerene Topologies. *Angew. Chem. Int. Ed.*, **48**, 2737–2740.

[298] Sigmon, G. E., Weaver, B., Kubatko, K.-A., and Burns, P. C. (2009) Crown and Bowl–Shaped Clusters of Uranyl Polyhedra. *Inorg. Chem.*, **48**, 10907–10909.

[299] Burns, P. C., Ewing, R. C., and Hawthorne, F. C. (1997) The Crystal Chemistry of Hexavalent Uranium: Polyhedron Geometries, Bond-Valence Parameters, and Polymerization of Polyhedra. *Can. Mineral.*, **35**, 1551–1570.

[300] Burns, P. C. (2005) U^{6+} Minerals and Inorganic Compounds: Insights into an Expanded Structural Hierarchy of Crystal Structures. *Can. Mineral.*, **43**, 1839–1894.

[301] Kubatko, K.-A., Forbes, T. Z., Klingensmith, A. L., and Burns, P. C. (2007) Expanding the Crystal Chemistry of Uranyl Peroxides: Synthesis and Structures of Di- and Triperoxodioxouranium(VI) Complexes. *Inorg. Chem.*, **46**, 3657–3662.

[302] Hagberg, D., Karlstrom, G., Roos, B. O., and Gagliardi, L. (2005) The Coordination of Uranyl in Water: A Combined Quantum Chemical and Molecular Simulation Study. *J. Am. Chem. Soc.*, **127**, 14250–14256.

[303] La Macchia, G., Brynda, M., and Gagliardi, L. (2006) Quantum Chemical Calculations Predict the Diphenyl Diuranium Compound [PhUUPh] to Have a Stable ^1A_g Ground State. *Angew. Chem. Int. Ed.*, **45**, 6210–6213.

[304] Clark, D. L., Conradson, S. D., Donohoe, R. J., Keogh, D. W., Morris, D. E., Palmer, P. D., Rogers, R. D., and Tait, C. D. (1999) Chemical Speciation of the Uranyl Ion Under Highly Alkaline Conditions. Synthesis, Structures, and Oxo Ligand Exchange Dynamics. *Inorg. Chem.*, **38**, 1456–1466.

[305] Ingram, K. I. M., Haeller, L. J. L., and Kaltsoyannis, N. (2006) Density Functional Theory Investigation of the Geometric and Electronic Structures of $[UO_2(H_2O)_m(OH)_N)]^{(2-n)}$ (n+m=5). *Dalton Trans.*, pp. 2403–2414.

[306] Huheey, J. E., Keiter, E. A., and Keiter, R. L. (1993) *Inorganic Chemistry: Principles of Structure and Reactivity*. HarperCollins, 4th edn.

[307] Nyman, M. and Alam, T. M. (2012) Dynamics of Uranyl Peroxide Nanocapsules. *J. Am. Chem. Soc.*, **134**, 20131–20138.

[308] Smith, W., Forester, T., and Todorov, I. T., The DL_POLY Classic User Manual. Published by Daresbury Laboratory, United Kingdom.

[309] Jorgensen, W. L., Chandrasekhar, J., Madura, J. D., Impey, R. W., , and Klein, M. L. (1983) Comparison of Simple Potential Functions for Simulating Liquid Water. *J. Chem. Phys.*, **79**, 926–925.

[310] Lee, S. and Rasaiah, J. C. (1996) Molecular Dynamics Simulation of Ion Mobility. 2. Alkali Metal and Halide Ions Using the SPC/E Model for Water at 25 °C. *J. Phys. Chem.*, **100**, 1420–1425.

[311] Fincham, D. (1992) Leapfrog Rotational Algorithms. *Mol. Simul.*, **8**, 165–178.

[312] Nosé, S. (1984) A Unified Formulation of the Constant Temperature Molecular-Dynamics Methods. *J. Chem. Phys.*, **81**, 511–519.

[313] Hoover, W. G. (1985) Canonical Dynamics: Equilibrium Phase-Space Distributions. *Phys. Rev. A*, **31**, 1695–1697.

[314] Fonseca Guerra, C., Snijders, J. G., te Velde, G., and Baerends, E. J. (1998) Towards an Order-N DFT Method. *Theor. Chem. Acc.*, **99**, 391–403.

[315] Andzelm, J., Kolmel, C., and Klamt, A. (1995) Incorporation of Solvent Effects into Density-Functional Calculations of Molecular-Energies and Geometries. *J. Chem. Phys.*, **103**, 9312–9320.

[316] Allen, P. G., Bucher, J. J., Shuh, D. K., Edelstein, N. M., and Reich, T. (1997) Investigation of Aquo and Chloro Complexes of UO_2^{2+}, NpO_2^{+}, Np^{4+}, and Pu^{3+} by X-ray Absorption Fine Structure Spectroscopy. *Inorg. Chem.*, **36**, 4676–4683.

[317] Guildbaud, P. and Wipff, G. (1996) Force field representation of the UO_2^{2+} cation from free energy MD simulations in water. Tests on its 18-crown-6 and NO_3 adducts, and on its calix[6]arene^{6-} and CMPO complexes. *J. Mol. Struct. (THEOCHEM)*, **366**, 55–63.

[318] Hitschka, F., Dedieu, A., Troxler, L., and Wipff, G. (1998) Theoretical Studies on the UO_2^{2+} and Sr^{2+} Complexation by Phosphoryl-Containing OPR_3 Ligands: QM ab Initio Calculations in the Gas Phase and MD FEP Calculations in Aqueous Solution. *J. Phys. Chem. A*, **102**, 3773–3781.

[319] Rai, N., Tiwari, S. P., and Maginn, E. J. (2012) Force Field Development for Actinyl Ions via Quantum Mechanical Calculations: An Approach to Account for Many Body Solvation Effects. *J. Phys. Chem. B*, **116**, 10885–10897.

[320] Burns, P. C. (2005) U^{6+} Minerals and Inorganic Compounds: Insights into an Expanded Structural Hierarchy of Crystal Structures. *CANADIAN MINERALOGIST*, **43**, 1839–1894.

[321] Unpublished results from J. Qiu and P. C. Burns.

[322] Unpublished work by R. Johnson, P. C. Burns, and W. Casey.

[323] Garcia-Ratés, M., Miró, P., Poblet, J. M., Bo, C., and Avalos, J. B. (2011) Dynamics of Encapsulated Water inside Mo_{132} Cavities. *J. Phys. Chem. B*, **115**, 5980–5992.

[324] Wang, S., Diwu, J., Alekseev, E. V., Jouffret, L. J., Depmeier, W., and Albrecht-Schmitt, T. E. (2012) Cation-Cation Interactions Between Neptunyl(VI) Units. *Inorg. Chem.*, **51**, 7016–7018.

[325] Wang, S., Alekseev, E. V., Depmeier, W., and Albrecht-Schmitt, T. E. (2011) $K(NpO_2)_3(H_2O)Cl_4$: A Channel Structure Assembled by Two- and Three-Center Cation-Cation Interactions of Neptunyl Cations. *Inorg. Chem.*, **50**, 4692–4694.

[326] Jin, G. B., Skanthakumar, S. ., and Soderholm, L. . (2011) Cation-Cation Interactions: Crystal Structures of Neptunyl(V) Selenate Hydrates, $(NpO_2)_2(SeO_4)(H_2O)_n$ (n=1, 2, and 4). *Inorg. Chem.*, **50**, 5203–5214.

[327] Jin, G. B., Skanthakumar, S., and Soderholm, L. (2011) Two New Neptunyl(V) Selenites: A Novel Cation-Cation Interaction Framework in $(NpO_2)_3(OH)(SeO_3)(H_2O)_2$ Center Dot H_2O and a Uranophane-Type Sheet in $Na(NpO_2)(SeO_3)(H_2O)$. *Inorg. Chem.*, **50**, 6297–6303.

[328] Arnold, P. L., Love, J. B., and Patel, D. (2009) Pentavalent Uranyl Complexes. *Coord. Chem. Rev.*, **253**, 1973–1978.

[329] Skanthakumar, S. ., Antonio, M. R., and Soderholm, L. . (2008) A Comparison of Neptunyl(V) and Neptunyl(VI) Solution Coordination: The Stability of Cation-Cation Interactions. *Inorg. Chem.*, **47**, 4591–4595.

[330] McKee, M. L. and Swart, M. (2005) Study of Hg_2^{2+} and Complexes of NpO_2^+ and UO_2^{2+} in Solution. Examples of Cation-Cation Interactions. *Inorg. Chem.*, **44**, 6975–6982.

[331] Guillaume, B., Begun, G. M., and Hahn, R. L. (1982) Raman Spectrometric Studies of Cation Cation Complexes of Pentavalent Actinides in Aqueous Percholorate Solutions. *Inorg. Chem.*, **21**, 1159–1166.

[332] Guillaume, B., Hahn, R. L., and Narten, A. H. (1983) Investigations of Cation Cation Complexes of NpO_2^+ Solutions by Large-Angle X-ray-Scattering. *Inorg. Chem.*, **22**, 109–111.

[333] Stout, B. E., Choppin, G. R., Nectoux, F., and Pages, M. (1993) Cation-Cation Complexes of NpO_2^+. *Radiochim. Acta*, **61**, 65–67.

[334] Den Auwer, C., Gregoire-Kappenstein, A. C., and Moisy, P. (2003) Np(V) Cation-Cation Interactions. A New Contribution from EXAFS Spectroscopy? *Radiochim. Acta*, **91**, 773–776.

[335] Adelani, P. O. and Burns, P. C. (2012) One-Dimensional Uranyl-2,2'-Bipyridine Coordination Polymer with Cation-Cation Interactions: $(UO_2)_2$(2,2'-bpy)(CH_3CO_2)(O)(OH). *Inorg. Chem.*, **51**, 11177–11183.

[336] Cousson, A., Dabos, S., Abazli, H., Nectoux, F., Pages, M., and Choppin, G. (1984) Crystal-Structure of a Neptunyl Cation-Cation Complex (NpO_2^+) with Mellitic Acid - $Na_4(Npo_2)_2C_{12}O_{12}.8H_2O$. *J. Less-Common Met.*, **99**, 233–240.

[337] Grigoriev, M. S., Krot, N. N., Bessonov, A. A., and Suponitsky, K. Y. (2007) Dimeric Dioxocations, $(NpO_2^+)_2$, in the Structure of Bis(μ-2-Fluorobenzoato-κ^2 O:O')Di-μ-Oxo-Bis[(2,2'-Bipyridine-κ^2N,N')Oxoneptunium(V)]. *Acta Crystallogr. Sect. E*, **63**, M561–M562.

[338] Forbes, T. Z., Burns, P. C., Skanthakumar, S., and Soderholm, L. (2007) Synthesis, Structure, and Magnetism of Np_2O_5. *J. Am. Chem. Soc.*, **129**, 2760–2761.

[339] Almond, P. M., Skanthakumar, S. ., Soderholm, L. ., and Burns, P. C. (2007) Cation-Cation Interactions and Antiferromagnetism in Na[Np(V)O-2(OH)(2)]: Synthesis, Structure, and Magnetic Properties. *Chem. Mater.*, **19**, 280–285.

[340] Ma, D., LI Manni, G., and Gagliardi, L. (2011) The Generalized Active Space Concept in Multiconfigurational Self-Consistent Field Methods. *J. Chem. Phys.*, **135**, 044128.

[341] Jin, G. B., Skanthakumar, S., and Soderholm, L. (2012) Three New Sodium Neptunyl(V) Selenate Hydrates: Structures, Raman Spectroscopy, and Magnetism. *Inorg. Chem.*, **51**, 3220–3230.

[342] Forbes, T. Z., Burns, P. C., Soderholm, L., and Skanthakumar, S. (2006) Crystal Structures and Magnetic Properties of $NaK_3(NpO_2)_4(SO_4)_4(H_2O)_2$ and

$NaNpO_2So_4H_2O$: Cation-Cation Interactions in a Neptunyl Sulfate Framework. *Chem. Mater.*, **18**, 1643–1649.

[343] Jobiliong, E., Oshima, Y., Brooks, J. S., and Albrecht-Schmitt, T. E. (2004) Magnetism and Electron Spin Resonance in Single Crystalline β-$AgNpO_2(SeO_3)$. *Solid State Commun.*, **132**, 337–342.

[344] Mitoraj, M. P., Michalak, A., and Ziegler, T. (2009) A Combined Charge and Energy Decomposition Scheme for Bond Analysis. *J. Chem. Theory Comput.*, **5**, 962–975.

[345] Mitoraj, M. P., Michalak, A., and Ziegler, T. (2009) On the Nature of the Agostic Bond between Metal Centers and beta-Hydrogen Atoms in Alkyl Complexes. An Analysis Based on the Extended Transition State Method and the Natural Orbitals for Chemical Valence Scheme (ETS-NOCV). *Organomet.*, **28**, 3727–3733.

[346] Ehrhradt, C. and Ahlrichs, R. (1985) Population Analysis Based on Occupation Numbers .2. Relationship Between Shared Electron Numbers and Bond-Energies and Characterization of Hypervalent Contributions. *Theor. Chem. Acc.*, **68**, 231–245.

[347] Adamo, C. and Barone, V. (1999) Toward Reliable Density Functional Methods Without Adjustable Parameters: The PBE0 Model. *J. Chem. Phys.*, **110**, 6158–6170.

Appendix A

Acronyms

Care has been taken in this thesis to minimize the use of acronyms, but this cannot always be achieved. This appendix contains a table of acronyms and their meaning.

Table A.1: Acronyms

Acronym	Meaning
ADF	Amsterdam Density Functional
ALD	Atomic Layer Deposition
An	Actinide
ANO-RCC	Atomic Natural Orbital Relativistic with Core Correlation Basis Sets
B3LYP	A hybrid functional with Becke's exchange and Lee-Yang-Parr's correlation functional
BCP	Bond Critical Point
BHM	Born-Huggins-Meyer
BPW91	A local functional with Becke's exchange and Perdew-Wang's correlation functional
CASSCF	Complete Active Space Self Consistent Field theory
CASSI	Complete Active Space State Interaction

Continued on next page

Table A.1 – continued from previous page

Acronym	Meaning
CASPT2	Complete Active Space Self Consistent Field theory with corrections from second-order perturbation theory
CCI	Cation-Cation Interaction
CN	Coordination Number
COSMO	Conductor-like Screening Model
CVD	Chemical Vapor Deposition
DFT	Density Functional Theory
DKH	Douglas-Kroll-Hess
DMADB	dimethyaminodiboranate
DOE	Department of Energy
EBO	Effective Bond Order
ECP	Effective Core Potential
ESR	Electron Spin Resonance
ETS–NOCV	The Extended Transition State Method Combined with Natural Orbitals for Chemical Valence Theory
EXAFS	Extended X-ray Absorption Fine Structure
FI-MS	Field Ionization Mass Spectrometry
FTIR	Fourier Tranform Infrared Spectroscopy
GASSCF	Generalized Active Space Self Consistent Field theory
HDEHP	di-(2-ethylhexyl)phosphoric
HOMO	Highest Occupied Molecular Orbital
LUMO	Lowest Unoccupied Molecular Orbital
Ln	Lanthanide
MBO	Mayer Bond Order
MO	Molecular Orbital
MN-GSM	Minnesota Gaussian Solvation Module
MP2	Second-Order Møller-Plesset Perturbation Theory
MUD	Mean Unsigned Difference
NMR	Nuclear Magnetic Resonance

Continued on next page

Table A.1 – continued from previous page

Acronym	Meaning
NPT	Constant Number of Particles, Pressure, and Temperature
NVE	Constant Number of Particles, Volume, and Energy
NVT	Constant Number of Particles, Volume, and Temperature
PBE	A local functional by Perdew, Burke, and Ernzerhof
$PhDipp_2$	C_6H_3-2,6-(C_6H_3-2,6-iPr_2)$_2$
PUREX	Plutonium–Uranium Extraction process
RASSI	Restricted Active Space State Interaction
RDF	Radial Distribution Function
SDD	Pseudopotentials of the Stuttgart/Bonn group
SDF	Spatial Distribution Function
SO	Spin-Orbit
SOMO	Singly Occupied Molecular Orbital
SQUID	Superconducting Quantum Interference Device
THF	Tetrahydrofuran
TIP	Temperature-Independent Paramagnetism
UV	Ultraviolet
VWN	A local correlation functional by Vosko, Wilk, and Nusair
XANES	X-ray Absorption Near Edge Structure
ZORA	Zero-Order Regular Approximation